Astron Report 7114-01

VIBRATION TEST PROCEDURES FOR ORBITER SIDEWALL-MOUNTED PAYLOADS PHASE I FINAL REPORT

A. G. Piersol
P. H. White
J. F. Wilby
P. J. Hipol
E. G. Wilby

NOVEMBER 1988

CONTRACT F04701-87-C-0010

Prepared for:

USAF/AFSC
H. Q. Space Division
P. O. Box 92960
Los Angeles, CA 90009-2960

Prepared by:

Astron Research and Engineering
3228 Nebraska Avenue
Santa Monica, CA 90404

UNCLASSIFIED
SECURITY CLASSIFICATION OF THIS PAGE

REPORT DOCUMENTATION PAGE

Form Approved
OMB No. 0704-0188

1a. REPORT SECURITY CLASSIFICATION UNCLASSIFIED	1b. RESTRICTIVE MARKINGS NONE
2a. SECURITY CLASSIFICATION AUTHORITY	3. DISTRIBUTION/AVAILABILITY OF REPORT UNLIMITED DISTRIBUTION
2b. DECLASSIFICATION/DOWNGRADING SCHEDULE	
4. PERFORMING ORGANIZATION REPORT NUMBER(S) 7114-01	5. MONITORING ORGANIZATION REPORT NUMBER(S)
6a. NAME OF PERFORMING ORGANIZATION Astron Research & Engineering 6b. OFFICE SYMBOL (If applicable)	7a. NAME OF MONITORING ORGANIZATION USAF/AFSC
6c. ADDRESS (City, State, and ZIP Code) 3228 Nebraska Avenue Santa Monica, CA 90404	7b. ADDRESS (City, State, and ZIP Code) HQ Space Division P.O. Box 92960 Los Angeles, CA 90009-2960
8a. NAME OF FUNDING/SPONSORING ORGANIZATION USAF/AFSC 8b. OFFICE SYMBOL (If applicable)	9. PROCUREMENT INSTRUMENT IDENTIFICATION NUMBER
8c. ADDRESS (City, State, and ZIP Code) HQ Space Division P.O. Box 92960 Los Angeles, CA 90009-2960	10. SOURCE OF FUNDING NUMBERS PROGRAM ELEMENT NO. / PROJECT NO. / TASK NO / WORK UNIT ACCESSION NO.
11. TITLE (Include Security Classification) Vibration Test Procedures for Orbiter Sidewall-Mounted Payloads, Phase I Final Report	
12. PERSONAL AUTHOR(S) Piersol, Allan G., White, Pritchard H., Wilby, Emma G., Wilby, John F.	
13a. TYPE OF REPORT FINAL 13b. TIME COVERED FROM _____ TO ~~JAN 89~~	14. DATE OF REPORT (Year, Month, Day) ~~1989 JAN 18~~ NOV 88 15. PAGE COUNT
16. SUPPLEMENTARY NOTATION	
17. COSATI CODES FIELD / GROUP / SUB-GROUP	18. SUBJECT TERMS (Continue on reverse if necessary and identify by block number)

19. ABSTRACT (Continue on reverse if necessary and identify by block number)

Mechanical vibration tests of payloads mounted on the Space Shuttle Vehicle (SSV) cargo bay sidewall are currently performed in compliance with USAF Space Division Document SD-CF-0206, which specifies an acceleration level at the input to the payload. This procedure does not take into account the "loading" of the sidewall structure by the payload at the resonance frequencies of the payload where the payload apparent weight becomes large. The result is potentially severe overtesting of payloads at their resonance frequencies where payload damage is most likely. In this study, a new mechanical vibration test procedure has been developed that takes into account the mounting point impedance of the sidewall structure, and allows a well defined reduction or "notching" of the input acceleration levels at payload resonances based upon an input force limit to the payload. The validity and practicality of the procedure has been demonstrated by experiments on a simulated OASIS payload with an Adaptive Payload Carrier (APC). A complete vibration test specification detailing the procedure is presented.

20. DISTRIBUTION/AVAILABILITY OF ABSTRACT ☒ UNCLASSIFIED/UNLIMITED ☐ SAME AS RPT ☐ DTIC USERS	21. ABSTRACT SECURITY CLASSIFICATION UNCLASSIFIED
22a. NAME OF RESPONSIBLE INDIVIDUAL	22b. TELEPHONE (Include Area Code) / 22c. OFFICE SYMBOL

DD Form 1473, JUN 86 Previous editions are obsolete

SECURITY CLASSIFICATION OF THIS PAGE

Table of Contents

List of Figures

List of Tables

List of Symbols

$A(f)$	Fourier transform of interface acceleration between mounting structure and attached payload in g-units
A_n	area associated with finite element node point n
$A_s(f)$	Fourier transform of free acceleration of unloaded mounting structure in g-units
c	damping coefficient
c_o	speed of sound in air
$C(f)$	Fourier transform of shaker armature current
f	frequency in Hz
f_n	undamped natural frequency
$F(f)$	Fourier transform of interface force between mounting structure and attached payload in lb.
$F_B(f)$	Fourier transform of "blocked force", $F_B(f) = W_s(f)A_s(f)$
$F_R(f)$	Fourier transform of "reaction force", $F_R(f) = W_s(f)A(f)$
$G_{AA}(f)$	autospectrum of acceleration at interface between mounting structure and payload in $(\text{g-units})^2/\text{Hz}$
$G_{BB}(f)$	autospectrum of "blocked force" in lb^2/Hz
$G_{CA}(f)$	cross-spectrum between shaker armature current and shaker table acceleration in amp(g-units)/Hz
$G_{CC}(f)$	autospectrum of shaker armature current in amp^2/Hz
$G_{FA}(f)$	cross-spectrum between interface force and acceleration in (g-units)lb/Hz
$G_{FF}(f)$	autospectrum of interface force in lb^2/Hz
$G_{nm}(f)$	excitation pressure cross spectral density
$G_{pp}(f)$	autospectrum of payload response
$G_{SS}(f)$	autospectrum of acceleration response of mounting structure without payload present in $(\text{g-units})^2/\text{Hz}$

$G_{SS}(f)_c$	computed autospectrum of unloaded mounting point vibration corresponding to a loaded mounting point vibration spectrum (Eq. 27)
$G_{TT}(f)$	autospectrum of specified vibration test level in $(g\text{-units})^2/Hz$
$G_{xx}(f)$	autospectrum of displacement at interface between mounting structure and payload in in^2/Hz
$G_{yy}(f)$	autospectrum of displacement response of mounting structure without payload present in in^2/Hz
H(f)	frequency response function between acceleration of mounting structure and acceleration at selected point on payload
$H_{CA}(f)$	frequency response function between shaker armature current and shaker table acceleration in g-units/amp
$H_{FA}(f)$	frequency response function between force applied to payload under test and the acceleration of the payload
$H_{ns}(f)$	frequency response function giving response at finite element node s due to a unit pressure at node n
I(f)	inertance in lb^{-1}, $I(f) = 1/W(f)$
j	$\sqrt{-1}$
k	spring constant or acoustic wavenumber
K(f)	calibration factor relating shaker armature current to force in lb/amp
m	mass
V(f)	Fourier transform of interface velocity between mounting structure and attached payload in in/sec
$V_s(f)$	Fourier transform of free velocity of unloaded mounting structure in in/sec
W_a	weight of shaker armature and shaker table
W_f	weight of fixture attached to shaker table
W(f)	apparent weight in lb, $W(f) = jgZ(f)/(2\pi f)$
$W_o(f)$	corrected mounting point apparent weight in lb, $W_o(f) = W_s(f) + W_T$

$W_p(f)$	apparent weight of payloads, in lb
$W_s(f)$	source apparent weight of payload mounting structure, in lb
W_{se}	conservative envelope of apparent weight in lb
W_T	total suspended weight of shaker table and fixture, $W_T = W_a + W_f$
$Y(f)$	mobility in in/lb-sec, $Y(f) = 1/Z(f)$
$Y_p(f)$	driving point mobility of payload, in in/lb-sec
$Y_s(f)$	source mobility of mounting structure, in in/lb-sec
$Z_{ep}(f)$	envelope of driving point impedance of payload, in lb-sec/in
$Z_{es}(f)$	envelope of source impedance of mounting structure
$Z_p(f)$	driving point impedance of payload (looking into payload mounting points) in lb-sec/in
$Z_s(f)$	source impedance of mounting structure (looking into mounting points for an attached payload) in lb-sec/in
$\gamma^2(f)$	coherence function between variables x and y, $\gamma^2(f) = \lvert G_{xy}(f)\rvert^2/G_{xx}(f)G_{yy}(f)$
ζ	damping ratio
η	loss factor; or separation distance in z-direction between nodes n and m of finite element model, $\eta = z_n - z_m$
ξ	separation distance in y-direction between nodes n and m of finite element model, $\xi = y_n - y_m$
ω	frequency, rads/sec
$< >$	average over given frequency band
$< >_m$	moving average in frequency domain
$*$	complex conjugate
$\lvert\ \rvert$	modulus of complex function

Acknowledgement

The authors wish to acknowledge the assistance provided by several people during the performance of the Phase I work. Lt. Charles Brown of U.S. Air Force Space Division and Mr. Don Wong of The Aerospace Corporation provided support throughout Phase I and ensured that required facilities and personnel were available at NASA Goddard Space Flight Center and NASA Johnson Space Center for planned test programs. Thanks are due to personnel at GSFC for their help in performing mechanical impedance tests on Shuttle Orbiter OV-101 and to personnel at JSC for help in measurements of panel and payload response to acoustic excitation. Thanks are also due to Dr. Sally McInerny and Dr. Sheldon Rubin of The Aerospace Corporation and Dr. Terry Scharton of Jet Propulsion Laboratory for their helpful comment. and suggestions.

1. INTRODUCTION

1.1 Background

Due to the high acoustic levels in the Space Shuttle orbiter payload bay, the final dynamic testing of orbiter payloads is usually accomplished using random acoustic excitation. This is appropriate for payloads with large exterior surface areas, since the vibration environment induced by acoustic impingement on the exposed surfaces dominates the structureborne vibratory energy transmitted through the payload attachment points from the orbiter vehicle, at least at frequencies above about 50 Hz. For smaller payloads, however, this is not always true, particularly for payloads with open truss structures or other exterior surfaces that have dimensions smaller than the wavelengths of the payload bay acoustic pressure field. In such cases, it is probable that the vibration transmitted through the attachment points from the orbiter structure will dominate the acoustic-induced vibration levels, meaning that the payload will be undertested by conventional acoustic tests, at least at frequencies below 300 Hz where the acoustic wavelengths at lift-off are in excess of 4 ft. Hence, direct mechanical vibration at the payload attachment points becomes necessary to test these payloads properly for their dynamic environment.

Mechanical vibration tests for space vehicle payloads were introduced in the late 1950's and were widely employed by both NASA and USAF, and their contractors, into the 1970's. Such testing techniques for full-scale payloads started yielding to acoustic tests in the late 1970's, at least at frequencies above 50 Hz, for three important reasons:

(a) It was assumed (sometimes incorrectly) that the payload vibration environment was due primarily to direct acoustic excitation rather than structureborne excitation through the payload attachment points.

(b) Acoustic test facilities became available which could provide the needed acoustic levels for testing purposes at reasonable cost.

(c) Accurate vibration testing of payloads exceeding a few hundred pounds in weight was not feasible due to the inability of vibration testing shakers to match the impedance of the actual structure to which the payload was attached in service. This problem was aggravated by the fact that some payloads have multiple attachment points with different vibration levels and source impedances.

The last noted problem is one that still restricts the ability to perform accurate vibration tests on entire payload assemblies today. Since there is clearly a need to perform vibration tests on certain types of small payloads where acoustic tests are not appropriate, a resolution to this testing machine interface impedance problem is needed.

1.2 Technical Discussion

A number of basic documents such as References 1 through 3, that summarize general procedures for arriving at vibration tests specifications for spacecraft and their components, have been published over the years. Beyond these basic documents, literally hundreds of other technical papers have been published on the subject. An underlying problem acknowledged in many of these documents and papers is the interface impedance and multiple attachment point problem inherent in the vibration testing of large structural assemblies such as spacecraft or other space vehicle payloads.

The interface impedance problem evolves from the fact that the vibration input at payload attachment points depends heavily upon the detailed dynamic characteristics of the payload and the structure to which it attaches. Using mechanical analogies to Morton's theorem, the problem can be illustrated using the circuit shown in Figure 1 where

$F(f)$ = Fourier transform of the force applied to a structure with a mounting point impedance of $Z_s(f) = F(f)/V_s(f)$

$V_s(f)$ = Fourier transform of the velocity response of the unloaded structure

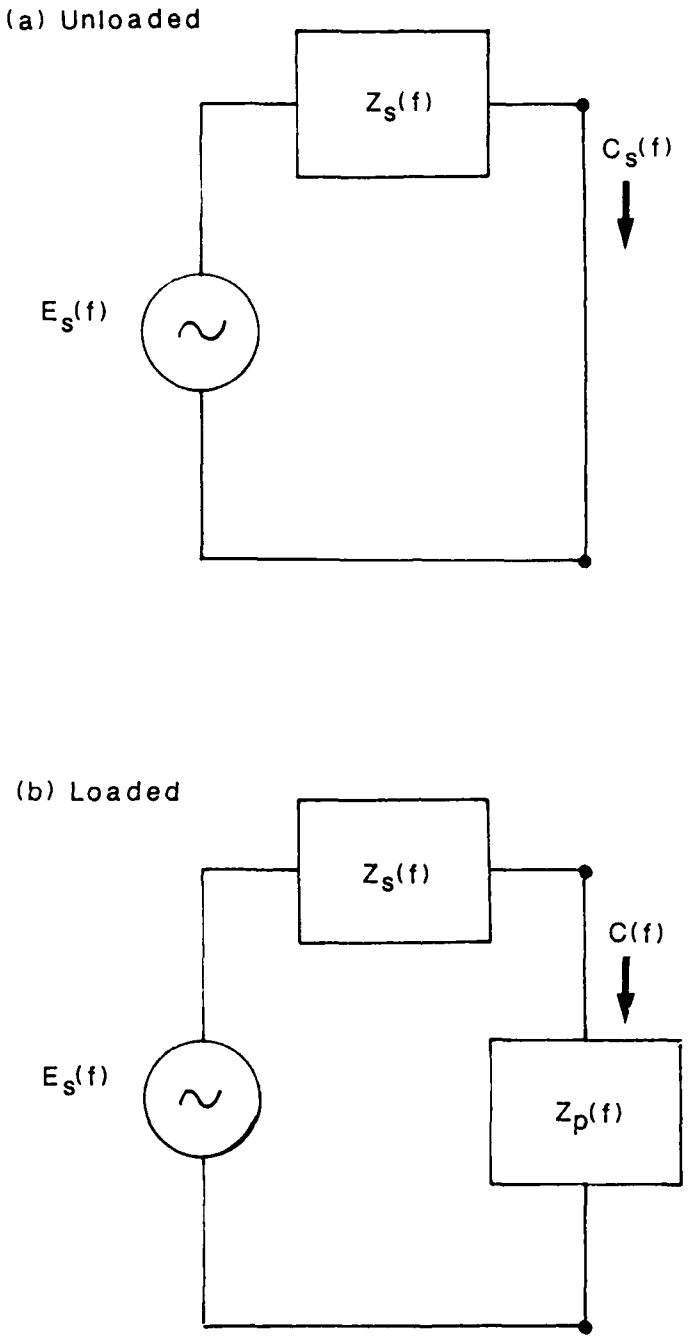

FIGURE 1. EQUIVALENT ELECTRIC CIRCUITS FOR UNLOADED AND LOADED MOUNTING STRUCTURE - PAYLOAD VELOCITY LEVELS.

$V(f)$ = Fourier transform of the velocity response of the structure loaded with a second substructure (payload) having a driving point impedance of $Z_p(f)$.

The force and velocities for the unloaded structure in Figure 1(a) are related by

$$F(f) = V_s(f)Z_s(f) \tag{1}$$

When a load with a driving point impedance of $Z_p(f)$ is introduced, as shown in Figure 1(b), the force and velocity relationship is

$$F(f) = V(f)[Z_s(f) + Z_p(f)] \tag{2}$$

It follows from Eqs. (1) and (2) that

$$V_s(f)Z_s(f) = V(f)[Z_s(f) + Z_p(f)] \tag{3}$$

which may be written as

$$V(f)/V_s(f) = 1/[1 + Z_p(f)/Z_s(f)] \tag{4}$$

It is clear from Eq. 4 that the interface velocity between the mounting structure and the payload is a function of the mounting point impedance, as well as the payload impedance. In particular, at the resonance frequencies of the payload, where $Z_p(f)$ becomes very large, the velocity of the mounting structure is reduced. However, vibration test specifications, which generally represent an envelope of the free mounting structure vibration levels, do not allow for this reduction in vibration level at the resonance frequencies of the payload; they essentially test the payload as if the source impedance, $Z_s(f) \gg Z_p(f)$, which may not be true in practice.

Throughout the research and analyses described in this report it has been assumed that the structure of the orbiter, the adaptive payload carrier, and the payload are linear. This linearity assumption implies that the deflection of any point is directly proportional to the magnitude and direction of the

applied force, and that the damping is small and may be represented by an equivalent viscous or hysteretic damping. These are common and well justified assumptions for most aerospace structures. A feature not covered by the linearity assumption is the presence of gaps or clearances at the attachments of the Adaptive Payload Carrier (APC) to the orbiter sidewall. These gaps allow the APC to rattle; the influence of the gaps on a vibration test procedure will be investigated in the Phase II effort.

1.3 Testing Procedures

In practice, direct mechanical vibration tests of large test articles, like space vehicle payloads, are usually performed using either an electrodynamic or hydraulic driven shaker which has an output impedance that bears little resemblance to the output impedance of the structure to which the payload attaches in service. More importantly, it has been traditional to specify vibration test criteria in terms of a shaker table motion, usually stated in terms of an acceleration spectral density (in g^2/Hz) as a function of frequency. An equalizer system in the shaker control system then adjusts the input power to the shaker to whatever value is needed to maintain the specified table motion. This is essentially forcing the shaker to appear as if it has an infinite output impedance; i.e., the test item does not load the shaker table nor does its presence cause the shaker to change its vibratory motion. The result is often severe overtesting of the test article, particularly at the resonance frequencies of the test article.

Many approaches have been proposed over the years to deal with this inherent problem in mechanical vibration testing, including the following.

1. Force-controlled vibration testing.
2. Testing of the test article on its support structure.
3. "Notching" of the specified test levels.
4. Testing with multiple mode test fixtures.
5. Response-controlled testing.
6. Analytical corrections for the interface impedance.

Vibration testing based on specified input forces rather than input motions would alleviate the interface impedance problem, but this approach requires an accurate prediction of the input forces from the support structure, which is not the customary way of predicting vibration environments. The procedure would also require the use of force transducers between the shaker table and test article during testing, which is more complicated than controlling the motion of the shaker table.

Mounting the test article on its natural support structure and testing the entire assembly is a viable approach for relatively small components, but is generally impractical for Space Shuttle payloads since it would require a dynamically-accurate physical mode of the orbiter in a test facility that could reproduce the lift-off acoustic loads.

"Notching" of the specified test levels means that the shaker table vibration levels are allowed to decrease below the specified test levels at frequencies where the test article displays resonant responses. This procedure is somewhat arbitrary and, hence, allows for the possibility of undertesting.

Testing with a multiple mode test fixture that simulates a general multi-mode support structure was originally proposed in Reference 4. Like notching, the procedure is somewhat arbitrary since the test fixture impedance will not necessarily represent the mounting point impedance for the test article in practice.

Response-controlled testing is the most common approach employed at this time to suppress the overtesting that may result due to the interface impedance problem. References 5 and 6 present early arguments for response-controlled testing, which has since been recommended for the testing of relatively heavy aerospace payloads (such as externally carried aircraft stores) in MIL-STD-810C. Such an approach for Space Shuttle payloads is restricted by the fact that payload response environments are not well defined.

The use of analytical corrections to vibration test specifications that will account for the interface impedance has historically reduced to little more than mass law corrections which do not really solve the problem. In this

respect, it is often argued that one rarely has sufficient knowledge of the mounting point impedance of the support structure to justify any action beyond a mass law correction with "notching" at test article resonances.

Although none of the preceding approaches has been fully successful in eliminating the interface impedance problem in general vibration testing, the premise of the present study is that one or more of the approaches might be effective in dealing with the problem for the specific case of Space Shuttle payloads, for two reasons:

1. The Space Shuttle presents a relatively small number of mounting point impedance functions for payloads, and these impedance functions can be measured.

2. Most mechanical vibration testing today is accomplished using computer controlled shakers which allow enormous flexibility in the design of test levels.

Hence, a thorough study has been performed of possible procedures for specifying accurate mechanical vibration tests of Space Shuttle payloads, which properly account for the mounting point impedance problem. The study has the objective of improving payload vibration test procedures for those Space Shuttle payloads (generally the small, sidewall-mounted payloads) where the vibration environment is dominated by the structureborne transmission of energy from the orbiter through the payload attachment points.

1.4 Response Functions

The fundamental presentation given in Section 1.2 is in terms of mechanical impedance Z(f), which is defined as the ratio of excitation force to response velocity

$$Z_p(f) = F(f)/V(f) \qquad (5)$$

The inverse of the impedance is the mobility function Y(f). Equally well, the response could be presented in terms of the apparent weight $W_p(f)$

$$W_p(f) = F(f)/A(f) \tag{6}$$

where A(f) is the Fourier transform of the interface acceleration a(t), measured in g units. The reciprocal of the apparent weight is the inertance I(f). These parameters are interrelated, for example

$$\begin{aligned} V(f)/V_s(f) &= [1 + Z_p(f)/Z_s(f)]^{-1} \\ &= [1 + W_p(f)/W_s(f)]^{-1} \\ &= A(f)/A_s(f) \end{aligned} \tag{7}$$

The parameters are used essentially interchangeably in this report.

1.5 Report Organization

The report is divided into the main text and a number of appendices. Section 2 of the report presents the results of a literature search for documents associated with vibration test procedures and outlines the three procedures selected for study. The procedures are motion correction, blocked force-limit and apparent-weight-simulation. Most of the characteristics associated with the impedance problem are illustrated in Section 3 by means of the analysis of a 1-dof payload on a simple panel. Then Section 4 discusses a finite element analysis of an OASIS-1 payload attached to the sidewall of the Space Shuttle payload bay.

Sections 5 through 8 present the results from a variety of experiments. Impedance measurements were made on the sidewall structure of Shuttle orbiter OV-101 (Enterprise); the results are presented in Section 5. In laboratory studies, a simple stiffened panel and a multi-dof payload were tested with reverberant acoustic (Section 6) and mechanical vibration (Section 7) excitations. The results from these two tests are evaluated in Section 8. Then, conclusions from Phase I and recommendations for Phase II are given in Section 9.

Four appendices are attached to the report. Appendix A presents short reviews of 66 documents reviewed as a result of the literature search. Appendix B

contains data from the OV-101 impedance measurements. Appendix C presents data from the acoustic excitation tests on the simple panel and Appendix D contains data from the vibration (shaker) tests on the simplified payload.

2.0 DISCUSSION OF APPROACHES

The study began with a thorough literature search and review of prior investigations of the mounting point impedance problem in mechanical vibration testing. Various references were evaluated in the specific context of possible vibration testing procedures appropriate for Space Shuttle orbiter sidewall-mounted payloads. From these evaluations, candidate procedures were selected for experimental investigations.

2.1 Literature Survey

Using primarily the STAR and DIALOG information services, a total of 64 references were identified that directly relate to the mounting point impedance problem in mechanical vibration testing. These references are listed with brief summaries in Appendix A. It is seen in Appendix A that the references are divided into six broad categories, as follows:

(a) General References - 24
(b) Input Force Control Procedures - 12
(c) Response Control Procedures - 9
(d) Impedance Correction Procedures - 7
(e) Impedance Simulation Procedures - 7
(f) Acoustic Testing Procedures - 5

It should be emphasized that the above division of the references is very general and many of the references actually suggest procedures that fall into two or more of the noted categories.

After a preliminary review of the references, several approaches were immediately discarded as being inappropriate for Space Shuttle sidewall-mounted payload applications. These immediately-discarded approaches were:

1. Those input force control procedures that require the use of force gages between the test item and its supporting structure or the shaker (e.g., Appendix A, [2-5]) were not considered practical because reliable transducers that will measure a net force into a test item with multiple

attachment points are not readily available. However, those input force control procedures based upon estimated input forces, using input acceleration and impedance measurements, or the armature current in an electrodynamic shaker, were viewed as practical and received further consideration.

2. Those response control procedures that require actual response measurements on the payload in service (e.g., Appendix A, [3-3]) were not considered practical for Space Shuttle applications since most Shuttle payloads represent unique designs. However, those response control procedures that use calculated response limits were viewed as practical and received further consideration.

3. Impedance simulation procedures involving mechanical devices (special fixtures) have shown some promise at the higher frequencies where the modal density of the mounting structure is high (Appendix A, [5-6]), but the technique is not effective at the lower frequencies of interest for Space Shuttle applications. However, electrical impedance simulation in the shaker was considered practical and received further consideration.

4. To be effective and accurate for Space Shuttle applications, the acoustic testing approach would require a detailed mechanical model of the orbiter sidewall structure, and an acoustic test facility that is large enough to enclose the sidewall model and simulate orbiter lift-off acoustic levels. Very few contractors have the capability to build and operate such a test facility and, hence, this approach was not considered further.

Those references covering the approaches considered viable were studied further to arrive at a final selection of candidate procedures. Actually, the final selection of candidate procedures was not made until after extensive parametric studies of simple computer models (covered in Section 3), and discussions with the Air Force contract monitors. The final selection involves three approaches, which will henceforth be identified as follows:

1. The motion correction procedure.
2. The blocked force limit procedure.
3. The apparent weight simulation procedure.

In each of the above listed procedures one common simplifying assumption is made; the motion of the structure at the payload mounting points can be represented by a spectrum (in each direction) at a single reference point, and the payload will be tested on a shaker table having uniform motion at all attachment points. This assumption reduces the complex, multi-degree-of-freedom motion of the mounting point and payload to rectilinear motion in the 3 principal axes. The assumption is justified by its success in many years of environmental testing experience, and by the lack of a credible and feasible procedure to do otherwise. Procedures for the determination of equivalent single point impedances (or mobilities, inertances, apparent weights) for payloads and structures with multiple attachment points are given in Section 7.4.

2.2 Orbiter Sidewall Vibration Test Specification

Before detailing the candidate vibration testing procedures, it is important to review the current vibration test criterion for Space Shuttle orbiter sidewall-mounted payloads, and the manner in which it may lead to the severe overtesting of payloads. The applicable test specification is SD-CF-0206 [7]. The specific vibration test criterion in terms of an acceleration auto (power) spectral density function at the mounting points of the payload is shown in Figure 2.

The vibration test levels shown in Figure 2 were arrived at by enveloping a collection of autospectra for vibration measurements made on the Space Shuttle orbiter sidewall during five separate STS launches, as summarized in Table 1. The full details of the measurements are available from the NASA "DATE" reports for those launches. Most of the measurements were made on "hard" structure near the mounting points of payloads or orbiter equipment. The test level was arrived at by drawing three straight lines on log-log paper that exceeded at each and every frequency the highest spectral density value of the 22 vibration measurements shown in Table 1. This approach is consistent with

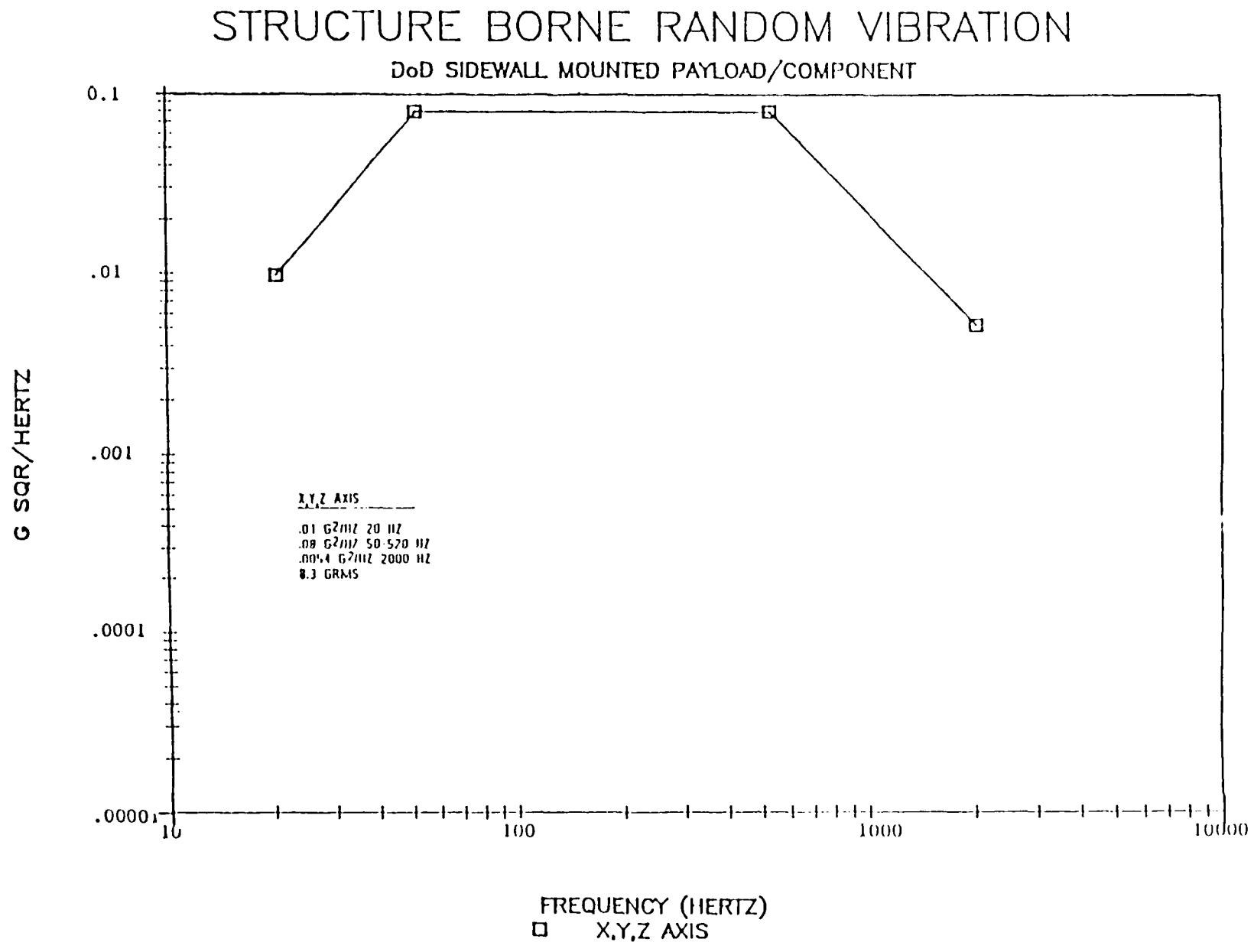

FIGURE 2. VIBRATION TEST SPECIFICATION FOR SPACE SHUTTLE ORBITER SIDEWALL-MOUNTED COMPONENTS [7]

Table 1. Summary of Vibration Measurements Used to Generate the Test Criteria in SD-CF-0206.

Measurement	Axis	Station Number	Description of Location	STS Flights
VO8D9249	x	868, -35, 357	OSTA-1 meas. shelf, LH*	2
VO8D9250	y	868, -35, 357	OSTA-1 meas. shelf, LH	2
VO8D9251	z	868, -35, 357	OSTA-1 meas. shelf, LH	2
VO8D9273	x	1187, -14, 428	DFI pallet beam, LH	2, 3
VO8D9274	x	1187, -14, 428	DFI pallet beam, LH	2, 3
VO8D9335	y	679, -96, 409	LH Manipulator	2, 3, 4
VO8D9336	x	679, -96, 409	LH Manipulator	2, 3, 4,5,13
VO8D9337	z	679, -96, 409	LH Manipulator	2, 3, 4, 13
VO8D9342	x	1070, 75, 419	Payload attach. structure	2, 3, 4, 5
VO8D9343	y	1070, 75, 419	Payload attach. structure	2, 3, 4, 5
VO8D9344	z	1070, 75, 419	Payload attach. structure	2, 3, 4, 5
VO8D9345	x	1069, -85, 414	Payload attach. structure	2, 3, 4, 5
VO8D9346	y	1069, -85, 414	Payload attach. structure	2, 3, 4, 5
VO8D9347	z	1069, -85, 414	Payload attach. structure	2, 3, 4, 5
VO8D9349	y	908, -105, 410	Longeron LH	2, 3, 4,5,13
VO8D9353	z	910, -105, 409	Longeron LH	2, 3, 4,5,13
VO8D9354	y	1200, 94, 409	Longeron LH	2, 3, 4, 13
VO8D9355	z	1200, 94, 409	Longeron LH	2, 3, 4, 13
VO8D9387	x	1183, 95, 409	Adjacent to payload att.	2, 3, 4, 5
VO8D9388	y	1183, 95, 409	Adjacent to payload att.	2, 3, 4, 5
VO8D9389	z	1183, 95, 409	Adjacent to payload att.	2, 3, 4, 5
VO8D9924	x	583, -103, 400	Longeron-pres. hull att.	2, 3, 4, 5

*LH - Left hand side

traditionally accepted practices for deriving vibration test specifications for aerospace vehicle components [8].

When applying the test criterion in Figure 2, or any similarly derived test specification, it is understood that the actual vibration spectrum that the payload will see when mounted on the orbiter sidewall (referred to hereafter as the service vibration input), will have peaks and notches, as illustrated in Figure 3. Hence, the service vibration input to the payload will be very much less than the specified vibration at most frequencies. This overtesting at most frequencies is usually justified as a necessary conservatism to assure that undertesting does not occur at those frequencies where the service vibration spectrum has a peak approaching the test specification envelope. It is further argued that it must be assumed that a spectral peak in the service vibration input might occur at any frequency, since the specification covers many different payloads and payload mounting locations.

It is true in applying a general vibration test specification, like SD-CF-0206, that it is not possible to predict the frequencies where spectral peaks in the service vibration input will occur for all payloads and payload mounting points. However, it is possible to predict the frequencies where spectral peaks in the service vibration input <u>will not occur</u>. Specifically, unless the mounting has an infinite apparent weight, there will be a spectral notch, rather than a peak, in the service vibration input spectrum at all frequencies where the payload has a significant resonance. This simple fact follows directly from the following relationship developed in Section 1, where it is assumed that the payload and mounting structure can be represented by single point values.

$$G_{AA}(f) \; / \; G_{SS}(f) = \left|1 + (W_p(f)/W_s(f))\right|^{-2} \qquad (8)$$

where

$G_{AA}(f)$ = autospectrum of service vibration input with payload present

$G_{SS}(f)$ = autospectrum of service vibration input without payload present

$W_p(f)$ = driving point apparent weight of payload (looking into the payload from its mounting points.)

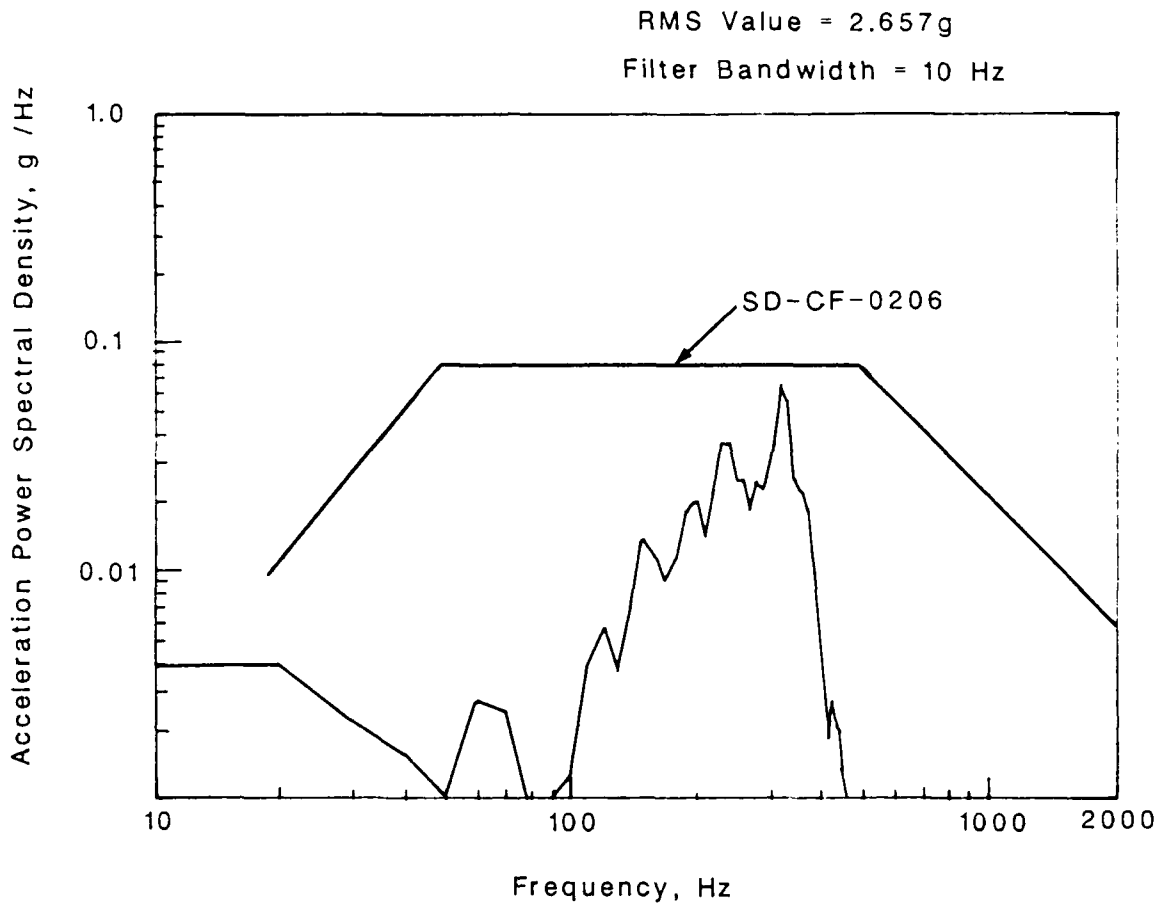

FIGURE 3. VIBRATION TEST SPECIFICATION COMPARED TO TYPICAL ACTUAL INPUT VIBRATION SPECTRUM FOR PAYLOAD.

$W_s(f)$ = source apparent weight of payload mounting structure (looking into the mounting structure from the payload mounting points.)

It is clear from Equation 8 that the spectrum of the service vibration input to the payload, $G_{AA}(f)$, is going to be significantly reduced relative to the unloaded service vibration level, $G_{SS}(f)$, at those frequencies where the payload driving point apparent weight $W_p(f)$, becomes large relative to the mounting structure source apparent weight, $W_s(f)$. The frequencies where $W_p(f)$ becomes large are the resonance frequencies of the payload. Furthermore, the specified vibration test spectrum is essentially equivalent to an envelope of maximum values of the unloaded source vibration spectrum, $G_{SS}(f)$, as will be demonstrated in Section 3. It follows that the most severe overtesting occurs at those frequencies (payload resonance frequencies) were the damage potential to the payload is highest.

The above points are well known to all experienced vibration test engineers and technicians. In fact, most such engineers and technicians probably have witnessed a vibration test where a perfectly acceptable test item (or a shaker) was destroyed by attempting to impose a specified motion input at a frequency where the test item had a strong (high apparent weight) resonance. The purpose here is to formulate a testing procedure that will suppress this extreme overtesting at resonances of test items consisting of Space Shuttle orbiter sidewall-mounted payloads.

2.3 Basic Requirements

2.3.1 Source Apparent Weight Data

All the candidate procedures selected for further study require a knowledge of the source apparent weight of the payload mounting structure. For more general applications, this would restrict the usefulness of the procedures since source apparent weight characteristics vary widely for all possible mounting structures for test items, and source apparent weight data are difficult to acquire for all test items of interest. However, for the application of interest here (Space Shuttle orbiter sidewall-mounted payloads), there are only a limited number of mounting points, all of which

are structurally similar. The source apparent weight is determined at each mounting point and the weights for all mounting points are combined, by the procedures described in Section 7.4, to estimate an equivalent single point apparent weight. It is therefore feasible to determine source apparent weights for the test items of concern, and this was done as part of the study, as described in Section 5.

2.3.2 Force Measurements

All three of the candidate procedures also require, at some point, a measurement of the interface force into the payload. Since procedures involving force transducers were ruled out in the preliminary evaluation of procedures, the approach chosen was to use the shaker armature current as a measure of force. Specifically, it is assumed (and later verified) that the interface force delivered to a payload by the shaker table is given by

$$F(f) = K(f)C(f) - (W_a + W_f)A(f) \qquad (9)$$

where

- $F(f)$ = interface force delivered to a test item in lb.
- $C(f)$ = armature current in amps.
- W_a = weight of armature and shaker table in lb (assumed to be rigid)
- W_f = weight of fixture attached to shaker table in lb (assumed to be rigid).
- $A(f)$ = acceleration response of fixture on shaker table in g's
- $K(f)$ = calibration factor in lb/amp.

As indicated earlier in Section 1, $F(f)$, $C(f)$ and $A(f)$ are Fourier transforms of the force, current and acceleration, respectively. Note that all terms in Equation 9 are complex numbers except for the weights of the armature (W_a) and the fixture (W_f). Further note that Eq. 9 applies only at frequencies well below the first resonance frequency of the shaker armature and any fixture. Final, it should be mentioned that Eq. 9 may not be strictly applicable to some of the larger Unholtz-Dickie shakers where the translation of armature current to electromagnetic force is not linear.

With no payload attached to the shaker, and known armature and fixture weights, it follows from Eq. 9 that

$$C(f) = [(W_a + W_f)/K(f)]A(f) = W_T A(f)/K(f) \tag{10}$$

where W_T denotes the total weight (in lb) of the moving elements of the shaker, armature and fixture. Hence, the determination of K(f) may be accomplished as follows:

1. Firmly bolt a relatively heavy but rigid fixture (a dead weight) to the shaker table and accurately determine its weight, W_f, as well as the weight of the armature and table, W_a.

2. Apply random excitation to the shaker table and simultaneously measure the acceleration response, a(t) in g, of the fixture, and the current, c(t) in amps, applied to the shaker armature.

3. Compute the Fourier transforms of a(t) and c(t) to obtain A(f) and C(f).

4. Compute the frequency response function between c(t) and a(t) given by

$$H(f) = G_{CA}(f)/G_{CC}(f) \tag{11}$$

where

$G_{CA}(f) = 2\ E[C(f)\ A^*(f)]/T$ = cross-spectral density function between c(t) and a(t).

$G_{CC}(f) = 2\ E[C(f)\ C^*(f)]/T$ = autospectral density function of c(t).

5. Calculate the calibration factor K(f) from

$$K(f) = (W_a + W_f)H(f) = W_T H(f) \tag{12}$$

6. To check the linearity of the relationship between c(t) and a(t), compute the coherence function given by

$$\gamma^2(f) = |G_{CA}(f)|^2/[G_{CC}(f)G_{AA}(f)] \tag{13}$$

where

$G_{AA}(f) = 2\ E[A(f)\ A^*(f)]/T$ = autospectral density function of a(t)

and all other terms are as defined in Eq. 11. The coherence function should be $\gamma^2(f) > 0.99$ at all frequencies.

The above calibration procedure need only be applied once to a given shaker, but each different shaker to be used for vibration testing purposes will have to be separately calibrated.

2.4 Candidate Procedures

2.4.1 Motion Correction Procedure

The first candidate procedure selected for experimental study is a direct application of Eq. 8. The information required to implement this procedure is as follows:

(a) The equivalent single point apparent weight of the payload, $W_p(f)$, as seen by a shaker with rectilinear motion.

(b) An equivalent single point apparent weight, $W_s(f)$, of the mounting structure (in this case, the orbiter sidewall), associated with motion in the same direction as for (a) above.

The test procedure would be as follows:

1. Determine the net driving point apparent weight of the payload, by procedures to be detailed later.

2. Using the measured net driving point apparent weight of the payload and the source apparent weight of the mounting structure given in Section 9, calculate a corrected autospectrum for the vibration test level, $G_{AA}(f)$, from Eq. 8, where $G_{SS}(f)$ is taken to be the specified autospectrum in Figure 2; i.e., $G_{TT}(f) = G_{SS}(f)$.

3. Attach the payload to the shaker and apply a broadband random excitation that is well below (by at least 20 dB) the specified test levels in Figure 2.

4. Identify all major resonant frequencies of the payload (this can be done either on the shaker or from the driving point apparent weight data determined in Step 1).

5. At each frequency of a major payload resonance, allow a "notch" in the specified test levels in Figure 2 equal to the ratio $G_{SS}(f)/G_{AA}(f)$ computed in Step 2.

6. Now bring the shaker vibration levels to the full values in Figure 2, except for the frequencies of major payload resonances where notches are allowed to an extent no greater than given by Eq. 8.

The above motion correction procedure is simply a controlled version of the usually "notching" procedure that is commonly allowed in both sinusoidal and random vibration test specifications. The singular advantage of the procedure is that it can be executed using present vibration test system equalizers based only upon shaker table motion measurements. There are a number of disadvantages, as follows:

1. The procedure requires an additional test to measure the driving point impedance of the payload.

2. A personal judgment is required to identify those payload resonances that should be considered sufficiently important to warrant notching.

3. Since the notching criteria are determined at a level below the final specified test level, there is a possibility of errors if the payload resonant response is significantly nonlinear.

Because most payloads have multiple attachment points, measurements of the individual mounting point apparent weights are not sufficient to determine accurately the effective single-point apparent weight. Procedures described in Section 7.4 show that it is necessary to measure the individual and cross impedances (or mobilities, inertances, apparent weights) in order to estimate that quantity. Such measurements, and the ensuing calculations, require considerable time, instrumentation, and data processing capability. There is,

however, an effective and accurate method to measure the single point apparent weight or inertance of the payload directly when mounted on a shaker table. For both theoretical reasons [Appendix A, 2-10] and signal-to-noise problems, it is actually desirable to measure the reciprocal of apparent weight, called inertance, I(f), defined as

$$I(f) = G_{FA}(f)/G_{FF} \tag{14}$$

where

$G_{FA}(f)$ = cross-spectrum between interface force and shaker table acceleration.

$G_{FF}(f)$ = autospectrum of shaker table interface force.

From Eq. 9,

$$G_{FA}(f) = 2E[F(f)A^*(f)]/T = 2E[[(K(f)C(f) - W_T A(f)]A^*(f)]/T$$
$$= K(f)G_{CA}(f) - W_T G_{AA}(f) \tag{15}$$

and

$$G_{FF}(f) = 2E[F(f)F^*(f)]/T = 2E[[K(f)C(f) - W_T A(f)][K^*(f)C^*(f) - W_T A^*(f)]]/T$$
$$= |K(f)|^2 G_{CC}(f) + W_T^2 G_{AA}(f) - 2 W_T \mathrm{Re}[K(f)G_{CA}(f)] \tag{16}$$

The inertance of the payload can be measured by the following procedure:

1. Attach the payload to the shaker and apply broadband random excitation at a level at least 20 dB below the test specification.

2. Compute the cross-spectrum between the shaker armature current and the table vibration, $G_{CA}(f)$

3. Compute the autospectra for the shaker armature current and table acceleration, $G_{CC}(f)$ and $G_{AA}(f)$.

4. Finally, compute the payload inertance function, I(f), using Eqs. 14 through 16.

The choice of shaker table vibration levels for the payload inertance measurements is based on a careful and considered balance of several factors. The level must be high enough to ensure that there is an adequate signal-to-noise ratio in all sensors, yet not too high so as to cause excessive vibration and potential damage to sensitive component elements at payload resonances during the preliminary testing. It is believed that a level approximately 20 dB below the vibration test specification will satisfy these requirements. As stated earlier, this phase of the work is conducted under the overall assumption that the system is linear, and that resonant frequencies and frequency response functions will not change with level.

2.4.2 Blocked-Force-Limit Procedure

This approach is based upon limiting the specified shaker vibration test levels such that the interface force, as monitored using the shaker current, is never allowed to exceed the so-called "blocked force". The blocked force is that force which would make the source vibration response of the unloaded mounting structure go to zero; i.e., the interface force between the payload and the mounting structure if the payload had infinite apparent weight (zero inertance).

The blocked force evolves analytically as follows. The interface force between the payload and its mounting structure is related to the interface acceleration, A(f), by

$$F(f) = W_p(f)\ A\ (f) \tag{17}$$

where $W_p(f)$ is the driving point apparent weight of the payload. Solving for $W_p(f)$ in Eq. 17 and substituting into Eq. 7 yields

$$F(f) = F_B(f) - F_R(f) \tag{18}$$

where

$F_B(f) = W_s(f)A_s(f)$ = blocked force

$F_R(f) = W_s(f)A(f)$ = reaction force

Given a vibration test specification calling for an input vibration autospectrum of $G_{TT}(f)$, the autospectrum of the blocked force for all components covered by that test specification can be estimated conservatively by

$$G_{BB}(f) \approx |W_{se}(f)|^2 G_{TT}(f) \tag{19}$$

where $|W_{se}(f)|^2$ is the squared magnitude of a conservative envelope of the apparent weight of the various attachment points on the mounting structure.

It is important to understand that the blocked force is not a theoretical limit on the interface force that might occur in the service environment at all frequencies. Specifically, from Eq. 18,

$$|F(f)| = |W_s(f)[A_s(f) - A(f)]| \tag{20}$$

meaning $|F(f)| > |F_B(f)|$ at those frequencies where $A(f) > 2A_s(f)$. This may happen at the lower frequencies, below the first normal modes of both the mounting structure and the payload, where the mounting structure appears essentially as a spring and the payload appears essentially as a mass. The apparent weight for a spring has a phase angle near -180 degrees, while the apparent weight for a mass has a phase angle near 0 degrees. From Eq. 7,

$$\frac{A(f)}{A_s(f)} = \frac{W_s(f)}{W_s(f) + W_p(f)} \tag{21}$$

Hence, if $W_p(f) \approx -W_s(f)$, $A(f) \gg A_s(f)$. In fact, the only reason $A(f) \to \zeta$ is that $W_s(f) + W_p(f)$ in the denominator of Eq. 21 will have a small imaginary component due to damping; i.e., the phase for $W_s(f)$ will always be a little greater than -180 degrees, and the phase for $W_p(f)$ will always be a little less than 0 degrees.

In practice, the above problem cannot occur at the frequency of a payload resonance, because the payload apparent weight will always have a phase near -90 degrees and hence, can never be out of phase with the mounting structure,

whose apparent weight phase is bounded by 0 and -180 degrees. The same will be true at the higher frequencies where the mounting structure becomes damping controlled with an apparent weight phase of -90 degrees.

It follows that the blocked force should always constitute a limit on the actual input force to the payload in its service environment at those frequencies of greatest concern, namely, the resonance frequencies of the payload. At frequencies below the first normal modes of both the mounting structure and the payload, the possibility of an under-test using the blocked force as a limit on the shaker input force should be fully negated by the enveloping procedure used to generate the vibration test specification (to be discussed further in Section 3).

To perform a blocked force limit test, it is necessary to determine the interface force on the payload applied by the shaker at the specified test level $G_{TT}(f)$. From Eq. 10,

$$F(f) = K(f)C(f) - W_T A(f) \tag{22}$$

The autospectrum of the interface force is then given by Eq. 16 as

$$G_{FF}(f) = |K(f)|^2 G_{CC}(f) + W_T^2 G_{AA}(f) - 2 W_T \, Re[K(f)G_{CA}(f)] \tag{23}$$

A block-force-limit vibration test would be performed by calculating the force spectrum in Eq. 23, and reducing the shaker current as required to make $G_{FF}(f) = G_{BB}(f)$ at all frequencies where $G_{FF}(f) > G_{BB}(f)$. The limiting of the test levels will occur primarily at the frequencies of major payload resonances. However, a very heavy payload may lead to a limiting of the test levels at other frequencies as well.

To clarify this matter further, it follows from Eqs. 17 and 18 that the blocked force limit requires that

$$G_{FF}(f) = |W_p(f)|^2 G_{AA}(f) < G_{BB}(f) = |W_{se}(f)|^2 G_{TT}(f) \tag{24}$$

Hence, the blocked force limit on the shaker table motion is given by

$$G_{AA}(f) < \frac{|W_{se}(f)|^2}{|W_p(f)|^2} G_{TT}(f) \qquad (25)$$

This result says that the blocked force will be exceeded before the shaker table motion reaches the specified test level, $G_{TT}(f)$, at all frequencies where the driving point apparent weight of the payload exceeds the source apparent weight of the mounting structure. Hence, if the apparent weight of the payload is known, Eq. 25 could be used to determine the final test levels. However, by using the force restriction in Eq. 23, a measurement of the driving point apparent weight of the payload is not required; it is implicit in Eq. 23.

A procedure for a blocked force limit test is as follows:

1. Set up the shaker control system to monitor the armature current as well as the table acceleration.

2. Attach the payload to the shaker, and apply a broadband random excitation which is well below (by at least 20 dB) the specified test levels in Figure 2.

3. Compute the autospectrum of the shaker armature current, $G_{CC}(f)$, the autospectrum of the shaker table acceleration, $G_{AA}(f)$, and the cross-spectrum of the armature current and table acceleration, $G_{CA}(f)$.

4. Compute the autospectrum of the shaker interface force, $G_{FF}(f)$, using Eq. 23, and compare to the autospectrum of the blocked force, $G_{BB}(f)$, given by Eq. 19.

5. At all frequencies where $G_{FF}(f) > G_{BB}(f)$, reduce the shaker current as required to make $G_{FF}(f) = G_{BB}(f)$.

6. Repeat the above steps in an iterative manner as the shaker vibration level is increased until the shaker vibration levels at all frequencies

are $G_{AA}(f) = G_{TT}(f)$ or such that $G_{FF}(f) = G_{BB}(f)$, whichever occurs first.

The advantages of the blocked force limit procedure are:

1. The procedure requires no knowledge of the driving point apparent weight of the payload (this information is inherent in the calculations).

2. The procedure is not vulnerable to errors due to nonlinear resonant responses of the payload since it is an iterative procedure which applies control up to the final test level.

3. The procedure will automatically make a mass load correction for heavy payloads, as well as provide accurate notching at the frequencies of major payload resonances.

The major disadvantages of the blocked force limit procedure are:

1. The procedure will require a modification of present vibration shaker equalizer systems to include the monitoring and control of armature current, as well as table acceleration, and on-line computing capability.

2. There may be difficulties implementing the procedure on shakers that do not nave a linear relationship between armature current and table motion, such as certain large Unholtz-Dickie shakers.

2.4.3 Apparent Weight Simulation Procedures

This approach, which was originally proposed by Ratz (Appendix A, [5-2]), controls the shaker table motion to reproduce the input motion to the payload that would occur in service, assuming the specified test level spectrum, $G_{TT}(f)$, were the unloaded vibration response of the mounting structure. Specifically, from Eqs. 18 and 22, it follows that

$$W_S(f)A_S(f) = K(f)C(f) + [W_S(f) - W_T]A(f) \qquad (26)$$

In terms of spectral density functions

$$G_{SS}(f)_c = [|K(f)|^2 G_{CC}(f) + |W_o(f)|^2 G_{AA}(f) + 2Re[K(f)W_o^*(f)G_{CA}(f)]] / |W_S(f)|^2 \quad (27)$$

where

$$W_o(f) = W_S(f) - W_T$$

and $G_{SS}(f)_c$ is a computed autospectrum of the unloaded mounting point vibration that would correspond to a loaded mounting point vibration spectrum, $G_{AA}(f)$.

A procedure for an apparent weight simulation test is as follows:

1. Set up the shaker control system to monitor the armature current as well as the table acceleration.

2. Attach the payload to the shaker, and apply broadband random excitation which is well below (by at least 20 dB) the specified test levels in Figure 2.

3. Compute the autospectrum of the shaker current, $G_{CC}(f)$, the autospectrum of the shaker table acceleration, $G_{AA}(f)$, and the cross-spectrum of the armature current and table acceleration $G_{CA}(f)$.

4. Compute the autospectrum of the pseudo-mounting structure acceleration, $G_{SS}(f)_c$, using Eq. 27, and compare to specified vibration test spectrum, $G_{TT}(f)$ in Figure 2.

5. Slowly increase the shaker test level to obtain, at all frequencies, a computed $G_{SS}(f)_c = G_{TT}(f)$, the specified test level, except for the restriction that $G_{AA}(f) \leq G_{TT}(f)$.

The advantages of the apparent weight simulation procedure are as follows:

1. Assuming $G_{TT}(f)$ represents an accurate measure of the unloaded mounting point vibration in service, the procedure provides an accurate simulation of the service input vibration to the payload.

2. The procedure requires no knowledge of the driving point apparent weight of the payload; as for the blocked force limit procedure, this information is inherent in the calculations.

3. The procedure is not vulnerable to errors due to nonlinear resonant responses of the payload, since it is an interactive procedure which continuously corrects the levels up to the final test level.

4. The procedure will automatically make a mass load correction for heavy payloads, as well as provide accurate notching at the frequencies of payload resonances.

The major disadvantages of the blocked force limit procedure are as follows.

1. The procedure will require a real time computer in the shaker equalizer system to compute the desired test level signal for equalization.

2. The procedure may be difficult to implement on certain large Unholtz-Dickie shakers, which do not have a linear relationship between armature current and table motion.

3. The procedure has no inherent conservatism, except for conservative values of $G_{TT}(f)$ and $W_s(f)$.

3. PARAMETRIC STUDY

3.1 Purpose of Study

The parametric study had the objective of providing insight into the roles played by different parameters in determining the response of the mounting point and payload when the payload is attached to the structure. In addition, the influence of various representations of parameters, such as mounting point impedance and unloaded vibration spectra, on the computed response of the loaded structure and payload, was investigated. In practice, these representations could result from empirical modelling of the functions, based on test or launch data, when detailed phase information is lost or when averaged values are obtained for a number of mounting points. The results of the parametric study are presented in this section.

3.2 Description of Model Structure

The model structure used for the parametric study consists of a flat (6 ft x 4 ft) panel with four stiffeners, two parallel to each axis of the panel. The stiffeners provide a region in the middle of the panel that should be reasonably free from the influences of the panel edge conditions. Simple payloads can then be attached to the panel in this middle region. The payloads of interest are single-degree-of-freedom systems, each of which consists of a mass, spring and damper. The payload is attached to four mounting points on the panel by means of a rigid link, as shown in Figure 4. The four mounting points on the structure, 1(a) through 1(d), are shown in Figure 5. The general characteristics of interest are well represented by this model, without the difficulties in interpretation that would be introduced by a multi-degree-of-freedom model.

The panel was modeled on the computer using MSC NASTRAN finite element codes; one quarter of the panel is shown in Figure 6. A typical stiffener considered in the analysis is shown in Figure 7. Calculations were performed to get estimated values of the natural frequencies. Typical results are given in Table 2 for symmetric-symmetric modes, with panel edge conditions assumed to be either simply-supported or fixed (built-in); an example of computed mode

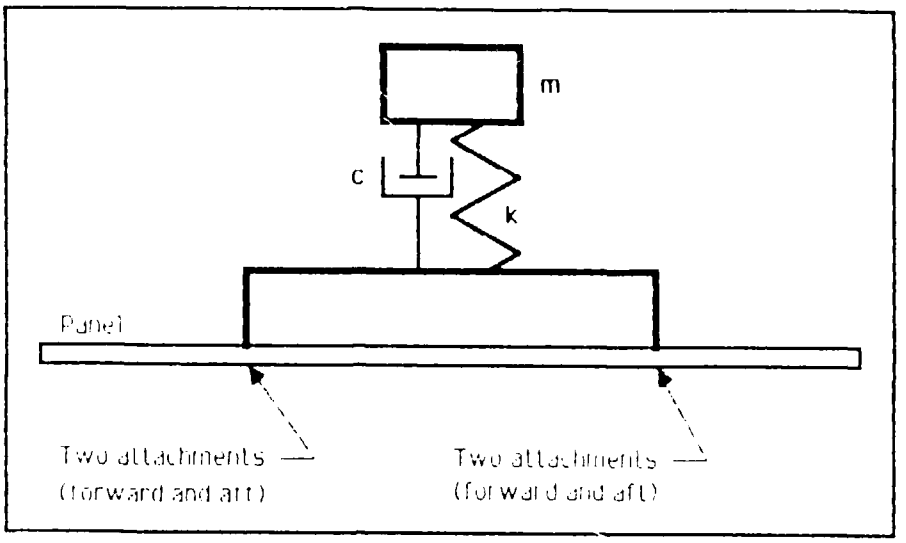

FIGURE 4. DIAGRAM OF SIMULATED PAYLOAD ON STRUCTURE

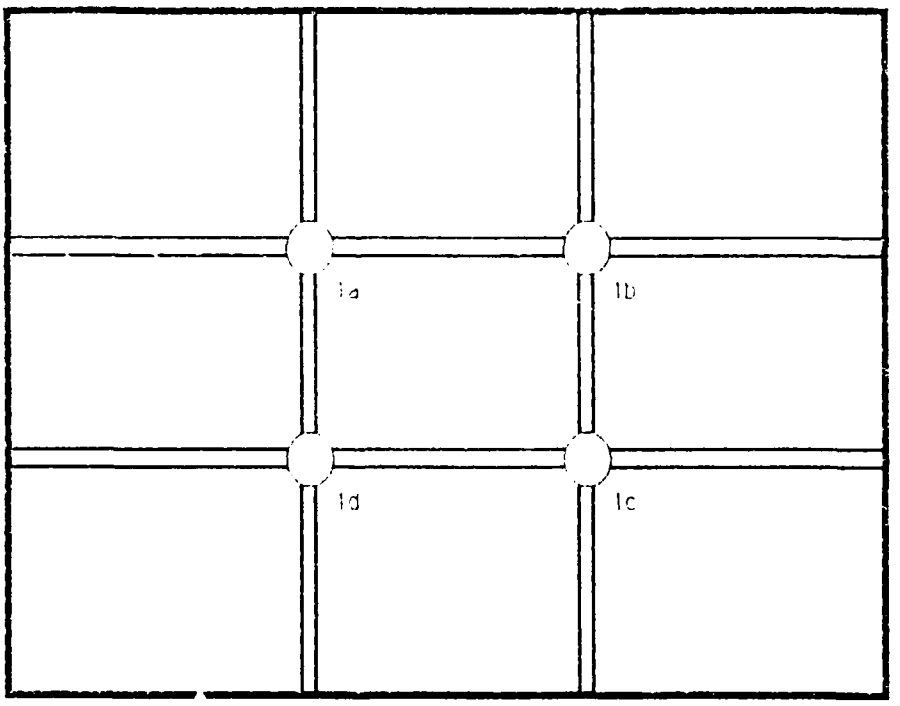

FIGURE 5. LOCATION OF PAYLOAD ATTACHMENT POINTS ON STRUCTURE.

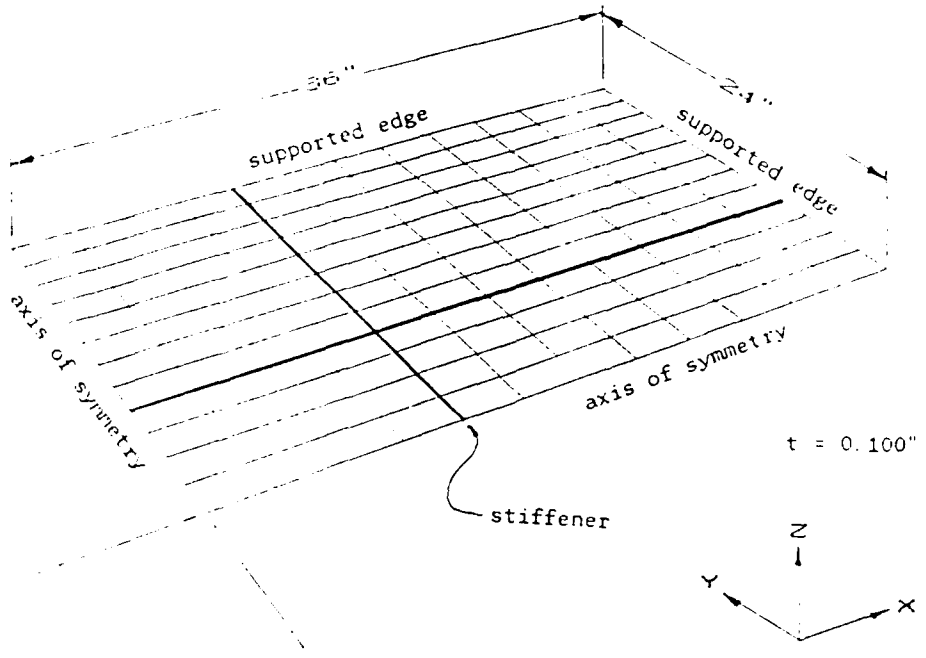

FIGURE 6. FINITE ELEMENT MODEL OF SIMPLE STRUCTURE.

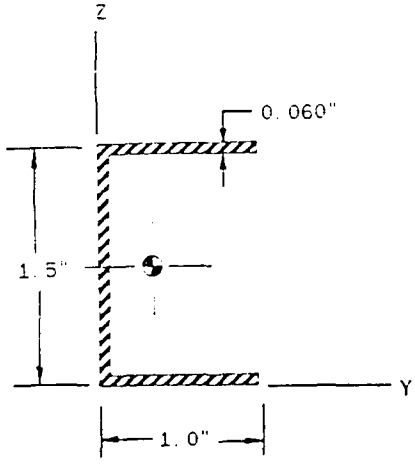

Area = 0.2028 in**2
c.g.- y = 0.3081 in
c.g.- z = 0.75 in
I-zz = 2.085e-02 in**4
I-yy = 7.538e-02 in**4
J-c = 2.520e-04 in**4

FIGURE 7. STIFFENER PROPERTIES

Table 2. Summary of Symmetric - Symmetric Normal Modes

Mode	Natural Frequencies (Hz)	
No.	Simple Supports*	Built-in*
1	39.7	73
2	70.7	92
3	77.0	93
4	87.5	96
5	111.1	134
6	124.2	150
7	139.6	160
8	183.8	228
9	199.8	236
10	211.0	244

* Boundary Conditions

Simple supports: $y=0$, $dy/dx \neq 0$, $M=0$

Built-in or fixed: $y=0$, $dy/dx=0$, $M \neq 0$

where y=displacement

dy/dx = slope

M = moment

shapes associated with the simply-supported boundary conditions is given in Figure 8.

The parameters to be varied in the parametric studies are the mass, stiffness and damping of the payload. However, it is more convenient to use payload resonance frequency as a parameter instead of stiffness. Then, the resonance frequency can be chosen to lie below, at, or above the fundamental frequency of the supporting panel. The corresponding stiffness of the payload can be calculated from the mass and frequency. The values selected for the parameters in the parametric study are:

Payload weight W: 25, 50, 100, 200, 400 lb
Payload resonance frequency f_n: 20, 40, 80, 160, 10,000 Hz
Payload loss factor: 0.004, 0.01, 0.025, 0.0625, 0.1563

With one exception, the values were selected to be in constant ratios of 2 or 2.5. The exception is the highest resonance frequency of 10,000 Hz which was selected to represent the upper-bound condition given by a mass attached directly to the supporting structure without any intervening spring.

3.3 Response Equations

The parametric studies on the 1-dof system were to be performed mainly with the use of closed form equations. However, finite element modelling was used to calculate the response power spectral density, at the payload mounting point on the unloaded panel, due to reverberant excitation and the (complex) point impedance of the structure at the mounting point. The impedance is the complex ratio of force to velocity at the point of interest.

For purposes of the finite element analysis, calculations of panel response were restricted to symmetrical modes so that the motion of the panel would be in-phase at all four mounting points for the payload. The size of the finite element model was minimized by modelling only one quarter of the structure (as shown in Figure 6) and using conditions of symmetry along the panel axes. The edges of the panel were assumed to be simply-supported.

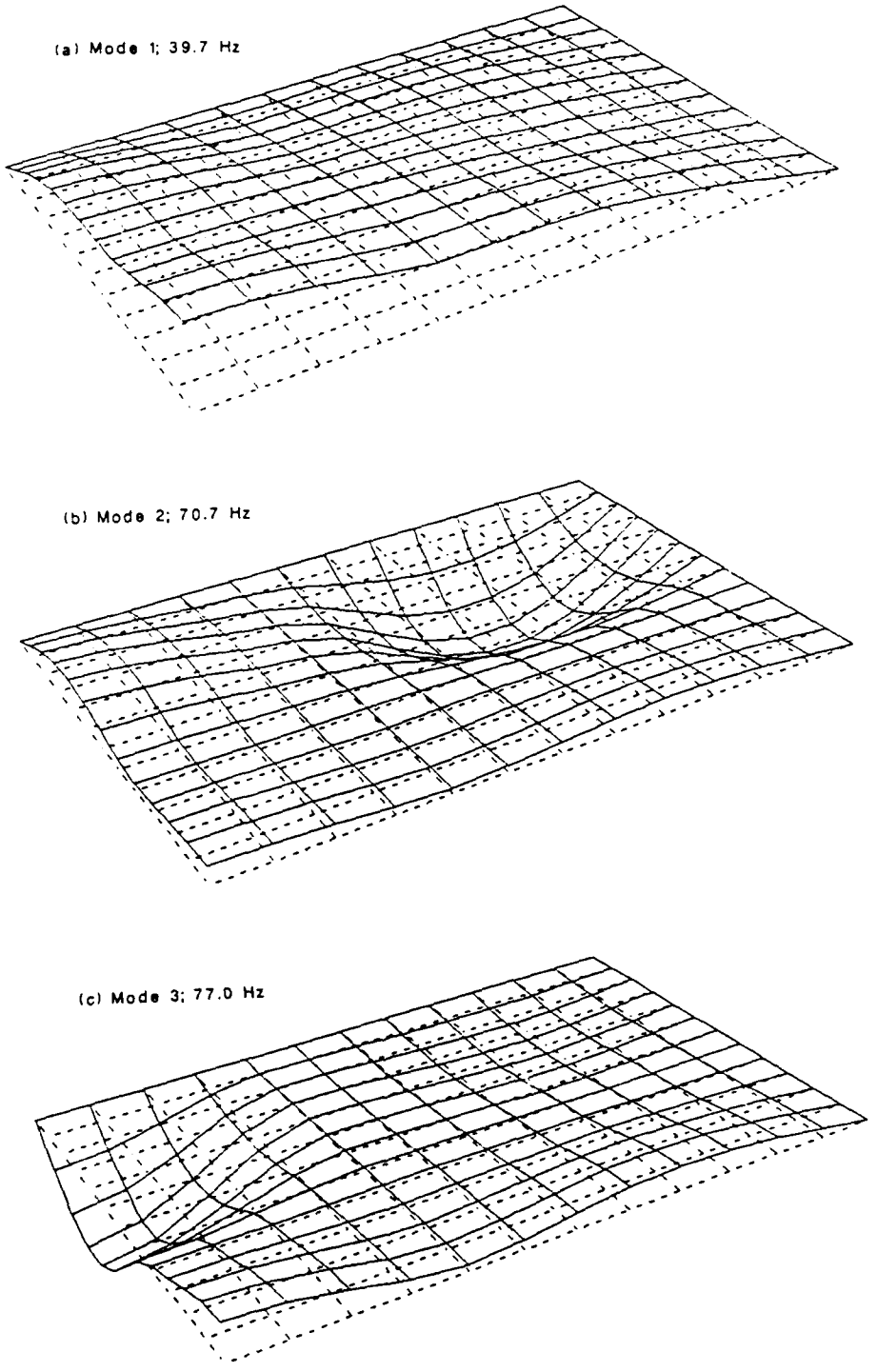

FIGURE 8. EXAMPLE MODE SHAPES FOR SIMPLE STRUCTURE WITH SIMPLY-SUPPORTED BOUNDARIES.

The two responses of interest in the present study are the motion of the structure/payload interface and the motion of the payload mass. The motion of the interface and impedance $Z_s(f)$ of the structure at the mounting points were computed for the unloaded condition using finite element analysis methods. The impedance $Z_s(f)$ is defined by

$$Z_s(f) = F_s(f)/V_s(f) \tag{28}$$

where $F_s(f)$ and $V_s(f)$ are the Fourier transforms of the applied force and resultant response velocity, respectively, at the payload mounting point. If the four mounting points are symmetric with respect to the panel, and those points move in phase with the same amplitude (only symmetric modes of the panel are in motion), then the panel motion can be completely described by the velocity, $v_s(t)$, at a single mounting point and only a single mounting point impedance must be computed. The impedance (mobility, inertance, apparent weight) at each mounting point is calculated using only the symmetric modes of vibration. This value is not that which would be experimentally measured with a force/velocity instrument, for that device would excite and measure response of all modes. In a like manner, an idealized, symmetric payload having an equivalent single point payload impedance (mobility, inertance, apparent weight) is defined. When this payload is mounted on the above described panel, it moves in a rectilinear manner (no rotational motion). Then the motion of the interface, when loaded by a particular payload, can be calculated using the equation

$$G_{xx}(f) = G_{yy}(f)/\left|1 + [Z_p(f)/Z_s(f)]\right|^2 \tag{29}$$

where $G_{yy}(f)$ is the autospectrum of the motion of the interface when the structure is unloaded (i.e. there is no payload) and $G_{xx}(f)$ is the motion of the interface when loaded by the payload. Motion can be expressed in terms of displacement, velocity or acceleration and Eq. (29) is applicable in all cases since the denominator on the right-hand side of the equation is non-dimensional. In practice, acceleration is most commonly used since it can be easily measured. However, in the present parametric study, displacement is sometimes used as an alternative. $Z_p(f)$, the impedance of the payload, is given in closed form by [9]

$$Z_p(f) = \omega m[\omega mc + j[c^2 - (km - k^2/\omega^2)]]/[c^2 + (\omega m - k/\omega)^2] \quad (30)$$

Once $G_{xx}(f)$ has been calculated, the corresponding response, $G_{pp}(f)$, of the payload can be calculated from

$$G_{pp}(f) = |H(f)|^2 G_{xx}(f) \quad (31)$$

where $G_{xx}(f)$ is given by Eq. (29) and, assuming hysteretic damping, the frequency response function, $H(f)$, of the system to an acceleration input from the structure, is given by

$$H(f) = [1 + j\eta]/[1 - (f/f_n)^2 + j\eta] \quad (32)$$

The symbols used in Eqs. 29 through 32 are defined as:

f_n = undamped natural frequency
η = loss factor = 2 x damping ratio
k = spring constant
m = mass
c = damping coefficient
j = $[-1]^{1/2}$

It was decided that hysteretic damping was more representative of typical payload damping than was viscous damping. The corresponding form of Eq. 32 for viscous damping would be

$$H(f) = [1 + j2\zeta f/f_n]/[1 - (f/f_n)^2 + j2\zeta f/f_n] \quad (33)$$

where ζ is the viscous damping ratio.

The preceding analysis is applicable only for the symmetric case where it is assumed that the four mounting points on the panel move in phase with perfect coherence, as would occur with unison excitation. This also means that only symmetric-symmetric response modes of the panel need be considered. Under

these conditions, the four mounting points will have the same point impedance and response spectra (unloaded and loaded).

3.4 Typical Response Spectra

Typical displacement response spectra calculated by the finite element analysis and by means of Eqs. 28 through 31 are given in Figures 9 through 12. For these particular examples, the payload weight was taken as 100 lb and the payload resonance frequency as 20 Hz. Since the predicted fundamental frequency of the unloaded structure is 39.7 Hz, the selected payload resonance frequency is approximately 50% of the structure fundamental frequency. Figure 10 shows predicted displacement spectra for the loaded structure at the payload mounting point for three different assumed values of the payload damping loss factor, 0.004, 0.025 and 0.156. The main characteristics of the spectra are the two strong response peaks at frequencies of 12.9 Hz and 57.1 Hz, and the spectral trough at 20 Hz. In this low frequency range the system can be viewed as a combination of two 1-dof systems. The resonance frequencies of the combined system will lie below and above the two frequencies associated with the two constituent 1-dof systems. Furthermore, since the payload acts as a tuned vibration absorbed, there is a notch in the response spectra at 20 Hz, the tuned frequency of the payload spring and mass. There is no evidence in the response spectra of the fundamental frequency (39.7 Hz) of the unloaded structure.

The corresponding response spectra for the payload are shown in Figure 11. At low frequencies, the vibration of the payload is dominated by the response at the two resonance frequencies of the coupled system. There is no indication of either of the resonance frequencies associated with the two individual uncoupled systems.

The spectra of perhaps greatest interest to the present program are those of the type shown in Figure 12. This spectrum represents the ratio of the response of the loaded panel to the response of the unloaded panel. A value of unity for this ratio would indicate that the vibration test level should be that of the unloaded structure. A value less than unity indicates the potential for over-test if the shaker response is controlled to a value equal

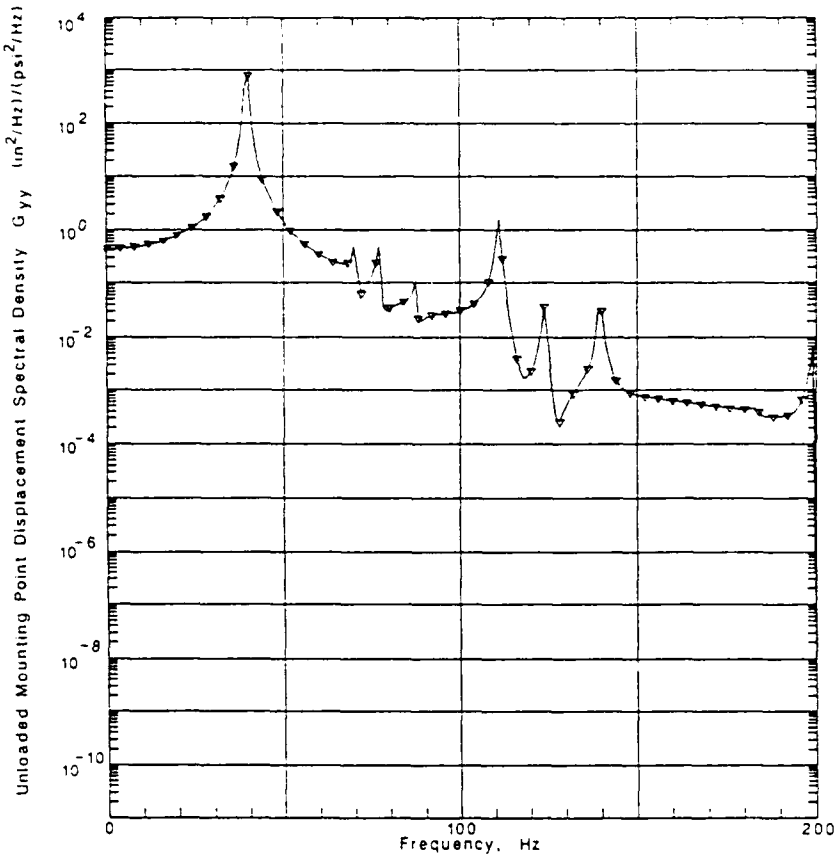

FIGURE 9. PREDICTED RESPONSE OF UNLOADED STRUCTURE TO REVERBERANT ACOUSTIC EXCITATION

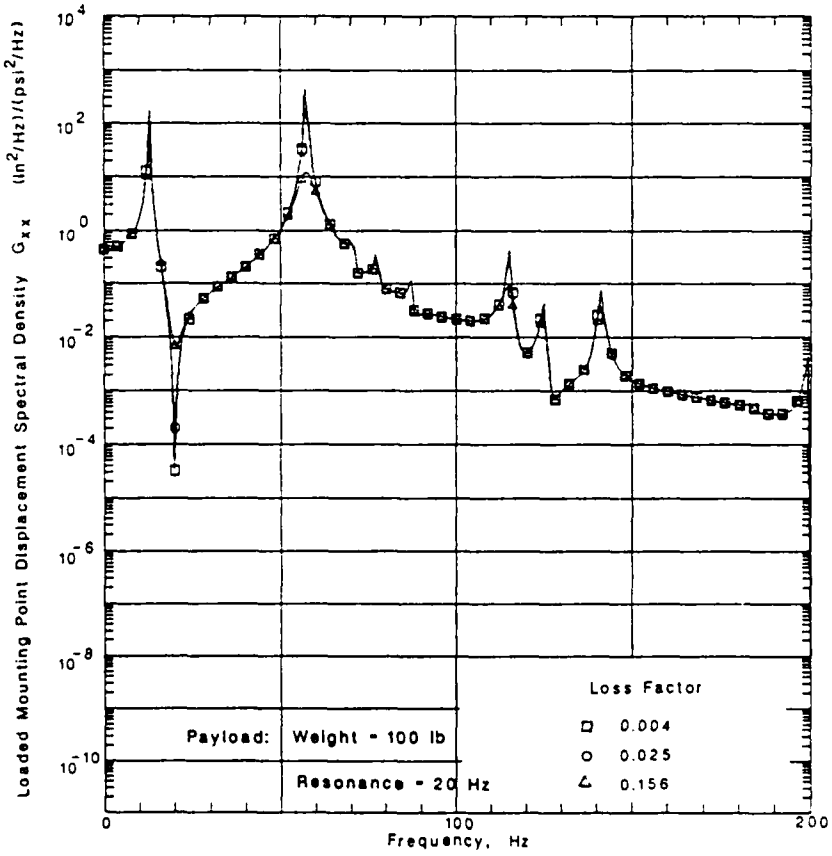

FIGURE 10. PREDICTED RESPONSE OF STRUCTURE TO ACOUSTIC EXCITATION: PAYLOAD WEIGHT 100 lb.

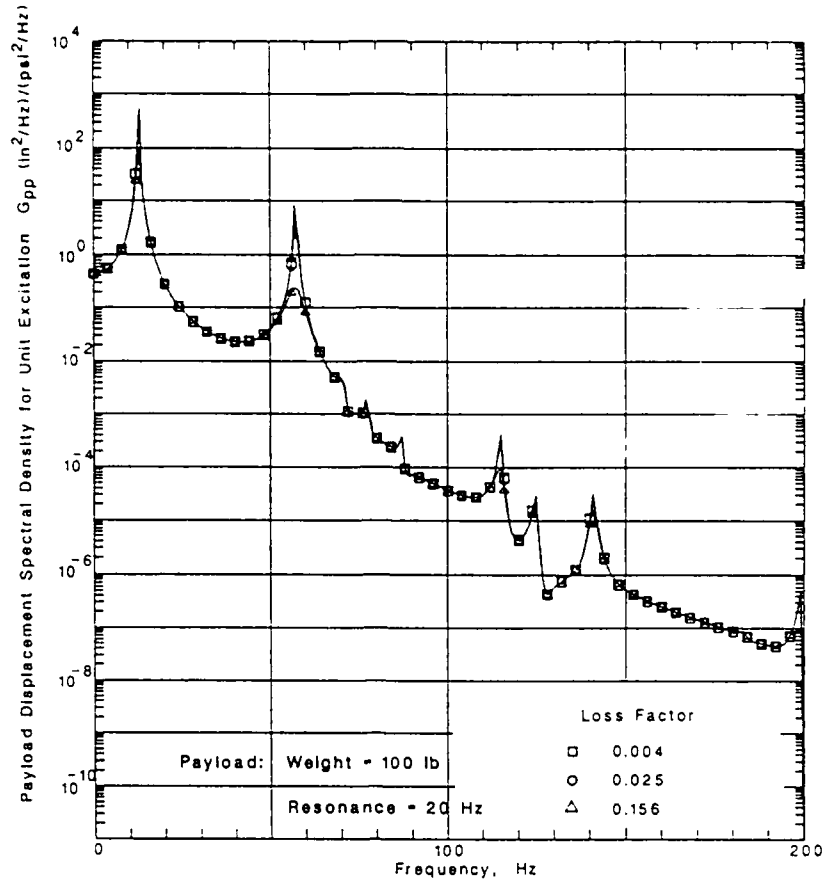

FIGURE 11. PREDICTED RESPONSE OF 100 lb PAYLOAD ON STRUCTURE SUBJECTED TO ACOUSTIC EXCITATION.

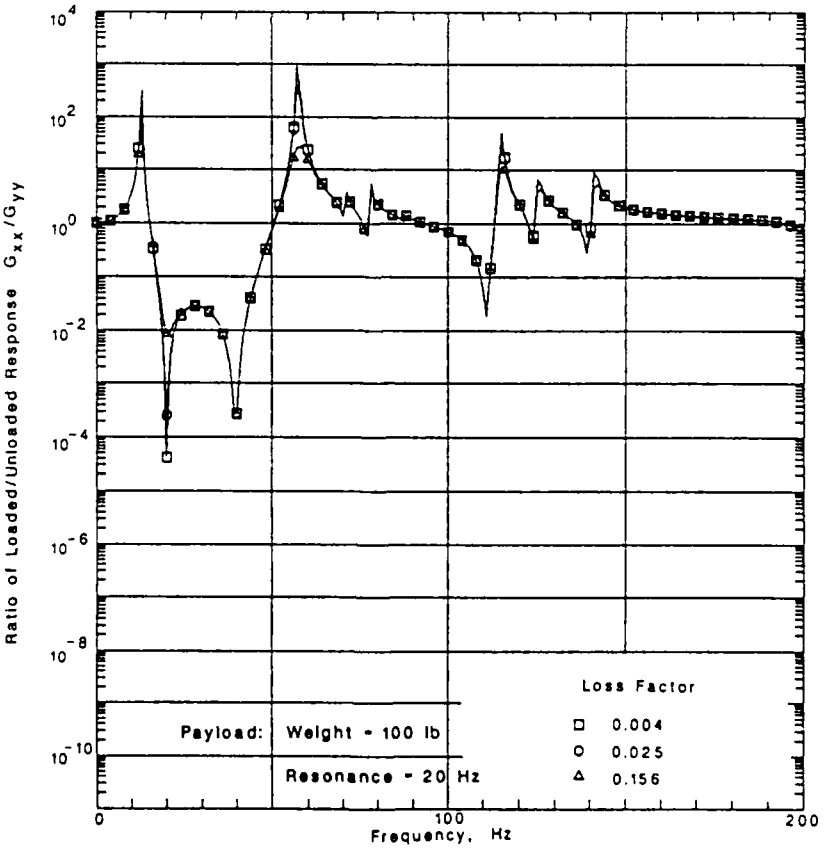

FIGURE 12. RATIO OF LOADED TO UNLOADED RESPONSE OF STRUCTURE AT PAYLOAD MOUNTING POINT : 100 lb, 20 Hz.

to the response level of the unloaded structure, and a ratio greater than unity indicates a potential for under-test if the unloaded response is used as the test criterion. Figure 12 shows two response peaks, with values greater than unity, at the resonance frequencies of the combined system, and two troughs, with values considerably less than unity, at the individual frequencies of the payload and structure. There are some relatively minor peaks and troughs associated with structural response in higher order modes, but these are not considered in the present discussion.

Figure 13(a) contains spectra for the ratio of loaded and unloaded responses for the case where the resonance frequency of the payload is essentially the same as the fundamental frequency of the unloaded structure. In this closely matched system, there is a single trough at low frequencies and it is very deep, with typical values of 10^{-9} to 10^{-6} for the ratio of spectral densities, depending on the damping of the payload.

Response ratio spectra for the case where the payload resonance frequency is twice the fundamental frequency of the unloaded structure are shown in Figure 13(b). Now there is a very strong peak at low frequencies, a trough at the fundamental frequency of the structure and other significant troughs at higher frequencies. The high frequency peaks in the response ratio spectra are relatively minor, at least for this particular example.

3.5 Parametric Variations

The influence of payload damping, mass and resonance frequency were investigated using the analysis methods discussed in Section 3.3. The results of this parametric study are presented in this section. Results are presented in terms of the ratio of response autospectra, $G_{xx}(f)/G_{yy}(f)$, which can be interpreted as a ratio of acceleration autospectra, $G_{AA}(f)/G_{SS}(f)$, or as a ratio of displacement autospectra or velocity autospectra.

3.5.1 Payload Damping

Figures 9 through 13 show the effect of payload damping on the response of the combined system. Inspection of the spectra shows that payload damping has a

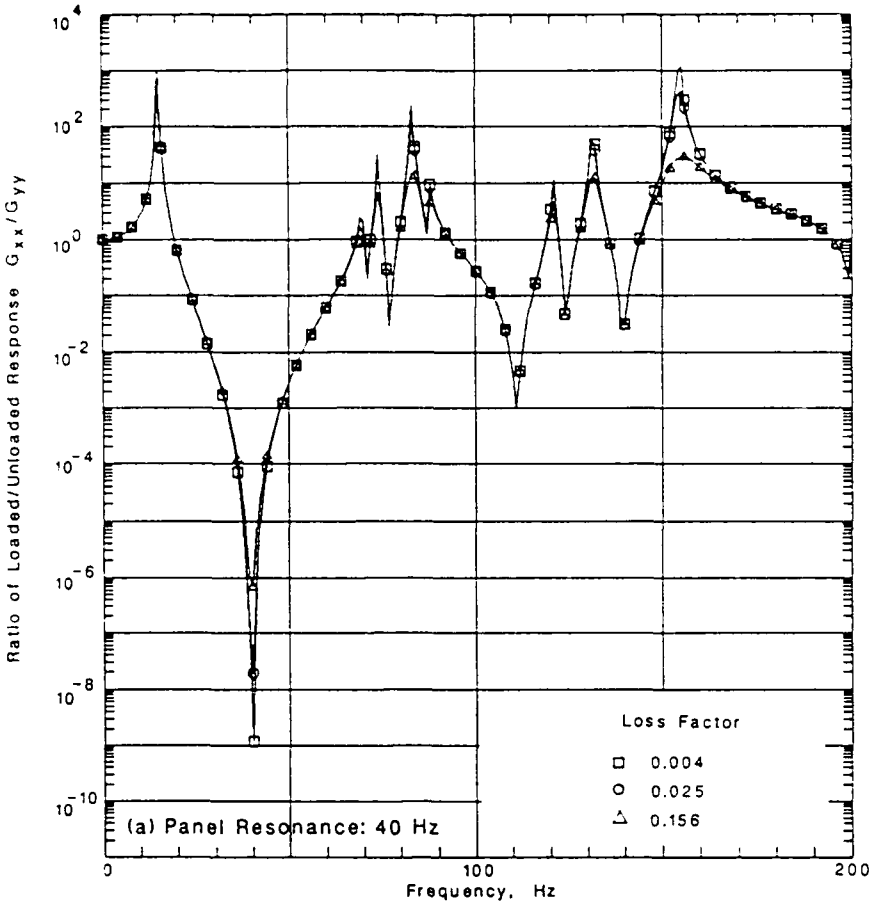

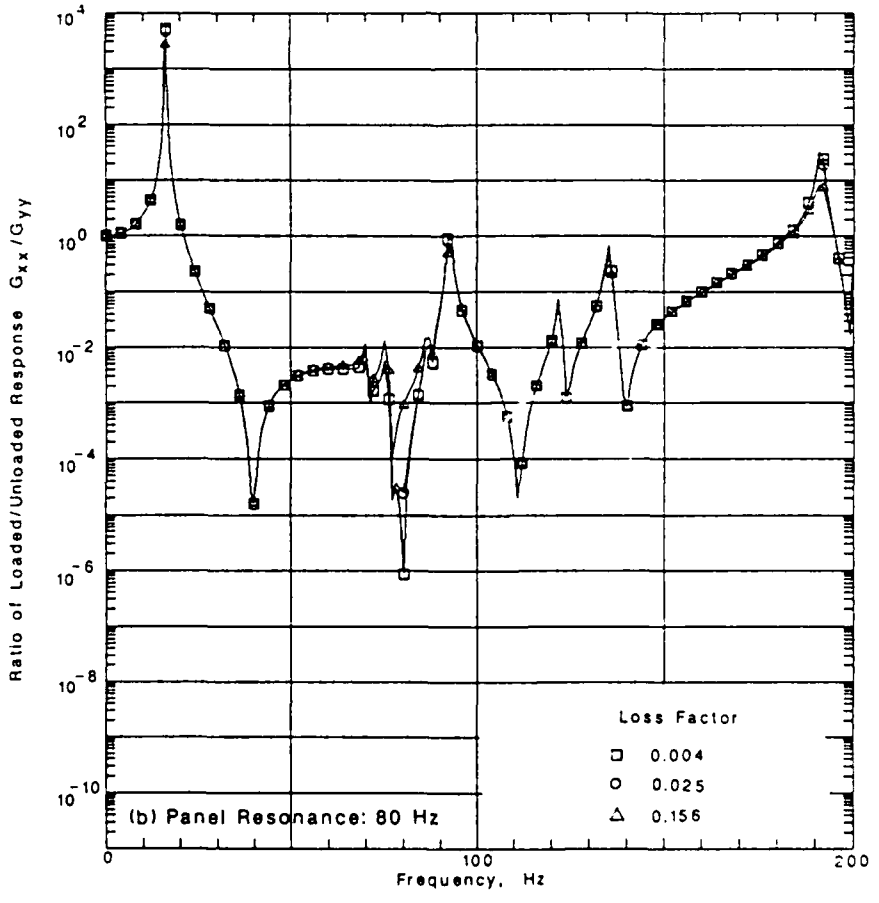

FIGURE 13. RATIO OF LOADED AND UNLOADED RESPONSE OF STRUCTURE AT PAYLOAD MOUNTING POINT: PAYLOAD RESONANCE 40 & 80 Hz.

significant effect at some frequencies but a negligible effect at others. For example, the damping has a strong effect in determining the depth of the trough in the response ratio spectra at the frequency of the payload resonance, as might be expected, but has no effect on the depth of the trough at the fundamental frequency of the structure, except when it is coincident with the payload frequency (Figure 13(a)). Damping appears to have weak effect on the response ratio at the first (lowest frequency) peak and to have a somewhat greater effect at the second peak.

3.5.2 Payload Mass

The influence of payload mass on the response ratio spectra can be seen in Figures 14(a) through (e) which refer to the five payload resonance frequencies and a payload damping loss factor of 0.025. Each figure contains five spectra associated with the five selected values of payload weight.

The immediate observation from an inspection of the spectra is that, for a given payload frequency, the payload weight or mass has little or no effect on the frequency of any of the spectral troughs. Also, at the higher values of the payload frequency (i.e. higher payload stiffness) the payload mass has little effect on the frequencies of most of the response peaks. Payload mass always affects the frequency of the lowest order peak and, for the lower payload stiffnesses, it affects the frequencies of the higher order peaks. However, the effect is not always in the same direction. Thus, an increase in payload mass decreases the frequency of the lowest order peak but it increases the frequency of the second order peak.

Payload mass also influences the magnitude of the response ratio. The depth of the response troughs appears to increase with payload mass and, at low frequencies, the height of the response peaks appears to increase with mass. However, at higher frequencies, there is no specific trend of response peak amplitude with payload mass.

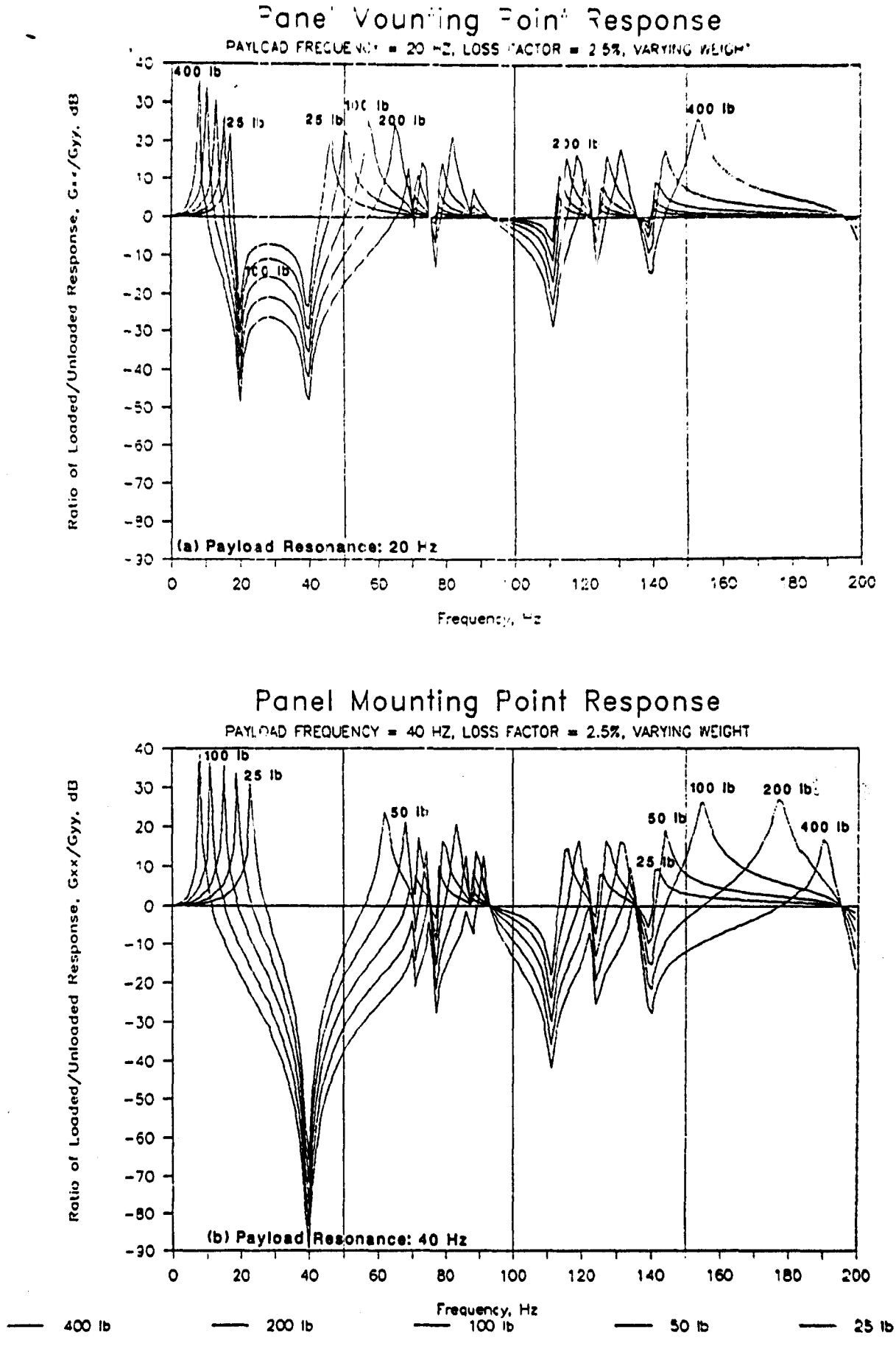

FIGURE 14. RATIO OF LOADED TO UNLOADED RESPONSE OF STRUCTURE AT MOUNTING POINT FOR DIFFERENT PAYLOAD WEIGHTS AND RESONANCE FREQUENCIES.

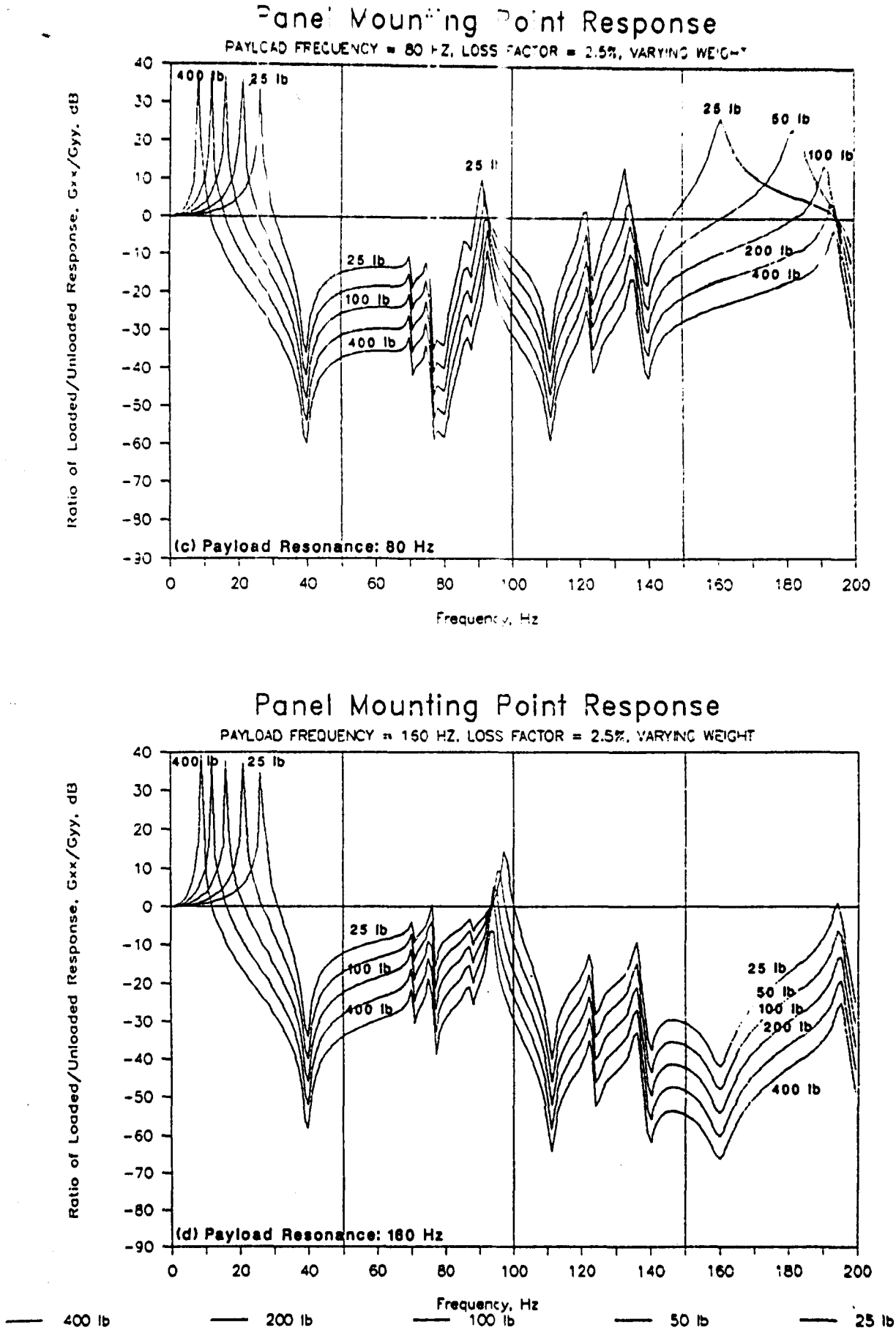

FIGURE 14. CONTINUED.

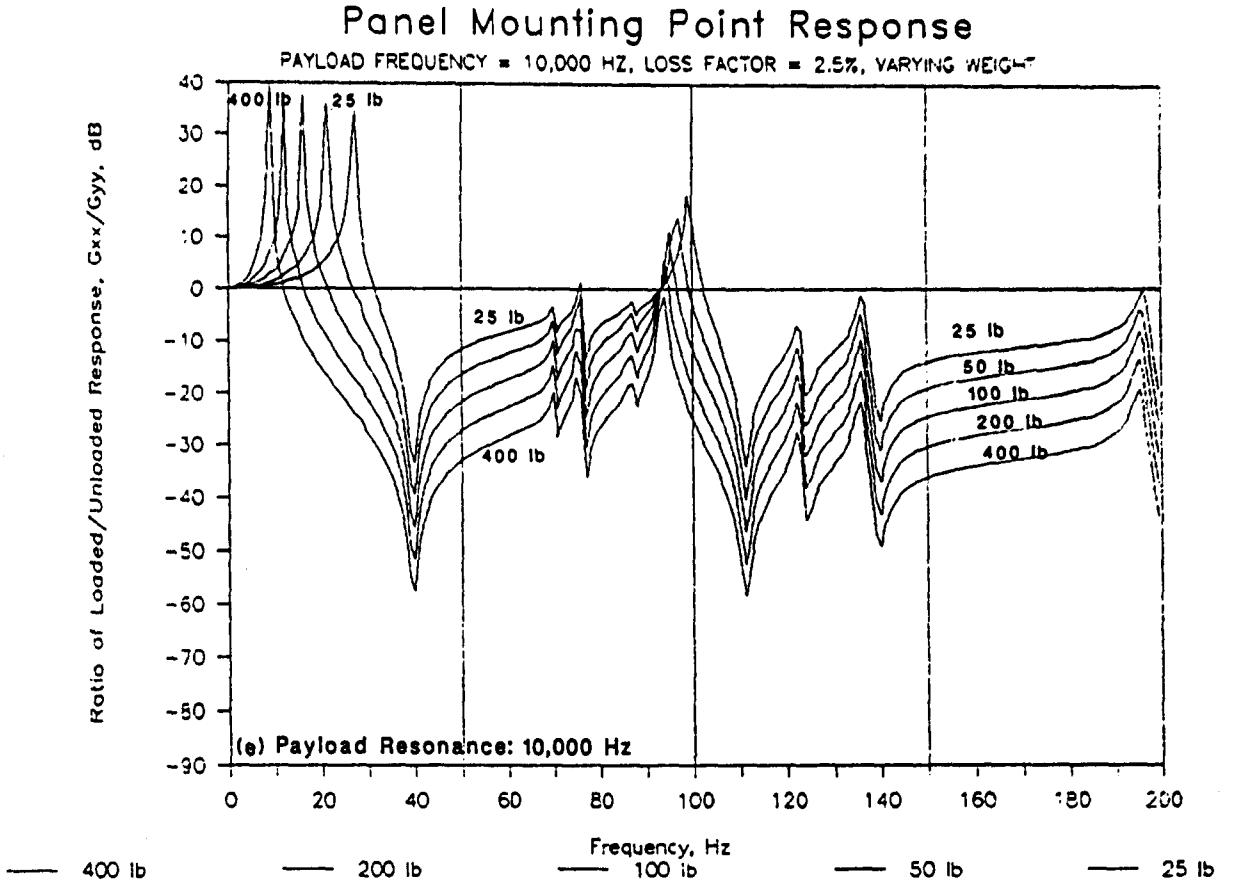

FIGURE 14. CONTINUED.

3.5.3 Payload Frequency

Plots of the response ratio as a function of payload frequency are more difficult to interpret than for damping and mass. Typical examples are shown in Figure 15. In this case the payload weight is 100 lb and the damping loss factor is 0.025. The data in Figure 15(a) refer to payload frequencies of 20, 40 and 80 Hz, and in Figure 15(b) to frequencies of 80, 160 and 10,000 Hz. In the latter case the family of curves is fairly well defined but in Figure 15(a), where one of the payload frequencies is below the fundamental frequency of the structure, the plots are more complicated. No general trend is immediately evident.

3.6 Modifications to Response Equations

3.6.1 General Approach

The response spectra discussed in the preceding sections were computed at 1 Hz intervals. This implies that, in practice, the response and impedance spectra for supporting panel and payload are known in detail. This will not be true for the Space Shuttle because (a) the vibration spectra for the mounting points could be given as an envelope for various locations on the sidewall and different loadings of the sidewall by payloads other than the one of interest, and (b) typical values (e.g. average or envelope) will have to be used for the mounting point impedance since the precise location of the payload in the payload bay will not be known at the time of the vibration test. Consequently, various representations have been assumed for parameters contained in the response functions defined by Eqs. 29 through 32, to determine the influence of the assumptions on the computed response. The premise is that, in practice, response and impedance functions are measured and averaged in some manner, to provide approximations to Eq. 29.

The representations essentially involve averaging in the frequency domain and can be summarized as follows:

(a) Use of $\langle|Z_p|\rangle$ and $\langle|Z_s|\rangle$ in place of Z_p and Z_s, respectively, in Eq. 29, where $\langle\ \rangle$ denotes an average over a given frequency band.

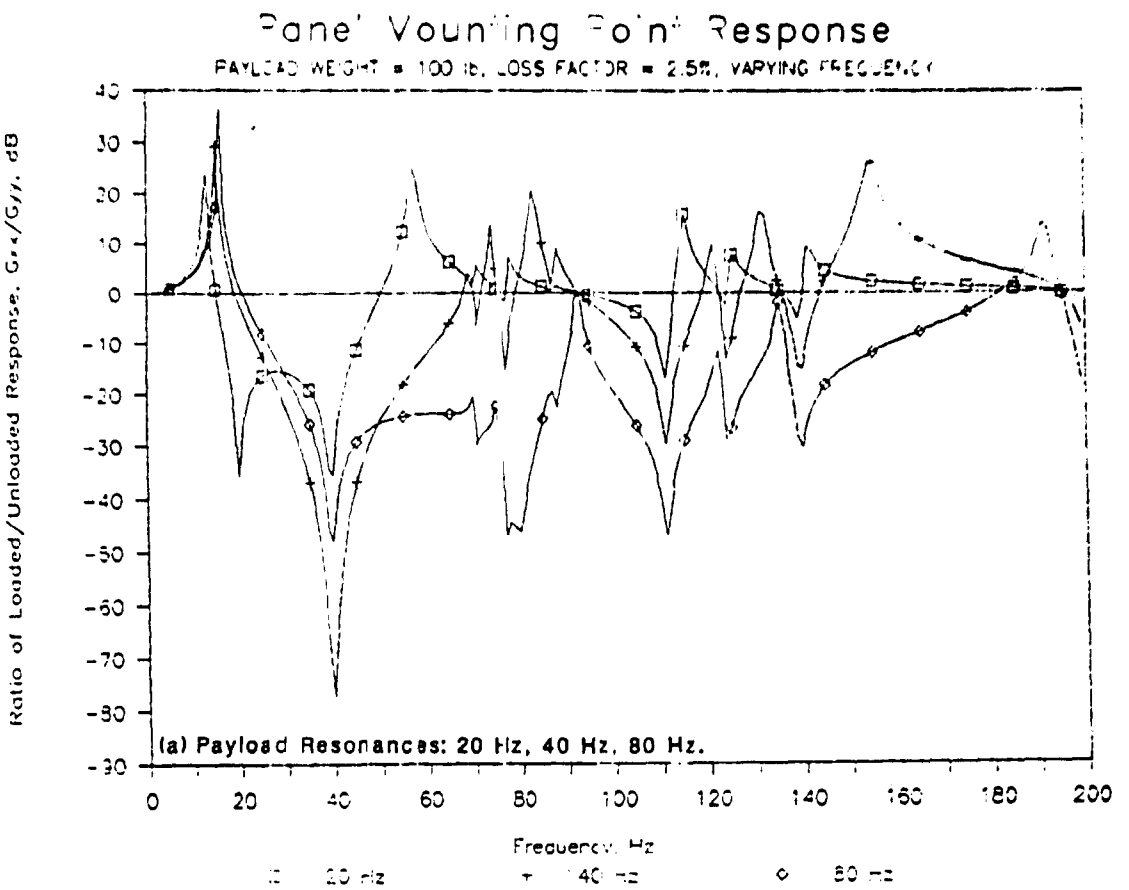

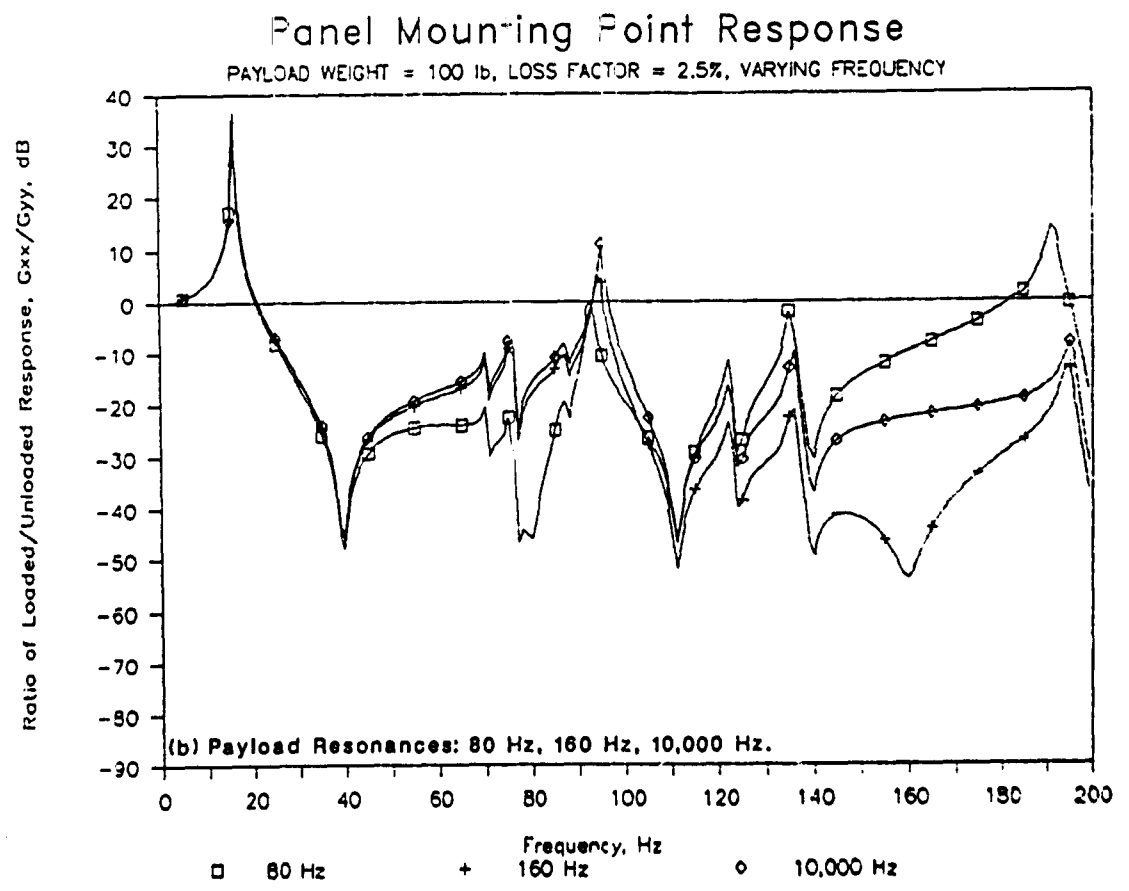

FIGURE 15. RATIO OF LOADED TO UNLOADED RESPONSE OF STRUCTURE FOR VARIOUS PAYLOAD RESONANCE FREQUENCIES.

(b) Use of $\langle Z_p \rangle$ and $\langle Z_s \rangle$ in place of Z_p and Z_s, respectively, in Eq. 29.

(c) Use of $\langle Z_s \rangle$ in place of Zs in Eq. 29.

(d) Use of $\langle Z_s \rangle_m$ in place of Z_s in Eq. 29, where $\langle \ \rangle_m$ denotes a moving average in the frequency domain.

(e) Use of Z_{ep} and Z_{es} in place of Z_p and Z_s, respectively, in Eq. 29, where Z_{ep} and Z_{es} denote envelopes of Z_p and Z_s, respectively.

Before considering the effects of four of these representations on the computed values of G_{xx}/G_{yy} (or G_{AA}/G_{SS}) and G_{pp}, it is useful to see how the averaging process modifies the predicted response of the unloaded structure, the mounting point impedance and the payload impedance. The response spectrum, in terms of acceleration power spectral density, for the mounting point on the unloaded structure is shown in Figure 16. The figure contains three spectra, one computed with a resolution of 1 Hz and two obtained by averaging the 1-Hz spectrum in either 5 Hz or 25 Hz bandwidths. As expected, the band-averaging reduces spectral peaks and fills in spectral troughs.

Mounting point impedance spectra are shown in Figure 17 in terms of magnitude and phase. The averaging process involved, first, band-averaging of the real and imaginary components of the impedance separately and then combining the averages to obtain the mean square average magnitude $\langle Z_s \rangle^2$ and average phase ($\arg \langle Z_s \rangle$). It is interesting to note that, in this approach, the trough which occurs in the magnitude spectrum for the impedance at the fundamental resonance frequency of the unloaded panel can increase in depth due to the averaging, whereas the opposite would be true if the averaging process were applied directly to $|Z_s|$ (i.e. if $\langle |Z_s| \rangle$ were plotted rather than $|\langle Z_s \rangle|$).

Figure 18 contains spectra for the impedance of the 100 lb/80 Hz payload. Similar results were obtained for the other payloads. As for the structure, real and imaginary parts were averaged separately and then the averages combined to obtain $|\langle Z_p \rangle|2$ and $\arg \langle Z_p \rangle$.

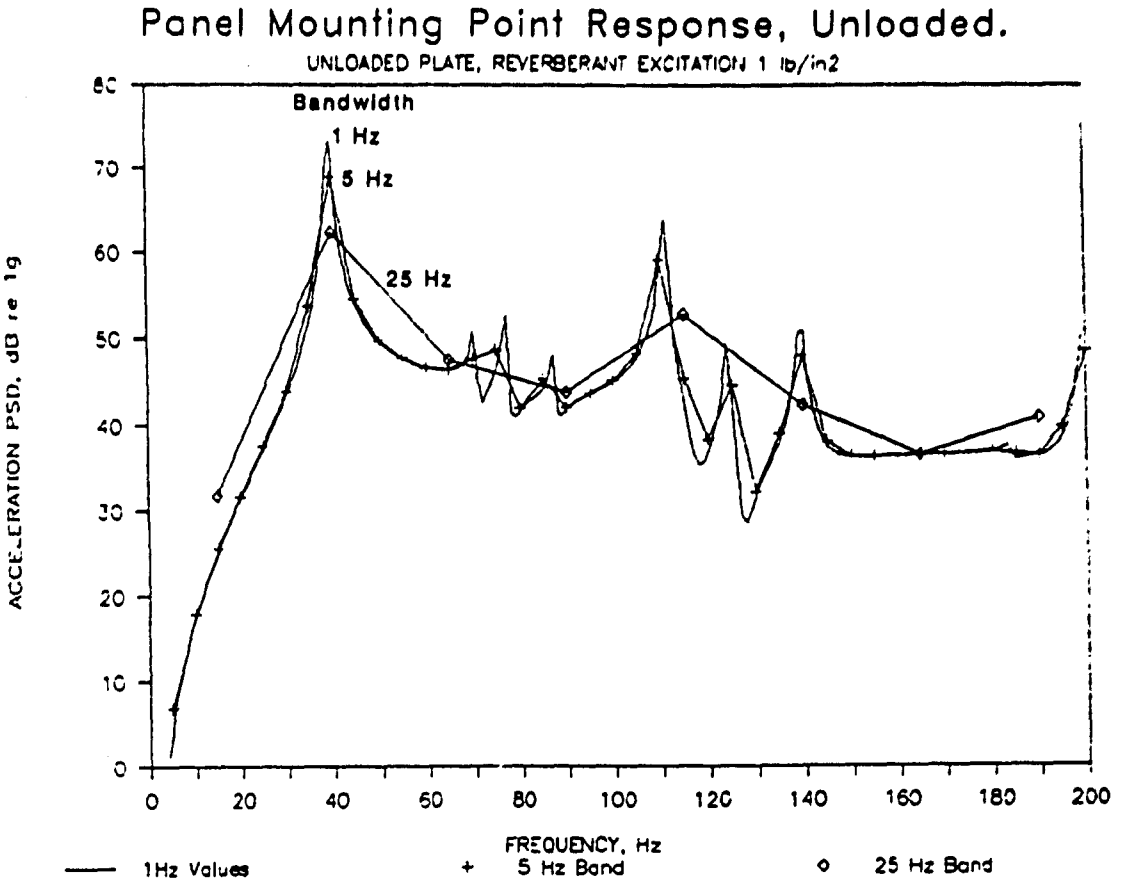

FIGURE 16. EFFECT OF FREQUENCY AVERAGING ON CALCULATED RESPONSE OF UNLOADED STRUCTURE.

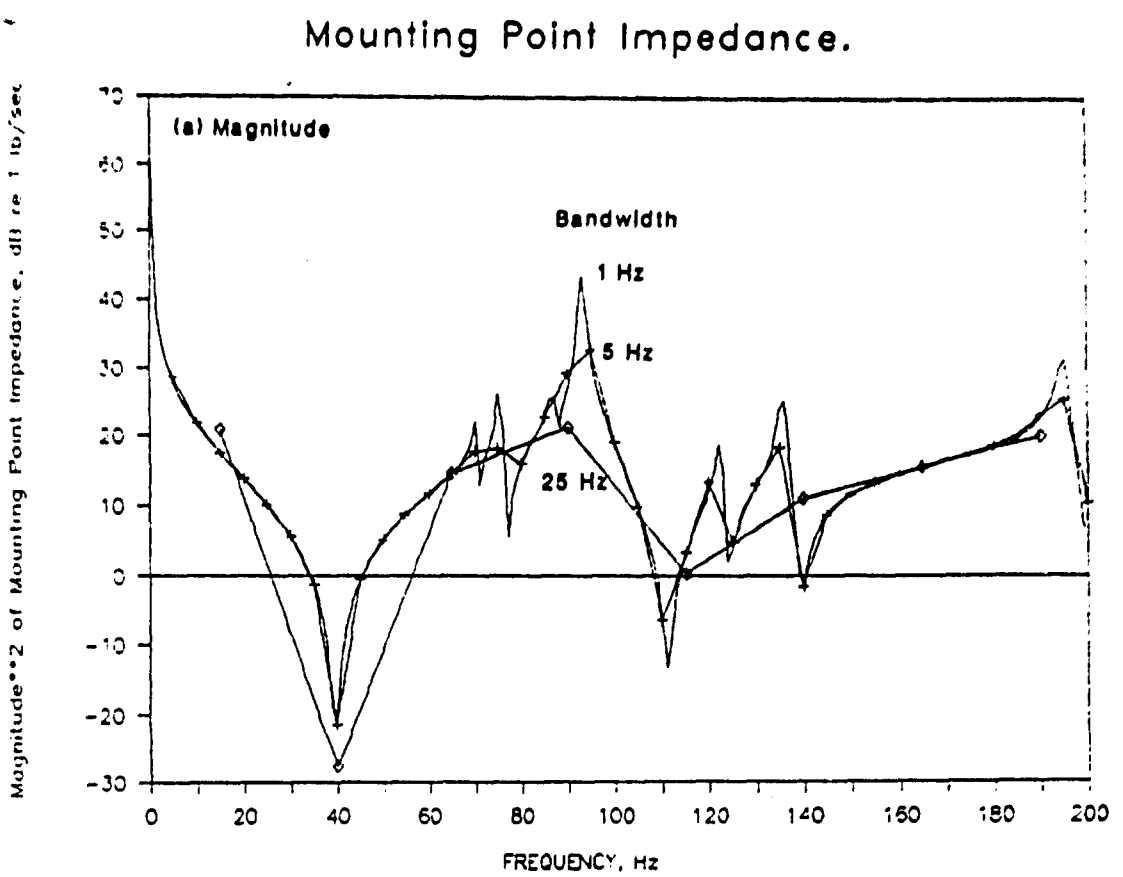

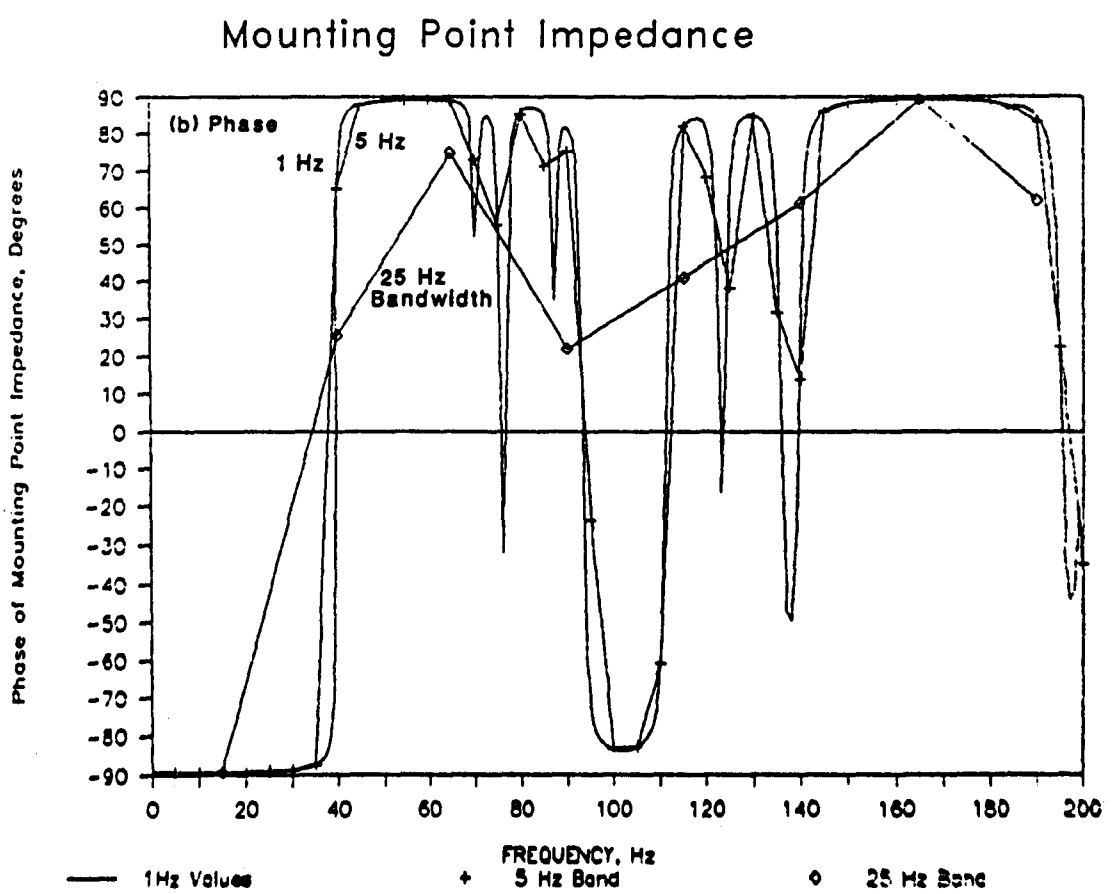

FIGURE 17. EFFECT OF FREQUENCY BAND AVERAGING ON CALCULATED MOUNTING POINT IMPEDANCE.

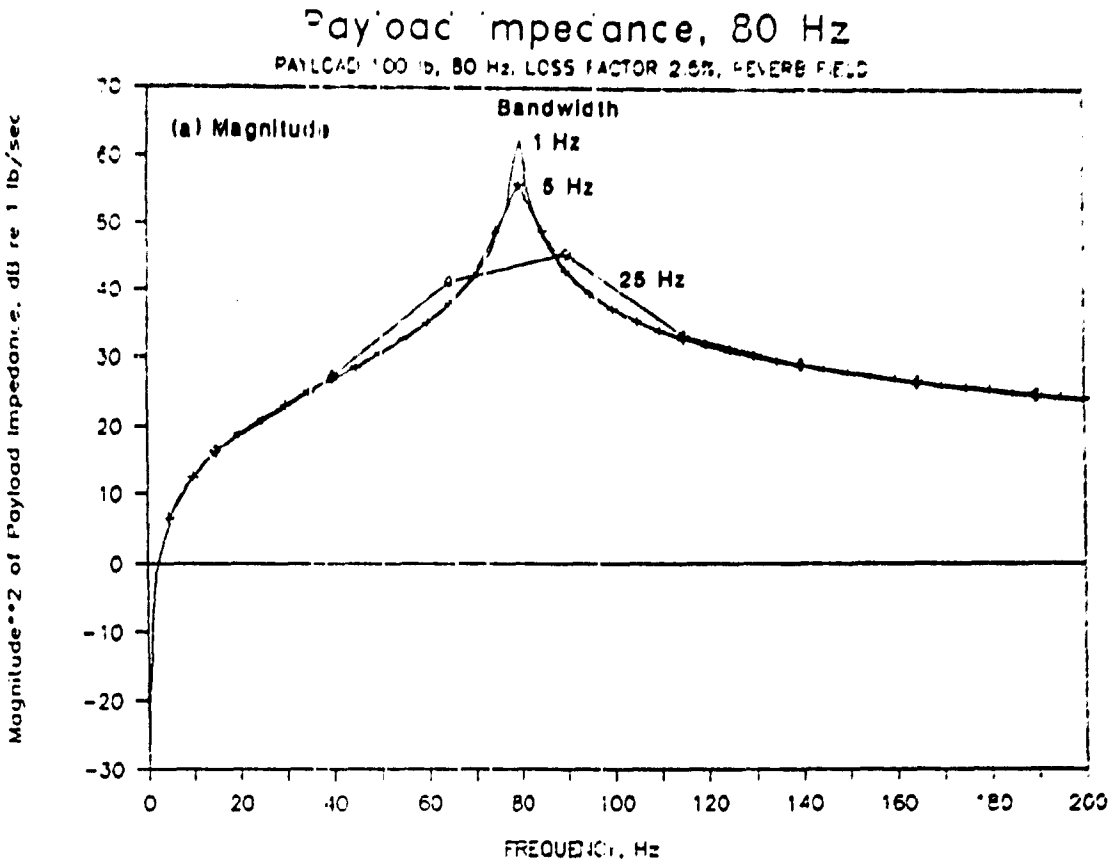

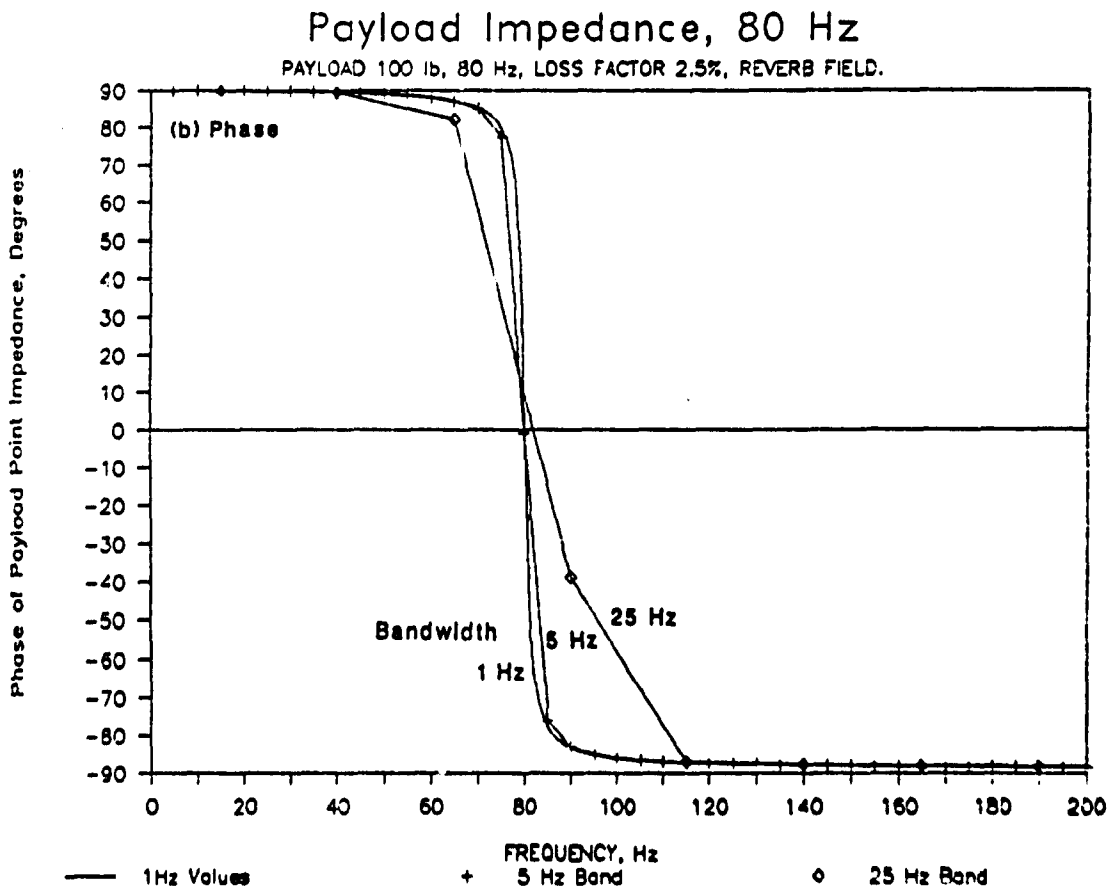

FIGURE 18. EFFECT OF FREQUENCY BAND AVERAGING ON CALCULATED PAYLOAD IMPEDANCE.

Now consider the introduction of different representations for the impedance terms in Eq. 29. In the following discussion, all averaging processes use, as a basis, results computed with a resolution of 1 Hz.

3.6.2 Representation (a)

When the impedances are used in the form $<|Z_p|>$ and $<|Z_s|>$, Eq. 29 takes on the approximate form:

$$G_{AA}/G_{SS} = G_{xx}/G_{yy} = 1/[1 + <|Z_p|>/<|Z_s|>]^2 \qquad (34)$$

In this approach, the complex ratio Z_p/Z_s is replaced by the totally real ratio $<|Z_p|>/<|Z_s|>$. Phase information is not retained since the ratio involves only the amplitudes of the impedances. Typical response ratios for the payload mounting point are shown in Figure 19 for two 1-dof payload configurations with resonances at one-half (20 Hz) and twice (80 Hz) the fundamental frequency of the support structure. Averaging is performed in 5 Hz and 25 Hz bandwidths. The most important characteristic of the figures is that the approximation results in a response ratio that is always less than unity, whereas the correct response ratio can be greater than unity at some frequencies. The implication of this result is that there is potential for <u>undertest</u> of the payload, particularly at low frequencies, as can be seen in the associated computed spectra for payload response (Figure 20). The frequencies of concern are the resonance frequencies of the combined structure/payload system. In computing the payload response spectra, band-averaged values ($<G_{yy}>$) for G_{yy}, the displacement response spectrum for the unloaded structure, were used to represent the enveloping of that data. There is also the potential for <u>overtest</u> at frequencies corresponding to the resonances of the payload and unloaded structure, especially for the higher averaging bandwidth.

3.6.3 Representation (b)

The second approximation is to assume that the impedances are averaged such that phase is retained -- in this case by averaging the real and imaginary

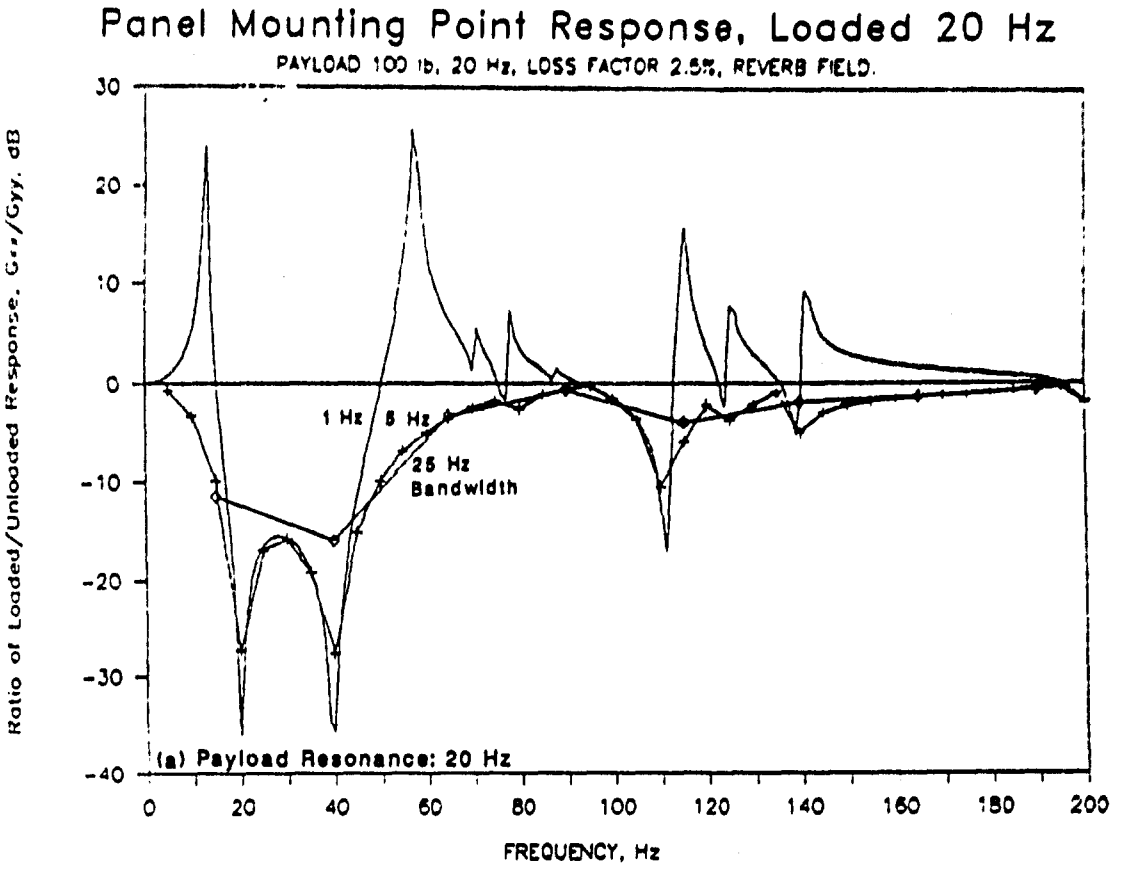

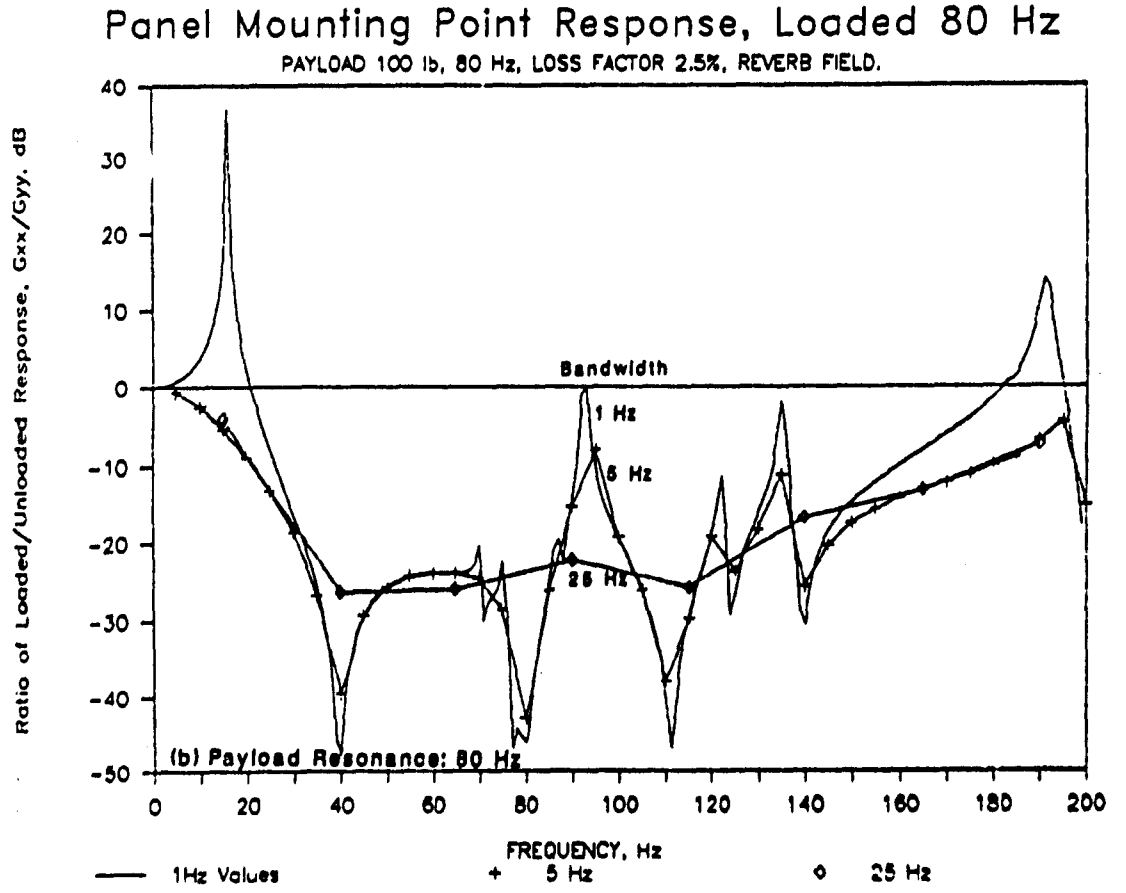

FIGURE 19. RATIO OF LOADED TO UNLOADED RESPONSE OF STRUCTURE COMPUTED USING EQUATION 34.

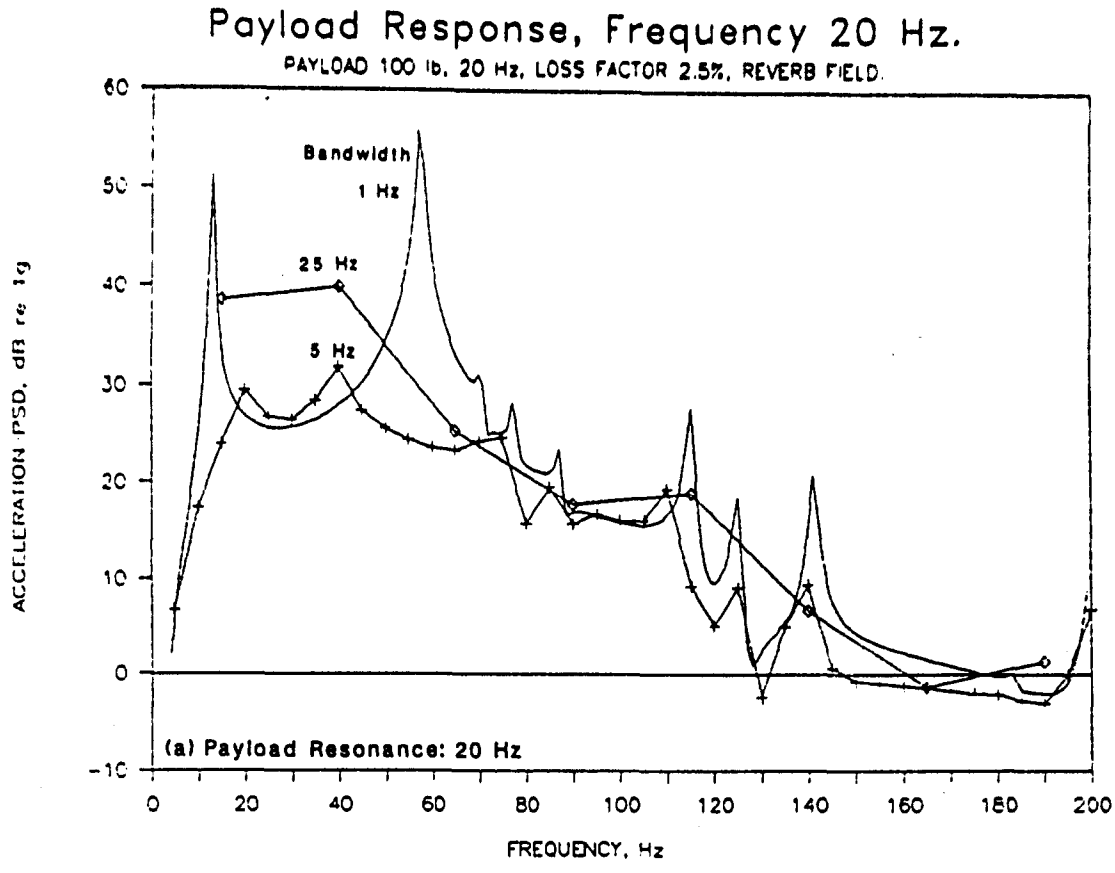

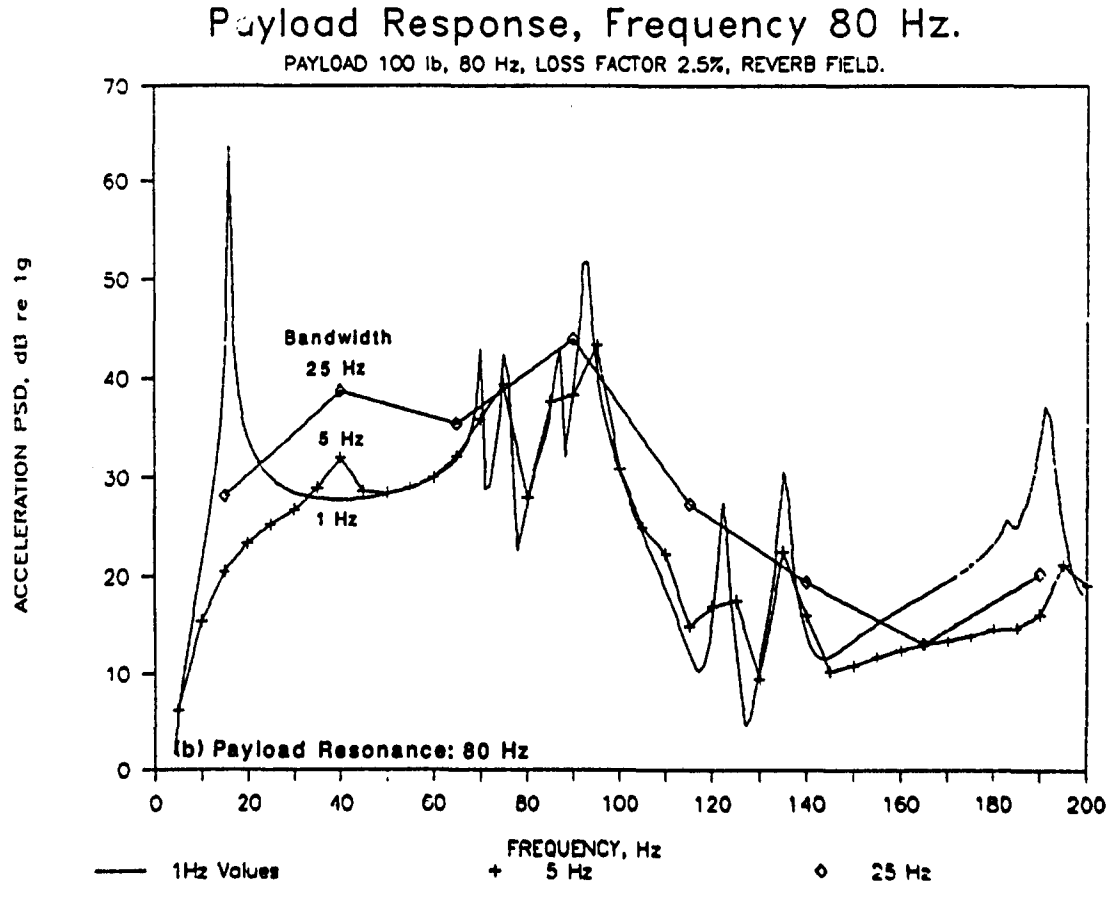

FIGURE 20. PAYLOAD RESPONSE COMPUTED USING EQUATIONS 34 AND 31.

parts of the impedance separately. The approximation to Eq. 29 then has the form:

$$G_{AA}/G_{SS} = G_{xx}/G_{yy} = 1/\ |1 + \langle Z_p \rangle/\langle Z_s \rangle|^2 \qquad (35)$$

It is now seen (Figure 21) that both the approximate and correct response ratios can have values greater than and less than unity, depending on frequency. Thus, the potential for undertest of the payload at the resonance frequencies of the combined system is reduced, but it appears that there is potential for overtest at resonance frequencies of the unloaded structure (Figure 22). In computing the payload response, band-averaged values were also used for the acceleration response spectrum of the unloaded structure (i.e. $\langle G_{SS} \rangle$).

3.6.4 Representation (c)

This representation is based on the premise that the payload impedance is known in detail, since it can be measured prior to the vibration qualification test, but the mounting point impedance will be known only as some form of average value (but retaining phase information). Eq. 29 now takes the approximate form:

$$G_{AA}/G_{SS} = G_{xx}/G_{yy} = 1/\ |1 + Z_p/\langle Z_s \rangle|^2 \qquad (36)$$

Since Z_p is computed with 1 Hz resolution, G_{xx}/G_{yy} also has a 1 Hz resolution, even though $\langle Z_s \rangle$ is computed only at intervals of 5 Hz or 25 Hz. This accounts for the "sloping-step" appearance of the response-ratio spectra in Figure 23 (5 Hz bandwidth) and Figure 24 (25 Hz bandwidth). The spectra indicate that a 5-Hz frequency band provides a reasonably good approximation to the correct response-ratio spectrum. However, it may not be practical to obtain information for the structure with this amount of detail. In contrast, averaging in 25 Hz bandwidths results in response-ratio spectra that are too coarse. Thus, a moving average procedure was also investigated; this is the form for Representation (d).

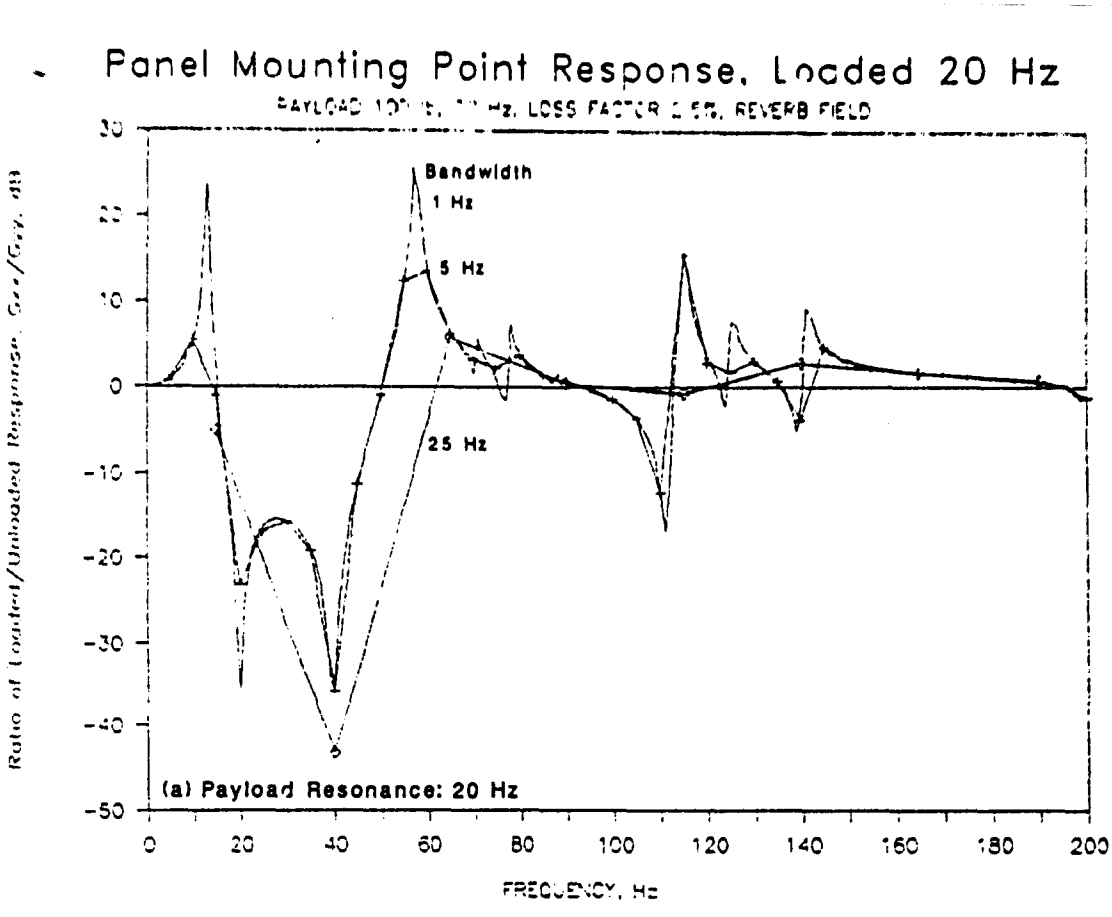

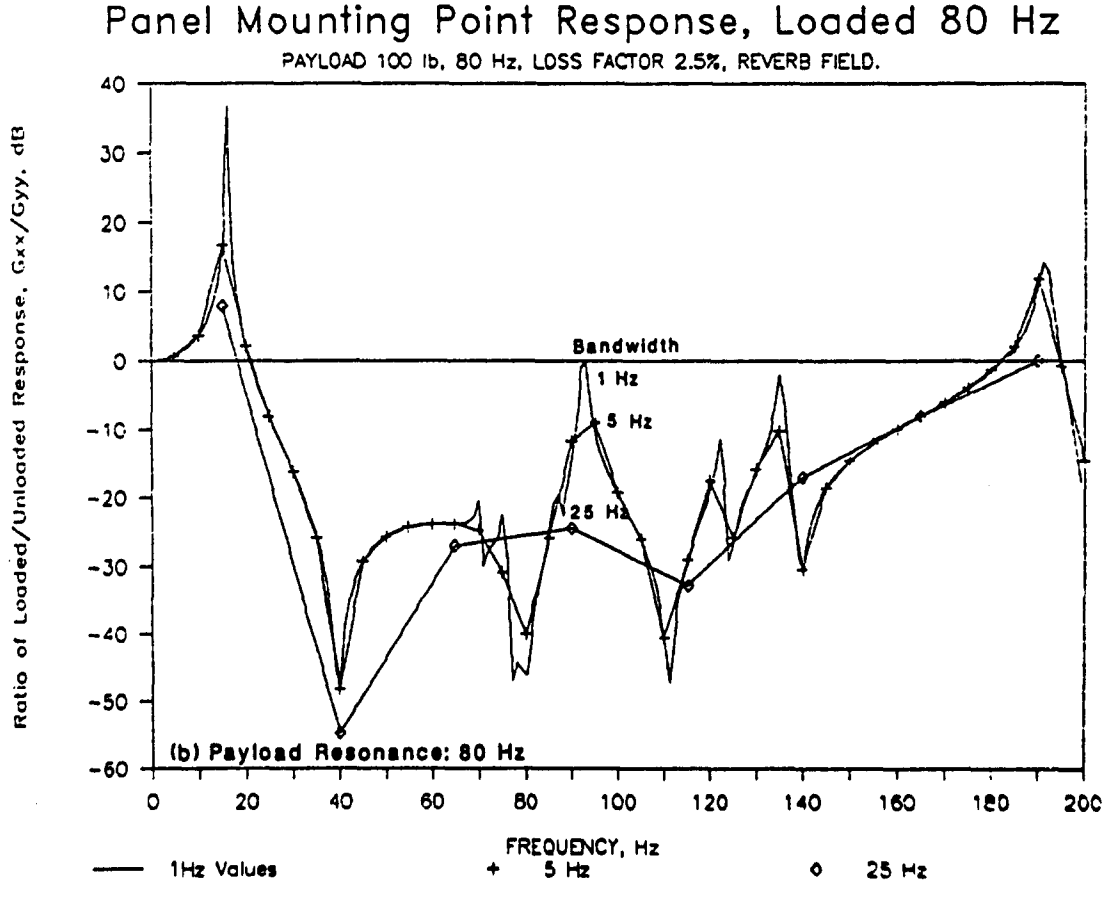

FIGURE 21. RATIO OF LOADED AND UNLOADED RESPONSE OF STRUCTURE COMPUTED USING EQUATION 35.

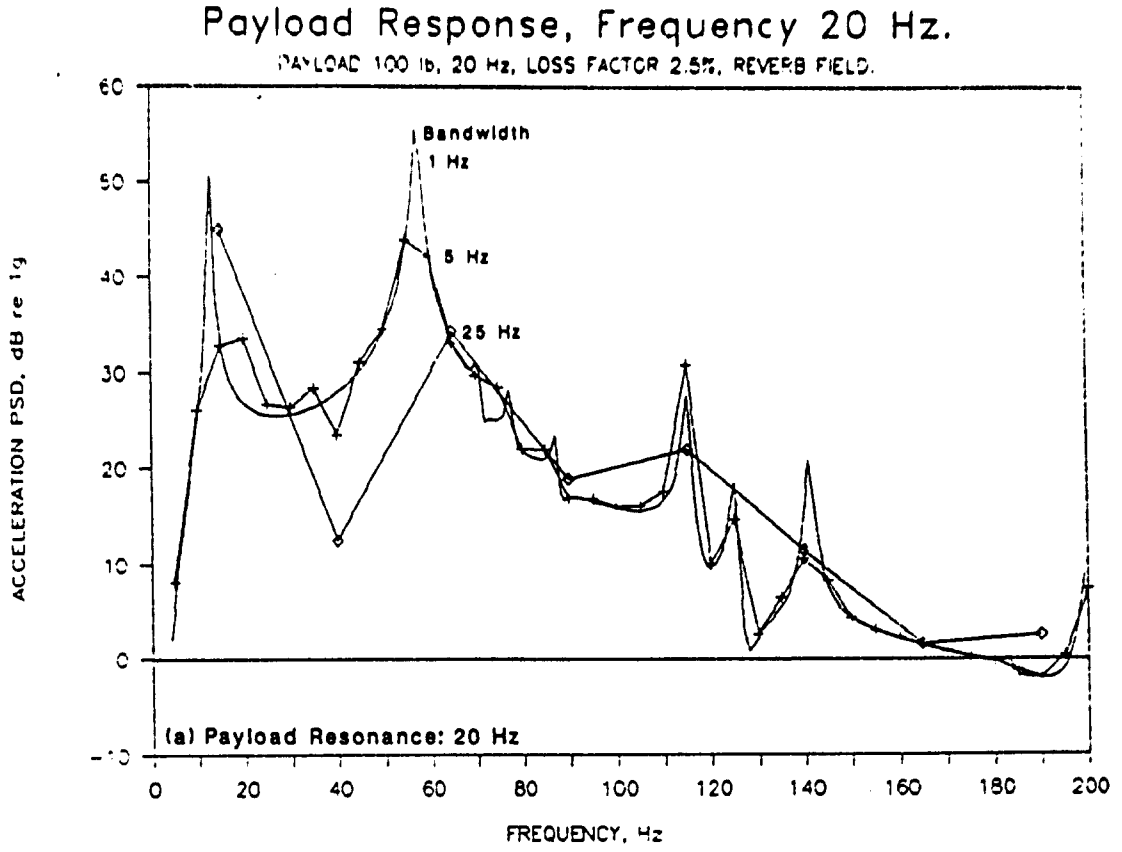

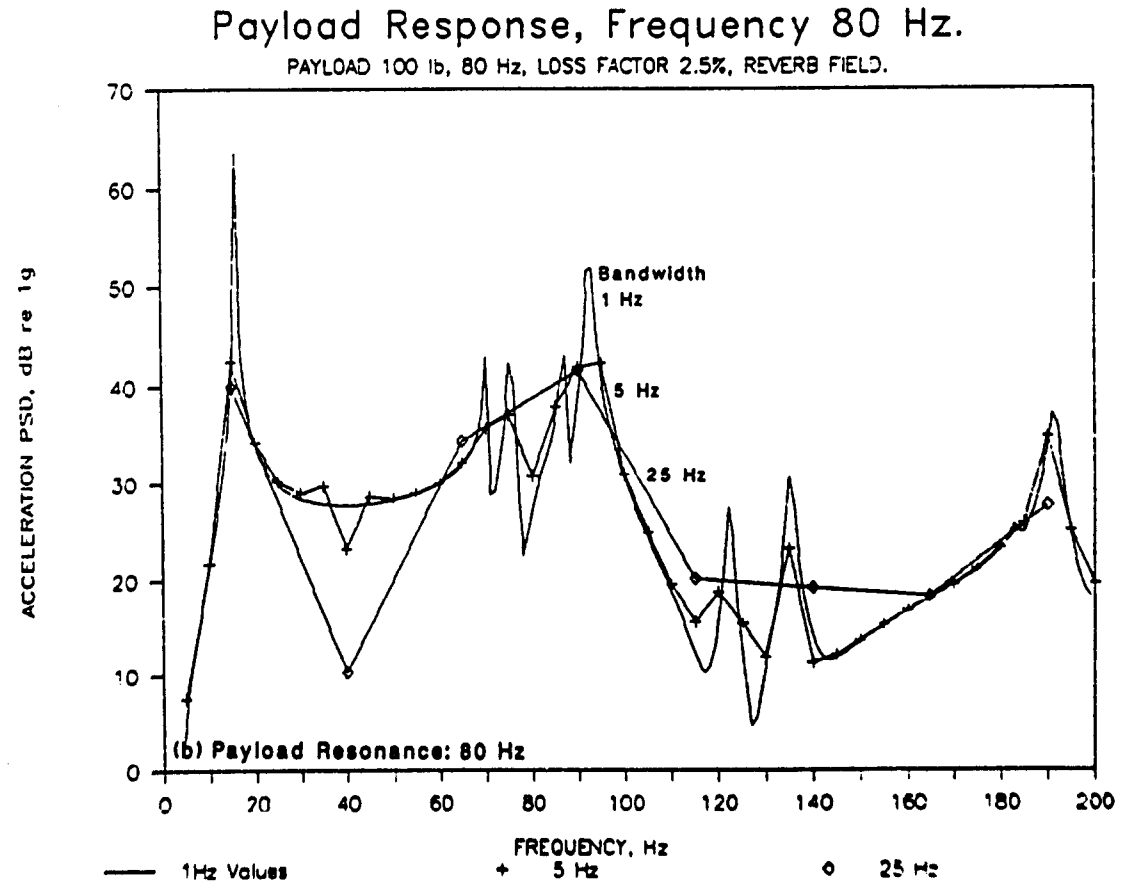

FIGURE 22. PAYLOAD RESPONSE COMPUTED USING EQUATIONS 35 & 31.

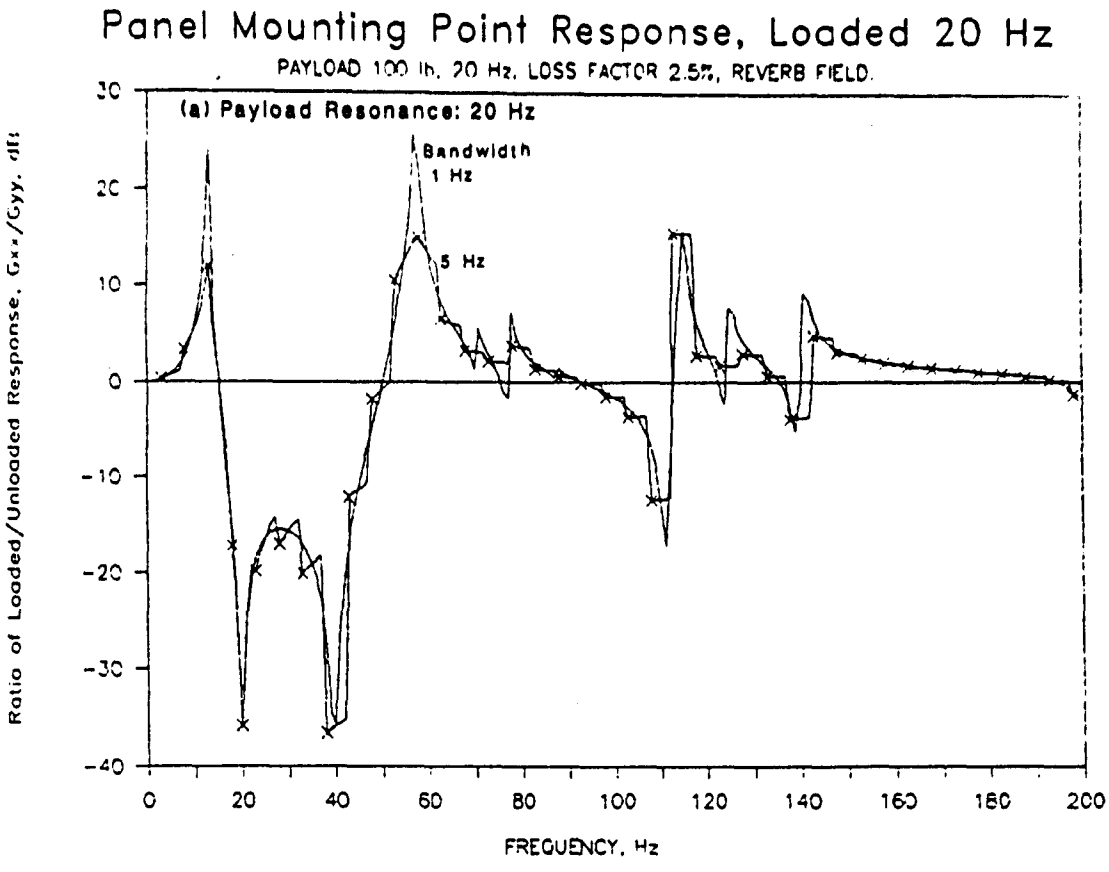

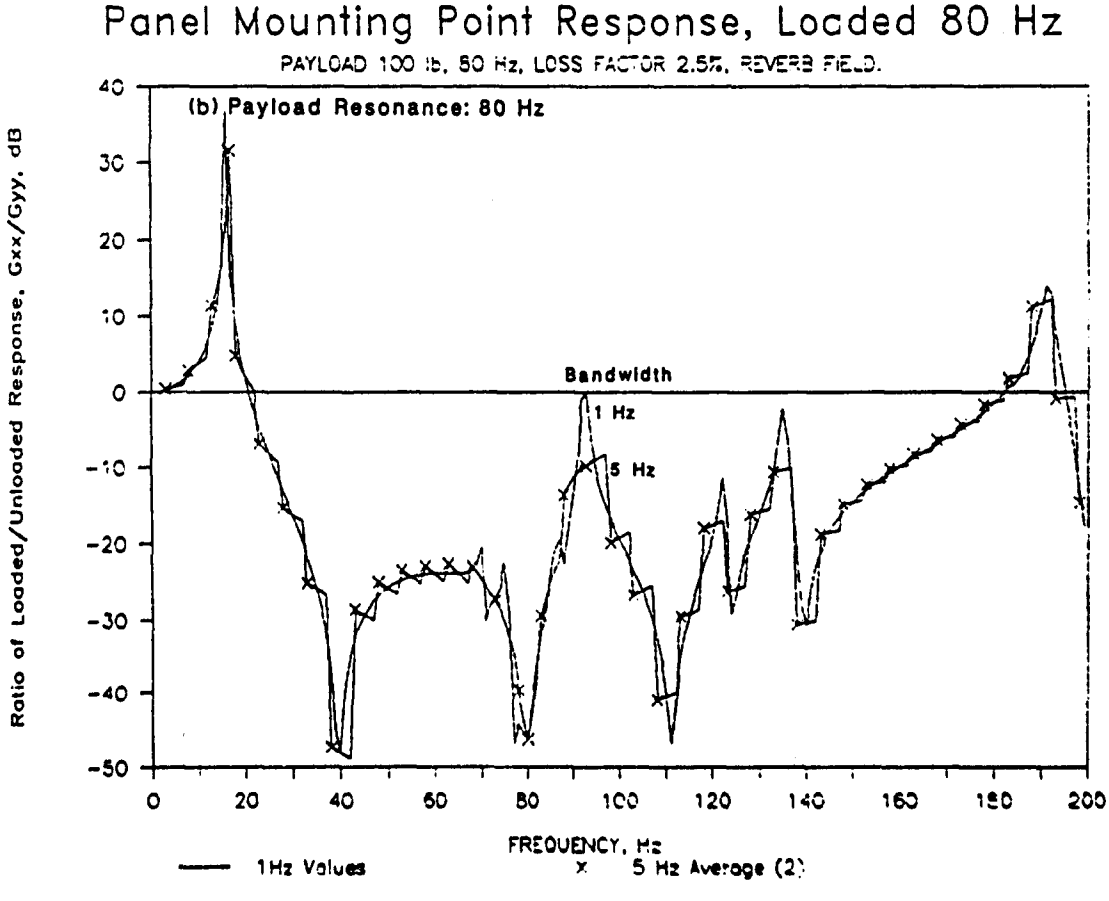

FIGURE 23. RATIO OF LOADED TO UNLOADED RESPONSE OF STRUCTURE COMPUTED USING EQUATION 36 (5 Hz BANDWIDTH).

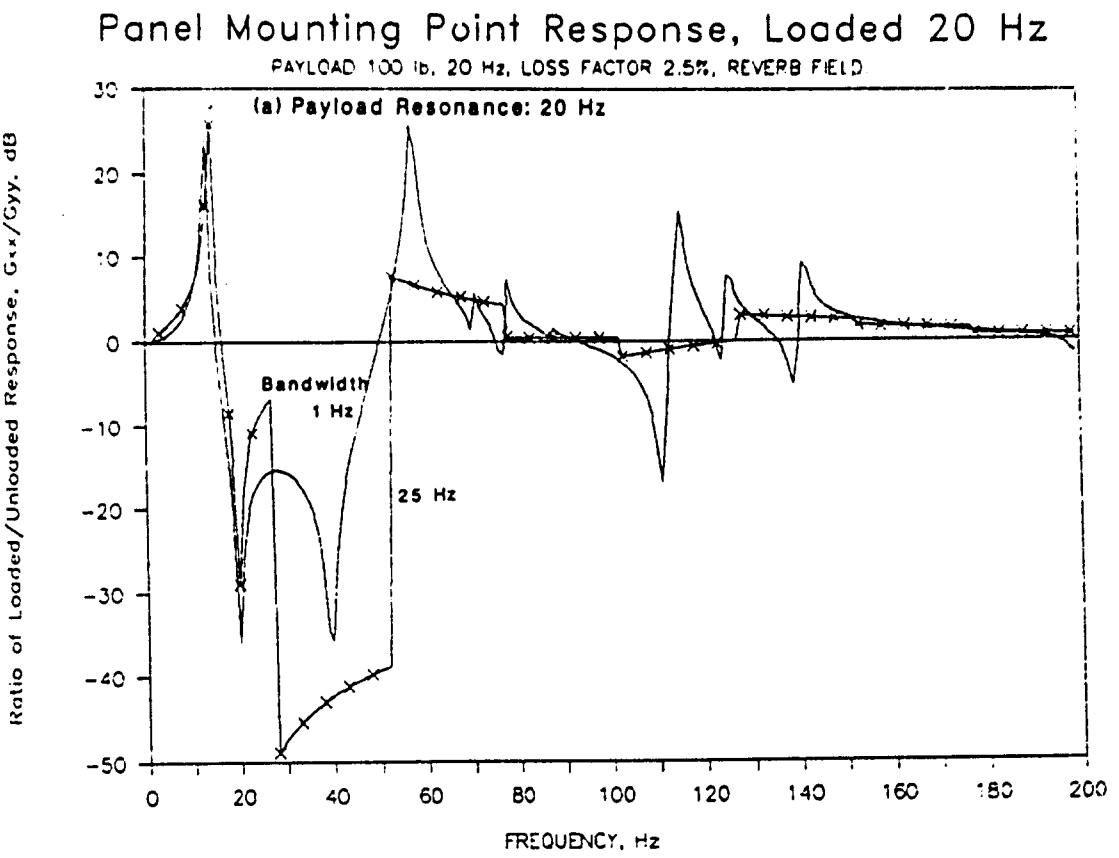

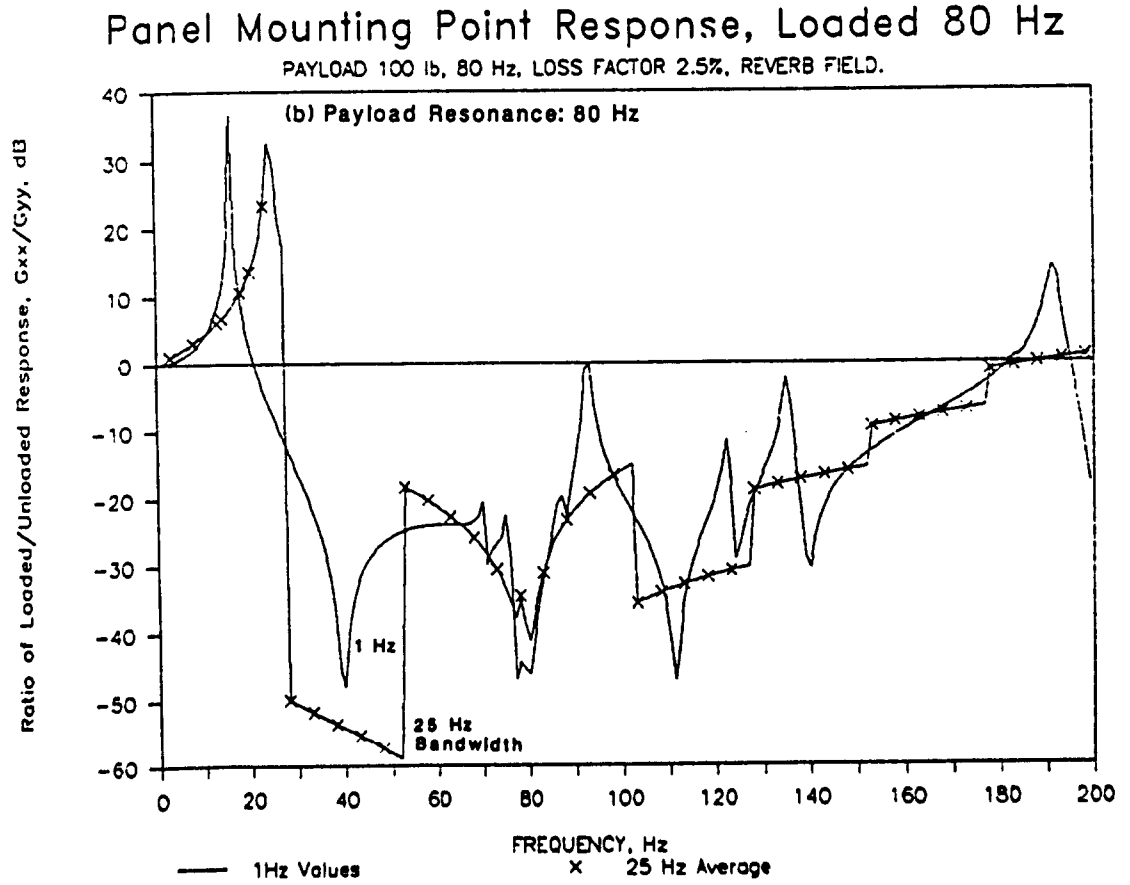

FIGURE 24. RATIO OF LOADED TO UNLOADED RESPONSE OF STRUCTURE COMPUTED USING EQUATION 36 (25 Hz BANDWIDTH).

3.6.5 Representation (d)

In this case, the response spectrum for the unloaded structure and the impedance function for the mounting point were frequency-averaged using a moving 10-Hz bandwidth. The resulting acceleration power spectral density function for the mounting point on the unloaded structure is compared in Figure 25 with the corresponding spectrum computed with 1 Hz resolution. The typical broadening and reduction of the spectral peaks is immediately apparent. The corresponding magnitude and phase of the mounting point impedance are shown in Figure 26, where, as before, the averaging is performed on the real and imaginary parts of Z_s separately. Resulting computed spectra for the response ratio are plotted in Figure 27, where there is generally good agreement between averaged and unaveraged values. In this representation, the response ratio is given by the equation:

$$G_{AA}/G_{SS} = G_{xx}/G_{yy} = 1/\ |1 + Z_p/\langle Z_s \rangle_m|^2 \qquad (37)$$

Associated response spectra for the payload are shown in Figure 28, and, again, there is reasonably good agreement between averaged and unaveraged spectra, except in the vicinity of the fundamental frequency (40 Hz) of the unloaded structure.

Figure 28 also contains payload response spectra computed under the assumption that $G_{xx}/G_{yy} = 1$. This extreme situation would occur, in practice, if the shaker were controlled (without destroying the shaker!) to maintain a vibration amplitude equal to that of the unloaded structure at the mounting point location, at all frequencies. It is interesting to note that there would be no undertesting at the resonance frequencies of the combined system, but there would be severe overtesting at the resonance frequencies of the unattached payload and the unloaded structure. More surprisingly, for the 100 lb/80 Hz payload, there would be severe overtesting over a wide frequency range.

3.6.6 Representation (e)

The form of Eq. 29 associated with Representation (e) is

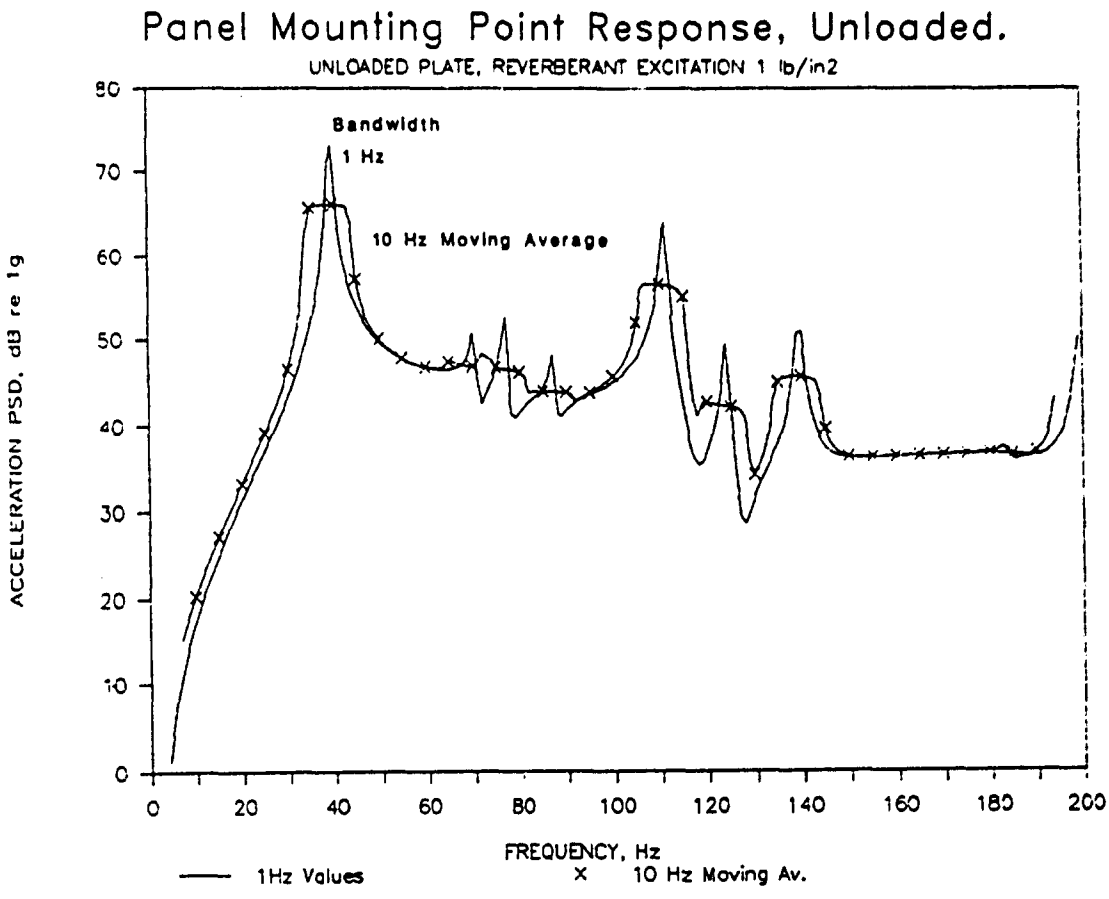

FIGURE 25. EFFECT OF MOVING FREQUENCY AVERAGE ON COMPUTED RESPONSE OF UNLOADED STRUCTURE.

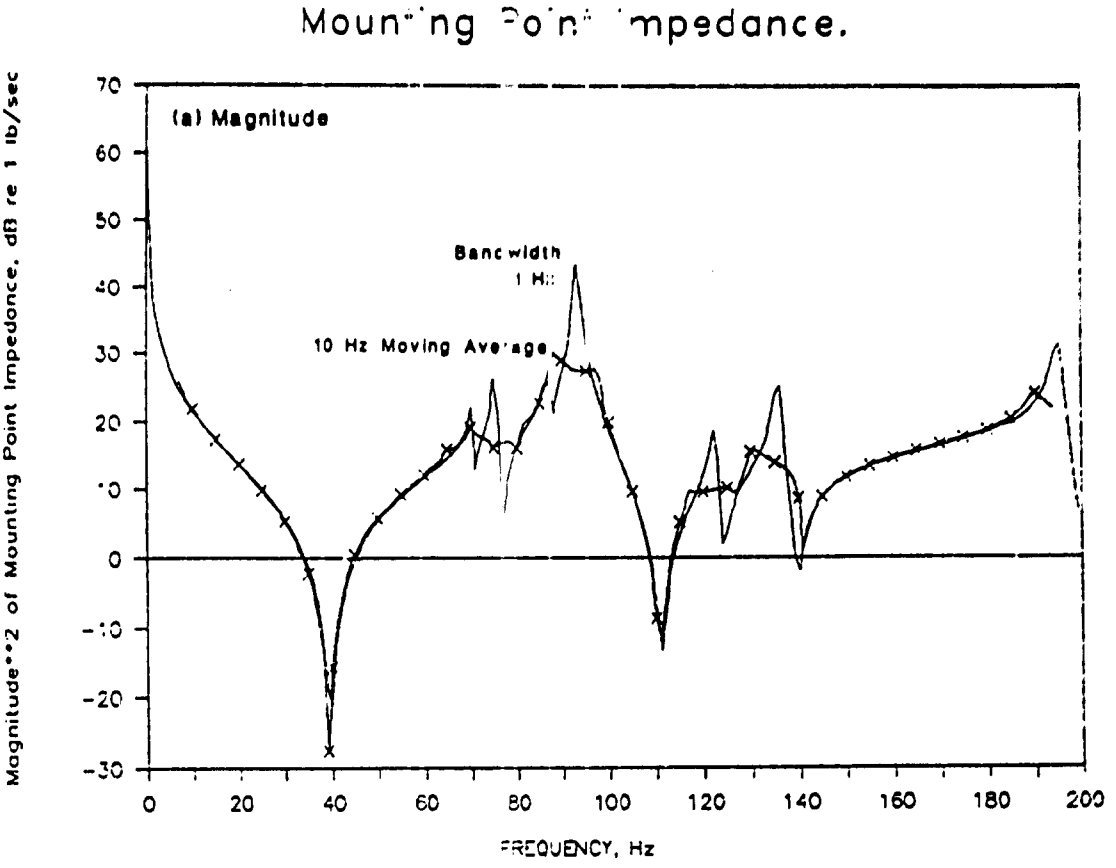

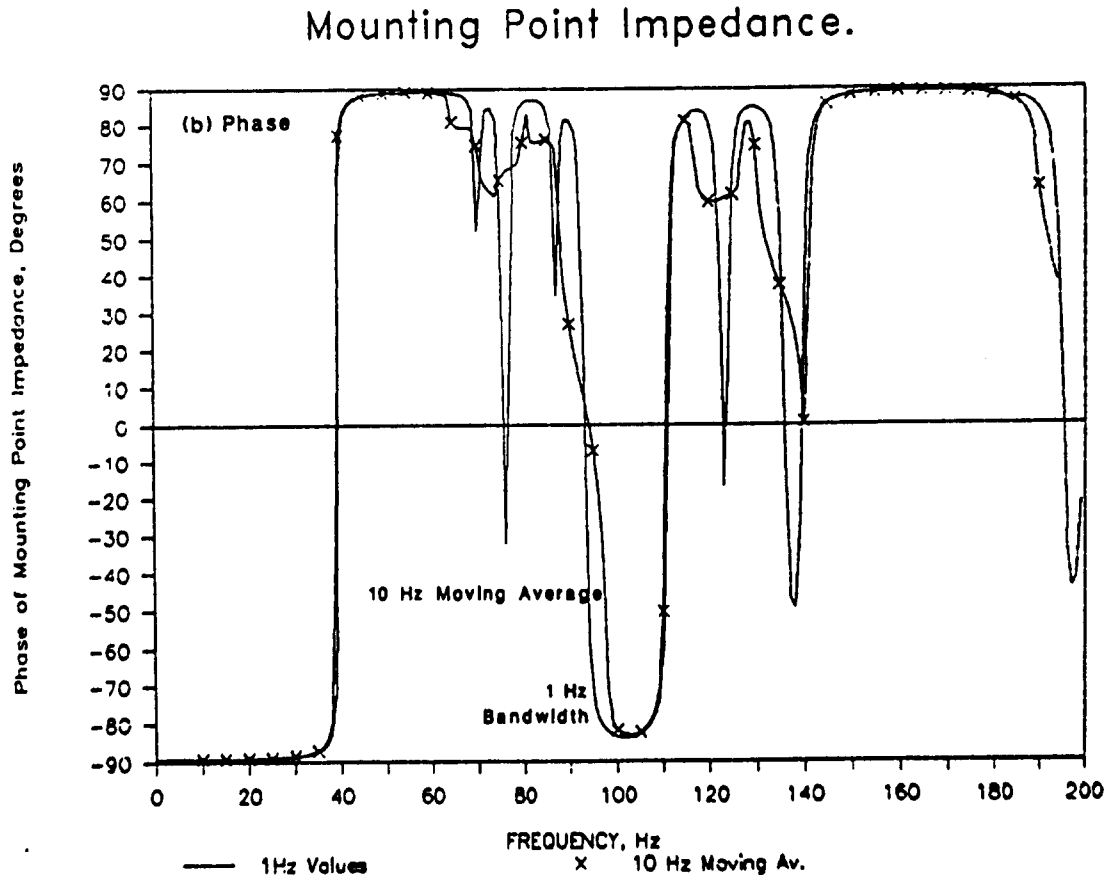

FIGURE 26. EFFECT OF MOVING FREQUENCY AVERAGE ON COMPUTED MOUNTING POINT IMPEDANCE.

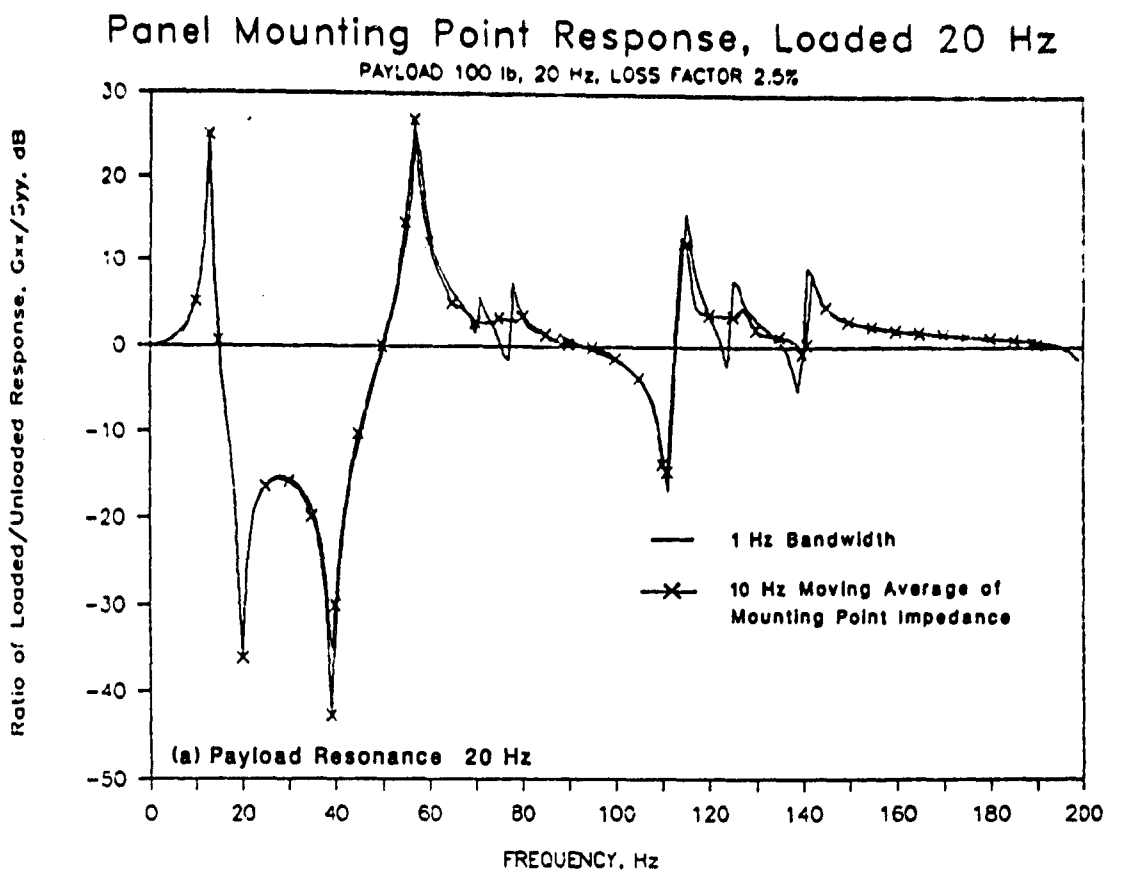

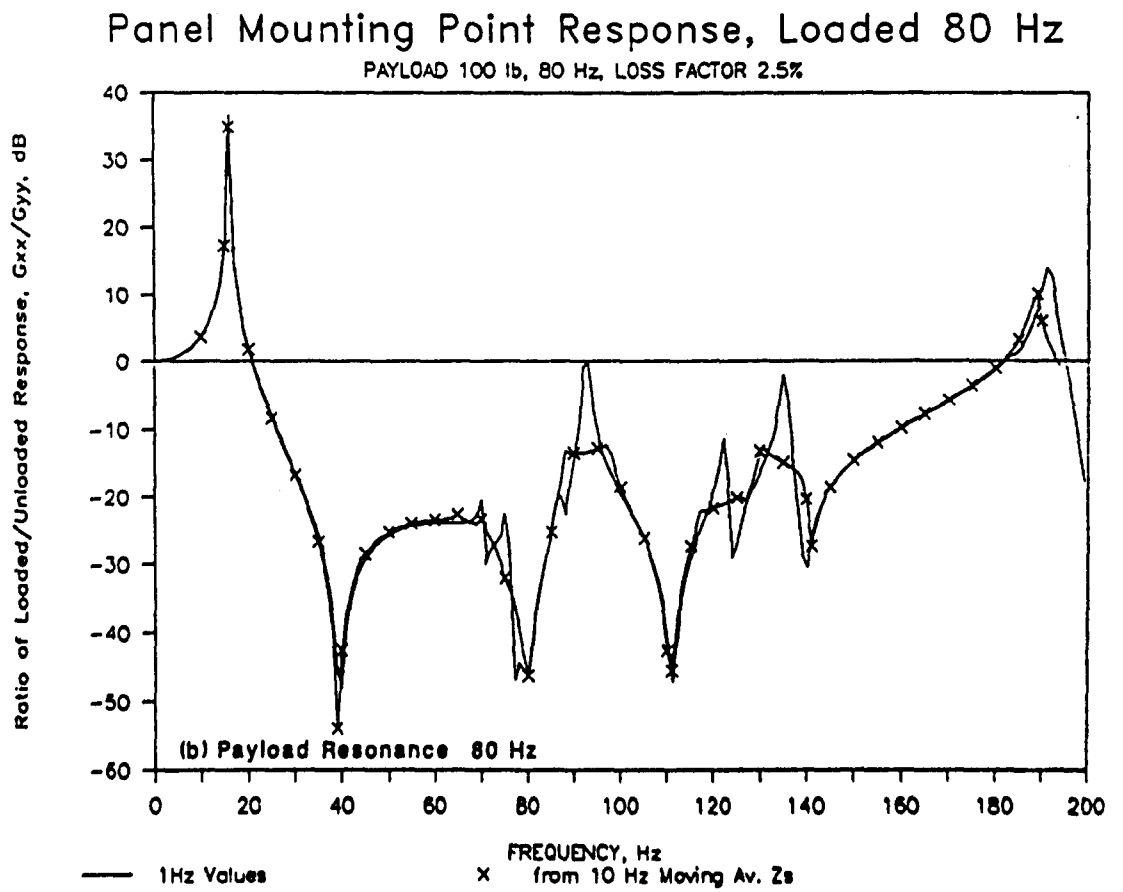

FIGURE 27. RATIO OF LOADED TO UNLOADED RESPONSE OF STRUCTURE COMPUTED USING EQUATION 37. (MOVING AVERAGE OF MOUNTING POINT IMPEDANCE).

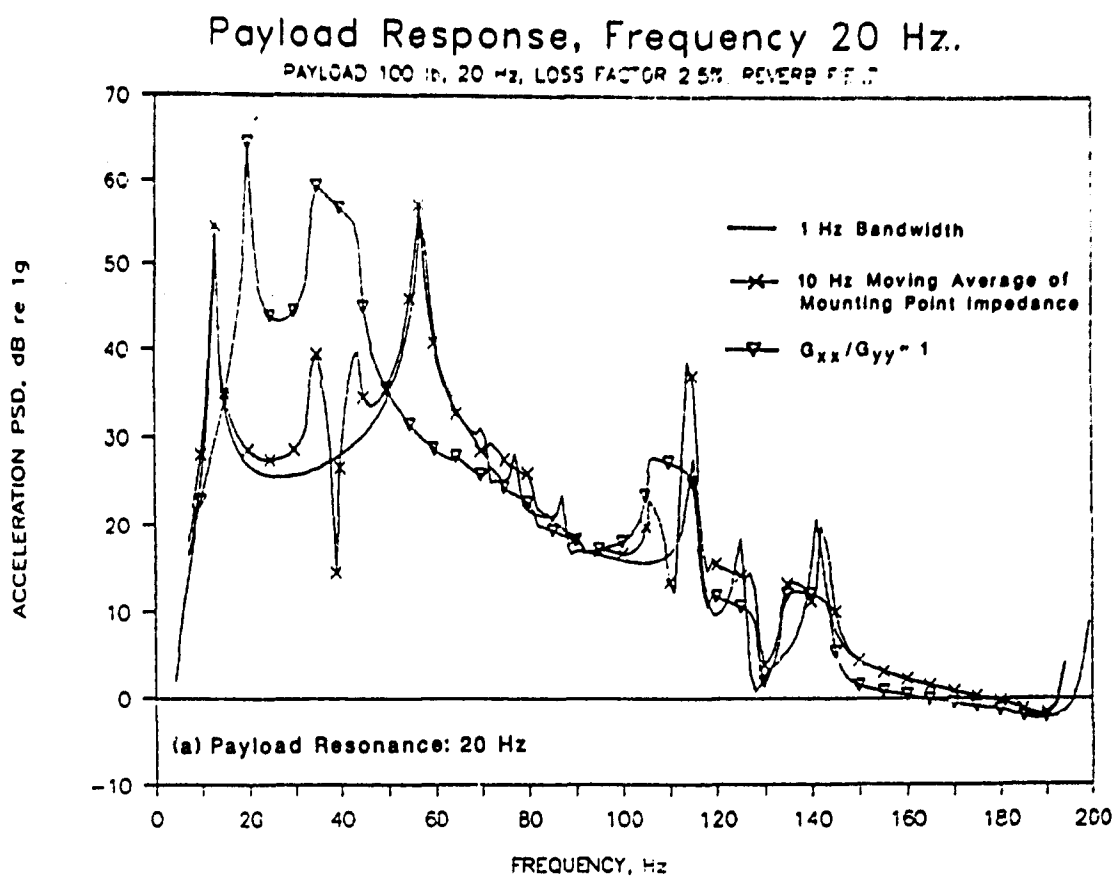

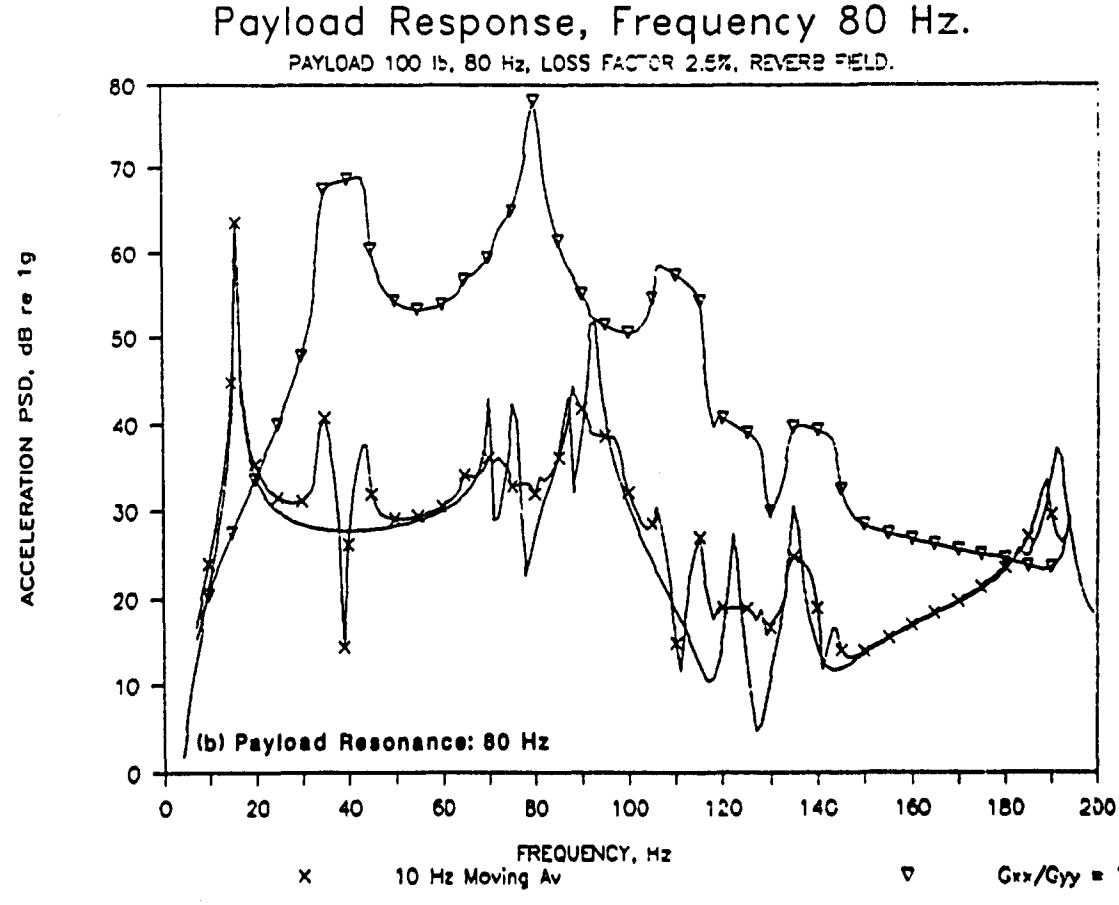

FIGURE 28. PAYLOAD RESPONSE COMPUTED USING EQUATIONS 37 & 31. (MOVING AVERAGE OF MOUNTING POINT IMPEDANCE).

$$G_{AA}(f) = G_{SS}(f)/[1 + |Z_{ep}(f)| \; / \; |Z_{es}(f)|]^2 \qquad (38)$$

where the enveloping of the impedance functions is performed on the magnitude of the functions without regard for phase. Typical results of applying Eq. 38 are shown in Figures 29 and 30. As might be expected, since phase information is not retained in the impedance functions, the results show some similarity to those associated with Representation (a), that is,

$$G_{AA}(f) = G_{SS}(f)/[1 + <|Z_p|>/<|Z_s|>]^2 \qquad (39)$$

The ratio of loaded to unloaded response, $G_{xx}/G_{yy} = G_{AA}/G_{SS}$, is always less than unity, so that there is under-prediction of the response of the mounting point and payload at resonance frequencies of the combined structure/payload system. There is some over-prediction of the response at resonance frequencies of the unloaded structure.

3.7 Mobility

The preceding discussion of the parametric studies considered the impedances of the mounting point and payload. Averaging or enveloping of the impedance function was performed as desired in an attempt to simulate the effects of uncertainties in response and impedance data from the Shuttle. Equally well, the equations could be expressed in terms of the mobility function, which is the reciprocal of the impedance, i.e.,

$$Y_s(f) = 1/Z_s(f); \quad Y_p(f) = 1/Z_p(f) \qquad (40)$$

However, the effects of averaging could be different when applied to mobility rather than impedance. Thus, it is of interest to investigate the effects of using mounting point mobility instead of mounting point impedance in the averaging process.

It is assumed for this study that the mounting point mobility is averaged using a 10-Hz moving bandwidth. Then, Eq. 29 has the form

$$G_{AA}(f) = G_{SS}(f)/\; |1 + [Z_p(f)<Y_s(f)>_m]|^2 \qquad (41)$$

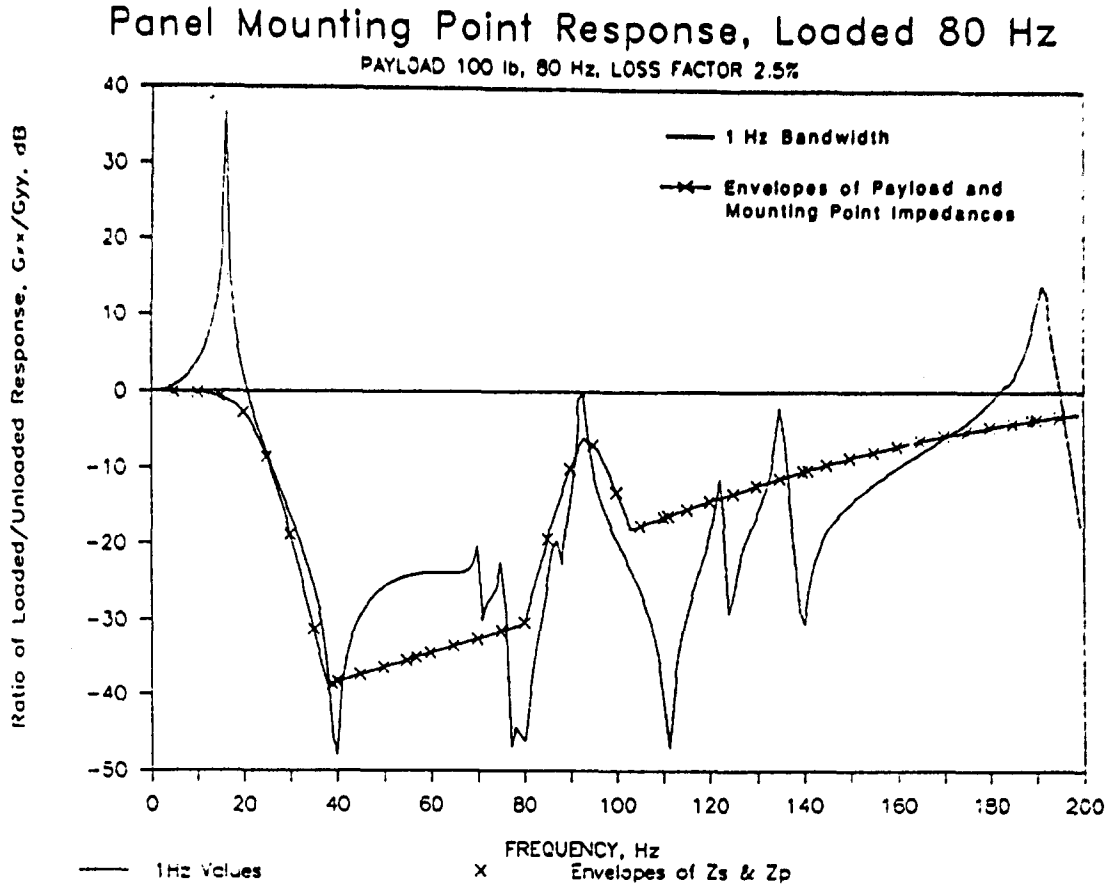

FIGURE 29. RATIO OF LOADED TO UNLOADED RESPONSE OF STRUCTURE USING EQUATION 38. (IMPEDANCE ENVELOPES)

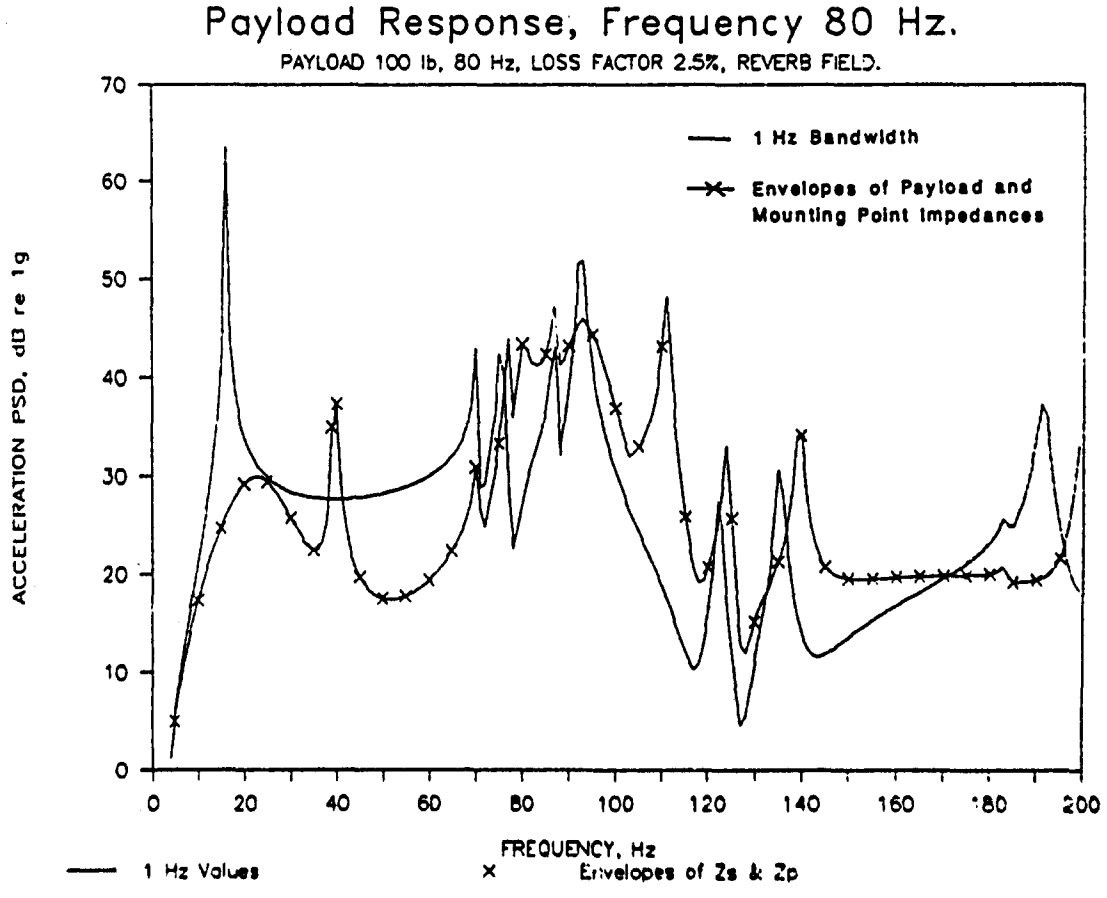

FIGURE 30. PAYLOAD RESPONSE COMPUTED USING EQUATIONS 38 & 31. (IMPEDANCE ENVELOPES)

where, as in Eq. 37, $< >_m$ denotes a moving frequency average.

The average mounting point mobility is compared with the correct value in Figure 31, in terms of magnitude and phase, respectively. Corresponding comparisons for the mounting point impedance are contained in Figure 26. In the case of the magnitude, a comparison of Figures 26(a) and 31(a) shows the different effects associated with averaging at a peak and at a trough or notch.

Structure mounting-point response ratios (ratio of loaded to unloaded vibration spectra) are shown in Figure 32 for the 100 lb payload with resonance frequencies of 20 and 80 Hz, respectively. These can be compared with corresponding results in Figure 27. It is seen that, at some frequencies, the mobility approach gives results that are closer to the correct value than does the impedance approach, but at otner frequencies the opposite is true.

Associated spectra for the payload response are presented in Figure 33 (compared with Figure 28). In the case of both payloads, there is a marked difference in the predicted response at frequencies in the neighborhood of the 40 Hz fundamental frequency of the structure. When the averaging is performed on the mobility (Figure 33), the response at 40 Hz is about 10 dB above the correct value. When the averaging is performed on the impedance (Figure 28), the predicted response at 40 Hz is about 10 dB below the correct value but, on either side of 40 Hz, the predicted response is about 10 dB above the correct value.

An alternative frequency-averaging approach is to compute the average magnitude of the mobility from the moving average of the magnitude of the mobility, Y_s, while the phase is still computed from the moving averages of the real and imaginary parts of the mobility. The resulting magnitude of the mounting point mobility is shown in Figure 34. Comparing Figures 34 and 31(a), it is seen that peaks in the mobility spectrum are now represented more accurately than before. The averaged phase spectra are, of course, identical

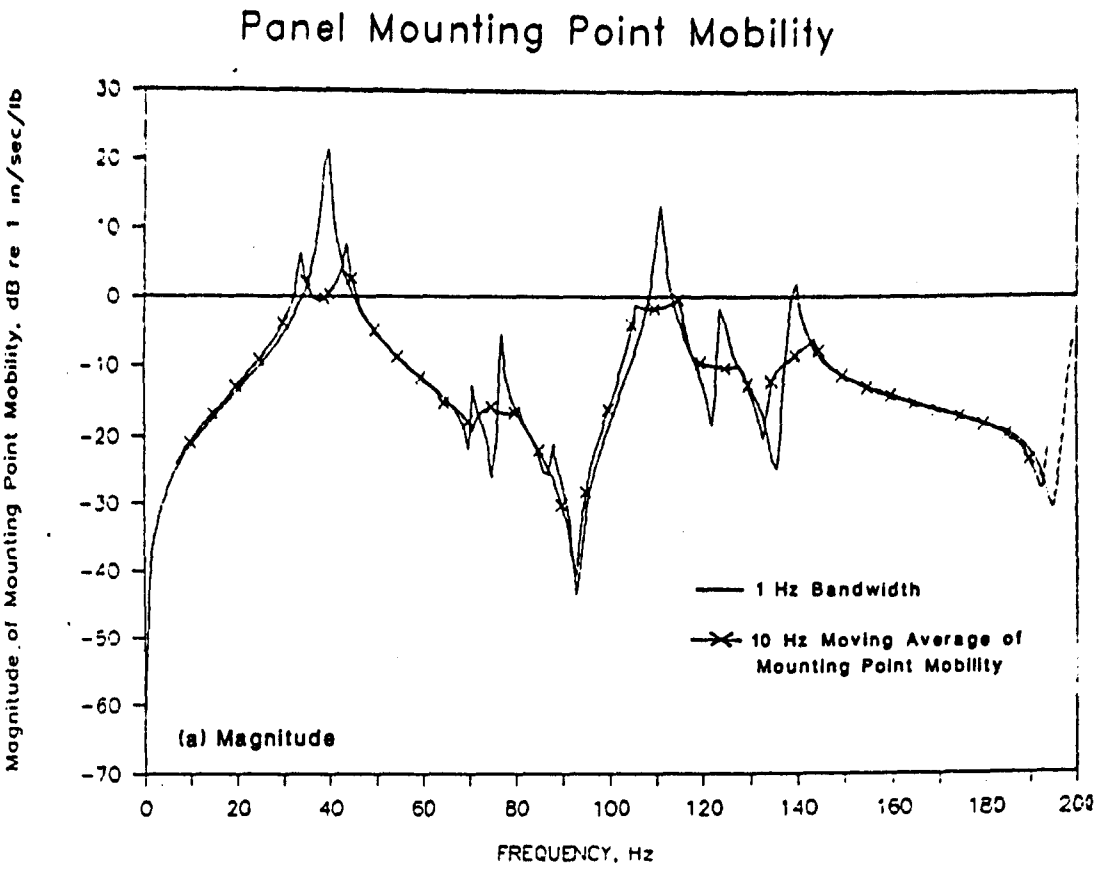

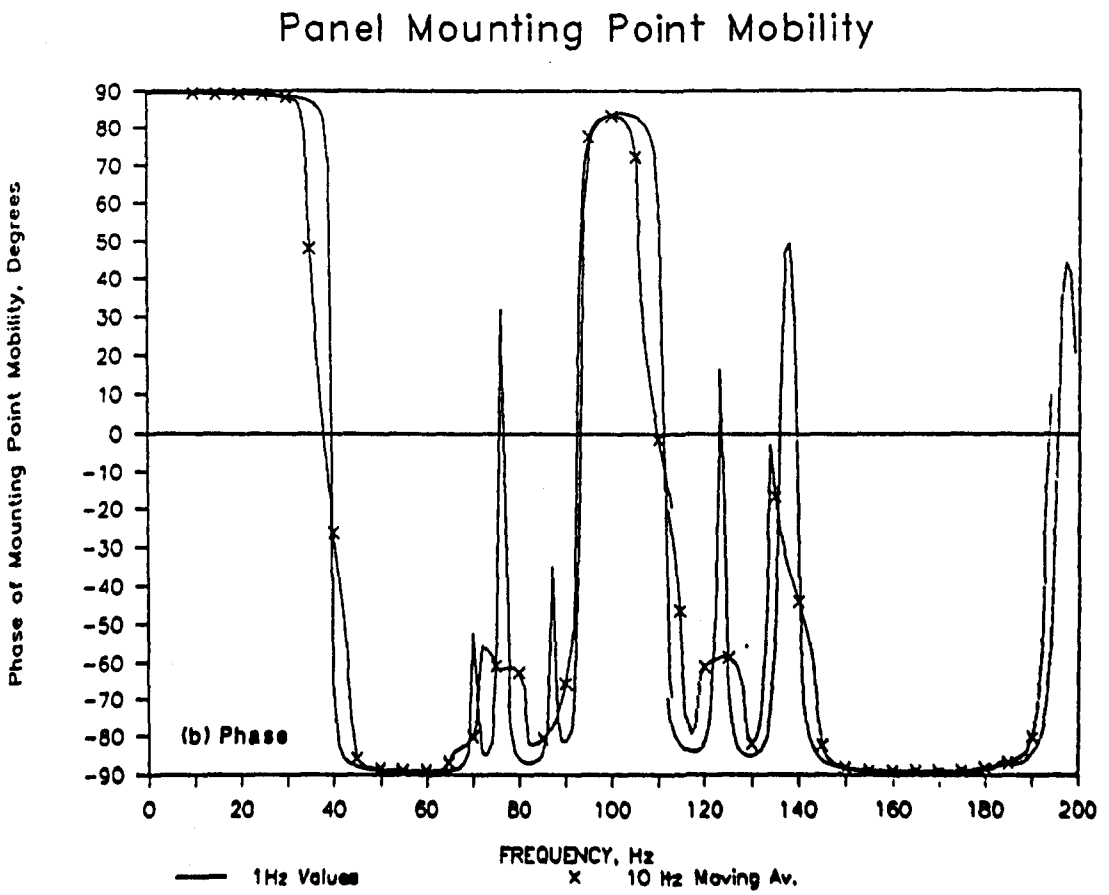

FIGURE 31. MOUNTING POINT MOBILITY COMPUTED WITH MOVING FREQUENCY AVERAGING.

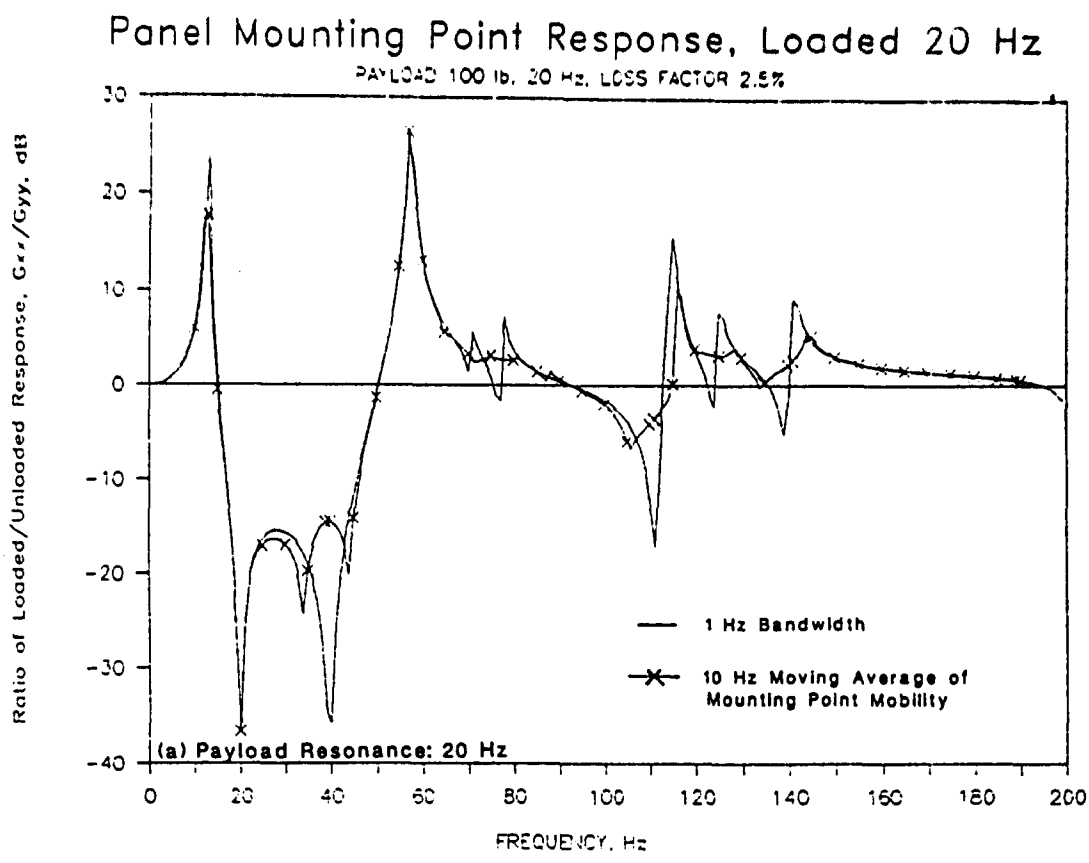

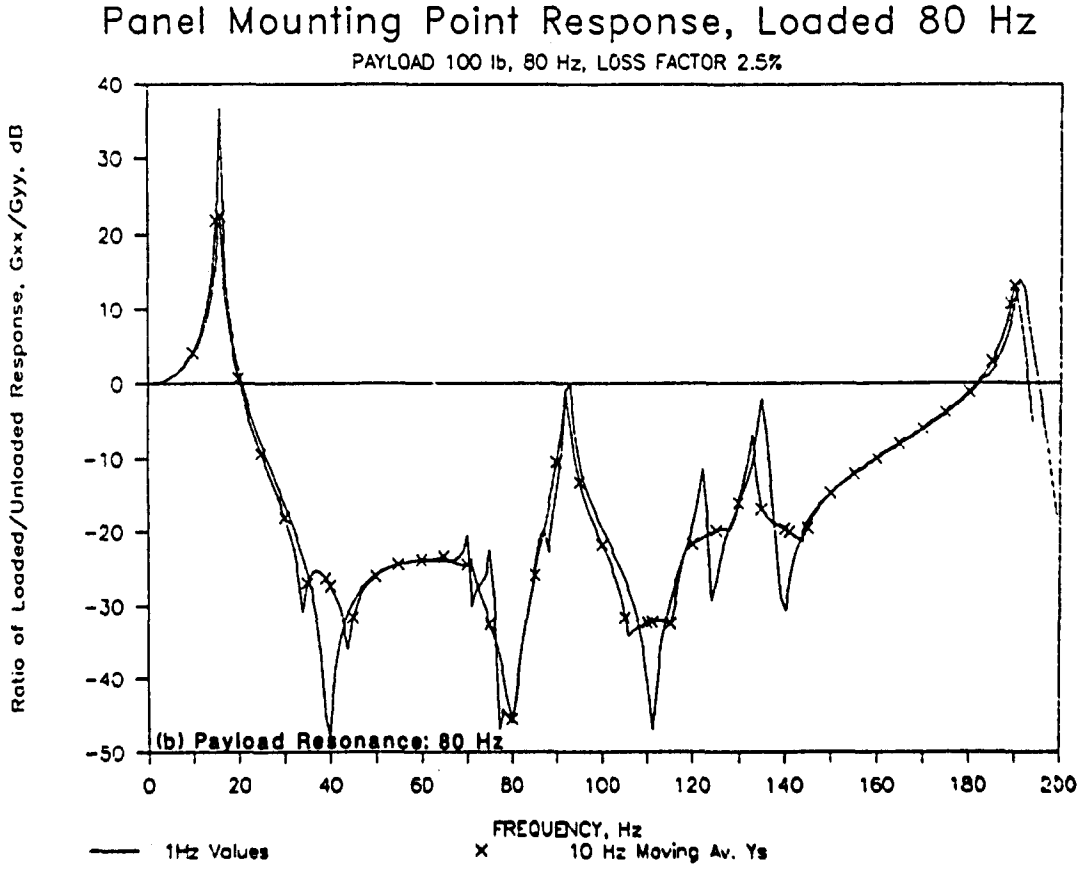

FIGURE 32. RATIO OF LOADED TO UNLOADED RESPONSE OF STRUCTURE COMPUTED USING EQUATION 41 (AVERAGING REAL AND IMAGINARY PARTS OF MOBILITY)

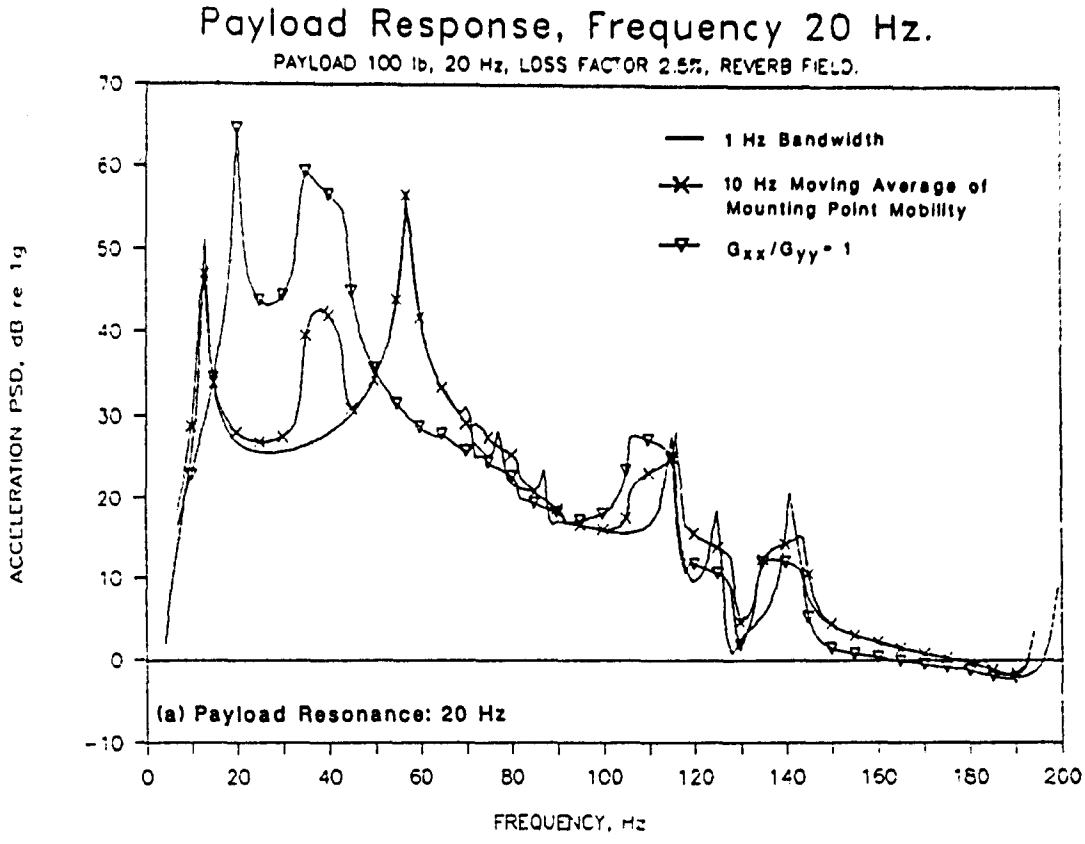

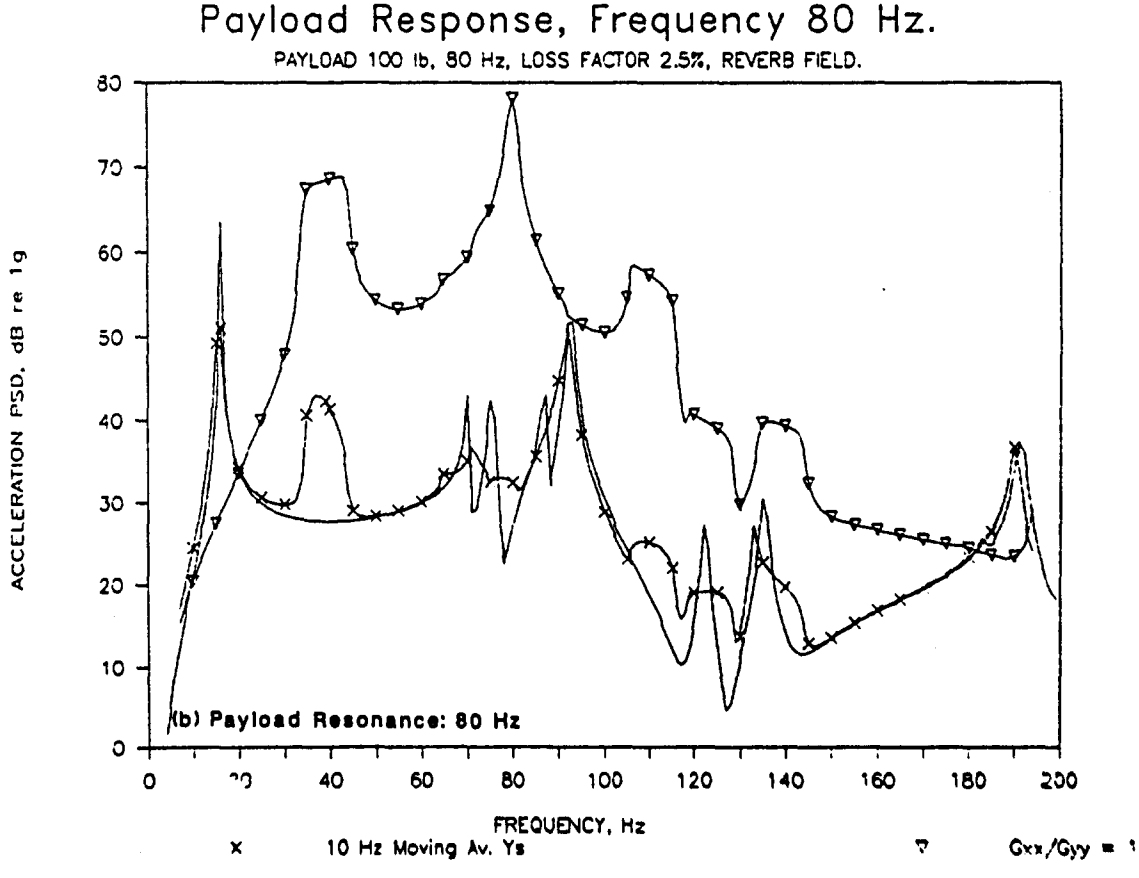

FIGURE 33. PAYLOAD RESPONSE COMPUTED USING EQUATIONS 41 & 31. (AVERAGING REAL AND IMAGINARY PARTS OF MOBILITY)

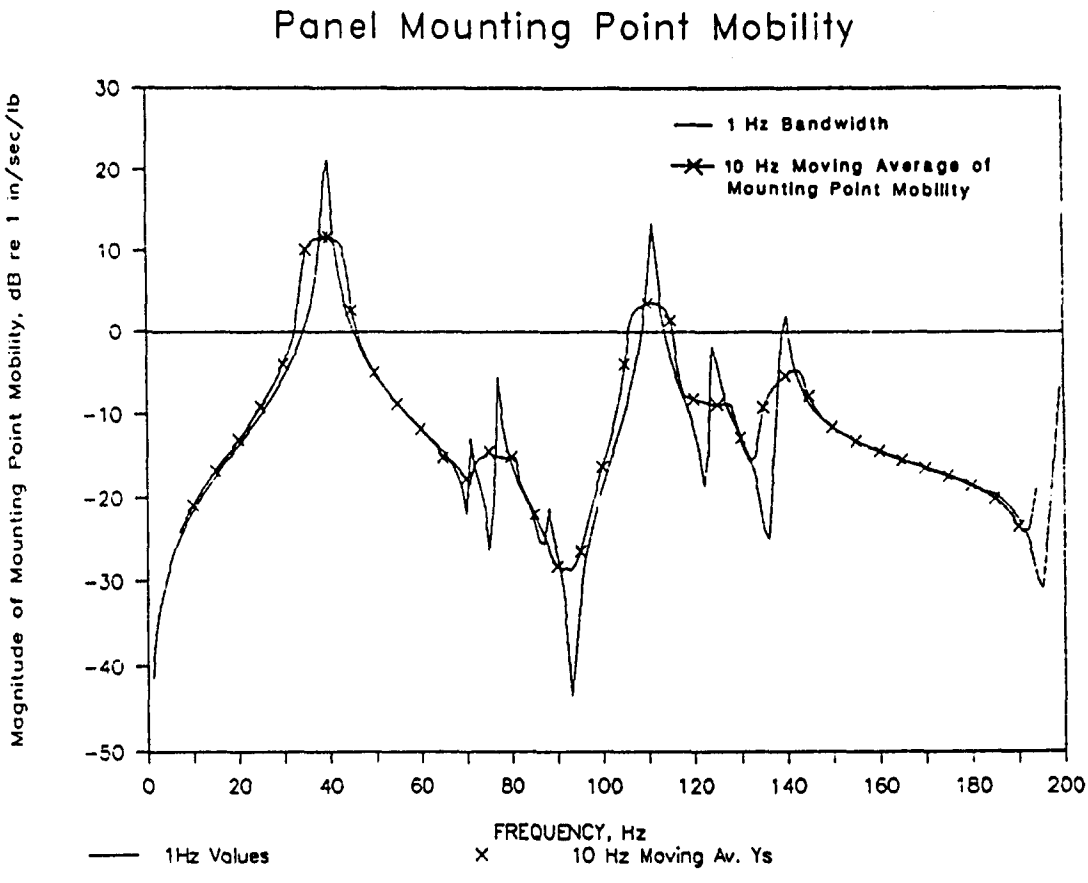

FIGURE 34. MAGNITUDE OF MOUNTING POINT MOBILITY COMPUTED WITH 10 Hz MOVING AVERAGE OF MOBILITY MAGNITUDE.

in the two cases. Response ratio spectra $G_{AA}/G_{SS} = G_{xx}/G_{yy}$ are shown in Figure 35. It is seen that there is now closer agreement between the approximate results and the correct predictions at the fundamental frequency of the structure than was the case for the previous averaging method. This is borne in the predicted response spectra for the payload (Figure 36) where the vibration level predicted at 40 Hz using the alternative moving average of the mobility is quite close to the correct prediction. In the case of the 80 Hz payload, the approximation still under-predicts the vibration at the lowest resonance frequency of the combined system (by about 10 dB) and also under-predicts (again by about 10 dB) the response at about 90 Hz. All the averaging procedures predict vibration levels that are below those obtained under the assumption that $G_{xx}/G_{yy} = 1$, (i.e. the shaker velocity is equal to the free velocity of the structure) except at the lowest frequency of the combined structure/payload system, where the assumption $G_{xx}/G_{yy} = 1$ cannot amount for the resonance.

3.8 Vibration Measurements on Loaded versus Unloaded Structure

As noted in Section 2, all three candidate procedures for vibration testing of Shuttle sidewall-mounted payloads assume that the specified spectral density values for the test specification present unloaded sidewall vibration measurements. However, as detailed in Table 1, most (but not all) of the vibration data used to create the Air Force specified orbiter sidewall vibration test levels in SD-CF-0206 [7] were measured at locations on, or near, payload attachment points.

To investigate the potential discrepancies associated with using vibration data measured near loaded locations as representations of unloaded vibration levels, computer simulation studies were performed using the simplified panel-payload model employed for the parametric studies. The payload weight for the studies was varied from 25 to 400 lb, and the resonance frequency of the payload was varied from 20 to 160 Hz. Again, the weight of the supporting panel was about 40 lb, and the unloaded resonance frequency was 40 Hz. Hence, the parametric variations of the payload relative to the panel in the computer simulations covered a range of values typical of the anticipated parameter ratios for orbiter sidewall mounted payloads.

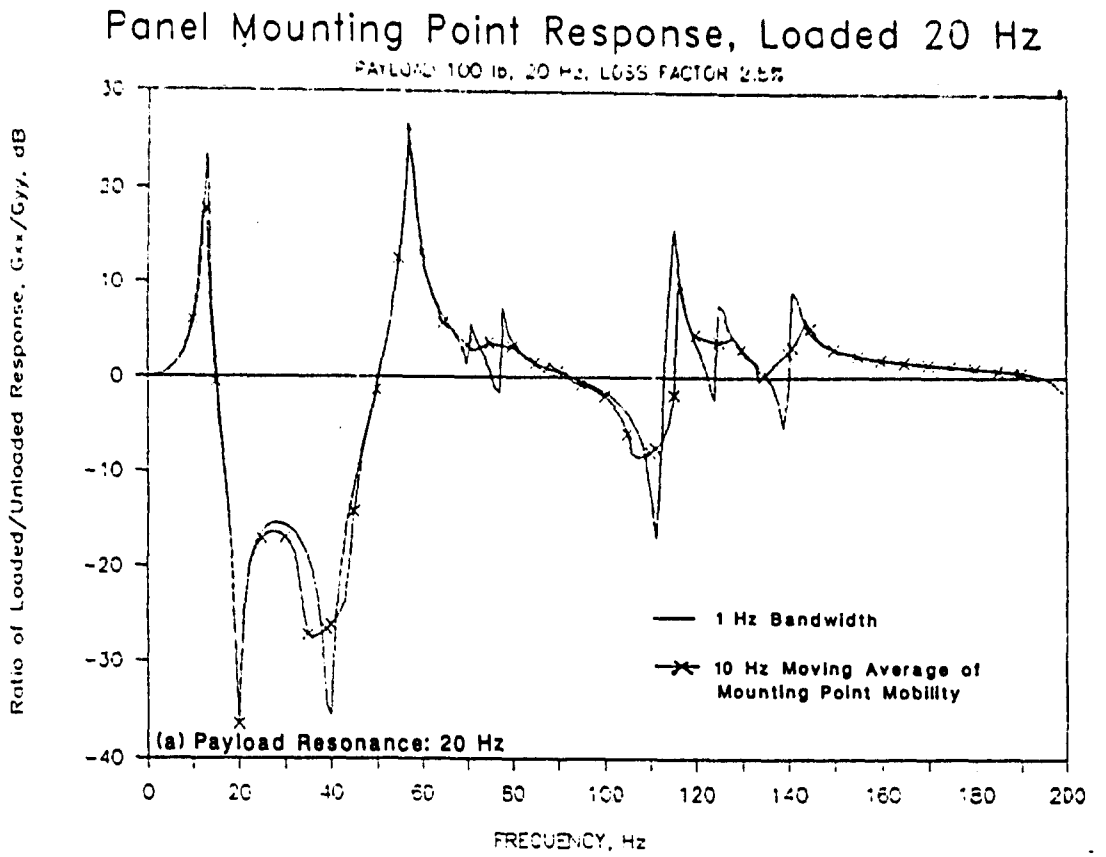

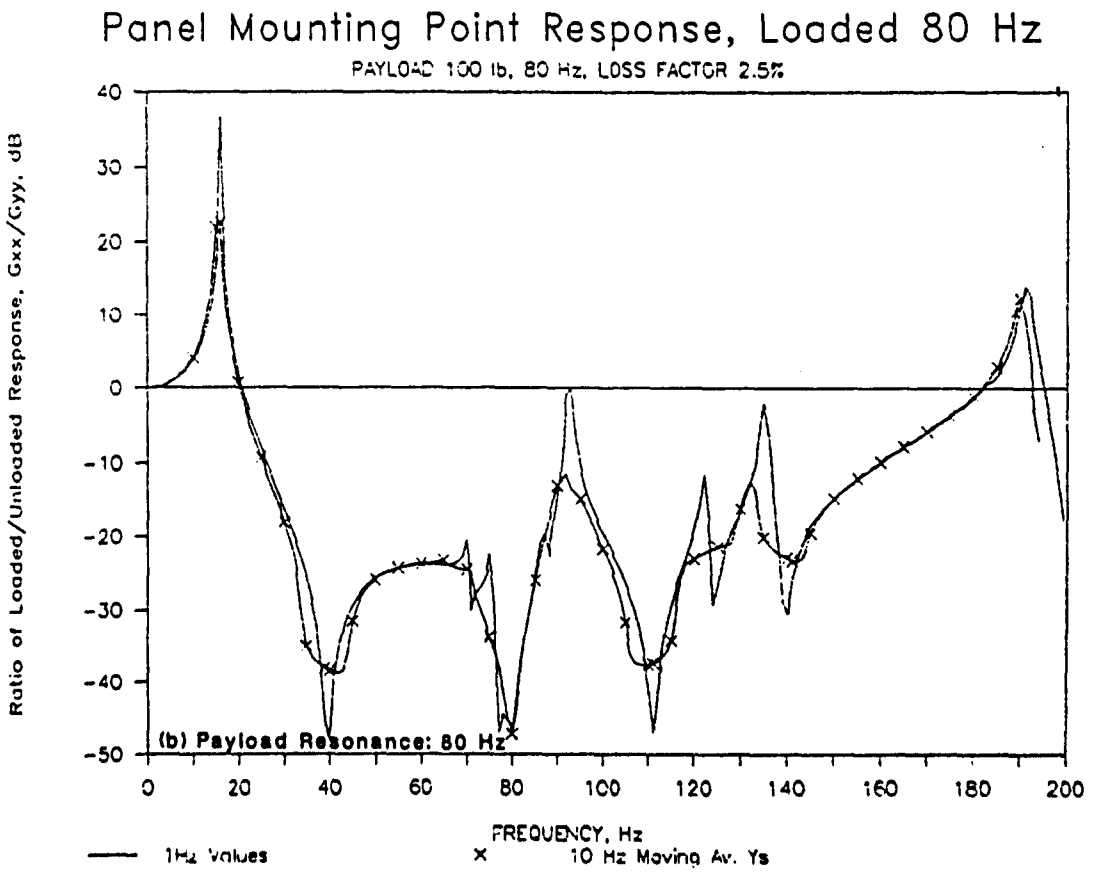

FIGURE 35. RATIO OF LOADED TO UNLOADED RESPONSE OF STRUCTURE COMPUTED USING EQUATION 41 (AVERAGING MAGNITUDE OF MOUNTING POINT MOBILITY).

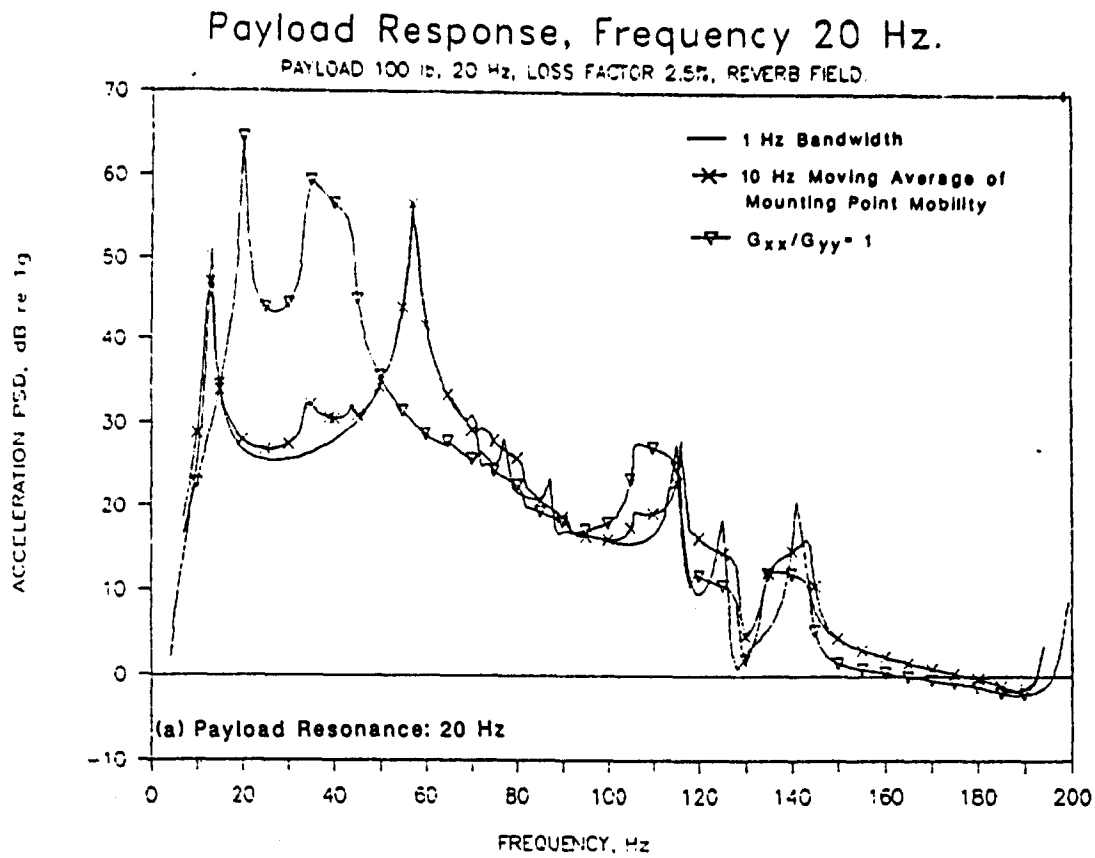

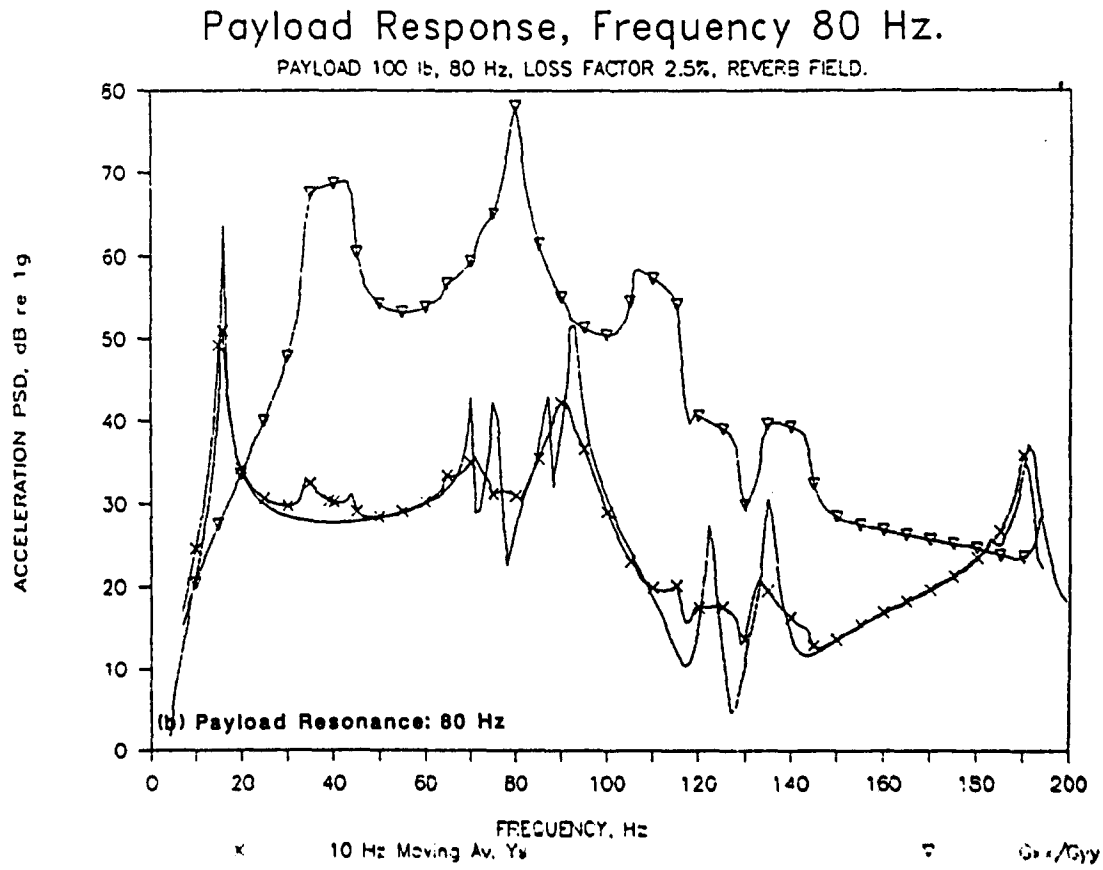

FIGURE 36. PAYLOAD RESPONSE COMPUTED USING EQUATIONS 41 & 31. (AVERAGING MAGNITUDE OF MOUNTING POINT MOBILITY)

The panel in the computer simulated model was excited with reverberant acoustic excitation, and the response was computed with the various payload parameter values. Since test specifications, including SD-CF-0206, generally represent an envelope of spectral peaks in measured data, it is the peak values of the spectral responses predicted for the various payload configurations that are of interest. These peak values are shown in comparison to the unloaded panel response in Figure 37. Also shown in Figure 37 is an envelope of the spectral peaks for the loaded panel response. It is seen that the envelope of the spectral peaks for the loaded panel responses broadly covers the spectral peaks for the unloaded panel response.

The results in Figure 37 support the conclusion that there is no need for concern over the fact that most of the data used to generate the levels in SD-CF-0206 represented loaded sidewall vibration responses, even though the candidate test procedures assume unloaded vibration responses, since the use of envelope data for the basic test specification generally eliminates the distinction between the two situations. During the course of the combined loads study reported in [10], that were illustrations of vibration measurements on unloaded structure that were substantially higher in all 1/3 octave bands than the vibration measurements at other loaded locations in the bay. However, this could have been due to a basic difference in the vibration response at the two different locations, rather than the loading condition. In any case, those high level measurements at unloaded locations reported in [10] were used in the derivation of the specified test levels in SD-CF-0206 (see VO8D9349, 53, 54, and 55 in Table 1).

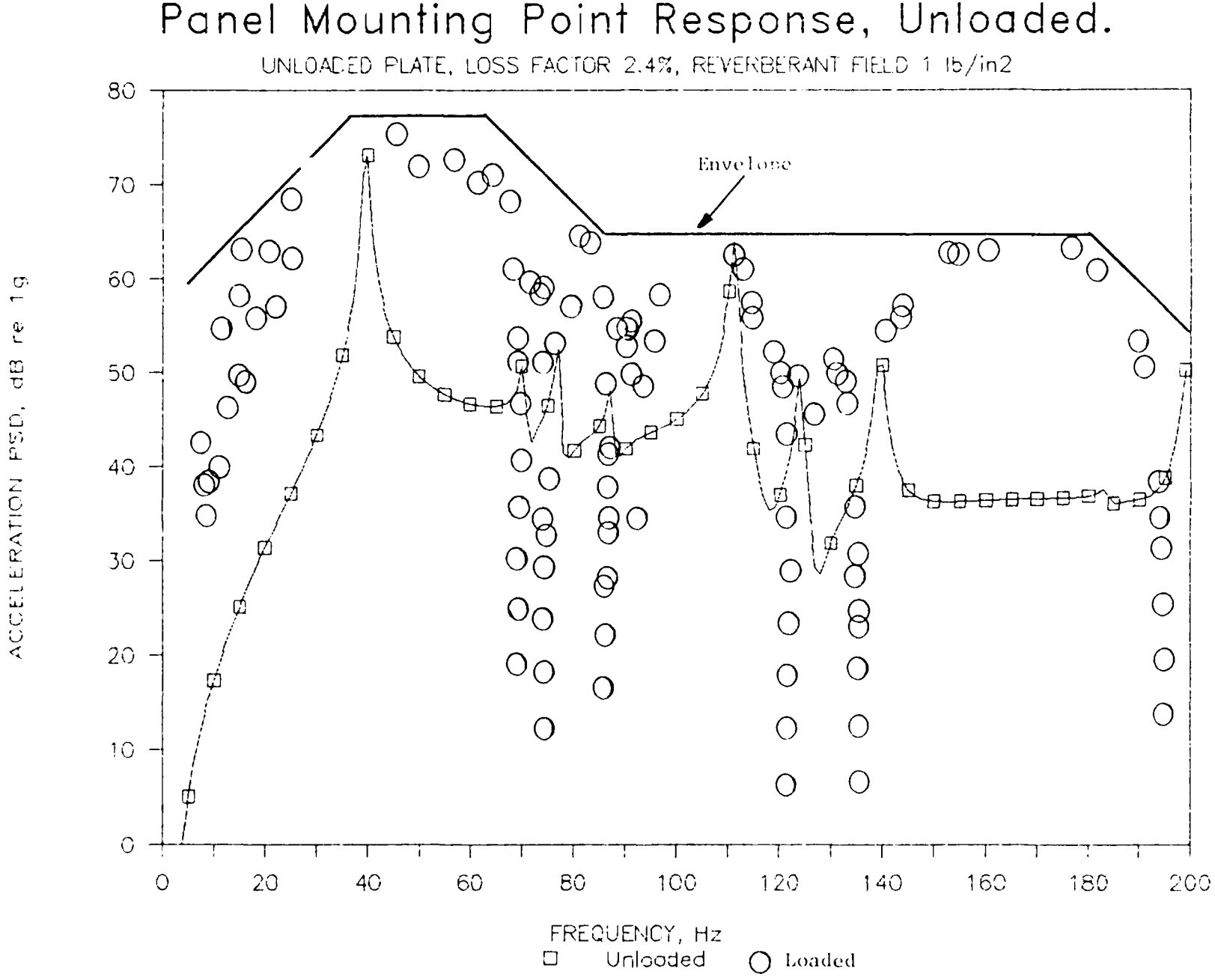

FIGURE 37. COMPARISON OF SPECTRAL PEAKS IN PANEL VIBRATION RESPONSE WITH AND WITHOUT PAYLOAD.

4. DETAILED FINITE ELEMENT STUDY

The objective of the detailed finite element study was to examine analytically the mounting point response of both the unloaded and loaded sidewall to acoustic excitation. In particular, it was of interest to estimate the influence of a sidewall-mounted payload on the vibration of the sidewall during lift-off. Such an analysis gives perspective to the parametric studies and model scale experiments described elsewhere in this document.

A high frequency, high fidelity finite element model of the Space Shuttle cargo bay [11] was used in conjunction with a detailed stress model of the OEX Autonomous Supporting Instrumentation System (OASIS-1 payload) [12], and a simplified model of the Adaptive Payload Carrier. The OASIS-1 model was used since flight data existed for this payload [13], enabling the direct comparison of analytical and experimental results.

4.1 Finite Element Models

A detailed description of the finite element models can be found in References 11 and 12. A brief overview of these models and specialized modeling and analysis techniques employed for their adaptation to the present study are discussed below.

The Space Shuttle cargo bay finite element model and its boundary conditions can be seen in Figures 38 and 39. These boundary conditions were used to simplify the model and facilitate its application to the high frequency range (20 - 200 Hz). The model was sub-divided into the MSC/NASTRAN superelements (i.e. substructures) given in Table 3 and shown in Figure 40. Component mode reduction was specified for superelements 1 through 4, and the first two hundred normal modes were extracted for these superelements and the residual structure (Table 4).

In order to facilitate the connection of the OASIS-1 payload to the cargo bay, the cargo bay finite element model was repartitioned into the superelements shown in Figure 41 and described in Table 5. Since the OASIS-1 payload

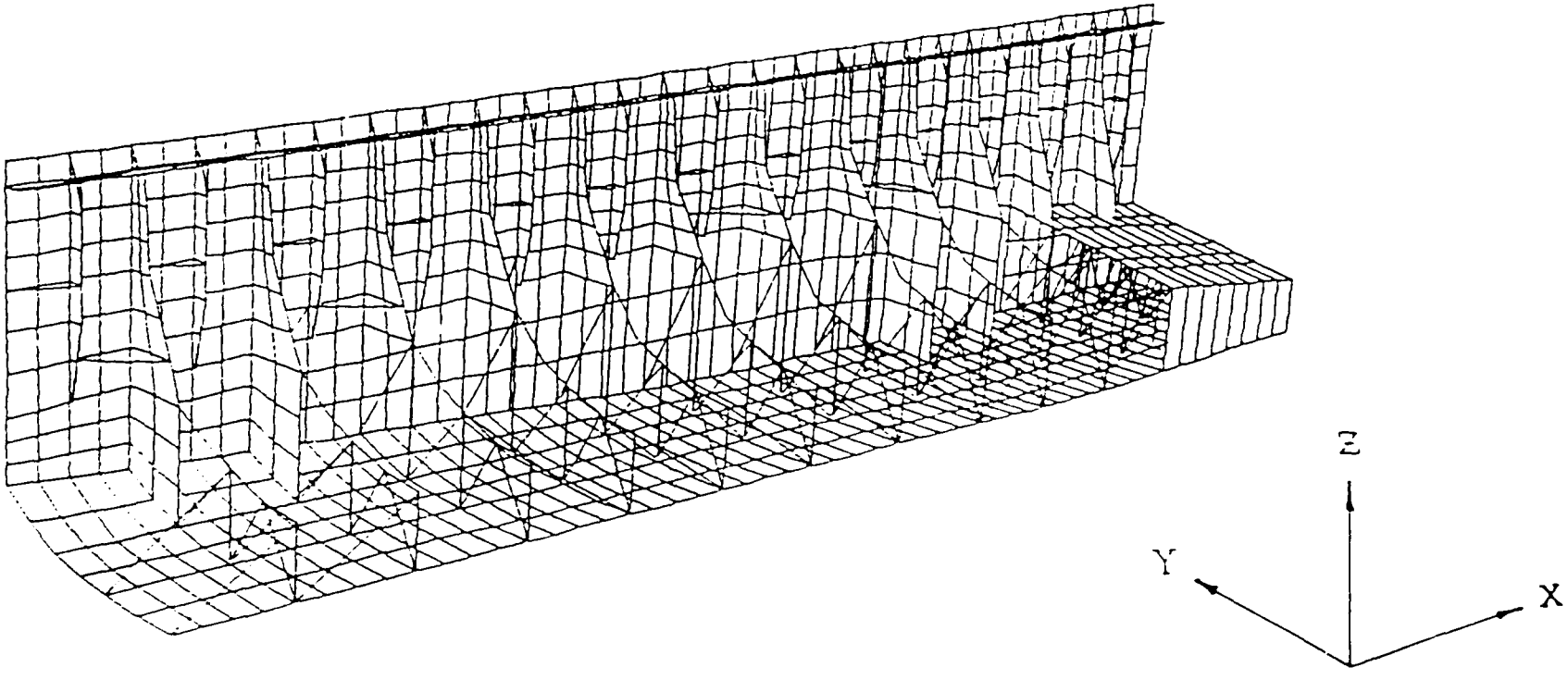

FIGURE 38.CARGO BAY FINITE ELEMENT MODEL

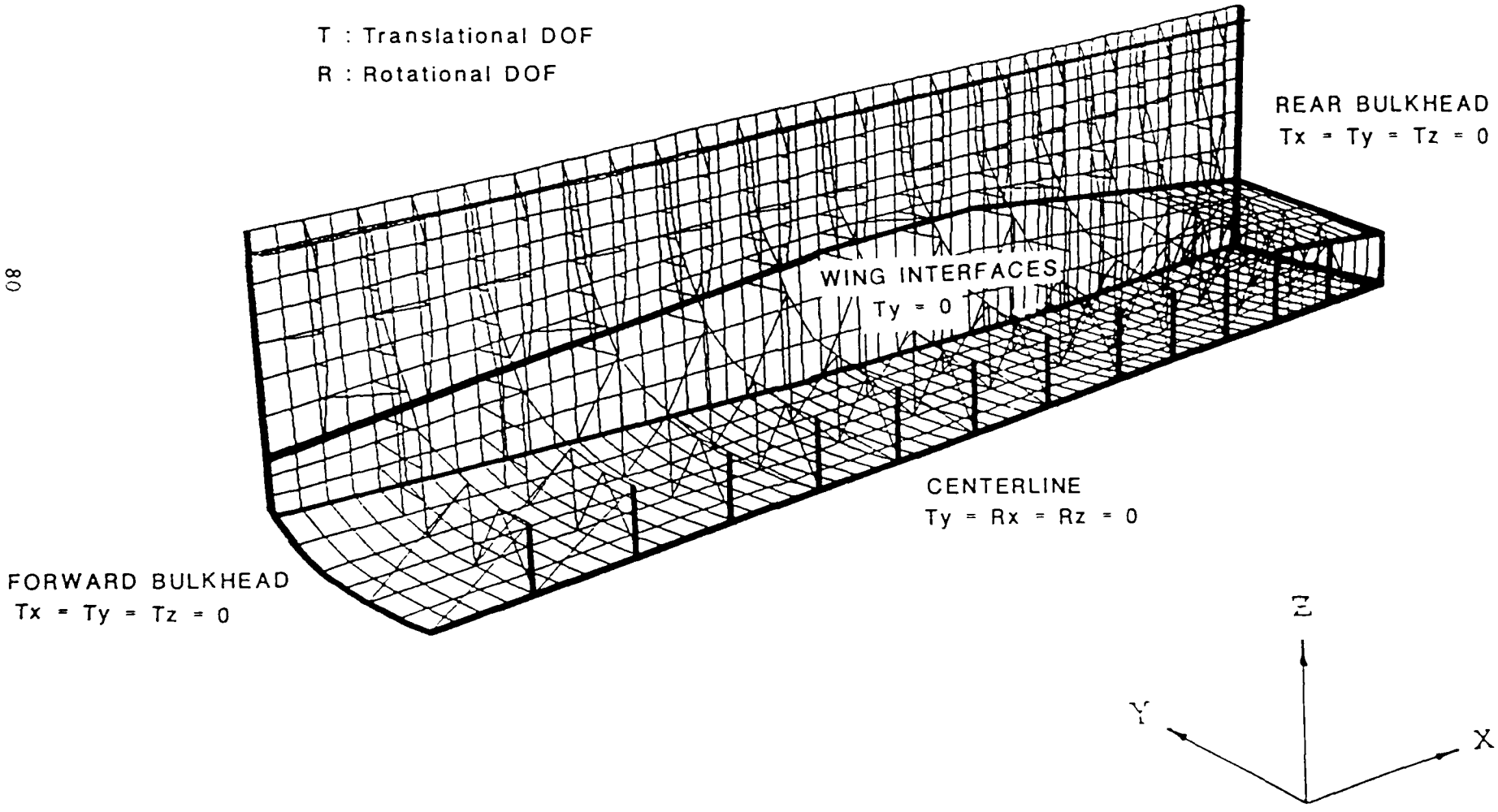

FIGURE 39. BOUNDARY CONDITIONS

Table 3. Superelement Definition

Superelement	Description
Residual	Main Frames 3, 6 & 9
1	Bays 1, 2 & 3
2	Bays 4, 5 & 6
3	Bays 7, 8 & 9
4	Bays 10, 11, 12a & 12b
5	Stub frames 1, 2 & 3
6	Stub frames 4, 5 & 6
7	Stub frames 7, 8, & 9
8	Stub frames 10, 11, 12a & 12b

Table 4. Eigenvalue Summary

Superelement	f_{max} (Hz)	# of modes
o Residual Structure	163.2	200
o Superelement 1	568.4	200
o Superelement 2	630.0	200
o Superelement 3	642.3	200
o Superelement 4	471.8	200

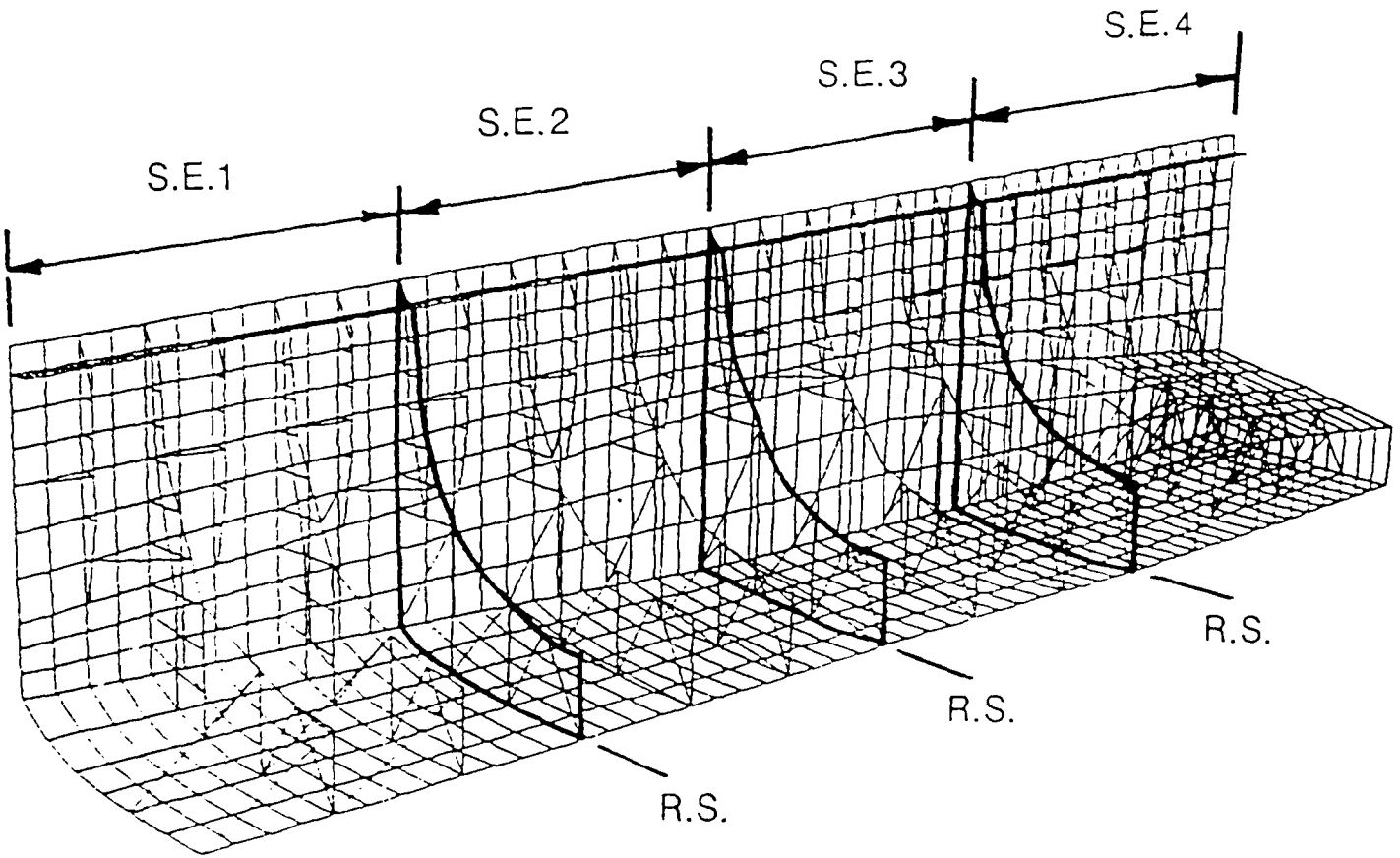

FIGURE 40. SUBSTRUCTURE DEFINITION

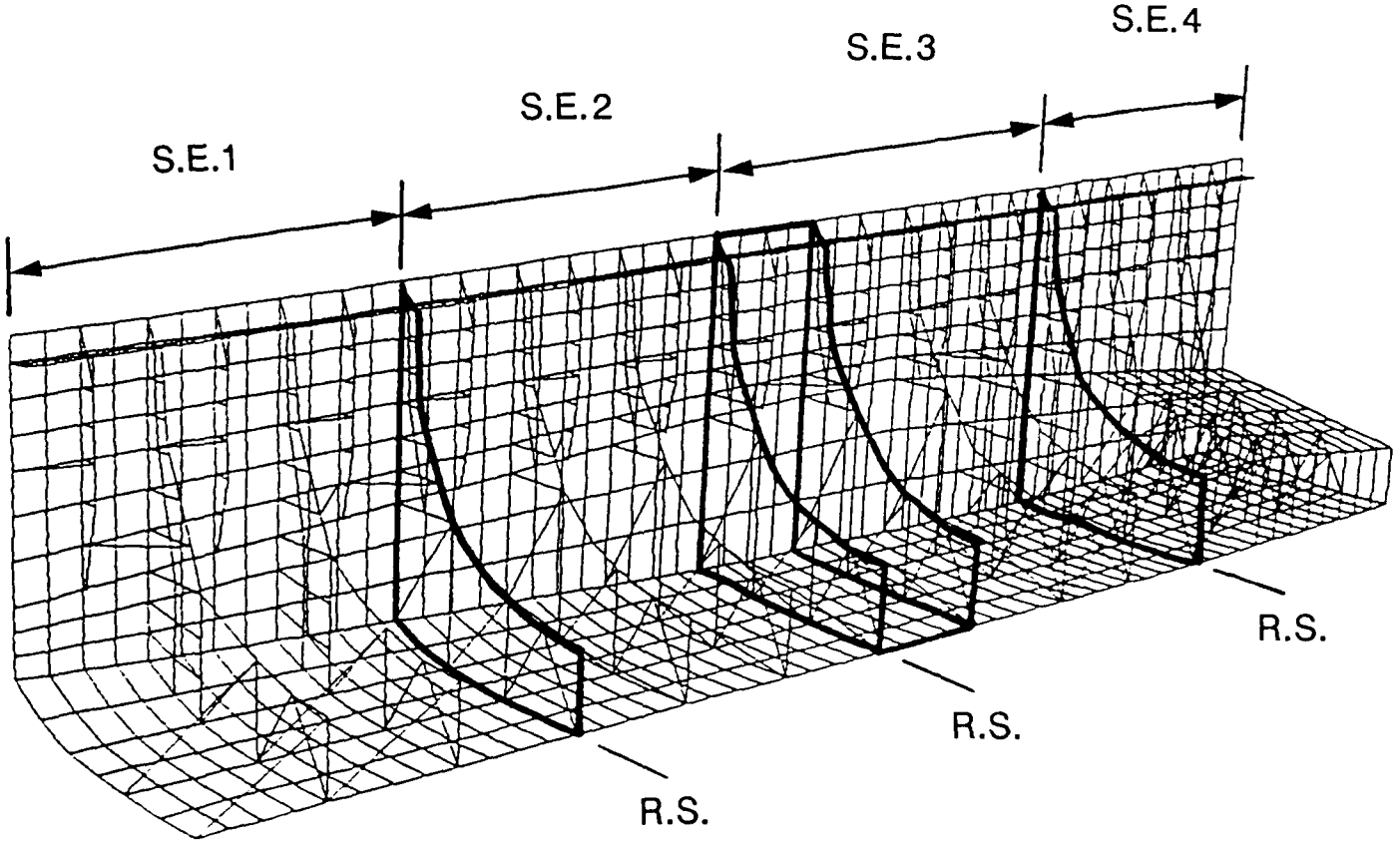

FIGURE 41. REPARTITIONED SUPERELEMENT MODEL

Table 5. Repartitioned Model

Superelement	Description
Residual	Main Frames 3, 6, 7 & 10
1	Bays 1, 2 & 3
2	Bays 4, 5 & 6
3	Bays 8, 9 & 10
4	Bays 11, 12a & 12b
5	Stub frames 1, 2 & 3
6	Stub frames 4, 5 & 6
7	Stub frames 8, 9 & 10
8	Stub frames 11, 12a & 12b
9	OASIS-1 Payload

attaches to bay 7 of the sidewall structure, it is convenient to define all points within bay 7 in the residual structure. This allows for greater flexibility in attaching the OASIS-1 payload to the sidewall, and simplifies the reduction order for the entire model in the event that modifications to either the payload or the sidewall model are necessary [14].

An exploded view of the OASIS-1 payload, showing all major components and its interface with the APC can be seen in Figure 42. The detailed stress analysis model of the OASIS-1 payload shown in Figure 43 was provided by Lockheed [12]. The total weight of the OASIS-1 payload was computed with MSC/NASTRAN to be 221 lb. This model was initially constrained to ground with a series of scalar springs ($K = 5x10^5$ lb/in) at eighteen locations on the adapter frame (Figure 44). The scalar spring representation was used by Lockheed to approximate the mounting stiffness of the payload on the APC. It is unclear whether the sizing of the scalar springs is an accurate dynamic representation of the APC, particularly in the higher frequency range (above 20 Hz). Preliminary hand calculations indicated that the first rigid-body payload mode on the springs (i.e. bouncing) would be roughly 630 Hz.

The OASIS-1 payload model was reoriented to the proper location on bay 7 of the sidewall model through the adjustment of parameters on local coordinate system definition cards in the NASTRAN bulk data deck. The scalar springs were removed from the ground and redefined on coincident grid points at each of the spring locations. Since the APC mounting stiffness is taken into account by the scalar springs, it was reasonable to define the APC as a concentrated mass (26 lb) rigidly connected to the free ends of the scalar springs (Figure 45). In practice, the connection of the APC on the sidewall is actually non-linear, since the APC is allowed to translate (rattle) with respect to the sidewall in certain degrees of freedom at the three mounting point locations (Figure 46). Since non-linearities are extremely difficult to include in modal formulations, the APC mounting on the sidewall was assumed to be statically determinate in the present finite element model. Consequently, there is no load transfer between the APC and sidewall, and it was possible to ignore the mounting stiffness between these components. The concentrated mass representing the APC was, therefore, rigidly attached to the sidewall at two

OASIS I HORIZONAL INSTALLATION

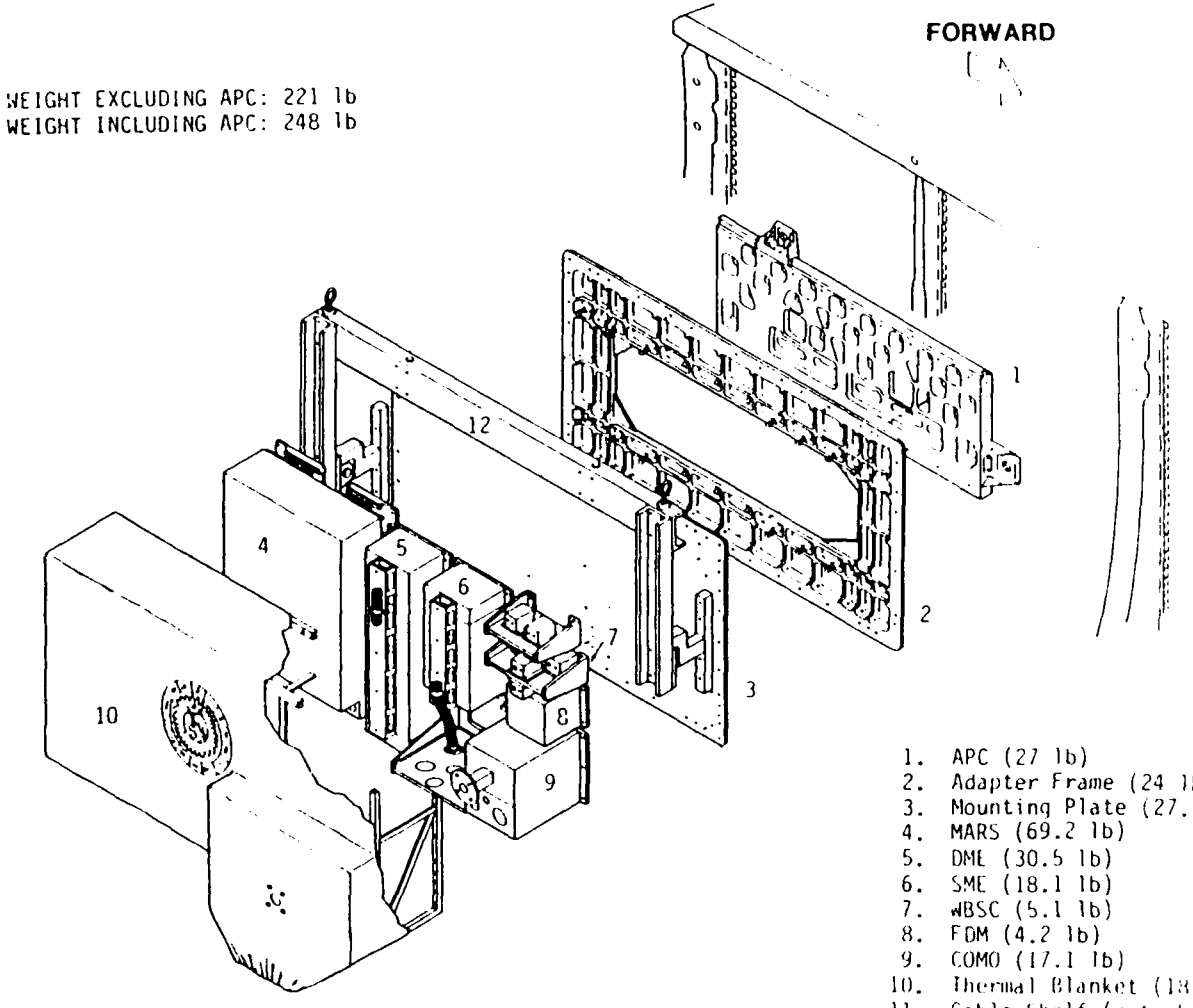

FIGURE 42. OASIS I HORIZONTAL INSTALLATION

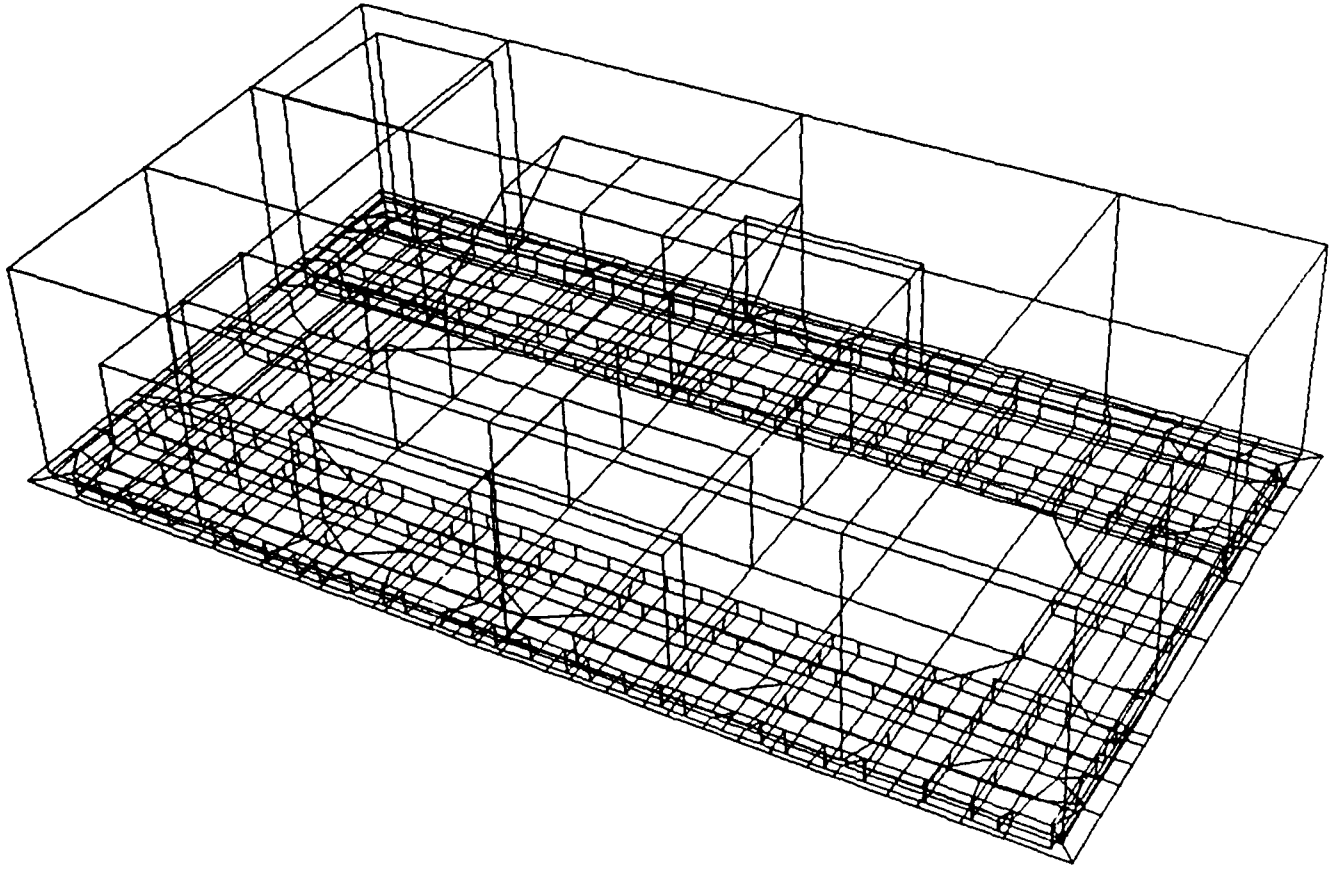

FIGURE 43. OASIS-1 FINITE ELEMENT MODEL

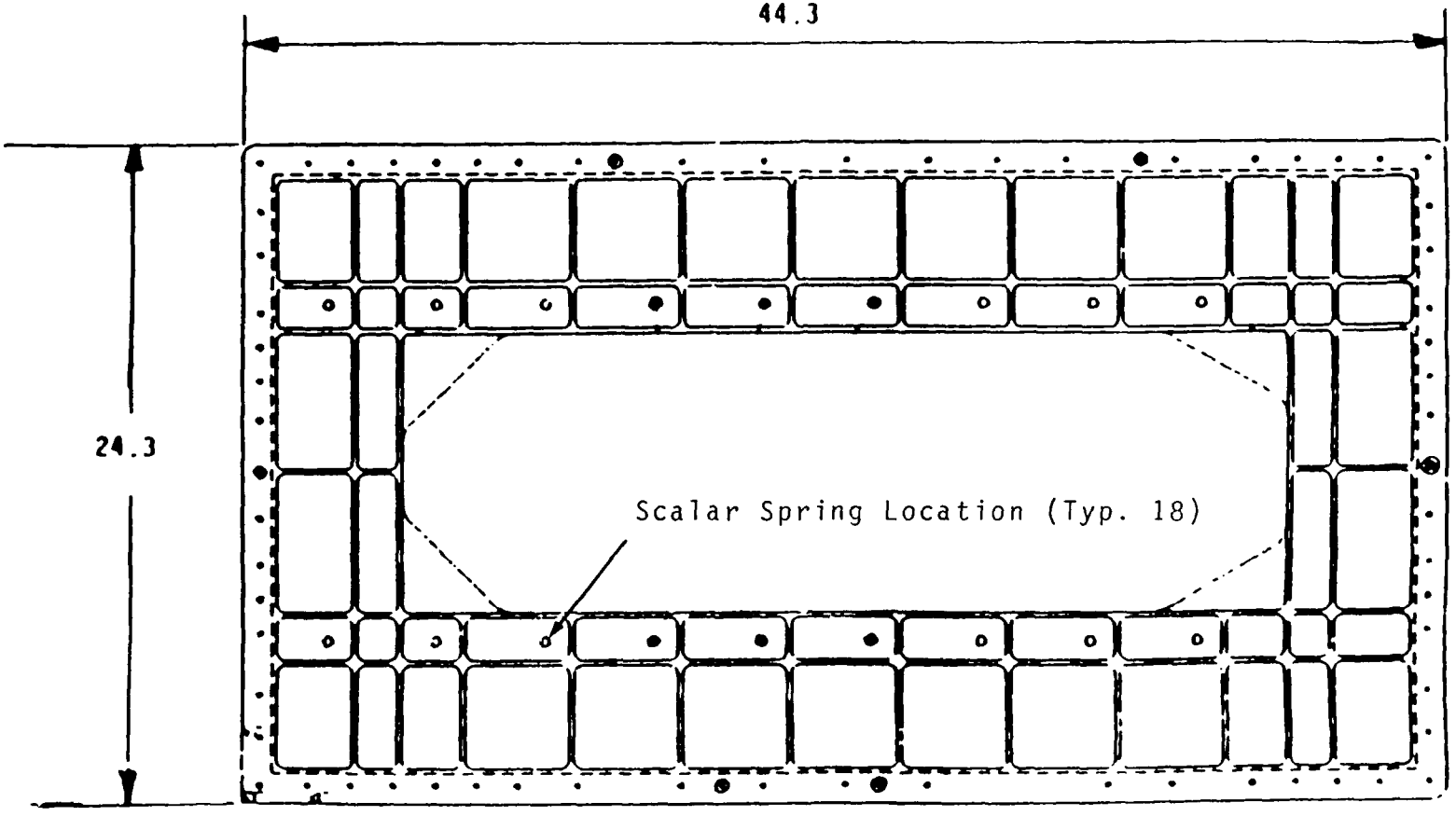

○ 1/4 inch bolts

● 1/4 inch shear bolts

FIGURE 44. ADAPTER FRAME MOUNTING POINT LOCATIONS (18).

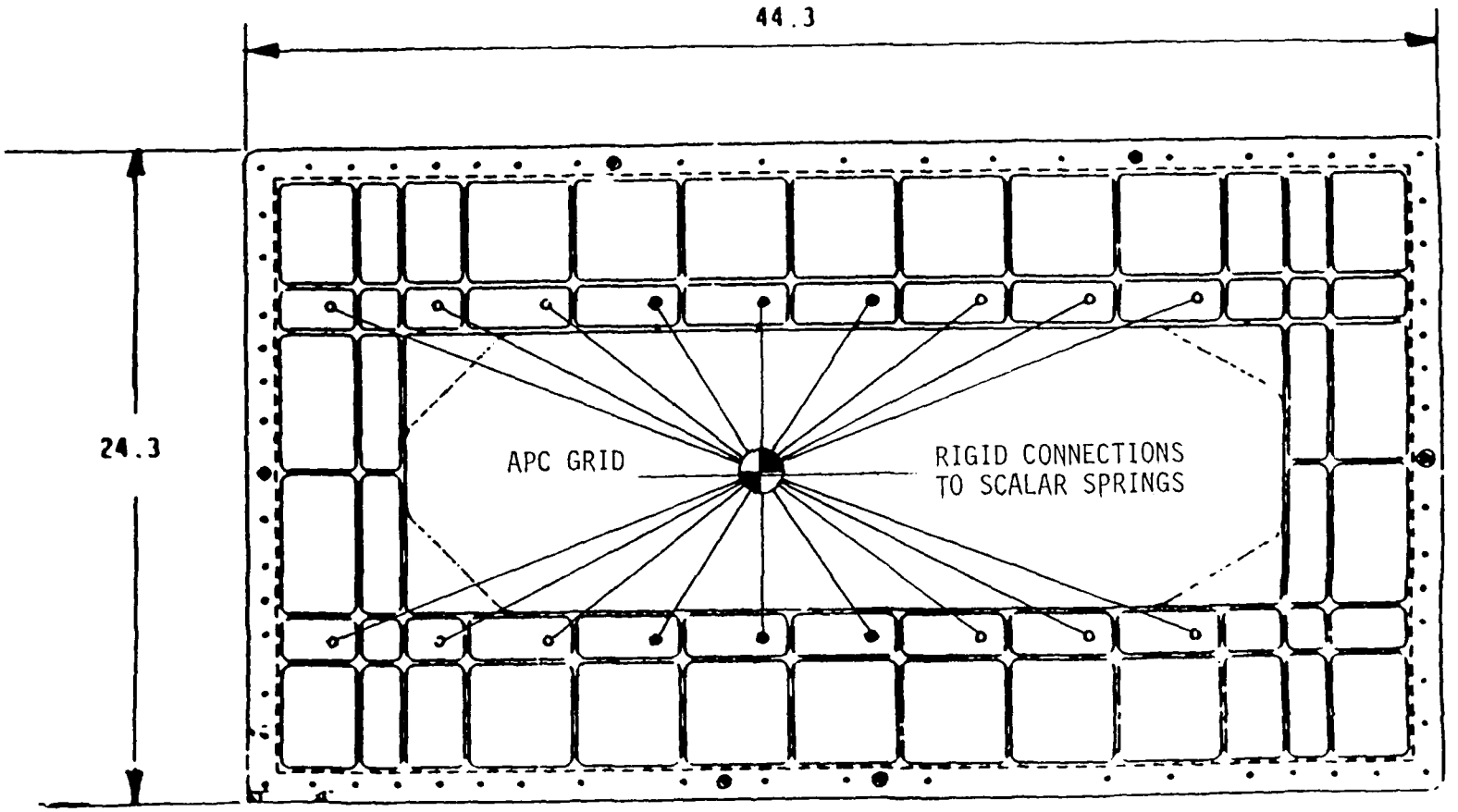

○ 1/4 inch bolts

● 1/4 inch shear bolts

FIGURE 45. APC CONNECTION TO ADAPTER FRAME.

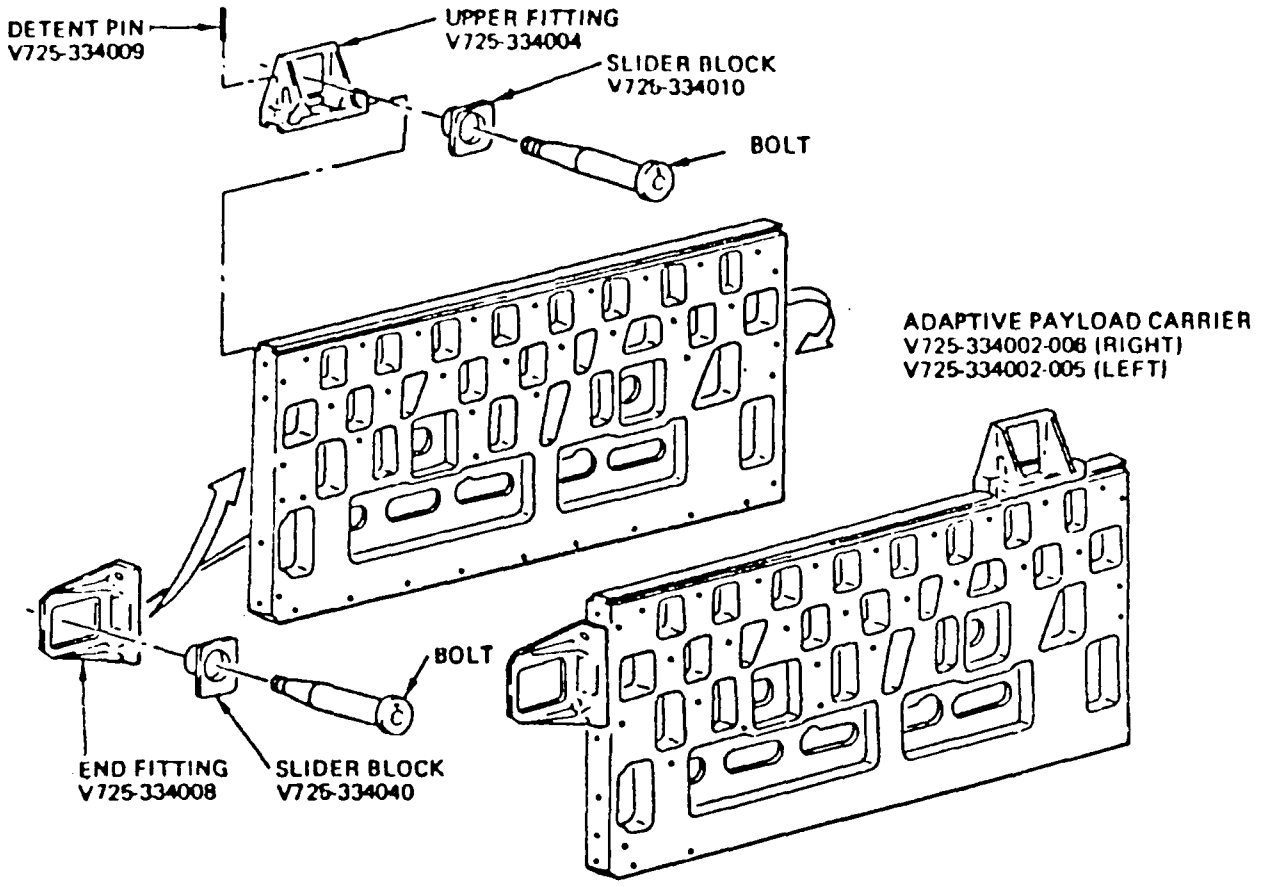

FIGURE 46. ADAPTIVE PAYLOAD CARRIER

locations in the degrees of freedom shown in Figure 47. For the loaded sidewall study, the APC was included in the residual structure, and the OASIS-1 payload was defined as a separate superelement on which component modes reduction was performed.

4.2 Normal Modes Analysis

Normal modes analysis with the superelement solution sequences in MSC/NASTRAN involve fixed boundary solutions of each of the superelements (component modes) and the dynamic reduction of these modes to the residual structure (system modes) [14]. Normal modes analysis techniques and results for the repartitioned cargo bay model unloaded and loaded with the OASIS-1 payload model are discussed below.

Component modes were obtained for each of the superelements which comprise the repartitioned cargo bay model shown in Figure 41. Earlier normal modes analysis results on the original cargo bay model indicated that it was probably over-conservative to retain 200 modes for each of the four superelements on which component mode reduction was specified [11]. Therefore, modal analysis was conducted by retaining only those component (superelement) modes under 400 Hz, and system (residual structure) modes under 200 Hz (Table 6). Normal modes for the unloaded residual structure are given in Table 7.

Table 6. Eigenvalue Summary

Superelement	f_{max} (Hz)	# of modes
o Residual Structure	200	298
o Superelement 1	400	134
o Superelement 2	400	124
o Superelement 3	400	120
o Superelement 4	400	114

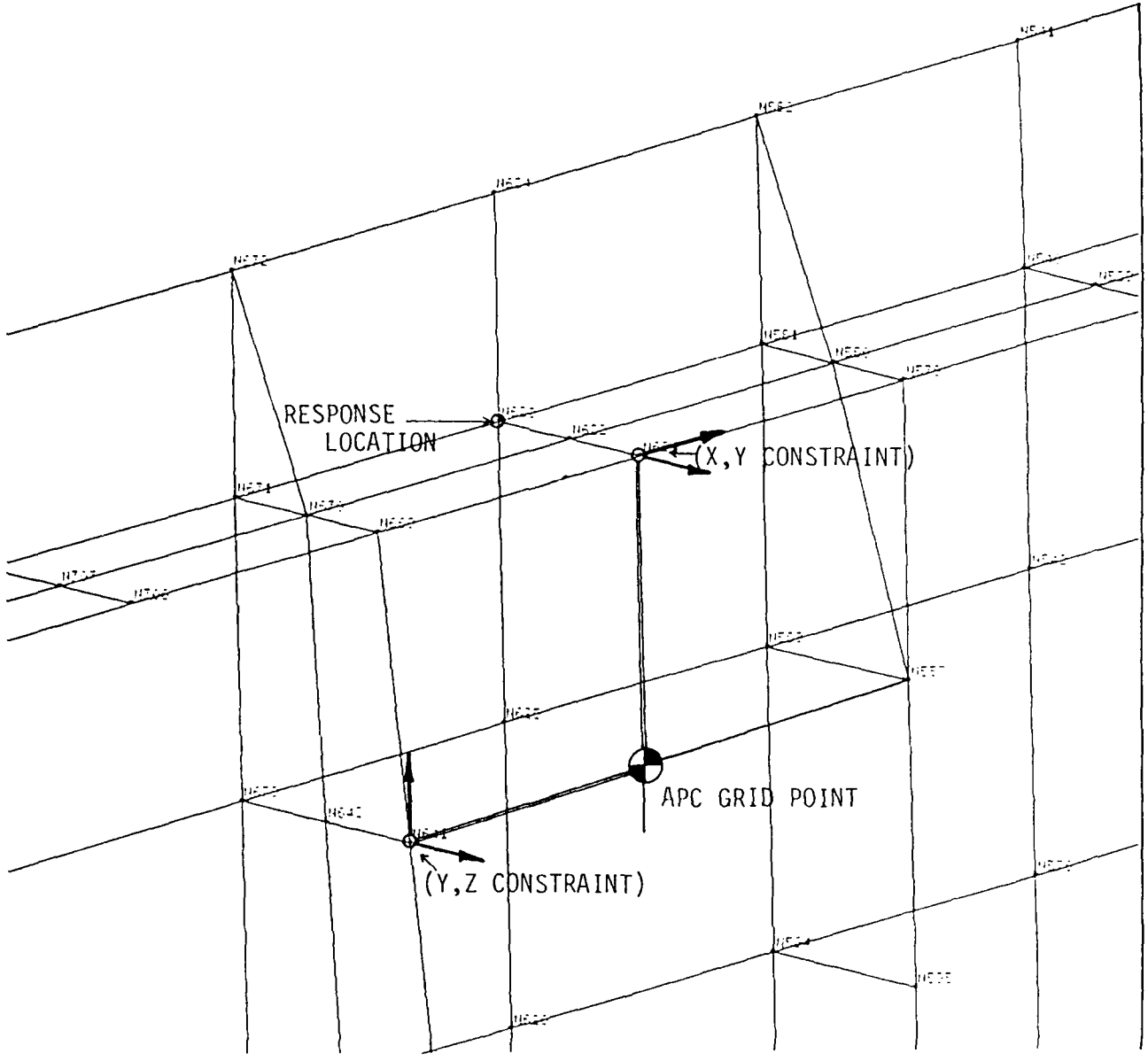

FIGURE 47. APC CONNECTION TO SIDEWALL

Table 7. Unloaded Sidewall Normal Modes

MODE NO.	CYCLES (HZ)	MODE NO.	CYCLES (HZ)	MODE NO.	CYCLES (HZ)
1	1.038979E+01	36	6.804195E+01	71	9.389733E+01
2	1.447329E+01	37	6.891605E+01	72	9.452747E+01
3	1.620333E+01	38	6.936876E+01	73	9.563206E+01
4	1.938252E+01	39	6.996799E+01	74	9.671622E+01
5	1.968513E+01	40	7.121472E+01	75	9.682703E+01
6	2.400912E+01	41	7.154206E+01	76	9.761726E+01
7	2.859937E+01	42	7.224448E+01	77	9.830292E+01
8	3.391807E+01	43	7.303226E+01	78	9.839344E+01
9	3.578965E+01	44	7.439841E+01	79	9.908426E+01
10	3.842188E+01	45	7.455004E+01	80	9.931632E+01
11	4.098336E+01	46	7.583659E+01	81	9.933836E+01
12	4.239032E+01	47	7.691617E+01	82	1.004192E+02
13	4.403539E+01	48	7.704983E+01	83	1.006924E+02
14	4.638419E+01	49	7.761315E+01	84	1.007476E+02
15	4.796577E+01	50	7.896764E+01	85	1.015353E+02
16	4.991444E+01	51	8.041471E+01	86	1.026949E+02
17	5.116837E+01	52	8.111749E+01	87	1.027925E+02
18	5.163507E+01	53	8.155401E+01	88	1.029385E+02
19	5.261024E+01	54	8.266924E+01	89	1.035939E+02
20	5.360092E+01	55	8.351028E+01	90	1.046029E+02
21	5.403441E+01	56	8.393359E+01	91	1.052917E+02
22	5.410949E+01	57	8.453246E+01	92	1.055622E+02
23	5.618816E+01	58	8.564990E+01	93	1.060583E+02
24	5.736843E+01	59	8.656197E+01	94	1.073170E+02
25	5.777452E+01	60	8.705741E+01	95	1.077346E+02
26	5.868780E+01	61	8.821654E+01	96	1.083038E+02
27	5.963998E+01	62	8.845341E+01	97	1.088641E+02
28	6.226117E+01	63	8.890353E+01	98	1.090046E+02
29	6.257488E+01	64	8.911674E+01	99	1.094658E+02
30	6.448792E+01	65	8.977717E+01	100	1.095283E+02
31	6.481052E+01	66	9.080924E+01	101	1.105592E+02
32	6.596871E+01	67	9.097629E+01	102	1.108931E+02
33	6.696810E+01	68	9.212223E+01	103	1.112370E+02
34	6.711728E+01	69	9.287757E+01	104	1.114173E+02
35	6.786729E+01	70	9.344403E+01	105	1.115280E+02

Table 7. (cont.)

MODE NO.	CYCLES (HZ)	MODE NO.	CYCLES (HZ)	MODE NO.	CYCLES (HZ)
106	1.116692E+02	151	1.295465E+02	196	1.559249E+02
107	1.118578E+02	152	1.301384E+02	197	1.563492E+02
108	1.118952E+02	153	1.308962E+02	198	1.568940E+02
109	1.120283E+02	154	1.312433E+02	199	1.574329E+02
110	1.121365E+02	155	1.314249E+02	200	1.581969E+02
111	1.121915E+02	156	1.318792E+02	201	1.584308E+02
112	1.122135E+02	157	1.320337E+02	202	1.586443E+02
113	1.122520E+02	158	1.330829E+02	203	1.599944E+02
114	1.122710E+02	159	1.333247E+02	204	1.604203E+02
115	1.123042E+02	160	1.339737E+02	205	1.605737E+02
116	1.130037E+02	161	1.346580E+02	206	1.612757E+02
117	1.138283E+02	162	1.347148E+02	207	1.619719E+02
118	1.145696E+02	163	1.352771E+02	208	1.623227E+02
119	1.148437E+02	164	1.371822E+02	209	1.632657E+02
120	1.156264E+02	165	1.381861E+02	210	1.634748E+02
121	1.163259E+02	166	1.384150E+02	211	1.636129E+02
122	1.164502E+02	167	1.390245E+02	212	1.643863E+02
123	1.169483E+02	168	1.394372E+02	213	1.648427E+02
124	1.173829E+02	169	1.395969E+02	214	1.654651E+02
125	1.176044E+02	170	1.403503E+02	215	1.659263E+02
126	1.177965E+02	171	1.409431E+02	216	1.666807E+02
127	1.183043E+02	172	1.416717E+02	217	1.668503E+02
128	1.184692E+02	173	1.419198E+02	218	1.675081E+02
129	1.186600E+02	174	1.422946E+02	219	1.679810E+02
130	1.200534E+02	175	1.430282E+02	220	1.680743E+02
131	1.204629E+02	176	1.437807E+02	221	1.687791E+02
132	1.208358E+02	177	1.442287E+02	222	1.691455E+02
133	1.212598E+02	178	1.443864E+02	223	1.692988E+02
134	1.215600E+02	179	1.451796E+02	224	1.694220E+02
135	1.222007E+02	180	1.460939E+02	225	1.694925E+02
136	1.231087E+02	181	1.464860E+02	226	1.695189E+02
137	1.232969E+02	182	1.469560E+02	227	1.695665E+02
138	1.239986E+02	183	1.477054E+02	228	1.697101E+02
139	1.243143E+02	184	1.480046E+02	229	1.697697E+02
140	1.246743E+02	185	1.494680E+02	230	1.697879E+02
141	1.250074E+02	186	1.497726E+02	231	1.698158E+02
142	1.251799E+02	187	1.505953E+02	232	1.698245E+02
143	1.254267E+02	188	1.518595E+02	233	1.700502E+02
144	1.255998E+02	189	1.520097E+02	234	1.709023E+02
145	1.258597E+02	190	1.528346E+02	235	1.711117E+02
146	1.262413E+02	191	1.530097E+02	236	1.713373E+02
147	1.265225E+02	192	1.533823E+02	237	1.715782E+02
148	1.271556E+02	193	1.543277E+02	238	1.720280E+02
149	1.274917E+02	194	1.547946E+02	239	1.725870E+02
150	1.284641E+02	195	1.552873E+02	240	1.737690E+02

Table 7. (cont.)

MODE NO.	CYCLES (HZ)
241	1.741149E+02
242	1.745343E+02
243	1.746875E+02
244	1.748875E+02
245	1.750939E+02
246	1.755788E+02
247	1.758100E+02
248	1.765877E+02
249	1.767782E+02
250	1.772831E+02
251	1.774090E+02
252	1.775153E+02
253	1.776338E+02
254	1.781657E+02
255	1.790467E+02
256	1.792673E+02
257	1.795801E+02
258	1.803510E+02
259	1.811791E+02
260	1.812408E+02
261	1.813270E+02
262	1.819642E+02
263	1.826972E+02
264	1.829867E+02
265	1.837821E+02
266	1.841345E+02
267	1.845017E+02
268	1.852105E+02
269	1.858056E+02
270	1.860358E+02
271	1.862926E+02
272	1.870079E+02
273	1.873857E+02
274	1.874797E+02
275	1.877123E+02
276	1.879810E+02
277	1.886234E+02
278	1.887287E+02
279	1.890033E+02
280	1.895549E+02
281	1.902669E+02
282	1.908613E+02
283	1.921675E+02
284	1.939342E+02
285	1.941848E+02
286	1.945807E+02
287	1.949109E+02
288	1.953339E+02
289	1.958915E+02
290	1.968891E+02
291	1.981444E+02
292	1.982379E+02
293	1.983637E+02
294	1.986966E+02
295	1.989215E+02
296	1.994395E+02
297	1.997420E+02
298	1.999556E+02

The fixed-boundary component modes for the OASIS-1 payload were obtained by constraining the APC grid point and performing the eigenvalue extraction up to 200 Hz. Twenty-one fixed-boundary modes were found; these are listed in Table 8 and shown graphically in Appendix E. These modes were then reduced and coupled to the residual structure at the APC grid point.

System modes of the cargo bay model with the OASIS-1 payload are given in Table 9. The first mode, which is a rigid body mode, is believed to be the y-axis rotation of the APC and OASIS-1 on the sidewall. This is justified on the basis that neither the unloaded sidewall nor the fixed-boundary OASIS-1 payload models contained rigid-body modes. Further examination of the APC mounting on the sidewall (Figure 47) indicates that the y-direction couple will properly constrain rigid-body rotation about the x- and z- axes. Since the APC grid point lies through the lines of action of the x- and z-constraints, constraint of the y-rotation is not guaranteed. Such a modeling technique was unavoidable, since additional x- or z- direction constraints at the APC attachment locations would have rigidized the interface between the APC and the sidewall. The first rigid-body mode was therefore partitioned out of subsequent frequency response analyses.

4.3 Frequency Response Analysis

After calculation of system modes it is appropriate to perform modal frequency response analyses to determine the response of both the unloaded and loaded sidewall models to acoustic excitation. The methodology which was employed for these studies is described in detail in Reference 15. A point on the sidewall in the vicinity of one of the APC mounting points was chosen as the response point for both the unloaded and loaded sidewall models. The response power (auto-) spectral density function $G_{SS}(f)$ at node points can be given by

$$G_{SS}(f) = \sum \sum H_{ns}^{*}(f) A_n G_{nm}(f) H_{ms}(f) A_m \qquad (42)$$

where A_n is the area associated with node point n, $H_{ns}(f)$ is the frequency response function giving the response at node s due to a unit pressure

Table 8. OASIS I Fixed Boundary Modes

MODE NO.	CYCLES (HZ)
1	4.945811E+00
2	5.136858E+00
3	1.110806E+01
4	5.126816E+01
5	5.500848E+01
6	6.679961E+01
7	7.588665E+01
8	7.838692E+01
9	8.307774E+01
10	9.074462E+01
11	9.473682E+01
12	1.101998E+02
13	1.159331E+02
14	1.224181E+02
15	1.369674E+02
16	1.564992E+02
17	1.613874E+02
18	1.730168E+02
19	1.811488E+02
20	1.944810E+02
21	1.987567E+02

Table 9. Loaded Sidewall Normal Modes

MODE NO.	CYCLES (HZ)	MODE NO.	CYCLES (HZ)	MODE NO.	CYCLES (HZ)
1	1.942995E-05	41	6.939169E+01	81	9.532048E+01
2	5.077756E+00	42	7.121456E+01	82	9.571457E+01
3	5.224607E+00	43	7.167839E+01	83	9.648990E+01
4	9.264296E+00	44	7.210238E+01	84	9.722215E+01
5	1.174726E+01	45	7.282044E+01	85	9.734774E+01
6	1.290602E+01	46	7.328907E+01	86	9.776502E+01
7	1.491515E+01	47	7.367381E+01	87	9.829196E+01
8	1.673237E+01	48	7.462929E+01	88	9.907520E+01
9	1.953594E+01	49	7.479678E+01	89	9.931754E+01
10	1.967234E+01	50	7.588123E+01	90	9.995138E+01
11	2.419342E+01	51	7.677238E+01	91	1.002521E+02
12	2.887931E+01	52	7.688346E+01	92	1.007226E+02
13	3.470331E+01	53	7.703786E+01	93	1.015508E+02
14	3.601926E+01	54	7.764828E+01	94	1.023313E+02
15	3.946805E+01	55	7.828588E+01	95	1.029673E+02
16	4.240527E+01	56	7.844739E+01	96	1.032449E+02
17	4.427385E+01	57	8.041782E+01	97	1.037608E+02
18	4.443751E+01	58	8.113173E+01	98	1.042956E+02
19	4.700646E+01	59	8.161214E+01	99	1.053033E+02
20	4.832541E+01	60	8.194070E+01	100	1.056772E+02
21	5.005508E+01	61	8.273244E+01	101	1.059039E+02
22	5.137508E+01	62	8.324359E+01	102	1.064122E+02
23	5.179819E+01	63	8.375327E+01	103	1.071201E+02
24	5.304218E+01	64	8.402524E+01	104	1.078119E+02
25	5.391960E+01	65	8.510593E+01	105	1.080915E+02
26	5.627720E+01	66	8.616029E+01	106	1.088587E+02
27	5.672466E+01	67	8.655154E+01	107	1.090005E+02
28	5.763962E+01	68	8.722767E+01	108	1.094764E+02
29	5.866005E+01	69	8.845521E+01	109	1.095591E+02
30	5.902487E+01	70	8.863297E+01	110	1.103555E+02
31	5.928036E+01	71	8.901215E+01	111	1.108913E+02
32	6.225285E+01	72	9.008446E+01	112	1.112108E+02
33	6.249527E+01	73	9.093328E+01	113	1.114199E+02
34	6.456031E+01	74	9.117377E+01	114	1.116662E+02
35	6.570993E+01	75	9.151903E+01	115	1.117333E+02
36	6.628754E+01	76	9.298723E+01	116	1.118676E+02
37	6.713506E+01	77	9.309585E+01	117	1.118967E+02
38	6.733310E+01	78	9.358123E+01	118	1.120161E+02
39	6.842239E+01	79	9.424027E+01	119	1.120411E+02
40	6.877951E+01	80	9.458274E+01	120	1.121402E+02

Table 9. (cont.)

MODE NO.	CYCLES (HZ)	MODE NO.	CYCLES (HZ)	MODE NO.	CYCLES (HZ)
121	1.121942E+02	166	1.319343E+02	211	1.553149E+02
122	1.122304E+02	167	1.321286E+02	212	1.565888E+02
123	1.122643E+02	168	1.324407E+02	213	1.568530E+02
124	1.122911E+02	169	1.329191E+02	214	1.572395E+02
125	1.123002E+02	170	1.330851E+02	215	1.574828E+02
126	1.125808E+02	171	1.332765E+02	216	1.584045E+02
127	1.132310E+02	172	1.342663E+02	217	1.592225E+02
128	1.136293E+02	173	1.345633E+02	218	1.595137E+02
129	1.141656E+02	174	1.349490E+02	219	1.604224E+02
130	1.154525E+02	175	1.352905E+02	220	1.606867E+02
131	1.160147E+02	176	1.356381E+02	221	1.609093E+02
132	1.161455E+02	177	1.363497E+02	222	1.617838E+02
133	1.166036E+02	178	1.374868E+02	223	1.623980E+02
134	1.169368E+02	179	1.378381E+02	224	1.627912E+02
135	1.169833E+02	180	1.391313E+02	225	1.632748E+02
136	1.173549E+02	181	1.394412E+02	226	1.635959E+02
137	1.174872E+02	182	1.395072E+02	227	1.637468E+02
138	1.180288E+02	183	1.398121E+02	228	1.640099E+02
139	1.185262E+02	184	1.404990E+02	229	1.648556E+02
140	1.188359E+02	185	1.415374E+02	230	1.650139E+02
141	1.195353E+02	186	1.421889E+02	231	1.656597E+02
142	1.198443E+02	187	1.425610E+02	232	1.668752E+02
143	1.199513E+02	188	1.428971E+02	233	1.673745E+02
144	1.205189E+02	189	1.437585E+02	234	1.677180E+02
145	1.208980E+02	190	1.444056E+02	235	1.681742E+02
146	1.210631E+02	191	1.447332E+02	236	1.685151E+02
147	1.217063E+02	192	1.450558E+02	237	1.687333E+02
148	1.228842E+02	193	1.453276E+02	238	1.691720E+02
149	1.232566E+02	194	1.463164E+02	239	1.693226E+02
150	1.235476E+02	195	1.467346E+02	240	1.695033E+02
151	1.240587E+02	196	1.471596E+02	241	1.695193E+02
152	1.247450E+02	197	1.477069E+02	242	1.695476E+02
153	1.248476E+02	198	1.484292E+02	243	1.696196E+02
154	1.250084E+02	199	1.497339E+02	244	1.697756E+02
155	1.254281E+02	200	1.502869E+02	245	1.697900E+02
156	1.256536E+02	201	1.506415E+02	246	1.698068E+02
157	1.257703E+02	202	1.509918E+02	247	1.698207E+02
158	1.260175E+02	203	1.520226E+02	248	1.698959E+02
159	1.267064E+02	204	1.527471E+02	249	1.702715E+02
160	1.274376E+02	205	1.528868E+02	250	1.707622E+02
161	1.277974E+02	206	1.538388E+02	251	1.709574E+02
162	1.283827E+02	207	1.542605E+02	252	1.715173E+02
163	1.296320E+02	208	1.546152E+02	253	1.715796E+02
164	1.308425E+02	209	1.547436E+02	254	1.720280E+02
165	1.315975E+02	210	1.549899E+02	255	1.726219E+02

Table 9. (cont.)

MODE NO.	CYCLES (HZ)
256	1.728377E+02
257	1.738400E+02
258	1.741708E+02
259	1.746008E+02
260	1.746688E+02
261	1.751150E+02
262	1.753233E+02
263	1.757507E+02
264	1.761328E+02
265	1.766028E+02
266	1.770703E+02
267	1.772943E+02
268	1.774675E+02
269	1.775222E+02
270	1.776400E+02
271	1.778032E+02
272	1.781749E+02
273	1.785992E+02
274	1.795429E+02
275	1.798276E+02
276	1.804821E+02
277	1.811777E+02
278	1.812564E+02
279	1.813476E+02
280	1.816381E+02
281	1.821950E+02
282	1.826516E+02
283	1.830499E+02
284	1.837910E+02
285	1.841680E+02
286	1.851038E+02
287	1.858276E+02
288	1.862451E+02
289	1.865508E+02
290	1.868625E+02
291	1.872722E+02
292	1.874614E+02
293	1.876133E+02
294	1.877434E+02
295	1.881425E+02
296	1.888527E+02
297	1.897089E+02
298	1.902195E+02
299	1.906797E+02
300	1.915421E+02

MODE NO.	CYCLES (HZ)
301	1.926150E+02
302	1.930257E+02
303	1.931271E+02
304	1.941712E+02
305	1.945673E+02
306	1.948573E+02
307	1.950181E+02
308	1.953270E+02
309	1.959442E+02
310	1.966497E+02
311	1.974893E+02
312	1.982361E+02
313	1.983579E+02
314	1.984424E+02
315	1.991933E+02
316	1.993985E+02
317	1.994575E+02
318	1.996618E+02
319	1.998064E+02

distributed over area A_n, and $G_{nm}(f)$ is the excitation pressure cross-spectral density function.

The actual acoustic field on the Space Shuttle during lift-off can be described best in terms of a convected pressure field. However, since the main purpose of this analytical study is to predict the relative response of an unloaded and loaded sidewall, it was assumed that the excitation pressure could be represented adequately as a reverberant acoustic field. This assumption simplifies the computation requirements. Also for ease of computation, it was assumed that the excitation pressure cross-spectral density function could be taken as separable in the y- and z-directions. Thus,

$$G_{nm}(f) \approx G_{nn}(f)\ [\sin(k\xi)/(k\xi)][\sin(k\eta)/(k\eta)] \qquad (43)$$

where $G_{nn}(f)$ is the pressure auto-spectrum (assumed homogeneous), $\xi=y_n-y_m$, $\eta=z_n-z_m$, and wavenumber $k=2\pi f/c_o$ where c_o is the speed of sound. This is a somewhat crude assumption but it is adequate for present purposes.

Values for the pressure autospectral density function $G_{nn}(f)$ were obtained from the empirical model of the exterior pressure field used in the PACES prediction procedure [16] for payload bay sound pressure levels. The empirical model in Reference 16 presents space-average values of the spectral density for both the forward and aft regions of the sidewall. In the present finite element model it is assumed that the autospectral density is uniform over the entire sidewall. Thus, values for the forward and aft regions were averaged. It was found that the resulting average values showed little frequency dependency over the frequency range of interest (20-200 Hz). Thus a constant value of 6.24×10^{-5} $(psi)^2/Hz$ was taken for $G_{nn}(f)$, for all frequencies of interest. The actual variation about this mean value was less than ±1.3 dB.

The computation assumed that the excitation pressure field was present only on the sidewall above the wing. Consistent with the PACES model [16], it was assumed that the excitation pressure field on the sidewall region covered by the wing could be neglected. Also, it was assumed that there was no

excitation pressure field on the bottom of the payload bay. This assumption was introduced to keep the computations within a manageable size. However, it can be justified on the basis of the results presented in Reference 10. In that study it was shown that, even at low frequencies, the response of the sidewall in the y-direction was controlled by the acoustic pressure field acting on the sidewall above the wing. The fluctuating pressure field on the bottom of the orbiter made a significant contribution to the motion of the sidewall in the z-direction only.

A point on the sidewall in the vicinity of one of the APC mounting points was chosen as the response point for both the unloaded and loaded sidewall models. This point, shown in Figure 47, corresponds to the outer edge of the upper longeron, halfway between the main frame and stub frame in bay 7.

The predicted response of the unloaded sidewall can be compared with vibration measurements made on the early launches of the Space Shuttle. An analysis of data from these early launches was performed in Reference 10 and the same data have been used to construct two acceleration spectra associated with maximum response (usually in the time slice from T+5.5 seconds to T+6.3 seconds). The data were provided as one-third octave band time histories. Thus the spectral comparison is made in terms of one-third octave bands. The comparison is shown in Figure 48 which contains two measured spectra. One spectrum is associated with accelerometer V08D9349A at location x=908, y=105, z=410 on STS-3 and the other with V08D9388A at location x=1183, y=95, z=414 on STS-4. The first location was on the orbiter longeron and the second on the orbiter attachment for the DFI trunnion. Thus, in the latter case the sidewall was loaded. The comparison shows the predicted spectrum lying between the two measured spectra. It should be noted that the measured vibration levels associated with accelerometer V08D9349A were much higher than those for any other locations measured on STS-3 and STS-4 [10].

The results in Figure 48 give confidence that the finite element model is predicting vibration levels that are consistent with measured values. The predicted vibration spectrum for the OASIS I base plate is compared with two measured spectra in Figure 49. The measured spectra were obtained from

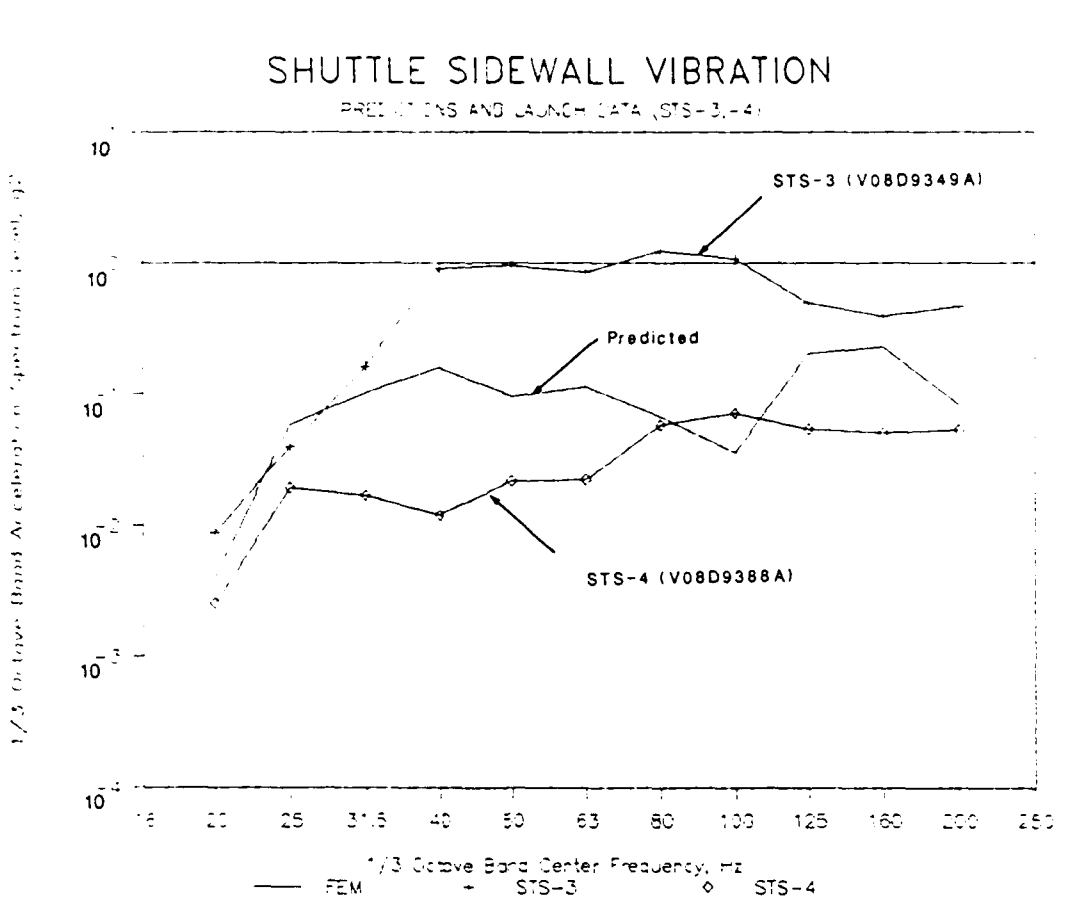

FIGURE 48. COMPARISON OF MEASURED AND PREDICTED VIBRATION OF SPACE SHUTTLE ORBITER SIDEWALL

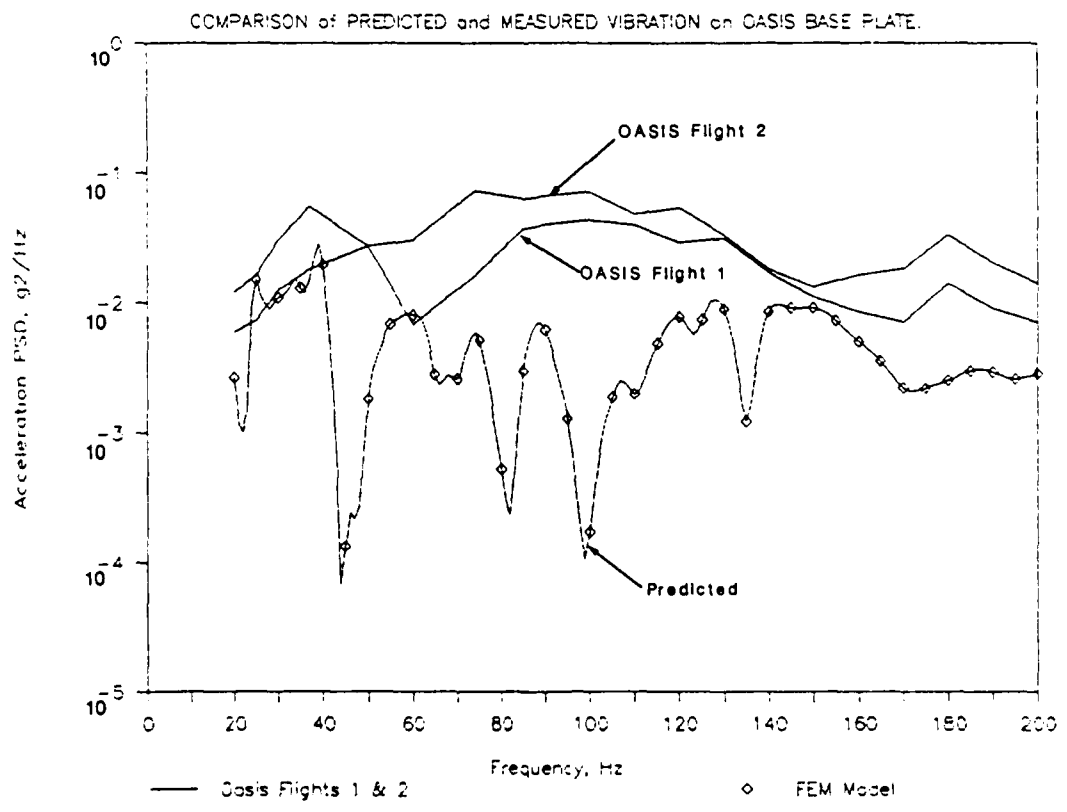

FIGURE 49. COMPARISON OF MEASURED AND PREDICTED VIBRATION OF OASIS I PAYLOAD BASE PLATE

Reference 13. In this case the predicted values are somewhat lower than both of the measured spectra.

It is now of interest to compare the predicted vibration spectra for the unloaded sidewall and the OASIS I payload base plate (which, because of the modelling procedure, is essentially the same as the loaded sidewall). Such a comparison is given in Figure 50 in terms of autospectral density function and one-third octave band spectra. The frequency range shown is 20 to 200 Hz. It is seen that, in general, the response of the loaded sidewall is lower than that of the unloaded sidewall. Inspection of the narrowband spectra (Figure 50(a) also show some frequency shifts at peaks or troughs. However, for both amplitude and frequency the changes are small.

These results can be reviewed in terms of the parametric studies performed with a single-degree-of-freedom payload (discussed in Section 3). Consider, for example the results shown in Figure 14(a) for the case where the resonance frequency of the payload was about half that of the lowest mode of the panel on which the payload was mounted. Also consider the payload with the smallest weight (25 lb). This weight was about 63% of the physical weight of the stiffened panel. In the case of the OASIS I payload on the shuttle sidewall, the lowest resonance frequency of the payload is below that of the sidewall, and the weight of the payload is much smaller than the weight of the sidewall and bottom structure (less than 10%).

Figure 40(a) shows that the 25 lb payload has only a small influence on the predicted response of the supporting structure except at frequencies below 60 Hz, i.e., at frequencies below $1.5f_1$ where f_1 is the lowest resonance frequency of the supporting structure. If this were the case for OASIS I on the sidewall of the structure, the presence of the payload would be expected to have most influence at frequencies below 20 Hz, that is, below the frequency range of interest in Figure 50.

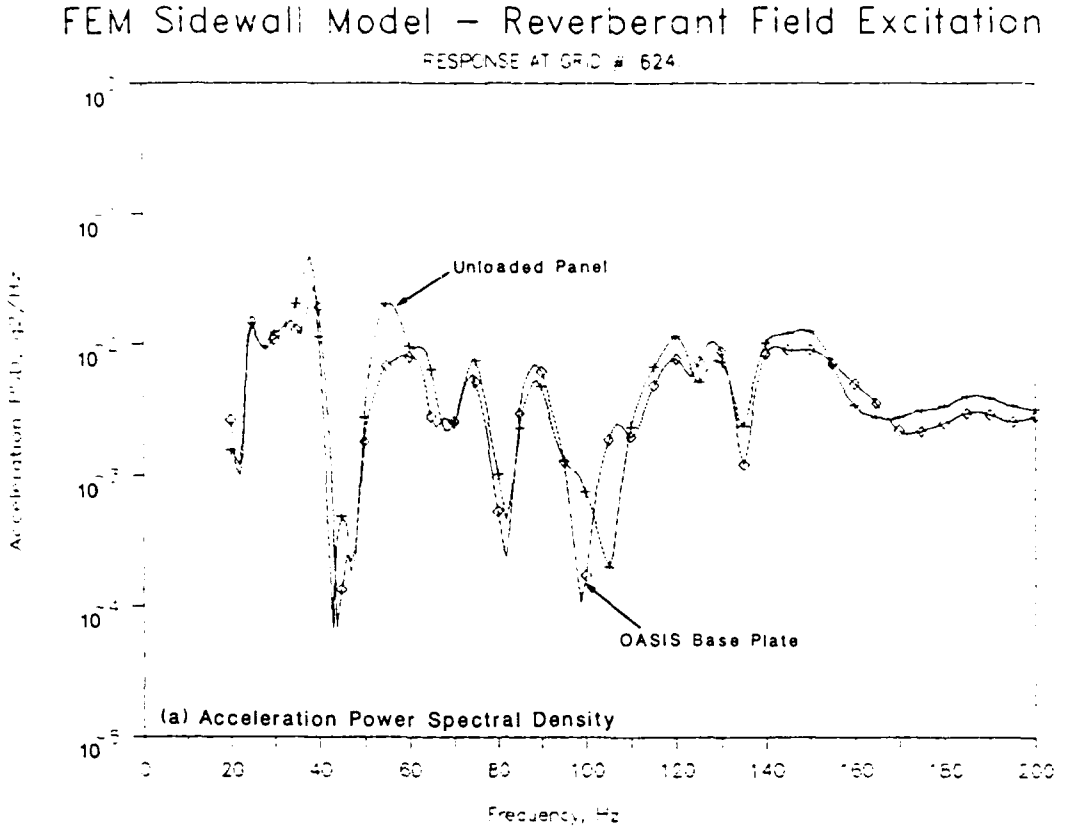

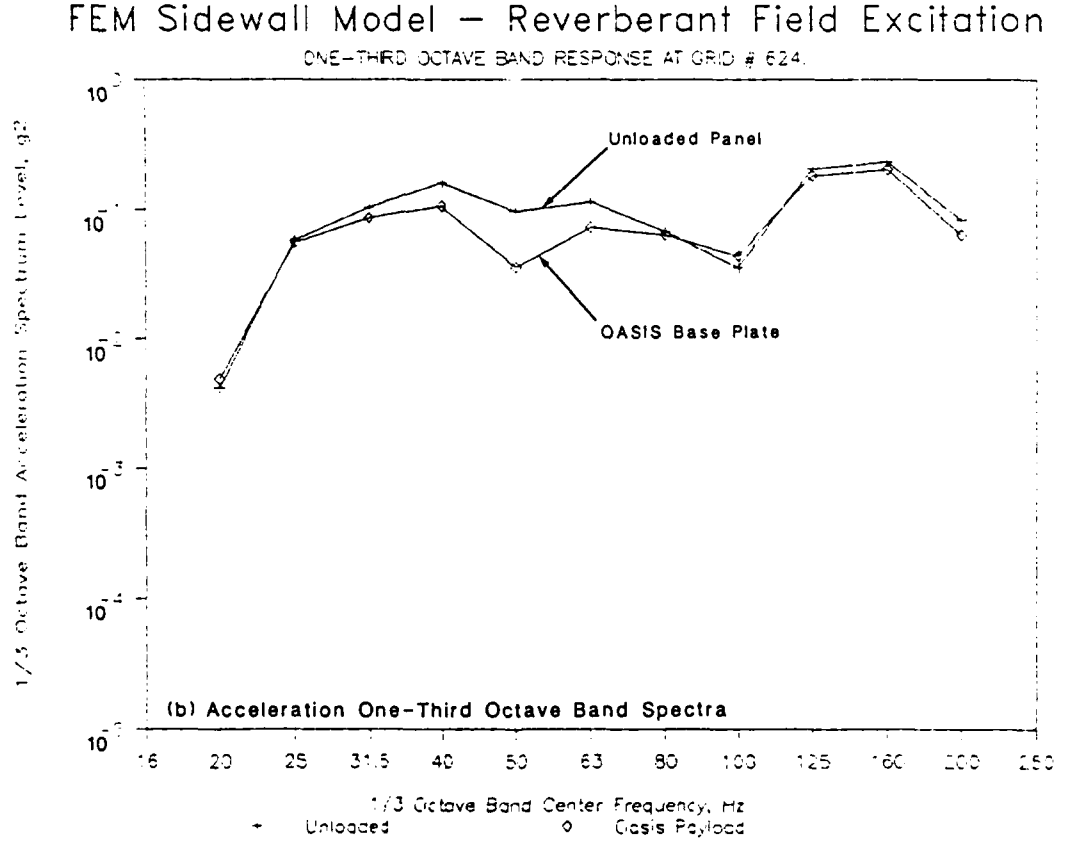

FIGURE 50. COMPARISON OF PREDICTED VIBRATION OF UNLOADED SIDEWALL AND OASIS I PAYLOAD BASE PLATE.

4.4 Summary

The finite element analysis of the vibration of the Space Shuttle sidewall gives results that are consistent with, and of comparable magnitude to, launch measurements. The predictions indicate that, when the OASIS I payload is attached to the sidewall, the changes in sidewall vibration are small. This indicates that the impedance of the payload is small relative to that of the sidewall mounting point. Comparisons with results for simple, single-dof, payloads again show consistency.

5. OV-101 SIDEWALL INERTANCE MEASUREMENTS

All of the vibration testing procedures discussed in Section 2 require a knowledge of the inertance (apparent weight) function for the orbiter structure at the payload mounting points. To estimate these mounting point inertance functions, a series of experiments were performed on Space Shuttle Orbiter OV-101 (the Enterprise), which is now the property of the Smithsonian Institution in Washington, D.C. The plan for the experiments is detailed in Reference 17. The basic data analysis was accomplished by the NASA Goddard Space Flight Center (GSFC), and the results were transmitted to Astron Research and Engineering for detailed evaluations.

5.1 Data Collection and Analysis

The OV-101 experiments were performed at Dulles International Airport on 19 and 20 August 1987. The inertance measurements were made by personnel of the NASA Goddard Space Flight Center (GSFC), Greenbelt, MD.

5.1.1 OV-101 Configuration

The OV-101 as tested was essentially a stripped orbiter configuration. There were no equipment items in the crew compartment, no interior thermal control system (TCS) material in the cargo bay, and no radiators or door seals on the cargo bay doors. The actual exterior thermal protection system (TPS) material was not installed, but was accurately simulated in terms of weight. The most serious discrepancy from a flight orbiter configuration was the presence of two large ballast structures that bridged the payload bay at, or near, Stations Nos. 950 (Bay 7) and 1180 (Bay 11), as indicated in Figure 51. These structures undoubtedly alter the fundamental sidewall normal modes of the orbiter and, hence, influence the inertance of the sidewall structure at the lower frequencies (at least below 10 Hz).

5.1.2 APC Configuration

All sidewall mounted payloads on Space Shuttle are carried on an Adaptive Payload Carrier (APC) or an Increased Capability Adaptive Payload Carrier

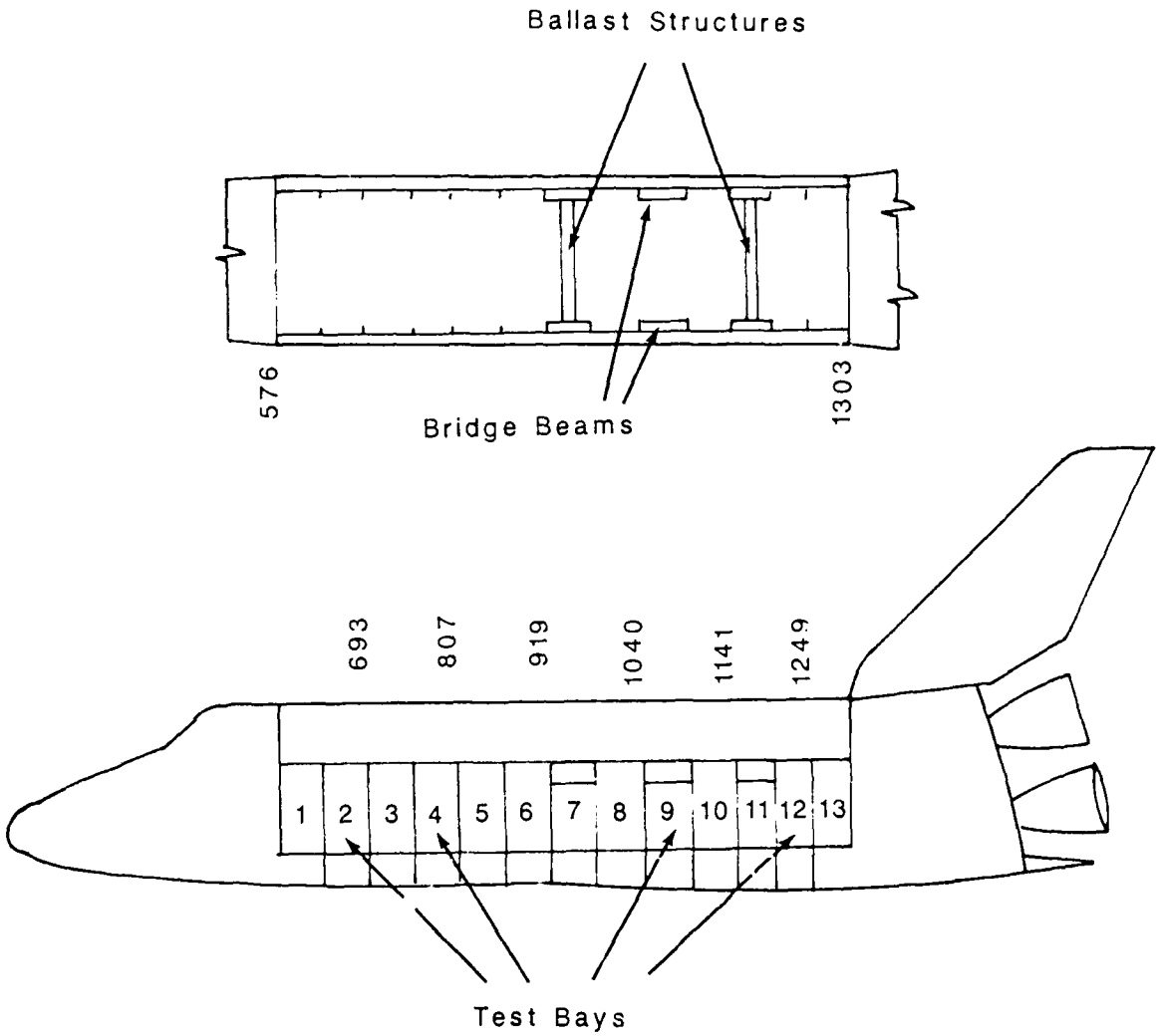

FIGURE 51. LOCATION OF TEST BAYS FOR INERTANCE MEASUREMENTS ON ORBITER OV-101

(ICAPC). An APC is illustrated in Figure 46. These APC can be mounted at 46 locations on the orbiter structure through three points, as follows:

(a) To the z = 410 longeron through an upper fitting on top of the APC that provides a positive fit along the x-axis, a loose fit along the z-axis, and a 25-mil gap fit along the y-axis.

(b) To a main frame through an end fitting on the side of the APC that provides a positive fit along the z-axis, a loose fit along the x-axis, and a 25-mil gap fit along the y-axis.

(c) To a stub frame through a hole in the APC that appears to provide a semi-positive fit along the x- and z-axes, and a 25-mil gap fit along the y-axis.

It is clearly these mounting locations that are of interest in the measurement of inertance functions of the orbiter structure.

5.1.3 Measurement Locations

Inertance measurements were made at, or near to, the attachment points for the APC (or ICAPC) illustrated in Figure 46. A total of 45 inertance measurements were made at these points in four sidewall bays on the starboard side of OV-101, namely, in Bays 2, 4, 9, and 12 (Figure 51). These sidewall bays were selected to provide a representative sample of mounting locations from the front to the rear of the cargo bay, while being at least one sidewall bay away from the two bridge structures in Bays 7 and 11. The measurement locations are identified in Figure 52, and are summarized in Table 10. It should be noted that inertance measurements along the y-axis (normal to the sidewall structure) could be made at the actual APC attachment point locations of interest. However, this could not be done for the measurements along the x (longitudinal) and z (vertical) axes, which are in the plane of the sidewall. Hence, the z-axis measurements were made on top of the z = 410 longeron (the rail at the top of the sidewall frames) directly over the desired measurement location. This produced repeated z-axis measurements at similar locations in

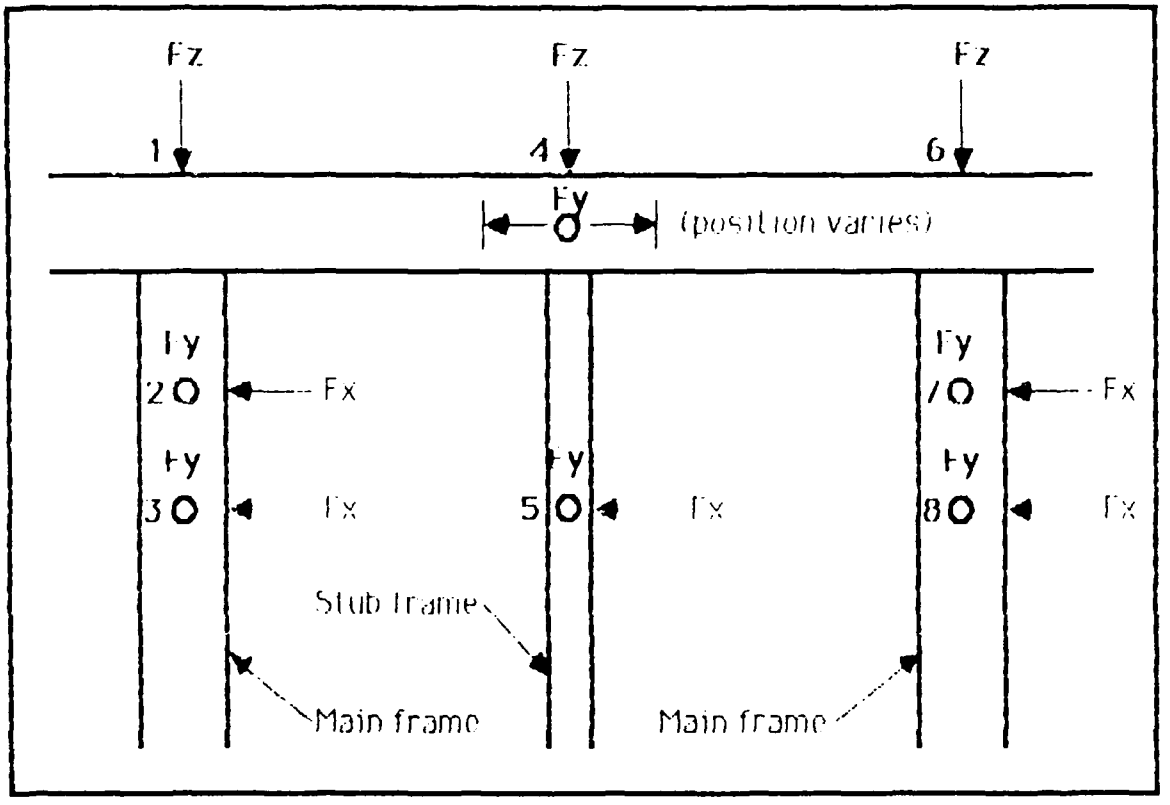

FIGURE 52. SKETCH OF LOCATIONS FOR INERTANCE MEASUREMENTS ON OV-101.

Table 10. Listing of Locations for Inertance Measurements on OV-101

Bay No.	Location See Fig46	Orbiter Axis	Bay No	Location See Fig46	Orbiter Axis	Bay No.	Location See Fig46	Orbiter Axis
2	2	x	4	2	x	9	2	x
2	2	y	4	2	y	9	2	y
2	2 (1)	z	4	2 (1)	z	9	2 (1)	z
2	3	x	4	3	x	9	8	x
2	3	y	4	3	y	9	8	y
2	3 (1)	z	4	3 (1)	z	9	8 (6)	z
2	4	y	4	4	y	12	1	y
2	4	z	4	4	z	12	1	z
2	5	x	4	5	x	12	2	x
2	5	y	4	5	y	12	2	y
2	5 (4)	z	4	5 (4)	z	12	2 (1)	z
2	7	x	4	7	x			
2	7	y	4	7	y			
2	7 (6)	z	4	7 (6)	z			
2	8	x	4	8	x			
2	8	y	4	8	y			
2	8 (6)	z	4	8 (6)	z			

some cases. The x-axis measurements were made on the web of the frame behind the desired measurement location.

The direction of the impacts relative to the orientation of the accelerometers in inertance measurements is of particular importance because it can produce a 180 degree phase shift in the desired results. For these experiments, the impact force was always applied along the axis from the top to the bottom of the accelerometer, which makes a positive force correspond to a negative acceleration (force is positive when the hammer applies a load, and acceleration is positive when the bottom of the accelerometer moves upward). Hence, all measurements produced by the experiments are 180 degrees out of phase with the desired results. This 180 degree phase correction was made to all measurements during the evaluation of the data.

During the course of the experiments, an additional 21 measurements were made on a sidewall panel installed in Bay 9, which was mistakenly believed to be an APC. However, it was later determined that the panel was a bridge beam, not an APC and was not representative of a payload sidewall-mounting structure. Hence, these measurements were not employed for the data evaluations.

5.1.4 Measurement and Analysis Procedures

The inertance measurements were made using a PCB Model SP205 impulse hammer with a Model 086B20 force gage, and Endevco Model 7251-100 accelerometers. A total of ten impacts were used to determine the inertance at each measurement location, so that a coherence function could be computed to assess the quality of the resulting inertance calculation. The inertance was computed using a GenRad Model 2515 multi-channel analyzer with an SDRC Modal Plus, Version 9.0, analysis program. The actual computation was

$$I(f) = G_{FA}(f)/G_{FF}(f) \tag{44}$$

where

$G_{FA}(f)$ = cross-spectral density function between force in lb and acceleration in gravity units (g).

$G_{FF}(f)$ = autospectral density function of force in lb.

The coherence function for each measurement was computed by

$$Coh(f) = |G_{FA}(f)|^2 / [G_{FF}(f)G_{AA}(f)] \tag{45}$$

where

$G_{AA}(f)$ = autospectral density function of acceleration in gravity units

and all other terms are as defined in Equation (44). All spectral quantities were computed over the frequency range from 3 to 255 Hz with a frequency resolution of B = 0.5 Hz using n_d = 10 averages of statistically independent samples. The time history records were tapered with an exponential weight prior to the Fourier transform calculations to suppress side-lobe leakage in the results.

The final inertance data were transferred to IBM-compatible digital disks for subsequent detailed evaluations. The evaluations were accomplished by Astron personnel using an IBM-AT-compatible personal computer with special data analysis software.

5.2 Data Evaluations

The 45 inertance measurements were stored for evaluation on digital disks in terms of real and imaginary components, as well as magnitude and phase. The inertance data and coherence results were also provided in the form of plots produced at GSFC. These plots are presented in Appendix B for all measurements. Note that the phase functions for the inertance data in Appendix B have been corrected for the 180 degree phase shift discussed in Section 5.1.3.

5.2.1 Data Quality

The digital data were plotted and visually inspected for obvious errors and wild points. A few wild points were detected in the inertance data, and were corrected by removing the wild value and replacing it with a value that represented a linear interpolation between the values that preceded and followed it. There were also a few cases where the values of both the real and imaginary parts of the data were zero. Since this would prevent the inversion of the inertance data to apparent weight functions, these zeros were replaced by interpolated values, as described above.

The primary assessment of the data quality was based upon the coherence function calculated for each measurement, as detailed in Appendix B. It is seen from Appendix B that the best coherence is generally associated with the y-axis measurements. Specifically, with only a few exceptions, the coherence for the y-axis measurements is greater than 0.9 at all frequencies between 10 and 200 Hz. The same is true of many of the x-axis measurements, although a number of the x-axis coherence values are poor below about 50 Hz, particularly at Location 3. The z-axis coherence values are generally in excess of 0.9 at frequencies above 20 Hz.

In a single-input, multiple-output system there will be high coherence between the input and each output, and between the outputs as long as the system is linear and there is high signal-to-noise in the measurement signals. Departure from these ideal conditions leads to a subsequent reduction in

coherence. If the instrumentation and data analysis systems have been properly calibrated, and the coherency of the measured signals is high, it follows then that the results are accurate and provide a true representation of the system. It may be argued that the exciting force of the small impact hammer was too low, and did not cause the structure to vibrate at levels typical of service use. Driving the structure more strongly with a larger hammer would not increase the signal-to-noise ratio appreciably, for it is quite high already. If anything, it could lead to rattle and other manifestations of non-linear behavior. While such conditions may exist in the actual service environment, their influence is not considered in the present work phase, and will be postponed until a later phase. The objective of the first phase is to study and understand the linear situation. Therefore, for the present work objectives, it is concluded that the quality of the inertance data is adequate over the following frequency ranges:

x-axis - 50 to 200 Hz; y-axis - 10 to 200 Hz; z-axis - 20 to 200 Hz

Below the noted lower frequencies, the accuracy of the measurements is questionable, but the data are not necessarily bad. Specifically, the poor coherence values at the lower frequencies are probably indicative of poor signal-to-noise ratios in the measurements, primarily in the acceleration measurements, as discussed in Section 5.1.3. The resulting inertance estimates may involve substantial random errors (which may be suppressed by averaging operations), but they should be unbiased. Hence, all the data measured along each of the three axes are used for later evaluations over the frequency range from 10 to 200 Hz.

There is one other uncertainty associated with the inertance data that should be mentioned. Specifically, it is not certain that the x-axis measurements, which were made on the frame webs, are fully representative of the actual inertance of the frame structures at the APC mounting points on the frame flanges. However, the form and magnitude of the resulting inertance values appear reasonable, so they are accepted as being representative.

This discussion regarding the quality of the impedance data should be placed in perspective with regard to the current objective of developing test

procedures for payloads mounted on the orbiter sidewall. Firstly, the frequency range of interest for the payload test procedures is 20-200 Hz. This frequency range is certainly covered by the measurements for the y- and z-directions. Secondly, the measured values of sidewall impedance or apparent weight in the y-direction are in good agreement with predicted values [11] in the frequency range above about 20 Hz. (At lower frequencies, the accuracy of the predicted values is open to question because of the assumed boundary conditions for the sidewall.) Thus, the OV-101 impedance data are considered adequate for application to payload vibration test procedures.

5.2.2 Data Groupings

The inertance data measured along each of the three axes of the orbiter were inverted to obtain apparent weight functions, which in turn were inspected for variations among the different measurement locations. It was found that the measurements were similar from the front to the rear of the orbiter vehicle, and could be pooled as detailed in Table 11.

It is noted in Table 11 that Location 5 is omitted form the data pools for the x and z axes because it is believed the stub frame fitting will not carry a significant load along these axes. On the other hand, locations 2, 3, 7, and 8 are used in the x-axis data pool, even though the main frame APC fitting does not carry the primary load along the x-axis; Location 4 is the primary

Table 11. Pooled Apparent Weight Measurements Along Each Axis

x Axis		y Axis		z Axis	
Bay	Location (see Fig 52)	Bay	Location (see Fig 52)	Bay	Location (see Fig 52)
2	2,3,7,8	2	2,3,4,5,7,8	2	2,3,4,7,8
4	2,3,7,8	4	2,3,4,5,7,8	4	2,3,4,7,8
9	2,8	9	2,8	9	2,8
12		12	1,2	12	1,2

load carrying point in this direction. However, there was no choice here since it was not possible to measure an apparent weight along the x-axis at Location 4 (or any other location on the z = 410 longeron).

Plots of the apparent weights for the individual measurements in each data pool along each of the three axes, with the 180 degree phase correction discussed in Section 5.1.2, are presented in Section B.2 of Appendix B. It is noted that the measurements in each data pool are reasonably similar over the

frequency range from 10 to 200 Hz, and hence, constitute a reliable basis for calculating representative apparent weight values along each axis in this frequency range. However, it must be remembered that the x-axis results are open to question because the apparent weights were measured on structure that is not fully representative of the actual structure that bears the loads in the x-direction.

5.2.3 Summary of Apparent Weight Data

The orbiter apparent weight data are summarized in Figures 53 through 55 over the frequency range from 10 to 200 Hz. The magnitude results are presented as an average magnitude, and the average plus 2.5 standard deviations. For the sample sizes involved in each group (11 to 16 measurements), the average plus 2.5 standard deviations constitutes a 95% upper normal tolerance limit for the data with about 95% confidence [19]; i.e., if measurements were made at other similar locations, at least 95% of them would fall below the stated limit. The phase data in Figures 53 through 55 are presented in terms of an average phase computed as follows. In each group, the average values of the real and imaginary components of the apparent weights were computed separately. The average phase was then calculated from the arctangent of the average of the imaginary components divided by the average of the real components.

5.2.4 Evaluation of Apparent Weight Data

For a simple (single degree-of-freedom) mechanical system, the apparent weight of the system, as seen by a load on the mass, and assuming viscous damping with lead angles positive, is given by [20]

$$W(f) = -k\,[1 - (f/f_n)^2 + j2\zeta f/f_n]\,/\,(2\pi f)^2 \qquad (46)$$

where f_n is the undamped natural frequency, k is the spring constant, and ζ is the damping ratio of the system. Consider three frequency regions, namely,

(a) $f \ll f_n$ (the stiffness controlled region),
(b) $f \approx f_n$ (the damping controlled region), and
(c) $f \gg f_n$ (the mass controlled)

From Equation (46), the response in these three regions can be approximated by

$$\text{(a) } W(f) \approx -k/(2\pi f)^2 \qquad \text{(b) } W(f) \approx -j2m\zeta f_n/f \qquad \text{(c) } W(f) \approx m \qquad (47)$$

where m is the mass and all other terms are as defined in Equation (46). It follows that, for a single degree-of-freedom system, the apparent weight (a) in the stiffness controlled region is inversely proportional to the square of frequency, and has a phase of -180 degrees, (b) in the damping controlled region is inversely proportional to the first power of frequency, and has a phase of -90 degrees, and (c) in the mass controlled region is independent of frequency and has a phase of zero degrees.

For a complex, multimodal structure like the Space Shuttle orbiter, a stiffness-controlled response would be expected below the first dominant normal mode of the structure in question, while a damping-controlled response would be expected near the resonance frequencies. At the higher frequencies where the modal density of the structure is high, all frequencies would be close to a resonance frequency, meaning a damping-controlled response would be expected at all frequencies (assuming the structural response is resonance dominated). However, since f_n in Eq. 47(b) increases with f, the apparent weight in the damping controlled region for a complex structure will not

change with increasing frequency, unless damping changes. In prior analytical studies of the Space Shuttle orbiter structure [16], it was determined that a damping ratio that was inversely proportional to frequency provided good agreement with measured data. Such an assumption here would mean that the apparent weight in the damping controlled region would be inversely proportional to the first power of frequency. As long as the response of a complex structure is resonance dominated, a mass-controlled frequency region will never be reached.

Based upon the above relationships, consider the data in Figures 53 through 55. Referring first to Figure 53, it is clear the average apparent weight along the x-axis is stiffness-controlled below about 200 Hz. This is consistent with expectations, since these x measurements were made on the web of the frames, which should constitute essentially stiffness elements in this frequency range. Now referring to Figure 54, the apparent weight along the y-axis appears to go from stiffness-controlled at the low frequencies to damping-controlled above about 40 Hz. The magnitude of the apparent weight in the damping-controlled region above 40 Hz suggests that the damping ratio varies approximately with the inverse of frequency, as assumed in [16]. Again, this is consistent with expectations, since the modal density in the y-direction above 40 Hz is high. Finally, referring to Figure 55, it appears that the apparent weight along the z-axis falls between the results expected for stiffness and damping control, which is a believable result for this axis.

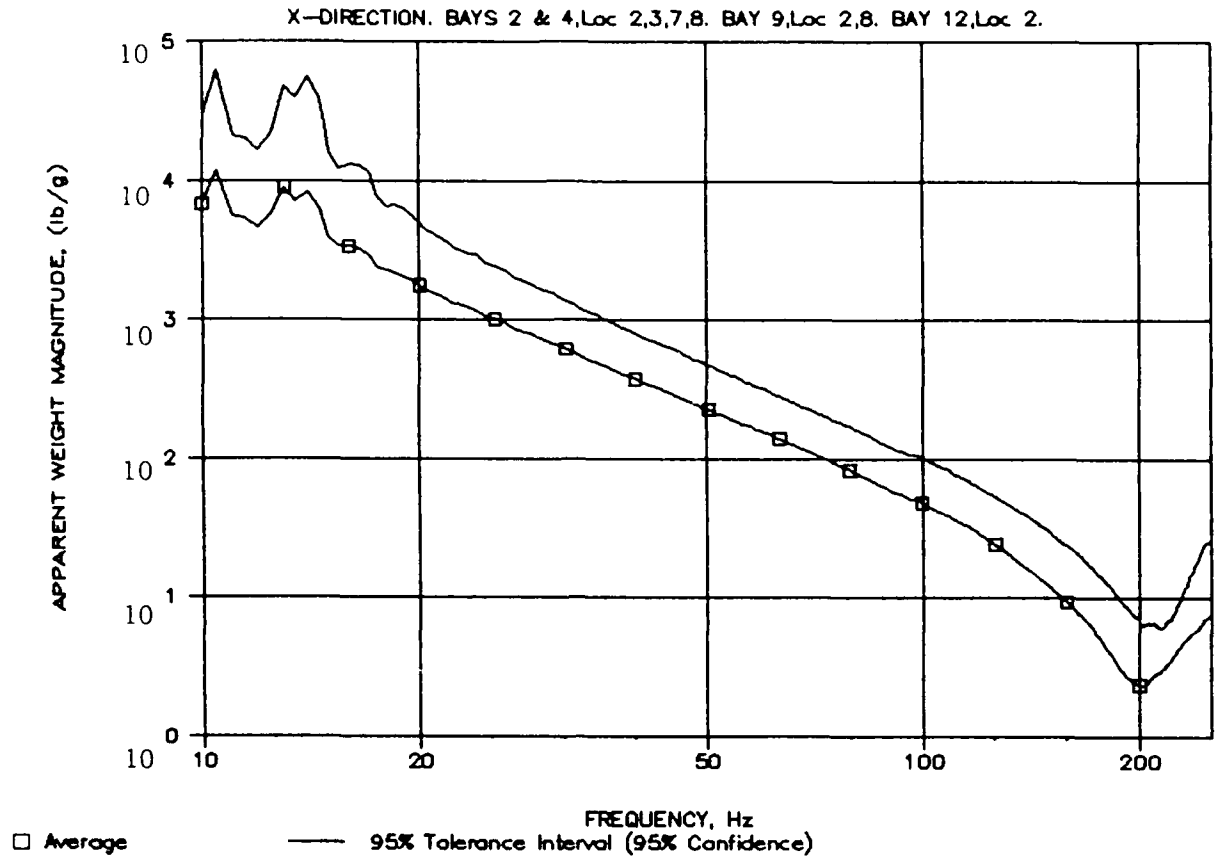

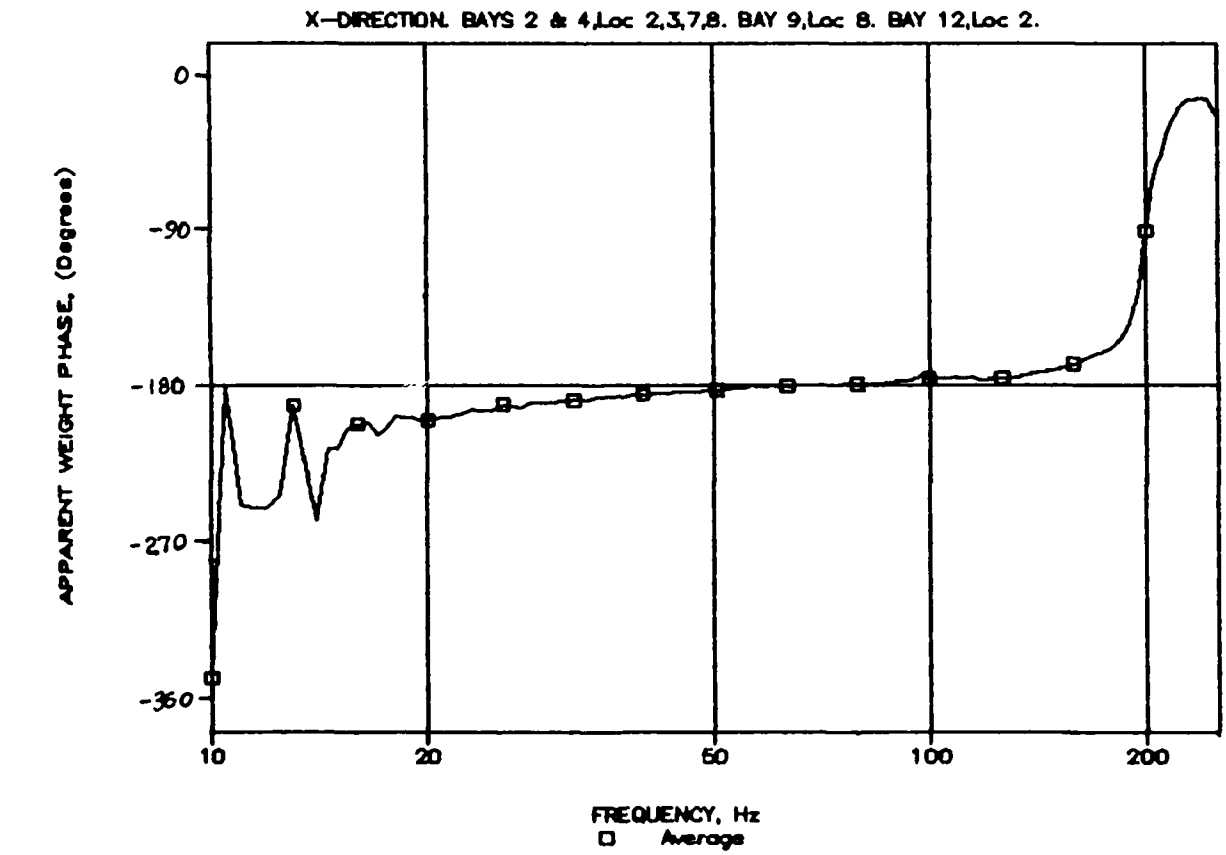

FIGURE 53. AVERAGE APPARENT WEIGHT OF OV-101 PAYLOAD MOUNTING POINTS - X AXIS.

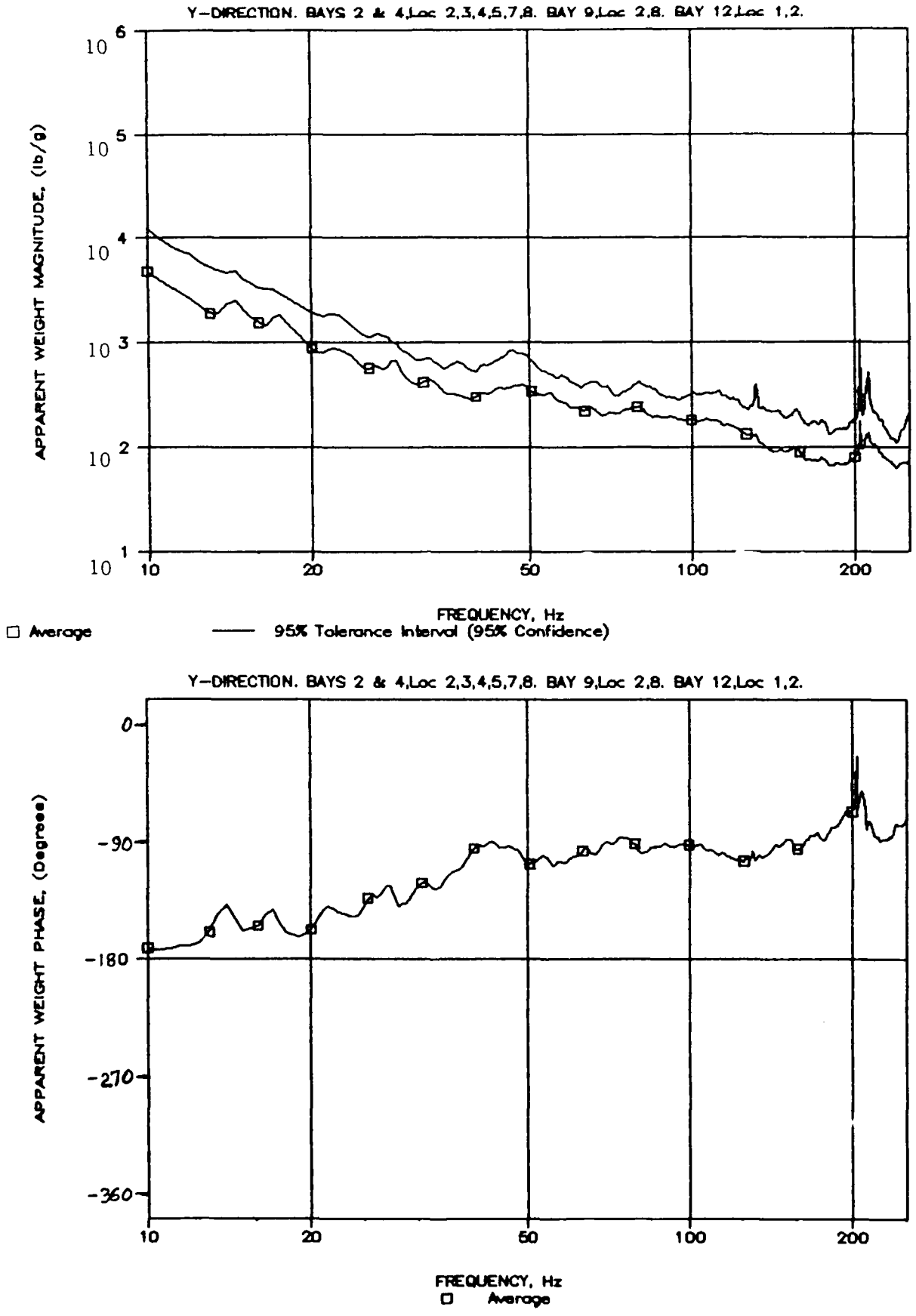

FIGURE 54. AVERAGE APPARENT WEIGHT OF OV-101 PAYLOAD MOUNTING POINTS - Y AXIS.

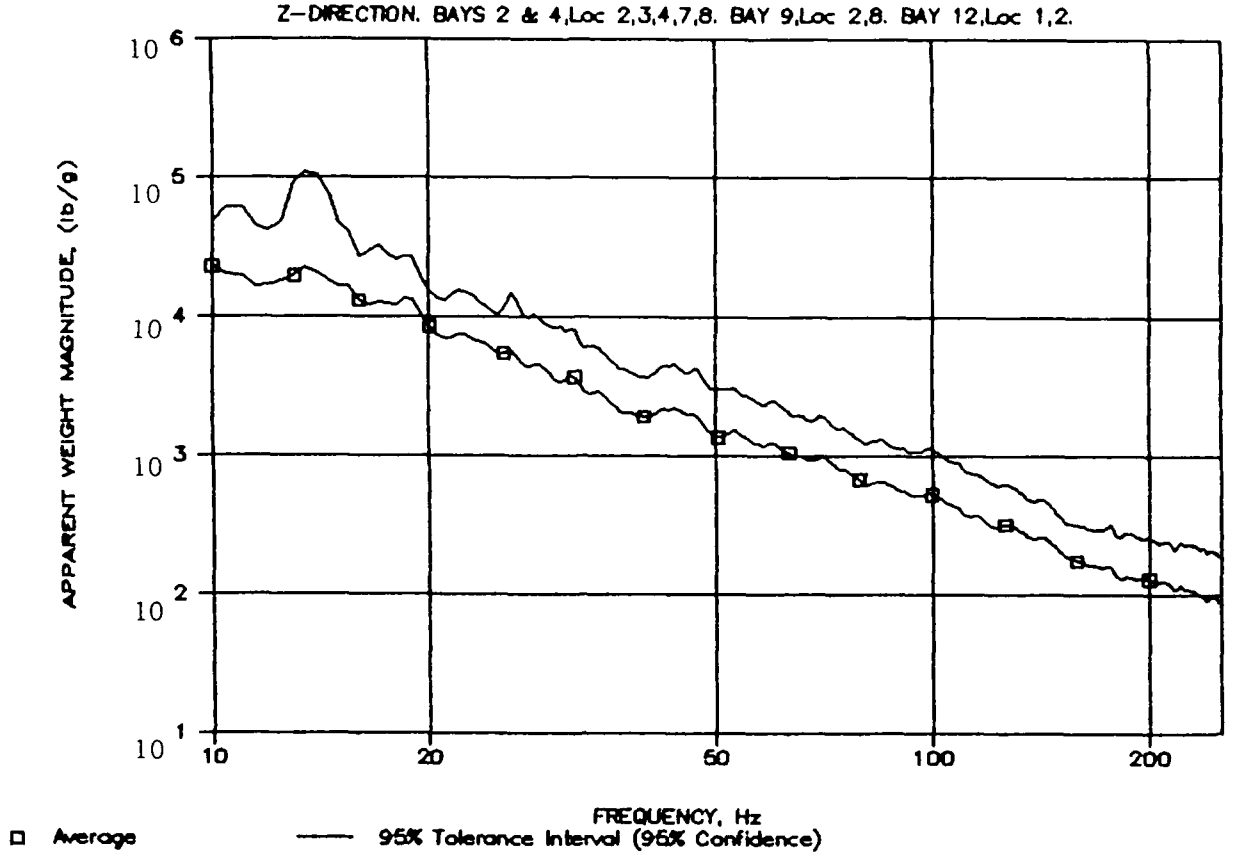

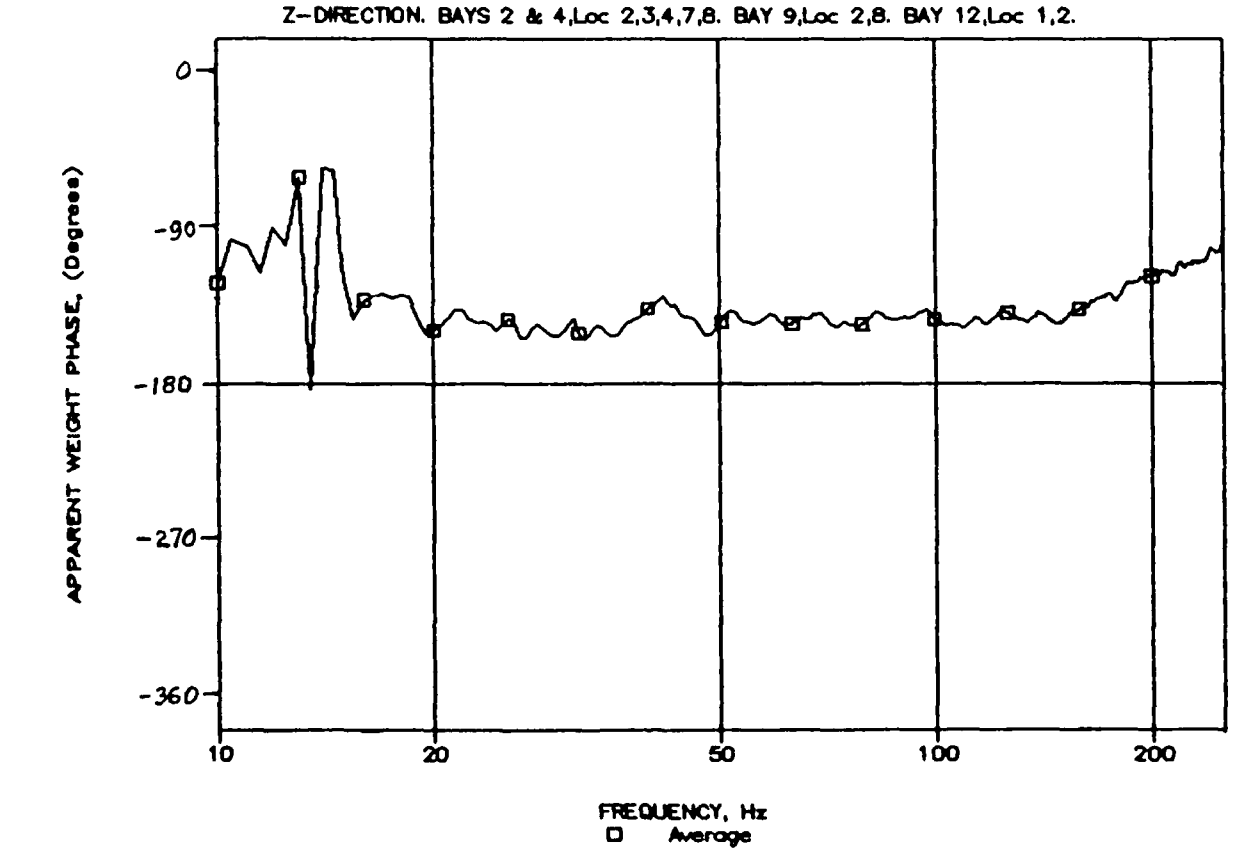

FIGURE 55. AVERAGE APPARENT WEIGHT OF OV-101 PAYLOAD MOUNTING POINTS - Z AXIS.

6. ACOUSTIC TESTS OF SIMULATED PAYLOAD

To validate physically the testing procedures formulated in Section 2, simulated (generic) payload and mounting structures were designed and fabricated for vibroacoustic testing. The design of the payload-mounting structure hardware and the acoustic tests performed on the hardware are discussed in this section. The vibration tests performed on the simulated payload are covered in Section 7.

6.1 Test Hardware

For the acoustic tests, the design of the panel structure to support the payload was driven by the following desired characteristics.

(a) A panel with overall dimensions of 36" x 48", to fit the available opening in the wall of the Johnson Space Center Acoustic Fatigue Laboratory reverberation chamber, where the acoustic tests were to be performed.

(b) A panel design that could be fabricated from readily available materials to limit costs and procurement times.

(c) A panel with a first normal mode frequency above 60 Hz, to reduce the difficulty in generating adequate acoustic inputs at the first normal mode.

With these considerations in mind, the ribbed panel structure shown in Figure 56 was designed and fabricated. The dimensions of this panel were such that it would fit into a window of the reverberation chamber at the NASA Johnson Space Center Acoustic Fatigue Laboratory. All materials were of standard size, and a 6061 aluminum alloy was used to facilitate welding, where required. The first normal mode of the panel, assuming built in edges, was about 74 Hz. To add some energy loss to the panel, two layers of Soundcoat GP-2 were attached to the ribbed side of the panel.

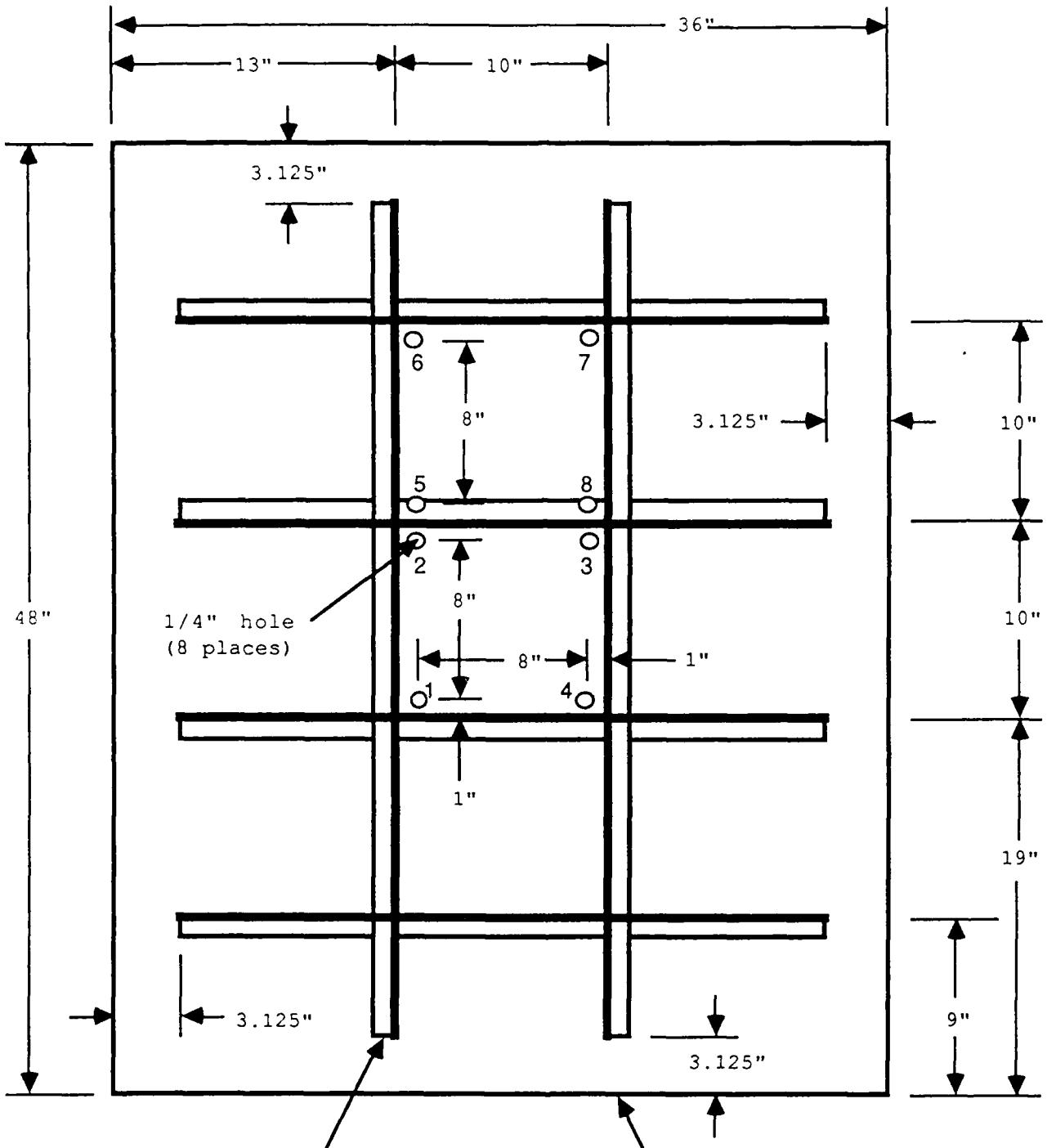

Construction: flush 1/8" rivets on 1" centers, except for welds on angle junctions.

FIGURE 56. PAYLOAD MOUNTING PANEL DESIGN FOR ACOUSTIC TESTS.

It is seen from Figure 56 that the panel has two sets of payload attachment points that allow two different payload positions on the panel, as follows:

Payload Position 1 - Locations 1 through 4 in the center of the panel, referred to hereafter as the middle bay position.

Payload Position 2 - Locations 5 through 8 in the first bay above the center bay, referred to hereafter as the upper bay position.

The considerations involved in the design of the payload for the acoustic tests were:

(a) The payload should have several normal modes (at least three) with high modal mass.

(b) The first normal mode frequency of the payload should be near the first normal mode frequency of the unloaded panel, to assure a strong influence of the payload on the panel response.

(c) The highest significant normal mode of the payload should be below 500 Hz, because of the difficulties associated with shaker tests above this frequency.

(d) The payload should be sufficiently small in size and weight to facilitate easy handling.

With the above considerations in mind, the payload shown in Figure 57 was designed and fabricated. The payload consisted essentially of a rigid frame with three resonant elements, each formed by a 1/4"-thick beam with fixed ends and masses (two steel blocks) mounted midspan. One block was mounted above the beam and the other below. The total weight of the blocks on the three beams were 9 lb, 3 lb, and 1.3 lb; the total weight of the simulated payload was 21.5 lbs.

For the acoustic tests, the payload resonant elements were positioned to provide the following two payload configurations:

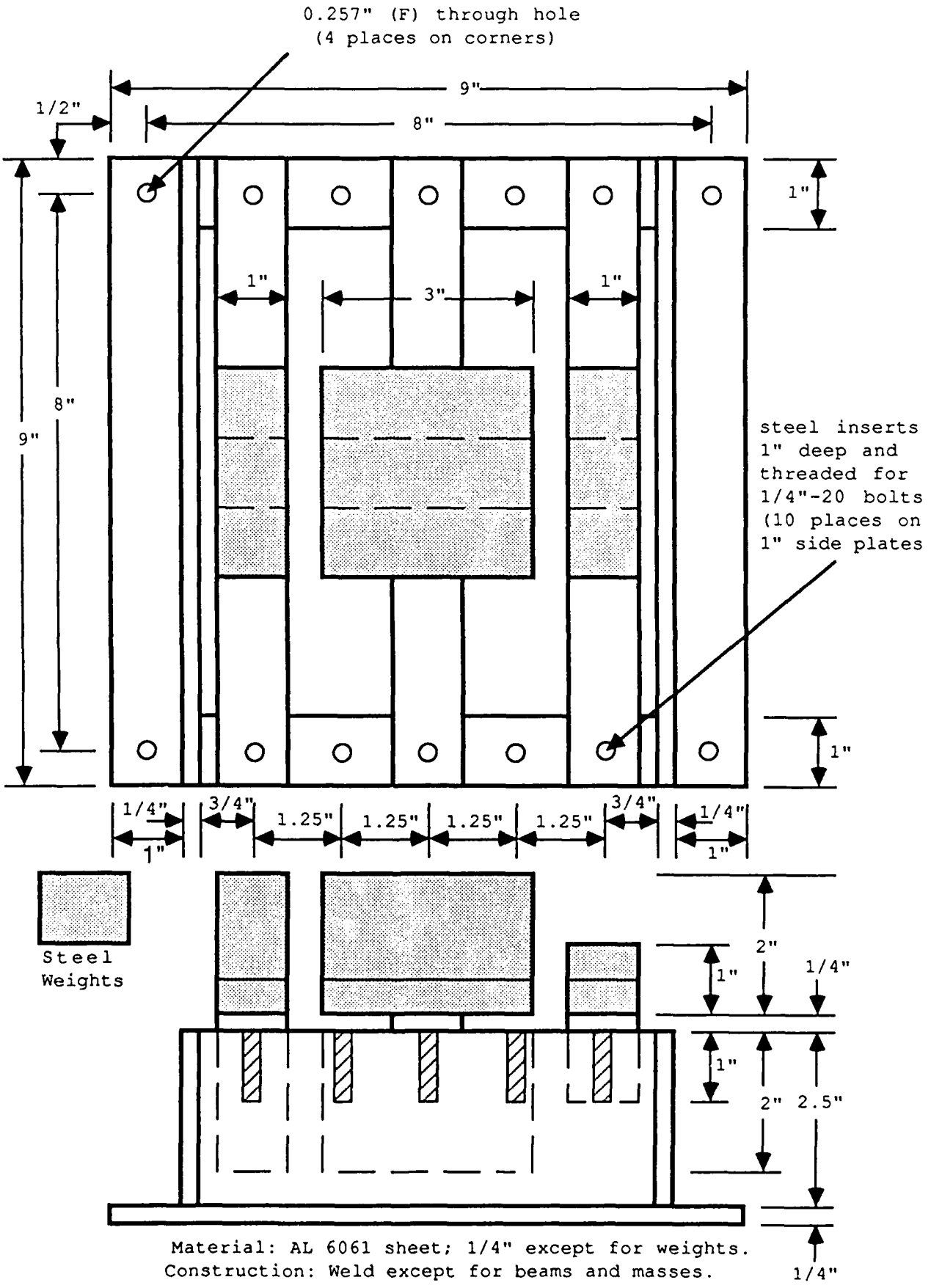

FIGURE 57(a). PAYLOAD DESIGN FOR ACOUSTIC AND VIBRATION TESTS (CONFIGURATION 1).

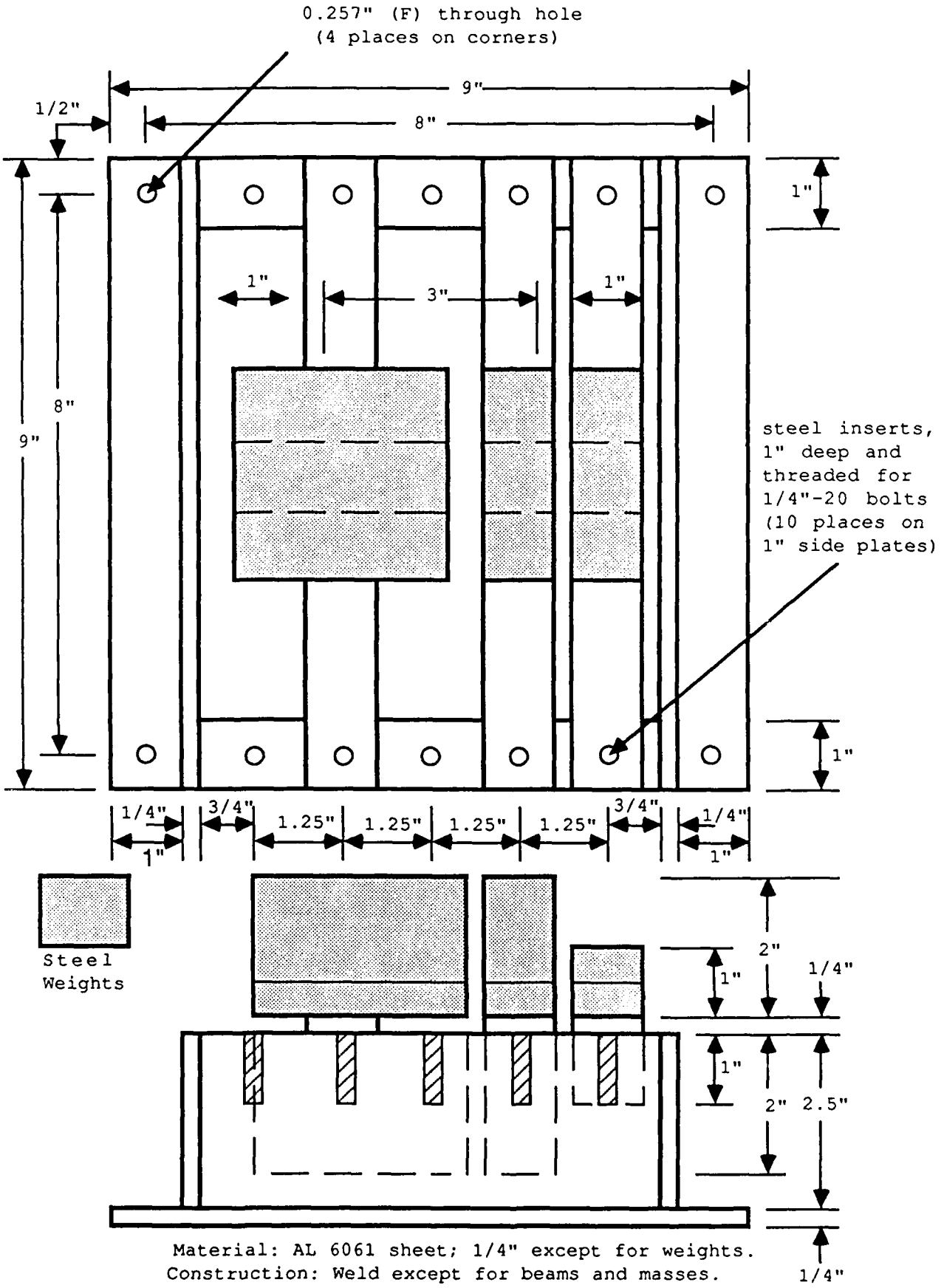

FIGURE 57(b). PAYLOAD DESIGN FOR ACOUSTIC AND VIBRATION TESTS (CONFIGURATION 2).

Payload Configuration 1 - The heaviest weight was mounted on the center beam, as shown in Figure 57a.

Payload Configuration 2 - The positions of the two weights on the left side of the payload were switched, as shown in Figure 57b.

6.2 Test Facility and Configurations

The acoustic tests were performed at the NASA Johnson Space Center (JSC) in Houston, TX, using the JSC Sonic Fatigue Laboratory reverberation chamber. This chamber is about 40 ft x 16 ft x 19 ft, giving a total volume of approximately 12,000 ft^3. The test panel was installed in a 3 ft x 4 ft window in the side of the reverberation chamber about half way between the floor and the ceiling. The chamber window faces into a receiving room, and has a 3-inch flange around the perimeter with 18 bolt holes to attach test items. The test panel was firmly bolted into this window with the ribbed side facing into the receiving room (the opposite side facing into the reverberation chamber), as shown in Figure 58. The simulated payload was attached to the ribbed side of the panel, as shown for Payload configuration 1 in Position 2 (upper bay location) in Figure 58a. The opposite side of the panel was essentially flush with the inside wall of the reverberation chamber, as shown in Figure 58b.

The acoustic tests were performed with four separate panel-payload test configurations:

Test Configuration 0 - Bare panel with no payload.
Test Configuration 1 - Payload configuration 1 (heaviest weight in the middle) attached to the panel in Position 1 (middle bay).
Test Configuration 2 - Payload configuration 1 (heaviest weight in the middle) attached to the panel in Position 2 (upper bay).
Test Configuration 3 - Payload configuration 2 (heaviest weight on one side) attached to the panel in Position 1 (middle bay).

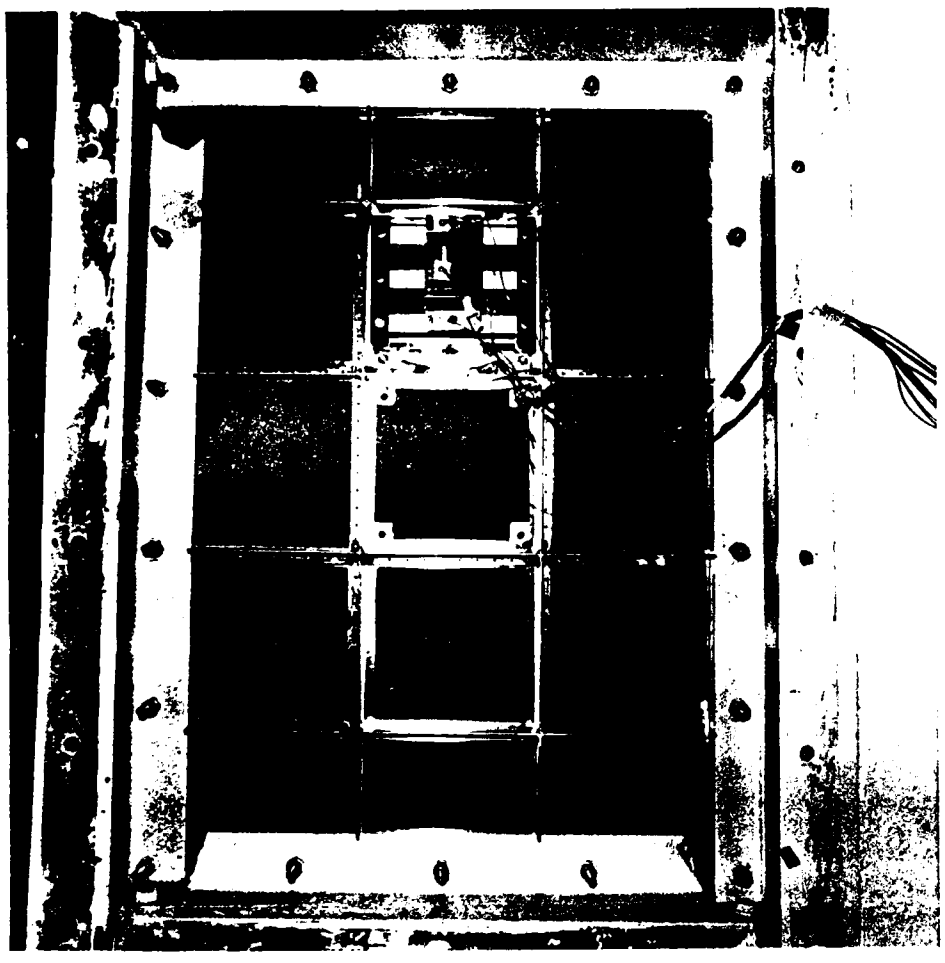

(a) View from receiving room outside reverberation chamber

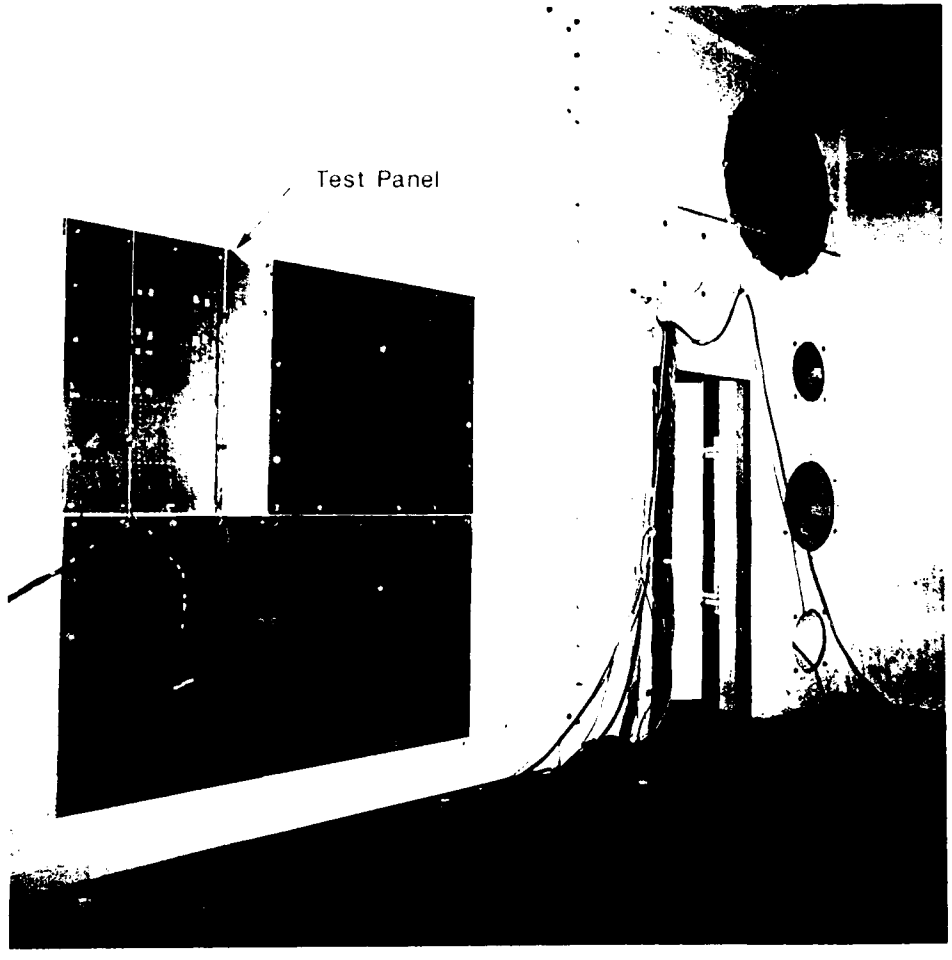

(b) View from inside reverberation chamber

FIGURE 58. TEST PANEL INSTALLATION IN JSC REVERBERATION CHAMBER

6.3 Panel Inertance Measurements

Before the acoustic tests, the mechanical inertance (acceleration/force) of the test panel, as installed in the reverberation chamber window, was measured at all eight payload mounting points. Data were acquired to measure both the self- and cross-inertances for each set of four payload mounting points shown in Figure 56. However, only the self-inertance data were analyzed. The inertance measurements were made using a Wilcoxon Research F-4 Driver with a piezoelectric force transducer (229 pF/lb), and four Endevco Model 2220 accelerometers with Endevco Model 2713 charge amplifiers. The accelerometers were calibrated prior to the inertance measurements using a GenRad Model 1557A acceleration calibrator. All data were recorded on a TEAC Model XR-510, 14 channel FM tape recorder. The measurement procedure was as follows:

1. The Wilcoxon driver was attached to the bare test panel at Location 1 for payload Position 1.
2. Four accelerometers were attached to the bare test panel at each of the four payload mounting points for payload Position 1 (locations 1 through 4 in Figure 56).
3. Broadband random excitation was applied from the Wilcoxon driver over the frequency range from 20 to 1000 Hz, and the output signals from the four accelerometers, as well as the driver force signal, were recorded for about 3 minutes.
4. Steps 1 through 3 were repeated with the Wilcoxon driver attached to each of the remaining payload mounting points for payload Position 1 (locations 2 through 4 in Figure 56).
5. Steps 1 through 4 were repeated with the Wilcoxon driver and the accelerometers attached at the payload mounting points for payload Position 2 (upper bay locations 5 through 8 in Figure 56).

The self-inertance functions were computed by calculating the frequency response function between the force and acceleration measured at each of the four mounting points for each of the two payload locations on the panel. To assess the accuracy and linearity of the inertance measurements, the coherence function for each inertance measurement was also calculated. These frequency response and coherence functions were computed using a Hewlett-Packard Model

3562A signal analyzer over the frequency range from 10 to 800 Hz with a frequency resolution of B=1 Hz and nd=10 statistically independent averages.

After the acoustic tests, the self-inertance measurements were repeated at the payload mounting points for payload Position 1 only. This was done to confirm that the test panel inertance had not changed during the acoustic tests due to panel damage or other factors.

The results of the self-inertance calculations are presented in Appendix C, Figures C-1 through C-7. Referring first to the coherence data in Figures C-1 through C-3, it is seen that the coherence values between the force and acceleration for the inertance measurements are generally near unity for frequencies above 30 Hz (except for a few notches at the frequencies of panel resonances, and at multiples of 60 Hz which are particularly strong in the upper bay data). Below 30 Hz, the coherence values fall rapidly to near zero below 10 Hz. This is due to the fact that the Wilcoxon driver could not deliver a sufficient force at these low frequencies to provide measurements with an acceptable signal-to-noise ratio. It follows that the inertance data can be considered reliable at frequencies above 30 Hz.

Now referring to the individual inertance measurements in Figure C-4 through C-6, it is seen that the inertance magnitude and phase for the four mounting points in the middle bay of the panel (Figures C-4 and C-5) are similar at frequencies between 30 and 100 Hz. Above 100 Hz, there are some differences, suggesting the panel, as installed in the reverberation chamber window, was not totally symmetric. However, the differences are not sufficient to warrant concern. The individual inertance values for the four mounting points in the upper bay (Figure C-6) show somewhat more variation from point to point, as would be expected since the upper bay locations are asymmetric about the horizontal axis. Also shown in Figures C-4 through C-6 are the net inertance values for each payload mounting location, computed from

$$I_n(f) = [\ 1/I_1(f) + 1/I_2(f) + 1/I_3(f) + 1/I_4(f)\ ]^{-1} \qquad (48)$$

where $I_n(f)$ is the net inertance and $I_i(f)$; i=1,2,3,4, are the measured inertances at the four payload mounting points. Eq. 48 assumes the inertances are in parallel and independent, as discussed in Section 7.4.

Finally, referring to the net inertance function in Figure C-7 for the middle bay, it is seen that the inertance magnitude values measured before and after the acoustic tests are nearly identical. The phase values are also similar up to about 400 Hz. These results confirm that there was no major change in the dynamic properties of the test panel during the course of the acoustic tests. Hence, the results of the pre- and post-test inertance measurements in the middle bay are averaged for later applications.

In summary, the results of the bare panel inertance measurements are as shown in Figure 59. There are some differences in the inertance values between the middle and upper bay payload locations, but the data at both locations behave as would be expected. Specifically, below the first normal mode of the panel at 74 Hz, the inertance magnitude increases at 10 dB/octave, and the phase is 180 degrees, exactly as should occur for the source inertance of a stiffness-controlled structure [9]. The magnitude data then reveal a peak, and the phase data make a 180 degree change, at the first normal mode of the panel at 74 Hz. At the higher frequencies where the modal density of the panel is high, the average phase approaches 90 degrees, as would be expected for a damping-controlled structural response.

6.4 Acoustic Test Levels

The acoustic tests were performed at two levels, about 135 dB and 147 dB. The 1/3 octave band spectrum, relative to the overall, for the tests at the two levels, is given in Table 12. The lower test level was dictated by the lowest level at which the JSC Sonic Fatigue Laboratory reverberation chamber could be operated with acceptable control over the air modulators providing the acoustic source. The upper level was believed to be as high as could be safely tolerated by the test panel and simulated payload. The 1/3 octave band spectrum in Table 12 was selected to approximate the spectrum of the acoustic noise measured on the exterior of the payload bay doors of the Space Shuttle orbiter vehicle during lift-off [16].

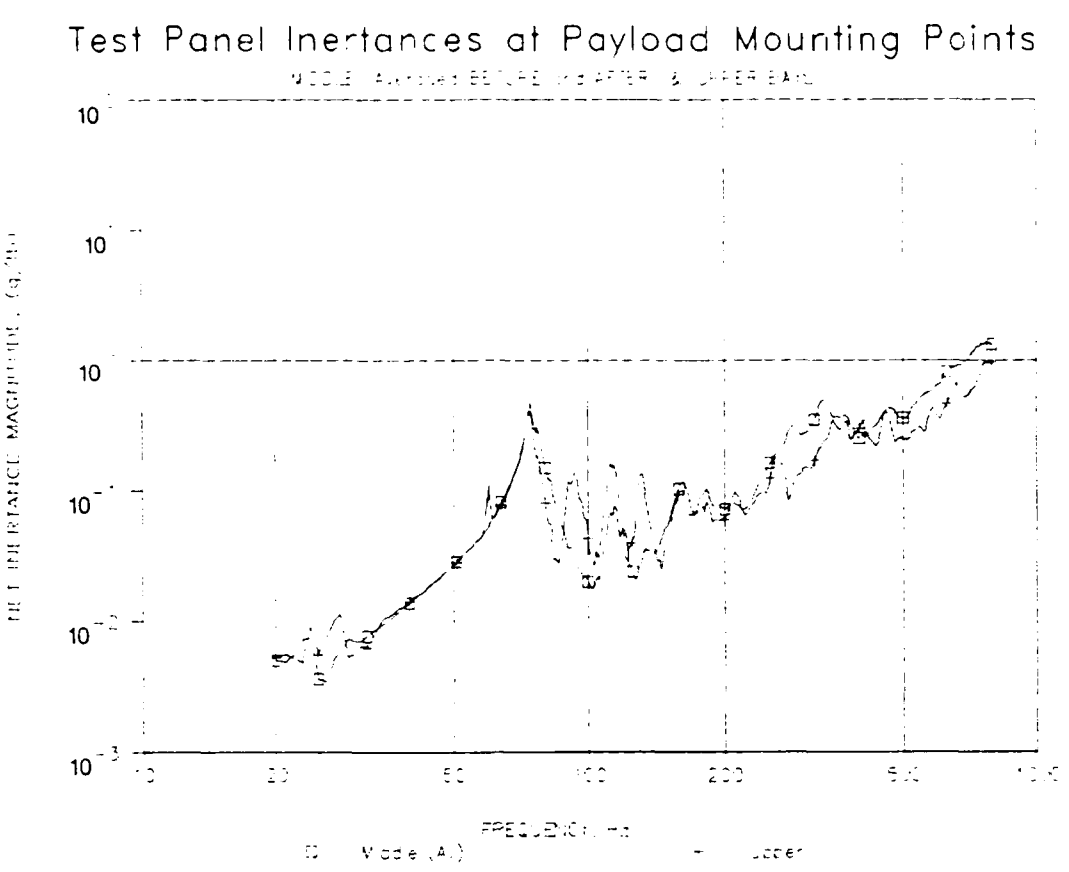

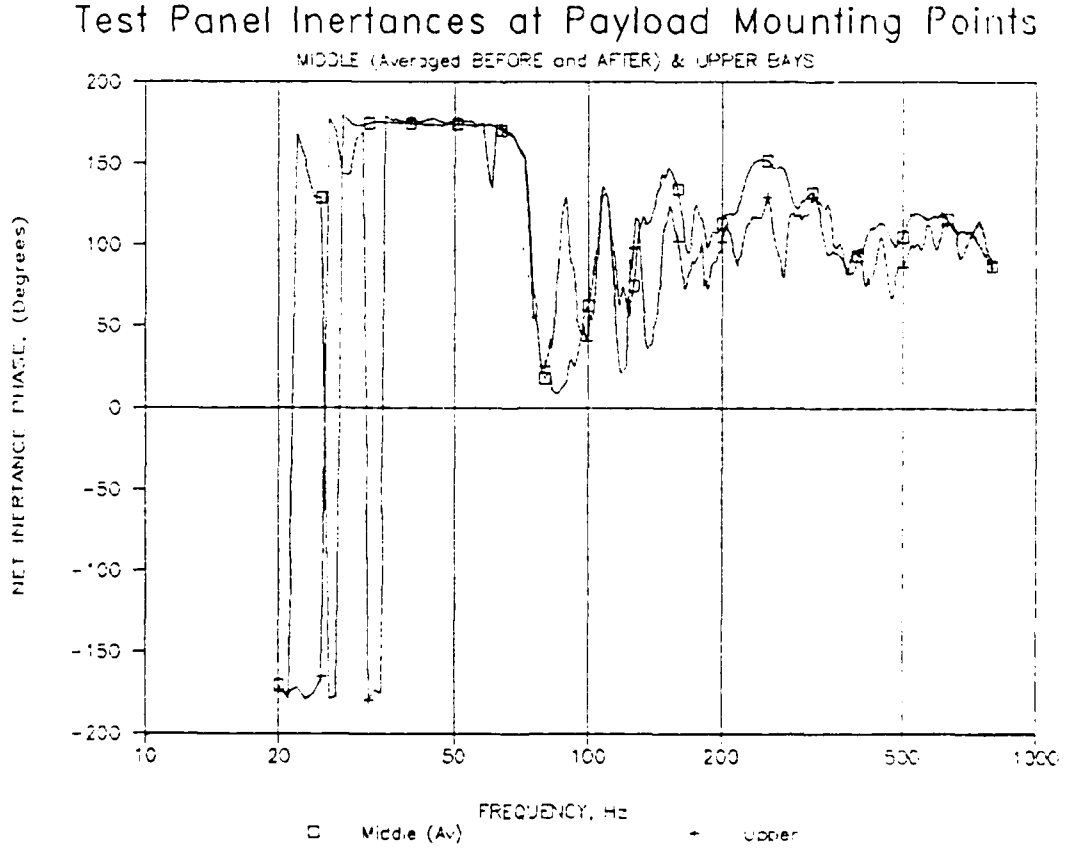

FIGURE 59. SUMMARY OF INERTANCE MEASUREMENTS AT PAYLOAD MOUNTING LOCATIONS. ACOUSTIC PANEL.

Table 12. 1/3 Octave Band Spectrum for Acoustic Tests

Center Frequency (Hz)	SPL re:OA (dB)	Center Frequency (Hz)	SPL re:OA (dB)	Center Frequency (Hz)	SPL re:OA (dB)
31.5	-15	100	-11	315	-11
40	-13	125	-10	400	-12
50	-12	160	-10	500	-12
63	-12	200	-10	630	-13
80	-12	250	-11	800	-14

A total of eight acoustic tests were performed, one for each of the four test configurations defined in Section 6.2, at each of the two test levels. For each acoustic test, the sound pressure levels inside the reverberation chamber were measured with four Gulton Model 10010052 microphones mounted about 2 inches from the test panel at the middle of each panel quadrant, as shown in Figure 58b. A fifth microphone was mounted in the receiving room to monitor the difference in the sound pressure levels across the test panel. The test sequence and the average of the four overall sound pressure level measurements inside the reverberation chamber are summarized in Table 13. The overall sound pressure levels measured in the receiving room were generally about 17 dB lower than in the reverberation chamber. The autospectra of the sound pressure levels measured by all microphones for the low and high level tests

Table 13. Test Sequence and Average Overall Sound Pressure Level

Test No.	Acoustic Level	Test Configuration (see Section 6.2)	Overall Sound Pressure Level, dB
1	Low	0 - Bare panel	134.3
2	Low	1 - Payload 1 in Position 1	135.9
3	Low	2 - Payload 1 in Position 2	133.9
4	Low	3 - Payload 2 in Position 1	134.2
5	High	3 - Payload 2 in Position 1	146.7
6	High	1 - Payload 1 in Position 1	146.7
7	High	2 - Payload 1 in Position 2	146.7
8	High	0 - Bare panel	146.7

are detailed in Appendix C, Figures C-8 through C-11. These spectra were computed with a frequency resolution of B=1 Hz and n_d=100 statistically independent averages. The measurements shown in Figures C-8 through C-11 were made during the low and high level tests of Configuration 0 (the bare panel test), but are typical of the measurements for all other test configurations.

Referring back to Table 13, it is seen that the overall sound pressure levels for the high level tests were reproduced for each test configuration with remarkable accuracy (to within 0.1 dB). For the low level tests, however, the overall levels varied by up to 2 dB from one test configuration to another, due to the difficulty in controlling such levels in the JSC facility. Hence, all the autospectra for the acoustic levels measured during the low level tests, and the spectra of the resulting vibration levels measured on the test panel and simulated payload, were linearly scaled to a common overall value of 134.7 dB for the low level tests (exactly 12 dB lower than the high level tests).

6.5 Vibration Measurements

For the acoustic test of the bare panel (Test Configuration 0), vibration levels were measured on the test panel at the eight payload attachment points shown in Figure 56. The measurements were made using Endevco Model 2222 accelerometers with Kistler Model 508 charge amplifiers, supplied by JSC. For the acoustic tests of the three panel-payload configurations (Test Configurations 1 through 3), vibration levels were measured on the payload at each of the four attachment points to the panel, and on each of the three weights forming the resonant elements of the payload, as detailed in Table 14. The measurements were made using Endevco Model 2220 accelerometers, supplied by Astron, with Kistler Model 508 charge amplifiers, supplied by JSC. All accelerometers were calibrated prior to the acoustic tests using a GenRad Model 1557A accelerometer calibrator. All data were recorded on a TEAC Model XR-510 14 channel FM tape recorder.

Table 14. Payload Accelerometer Locations for Acoustic Tests

Designation	Locations on Payload (see Figure 57)
1	On base at lower left mounting point
2	On base at upper left mounting point
3	On base at upper right mounting point
4	On base at lower right mounting point
5	On 3 lb resonant weight
6	On 9 lb resonant weight
7	On 1.3 lb resonant weight

The vibration data measured during each of the eight acoustic tests identified in Section 6.4 were reduced to autospectra using a Hewlett-Packard Model 3562A signal analyzer over the frequency range from 10 to 800 Hz with a frequency resolution of B=1 Hz and n_d=100 statistically independent averages. The overall values of the vibration levels measured at all locations during the eight tests are summarized in Table 15. Note that the vibration levels for the low level test have been scaled to a common acoustic input level of 134.7 dB, as discussed in Section 6.4.

It is seen from Table 15 that the panel and payload vibration levels do not increase linearly with the acoustic input level. Specifically, a 12 dB increase in the acoustic level (a factor of 4.0) caused an average increase in

Table 15. Overall Panel and Payload Vibration Levels

Panel or (Payload) Location	Overall Vibration Level, grms (db)							
	Config 0		Config 1		Config 2		Config 3	
	134.7	146.7	134.7	146.7	134.7	146.7	134.7	146.7
1 (1)	5.5	15.4	3.0	7.9	2.8	7.8	2.7	6.7
2 (2)	5.4	14.7	3.0	7.6	3.1	9.2	3.2	8.8
3 (3)	5.2	13.9	3.0	7.3	3.1	8.9	3.1	7.8
4 (4)	5.0	13.8	3.0	8.1	2.7	7.5	2.8	7.1
5 (5)	5.5	14.9	5.7	15.6	5.0	16.5	6.1	16.7
6 (6)	5.1	14.2	3.4	8.8	3.2	8.2	3.4	8.2
7 (7)	4.8	13.4	4.9	13.3	4.6	14.1	4.9	12.6
8 ---	5.0	13.8	---	---	---	---	---	---

the panel and payload vibration levels of only 8.6 dB (a factor of 2.7). From Figures C-12 and C-20, it is seen that the resonance frequency of the panel goes down slightly with the increased excitation level. This nonlinearity in the panel response is believed to be due to the Soundcoat damping material applied to the panel, as described in Section 6.1. This nonlinearity is significant in that the panel inertance measurements in Section 6.2 were made with lower vibration levels than those which occurred during the acoustic tests. Hence, the inertance measurements may not be accurately representative of the actual panel inertance function at the acoustic-induced panel vibration levels.

Again referring to Table 15, although the panel response is nonlinear, the response of the payload elements relative to the base vibration is quite linear. This is illustrated in Table 16, which shows the ratio of the overall vibration level of each payload element relative to the average base vibration for all three test configurations, at both acoustic test levels. Note that the ratios are essentially the same for the low and high level tests.

The autospectra of all panel and payload vibration data measured during the acoustic tests are given in Appendix C, Figures C-12 through C-27. The average autospectra of the measurements at the middle bay mounting points, with and without the payload present for the low level test, are reproduced in Figure 60. It is clear from these results that the attachment of the payload

Table 16. Ratio of Payload Element to Base Vibration Levels

Test Level	Element	Element/Average Base Vibration Level			
		Config 1	Config 2	Config 3	Average
Low Level (134.7 dB)	5	1.9	1.7	2.1	1.9
	6	1.2	1.1	1.2	1.2
	7	1.6	1.6	1.7	1.6
High Level (146.7 dB)	5	2.0	2.0	2.2	2.1
	6	1.1	1.0	1.1	1.1
	7	1.7	1.7	1.6	1.7

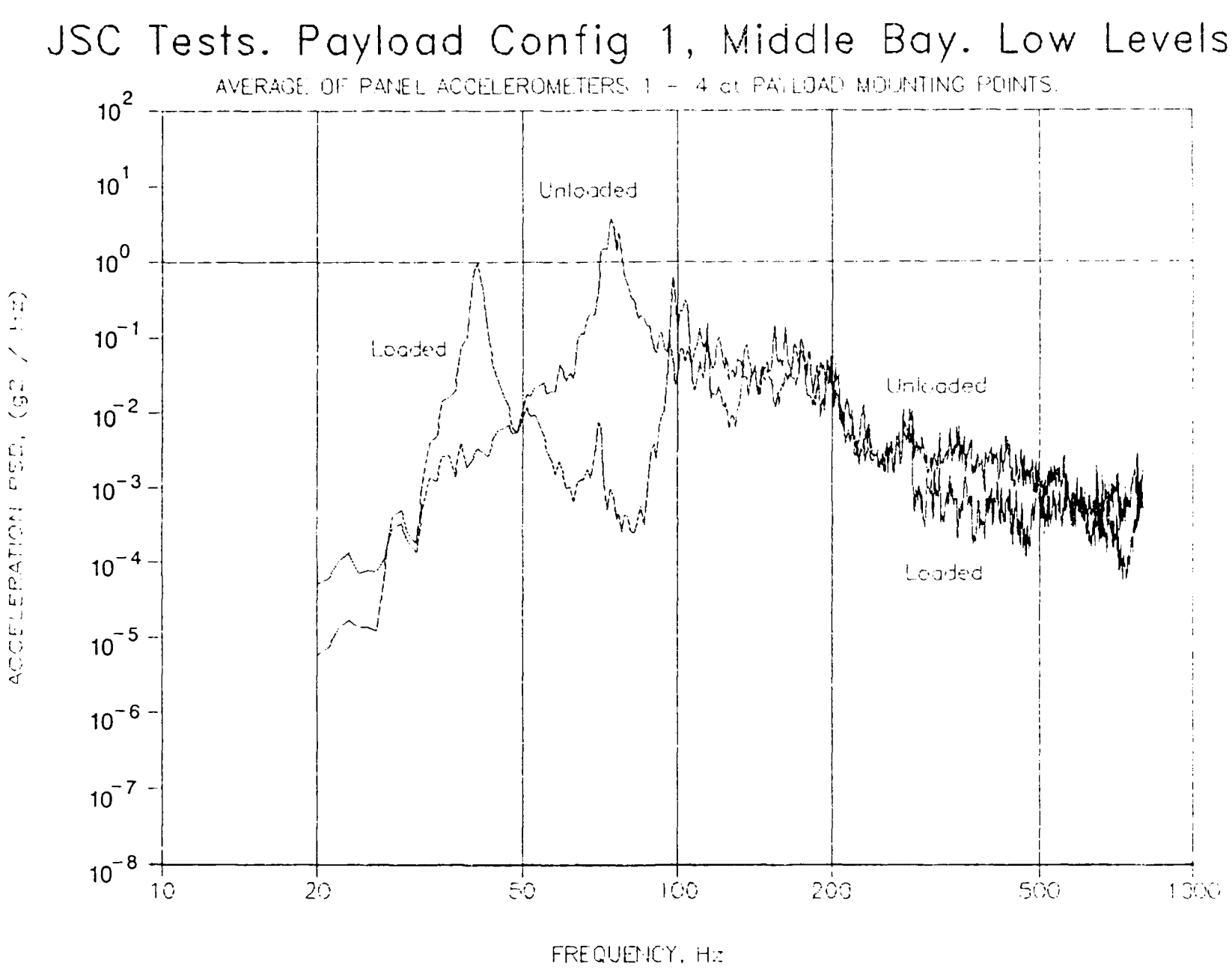

FIGURE 60. VIBRATION RESPONSE OF ACOUSTIC TEST PANEL AT PAYLOAD MOUNTING POINTS WITH AND WITHOUT PAYLOAD ATTACHED.

to the panel dramatically impacts the panel vibration levels. Specifically, the first normal mode of the panel at 74 Hz, shifts down to a coupled normal mode with the payload at 40 Hz. Also, the vibration levels are sharply reduced at the resonance frequency of the heaviest payload element, which occurs at about 88 Hz. These results are typical of all three test configurations for both test levels.

As a final point of interest, the gain factor (frequency response function magnitude) for each resonant element of the payload, relative to the payload base, was computed for all test configurations at both test levels using

$$|H(f)| = [G_{ii}(f)/G_{xx}(f)]^{1/2} \; ; \; i = 1,2,3 \qquad (49)$$

where $G_{ii}(f)$ is the autospectrum of the vibration measurement on the ith resonant element, and $G_{xx}(f)$ is the average autospectrum of the base vibration measurements. The results for Test Configuration 1 with the low acoustic input levels are shown in Figure 61. These results are typical of all test configurations at both test levels. The gain factors appear much like single degree-of-freedom systems, as would be expected for the resonant elements. Although the effects of secondary modes are clearly present, the results reveal dominant modes of vibration at about 140 Hz for the 3 lb element (measurement 5), 88 Hz for the 9 lb element (measurement 6), and 210 Hz for the 1.3 lb element (measurement 7). In all cases, the peak gain factor is about 10, corresponding to a damping ratio of about 5%.

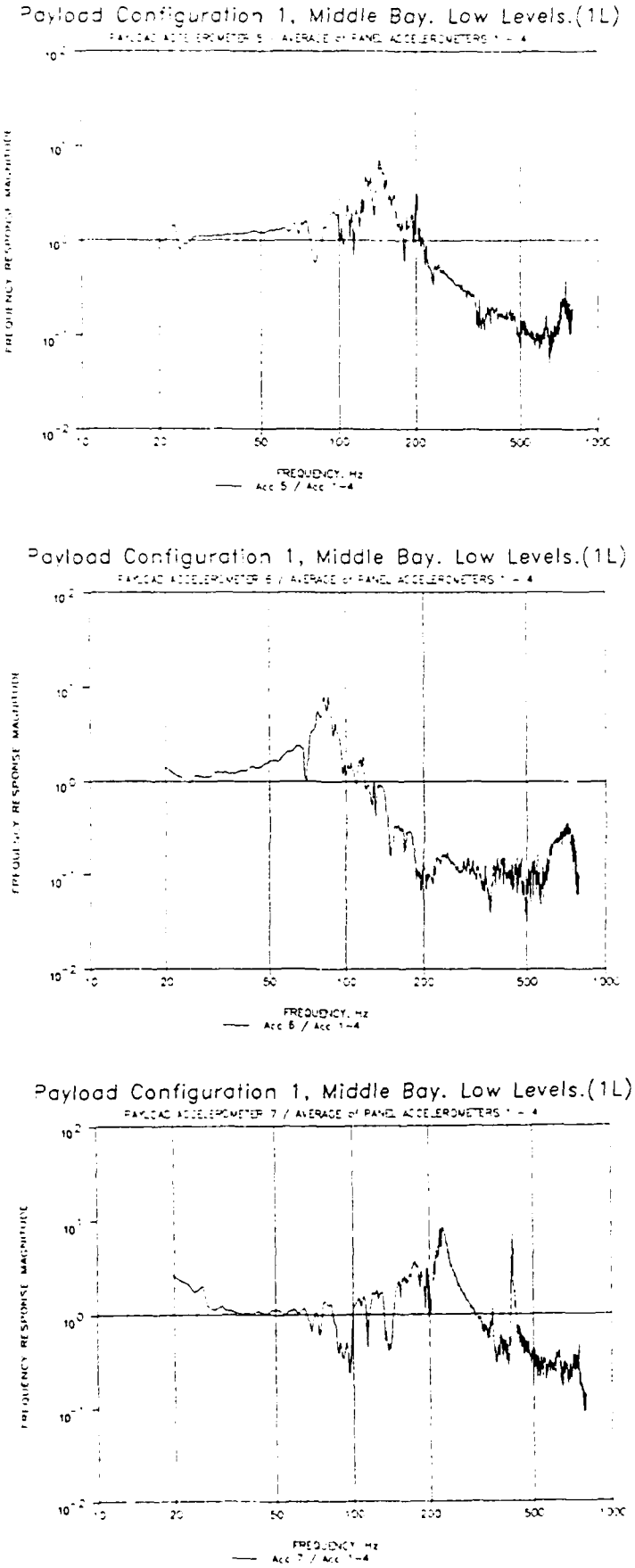

FIGURE 61. GAIN FACTOR FOR PAYLOAD RESONANT ELEMENTS.

7. SIMULATED PAYLOAD VIBRATION TESTS

7.1. Introduction

Two vibration experiments were performed on the simulated payload used in the JSC tests. The three objectives of the tests were:

A. To estimate the payload mounting point inertance,
B. To determine the relationship between shaker current and force,
C. To provide confirming data for vibration test procedures.

First, an electro-mechanical shaker was used to measure the self- and cross-inertances at each of the four mounting points of an unconstrained payload in the laboratory at Astron. Then, the relation between excitation current and shaker force for the MB C-60 shaker at the National Technical Services (NTS) facility in Los Angeles was determined. From this relation it was possible to determine the total inertance, or ratio of payload base acceleration to shaker table applied force. In these latter tests, the base of the payload was rigidly attached to the shaker table surface and constrained to move uniformly. The significance of these two measures of inertance, and the relation between them, is discussed in Section 7.4. Results of the tests show consistent and physically rational behavior. Test procedures, data analysis methods, and interpretation of results are given below.

7.2. Mounting Point Inertance Measurements

The inertance at each corner mounting point of the simulated payload was determined by applying a known force at the point, and measuring the vibration response at the point. Additionally, from simultaneous measurements of the motion of the other three corners and the individual masses, it was possible to estimate the cross inertance factors. The test configuration is shown in Figure 62 and associated instrumentation is described in Table 17.

The payload was suspended vertically on elastic cords attached to two mounting points, and the shaker attached to one of the lower mounting points. A broad band random force with flat spectrum from 10 to 800 Hz was applied to the

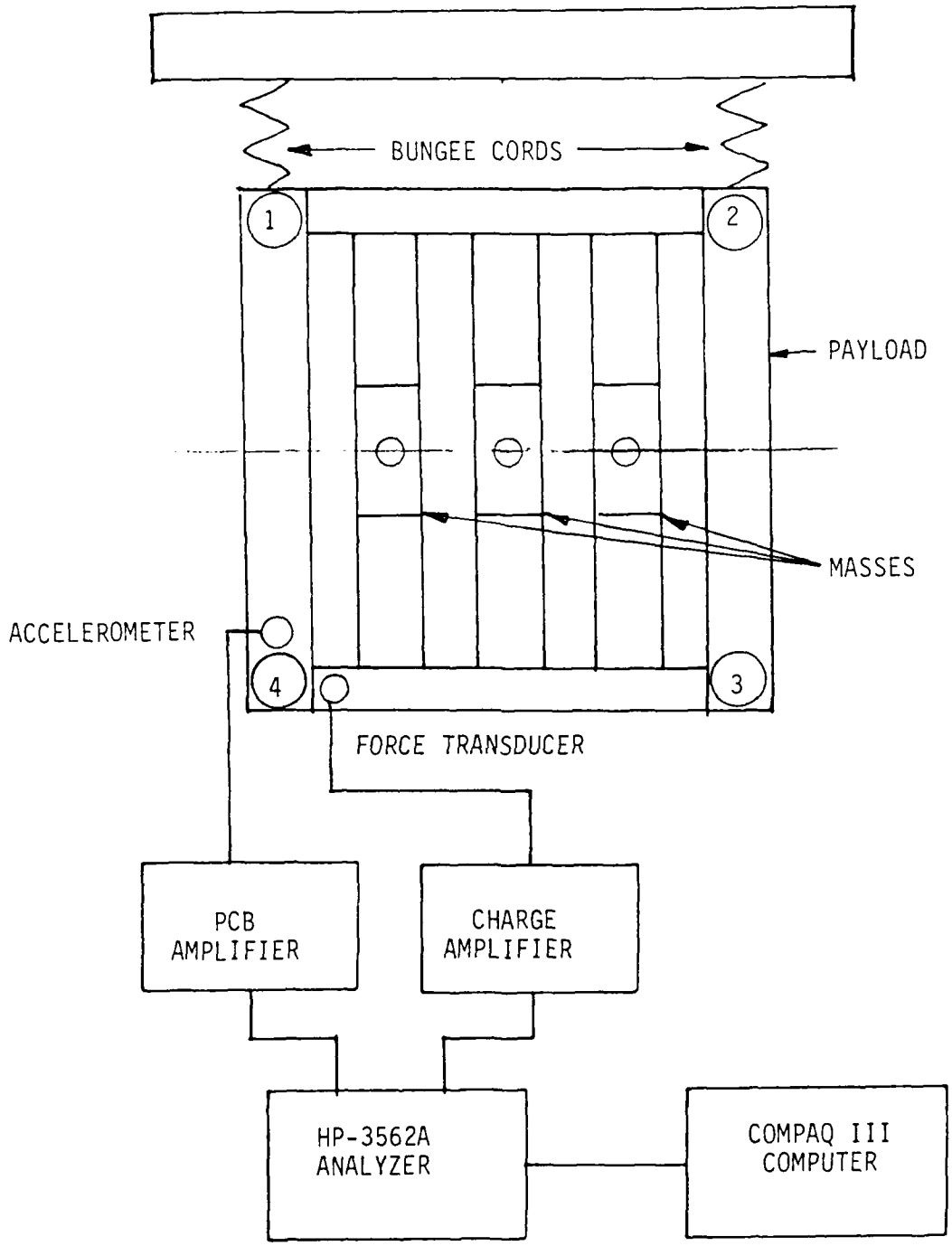

FIGURE 62. PAYLOAD MOUNTING POINT INERTANCE TEST

Table 17. Inertance Measurement Instrumentation

SHAKER: Wilcoxon F7/F4, Piezoelectric/Electromagnetic
FORCE GAGE: Wilcoxon L7
CHARGE AMPLIFIER: Endevco 2713
ACCELEROMETER: PCB 303A03, 2.3 gm., with 480B power supply
ANALYZER: Hewlett-Packard 3562A dynamic signal analyzer, 800 line FFT

mounting point, and acceleration response measurements made at each of the four corner mounting points. Each measurement set consisted of the force spectrum, acceleration spectrum, frequency response function $[G_{FA}(f)/G_{FF}(f)]$, and coherence function. In the analysis, 100 one-second-length records were used with a Hanning window of 1.5 Hz bandwidth to estimate the spectral functions at 1 Hz increments. These functions were transferred to a Compaq III computer via an IEEE-488 link for storage on a 1.2 MB floppy disk for later analysis, manipulation, and plotting.

As noted earlier in Section 6, two payload configurations were tested at JSC. The mounting point inertances of both of these configurations were measured at Astron. The total payload weight, and natural frequencies of the attached mechanical oscillators (weight/beam combination) was the same for both configurations, but the location of the oscillator attachments was different, as shown in Figure 63. This difference is reflected by a change in the individual mounting point inertances. All terms of the 4 X 4 inertance matrix associated with translational motion in the direction of the applied force have been calculated and stored on floppy disk, but only the diagonal or self-inertances are presented in this report.

Figures 64 and 65 show the measured self-inertances of the two payload configurations. It is noted immediately that there is a similarity between the inertances at locations 1 and 4, and between the inertances at locations 2 and 3. This is not surprising, for there is an axis of symmetry with both configurations and locations 1 and 2 are mirror images of locations 4 and 3, respectively. There are, in addition, obvious differences between the inertances of payload 1 and payload 2.

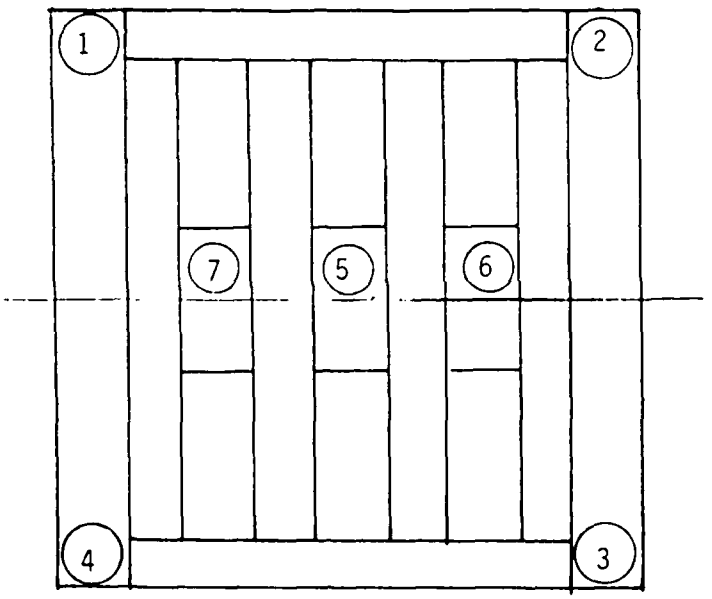

W_5=3 lbs
W_6=9 lbs
W_7=1.3 lbs

PAYLOAD CONFIGURATION 2

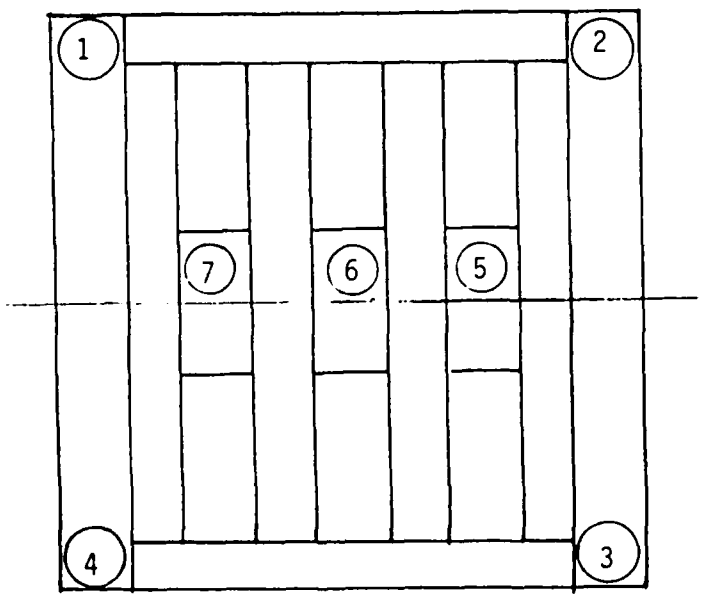

f_5=135 Hz
f_6=88 Hz
f_7=213 Hz

PAYLOAD CONFIGURATION 1

FIGURE 63. TEST PAYLOAD CONFIGURATIONS

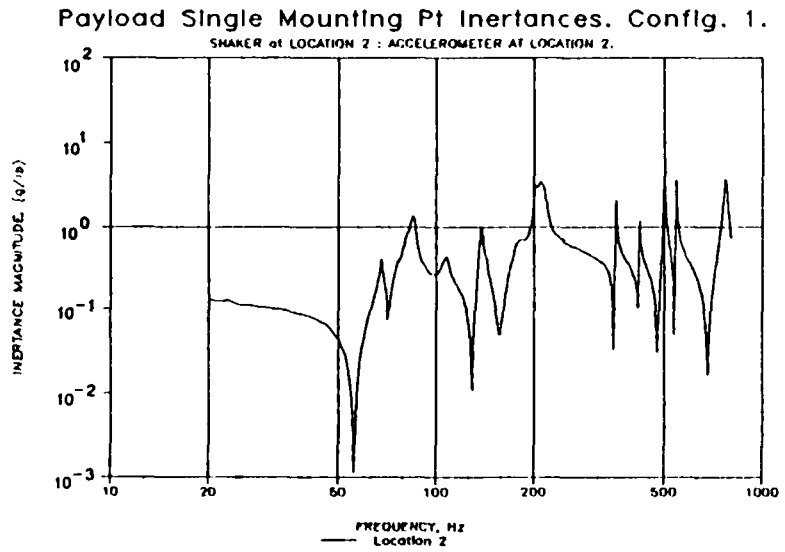

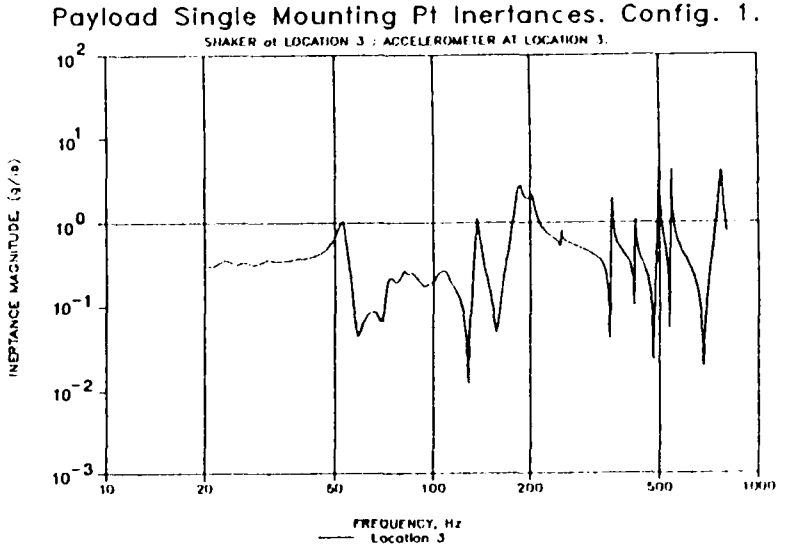

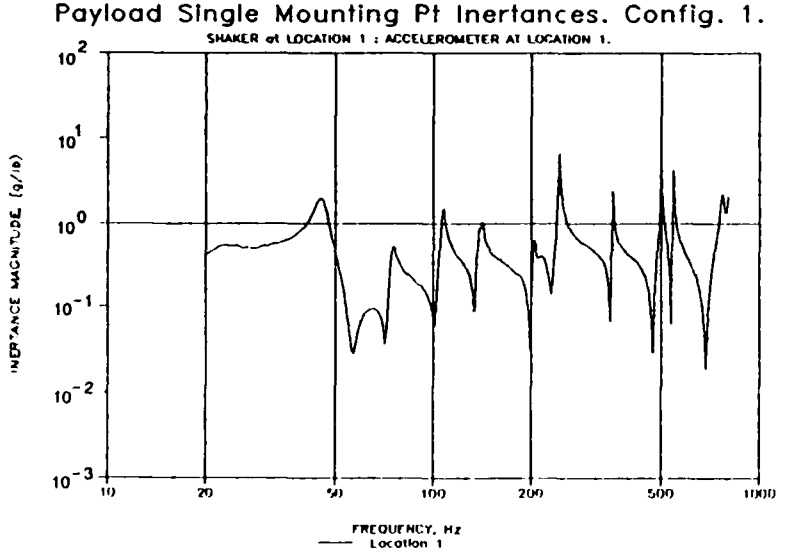

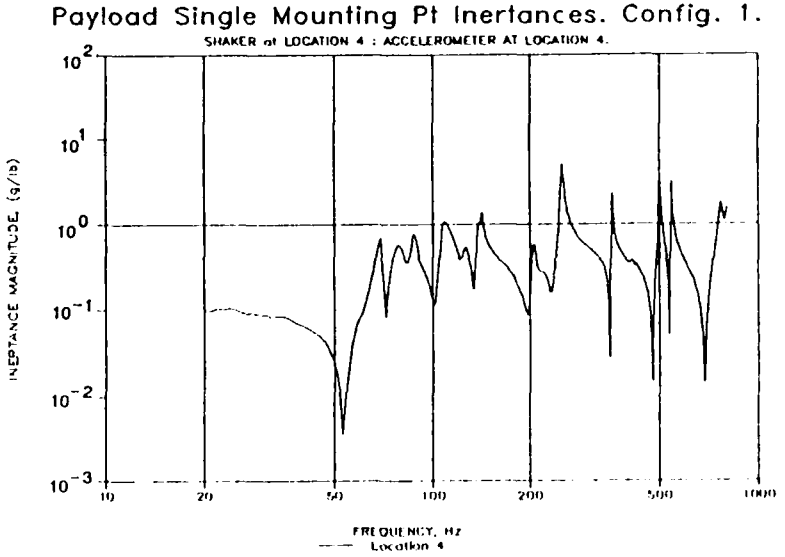

FIGURE 64. INERTANCE OF PAYLOAD MOUNTING POINTS, CONFIGURATION 1

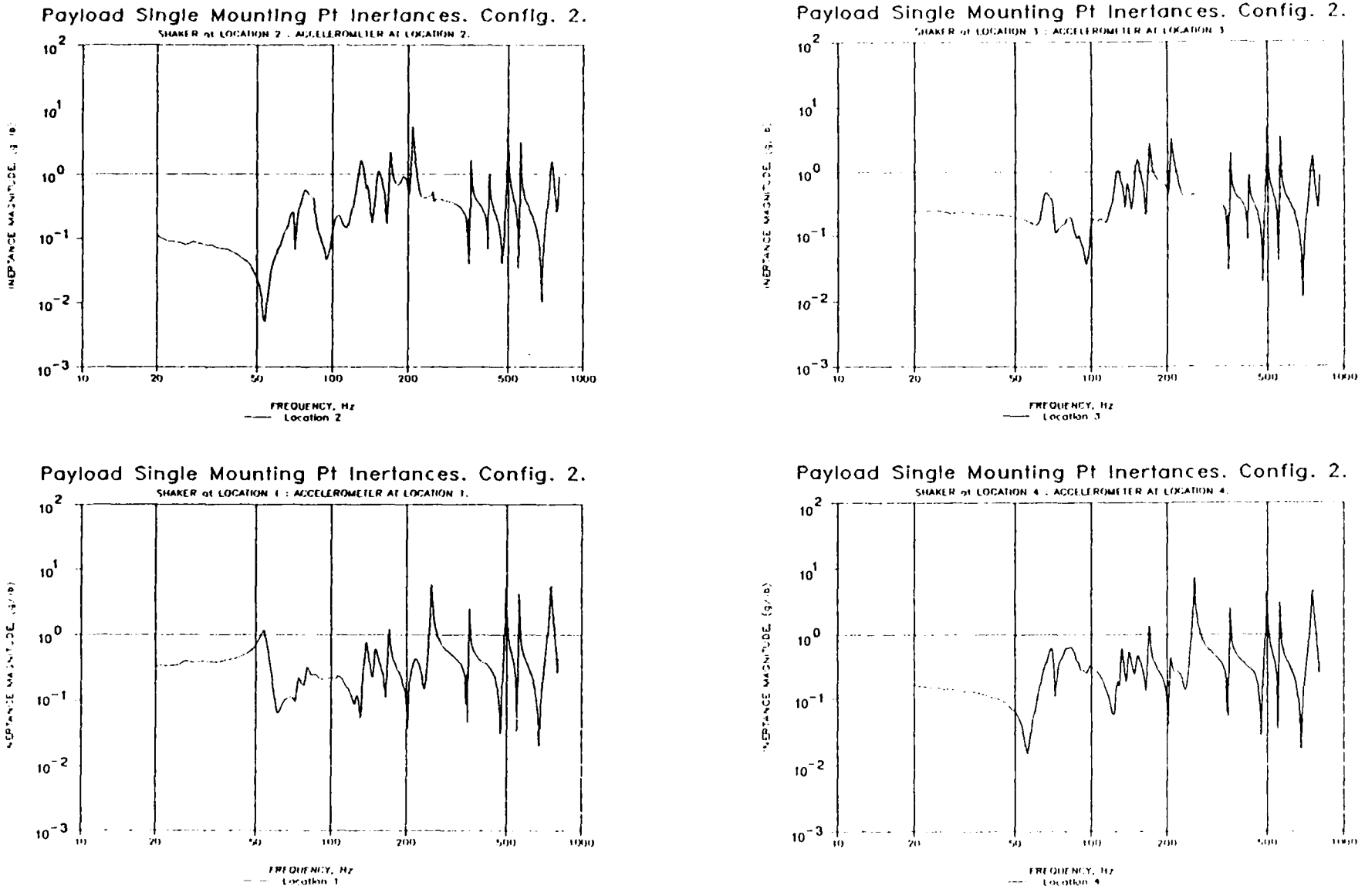

FIGURE 65. INERTANCE OF PAYLOAD MOUNTING POINTS, CONFIGURATION 2

The original simulated payload design was conceived to have three mechanical oscillators with three distinct natural frequencies. By its construction however, not only were the three original beam bending modes present, but other modes due to torsional and rocking vibration of the beam/masses were also excited by the eccentric excitation of a force at a single mounting point. The modal behavior of the payload masses is demonstrated in Figures 64 and 65. Dips or notches in the inertance correspond to natural frequencies of beam/masses when attached to a rigid frame, and the maxima correspond to resonant frequencies of coupled modes. If the frame were completely rigid, and were driven with planar motion (all points on the base moving in phase at the same amplitude), then only three notches and peaks would be present in the inertance curves. In such a case the inertances for both configurations would also be identical.

To develop the inertance of the complete payload on the basis of mounting point data, it is necessary to combine the measurements properly. Such a procedure is described in Section 7.4. This process requires the inversion of complex matrices and was not performed in the current work phase. Limiting approximations demonstrate the validity of the data, but more accurate inertance measurements can be made with less effort by exciting the complete payload with a large shaker. This procedure and results are given in the following section.

7.3 NTS Vibration Tests

The simulated payload in configuration 1 (large mass in center) was tested on an MB Electronics, Model C-60 electromechanical shaker at NTS facilities in Los Angeles. This shaker will support a 200 pound test item, and deliver a maximum of 6000 pounds force to it. The test payload was attached flat on the shake table so that all mounting points moved uniformly in phase. The objectives of this testing program were as follows.

A. Determine relationship between shaker current and output force.
B. Determine relationship between payload base acceleration and oscillator mass acceleration.

C. Determine inertance of payload to uniform base motion.

7.3.1 Current-to-Force Determination

In an electromechanical shaker there is linear relationship between excitation current and the electromotive force in the induced field. The electromotive force acts to move the armature and fixture, as well as any test item attached to the fixture. Under the assumption that the armature and fixture are rigid in the frequency range of interest, the force applied to any test item is given by

$$F(f) = K(f)C(f) - W_T A(f) \tag{50}$$

where

$F(f)$ = Force applied to test item, pounds
$C(f)$ = Shaker current, amps
W_T = Weight of shaker armature and fixture, pounds
$A(f)$ = Acceleration of shaker table, g's
$K(f)$ = Scale function, pounds/amp

In the above description, the frequency-dependent force, current, and acceleration may be defined as deterministic functions of a steady state vibration, or as Fourier transforms of a finite time sample of length T. The frequency-dependent functions may be complex to account for phase shifts.

To determine the scale function, K(f), a broad band random noise current with flat spectrum from 40 to 1000 Hz was applied to the bare shaker (armature and fixture only, no test item), producing a table acceleration of approximately 2 g rms. A signal proportional to the drive current was taken from the main power amplifier, and was identified as c(t). An accelerometer mounted on the fixture provided the acceleration signal a(t). A Hewlett-Packard 3562A Dynamic Signal Analyzer was then used to generate the frequency response function between the acceleration and current,

$$H_{CA}(f) = G_{CA}(f)/G_{CC}(f). \tag{51}$$

The scale function K(f) is then found from the relation

$$K(f) = W_T H_{CA}^{*}(f) \tag{52}$$

It can be noted in passing that the cross spectra and transfer functions generated by the H-P 3562A are the complex conjugates of those defined in Reference 20. In this report the analysis and data presented are in the Hewlett-Packard notation. Using the measured values of armature and fixture weights of 41 and 22.5 pounds respectively, the scale function relating shaker output force and driving current was computed. It is presented in Figure 66. The linearity of the relationship was checked by computing the coherence between current and acceleration by the relation

$$\gamma^2(f) = |G_{CA}(f)|^2/[G_{CC}(f)G_{AA}(f)] \tag{53}$$

This function was found to be near unity for all frequencies, except at several power line harmonics, thus indicating good linearity.

The scale function K(f) shown in Figure 66 is a very smooth, nearly constant in value, with phase angle near 180 degrees. In later calculations its exact value has been used at all frequencies, but in many situations it may be acceptably approximated by a real constant with the average value of -64.9 pounds/amp. Note that the signal used in developing K(f) is not the true current in the shaker, but is only proportional to it. The scale factor resulting from this test is applicable only to the particular shaker and amplifier used. Any other shaker must be individually calibrated in order to take into account how the signal proportional to current is actually generated in the power amplifier.

7.3.2 Payload Mass to Base Acceleration Function

Payload configuration 1 was attached to the fixture plate at the center of the shaker. Motion at the four corner mounting points and the three masses was measured by Endevco 2220 accelerometers driving Endevco 2713 charge

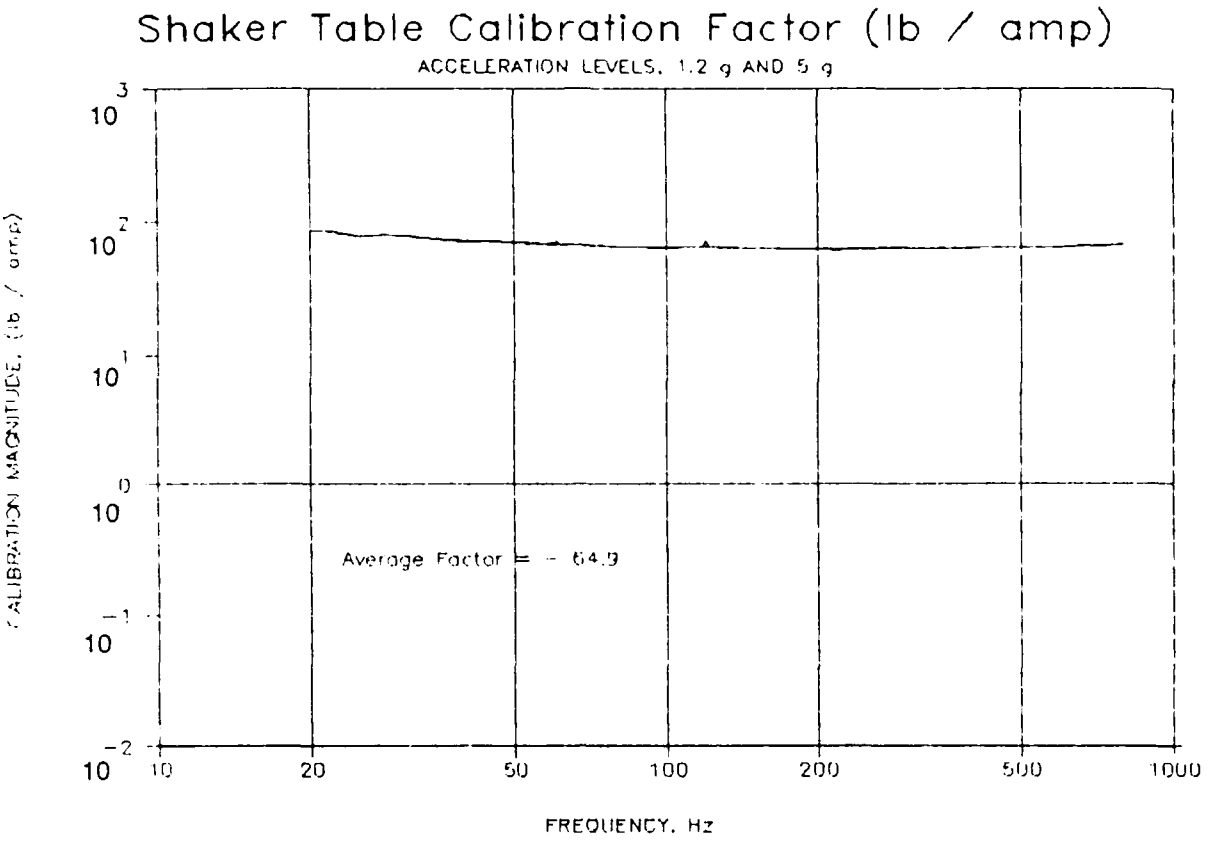

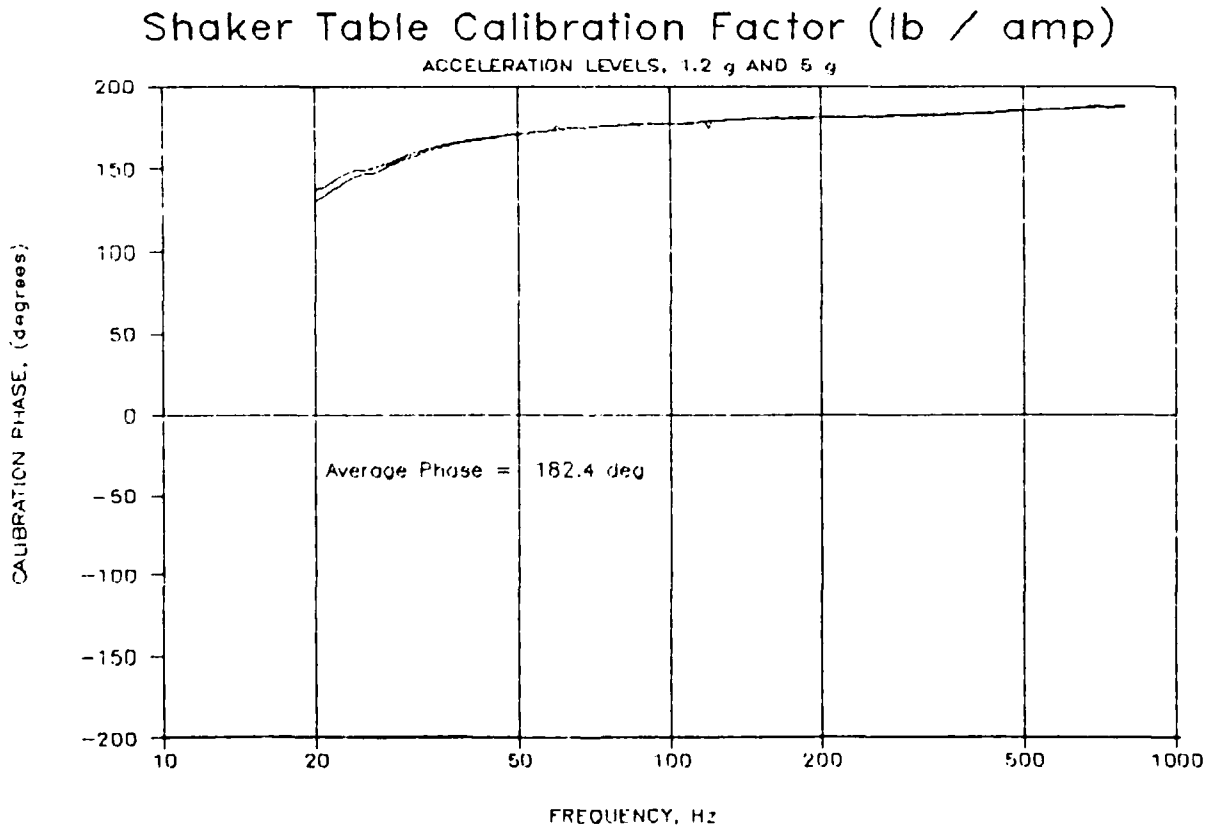

FIGURE 66. SHAKER CURRENT-ELECTROMAGNETIC FORCE RELATION, MB C-60 SHAKER

amplifiers. Prior to test, the accelerometers were amplitude- and phase-calibrated using a GenRad 1557 Vibration Calibrator. All accelerometers were mounted to provide a positive signal for upward table motion. All accelerometer signals, as well as excitation current, voltage, and an NTS reference accelerometer signal were recorded on a TEAC XR-50 14-channel FM tape recorder. Vibration calibration signals and voltage calibration signals were also recorded on the tape in order to provide an end-to-end system calibration.

Two tests were performed, and data recorded, using a table acceleration spectrum similar to the JSC unloaded panel spectrum, with overall levels of 3.1 and 6.1 g rms. Plots of these spectra are shown in Figures 67 and 68. On-line real-time analysis of accelerometer signals showed resonances near 44 Hz, 144 Hz, and 212 Hz. The lowest frequency gave cause for concern, for the natural frequency of the largest mass (#6) was previously measured to be approximately 87 Hz. Disassembly and inspection of the payload showed that the beam supporting the large mass had suffered fatigue failure from the vibration, and was completely broken at the mass-attachment point.

A new beam was installed and testing resumed, but at reduced levels. Vibration tests were performed and data recorded with table acceleration spectra similar to the JSC loaded-panel vibration spectra at 2.1 g rms, a modified loaded-panel spectrum at 3.94 g rms, and a uniform flat spectrum at 1 g rms. These spectra are shown in Figures 69 to 71. Vibration signals were closely monitored and analyzed during the tests to detect fatigue failure. No evidence of resonance frequency shift was observed during the tests, and inspection of the components after the tests revealed no fatigue failure. Following the above described tests, the payload was again excited with unloaded panel spectrum at a level of 3.43 g rms, but failed in fatigue before adequate data could be recorded.

Tape recorded signals were played back into the Hewlett-Packard 3562A analyzer for spectrum analysis. Prior to data analysis, the calibration signals were analyzed in order to establish proper sensitivity (g/v or amp/v). Spectra, frequency response functions and coherence between the individual mass accelerometers, the base mounting point accelerometers, and excitation current

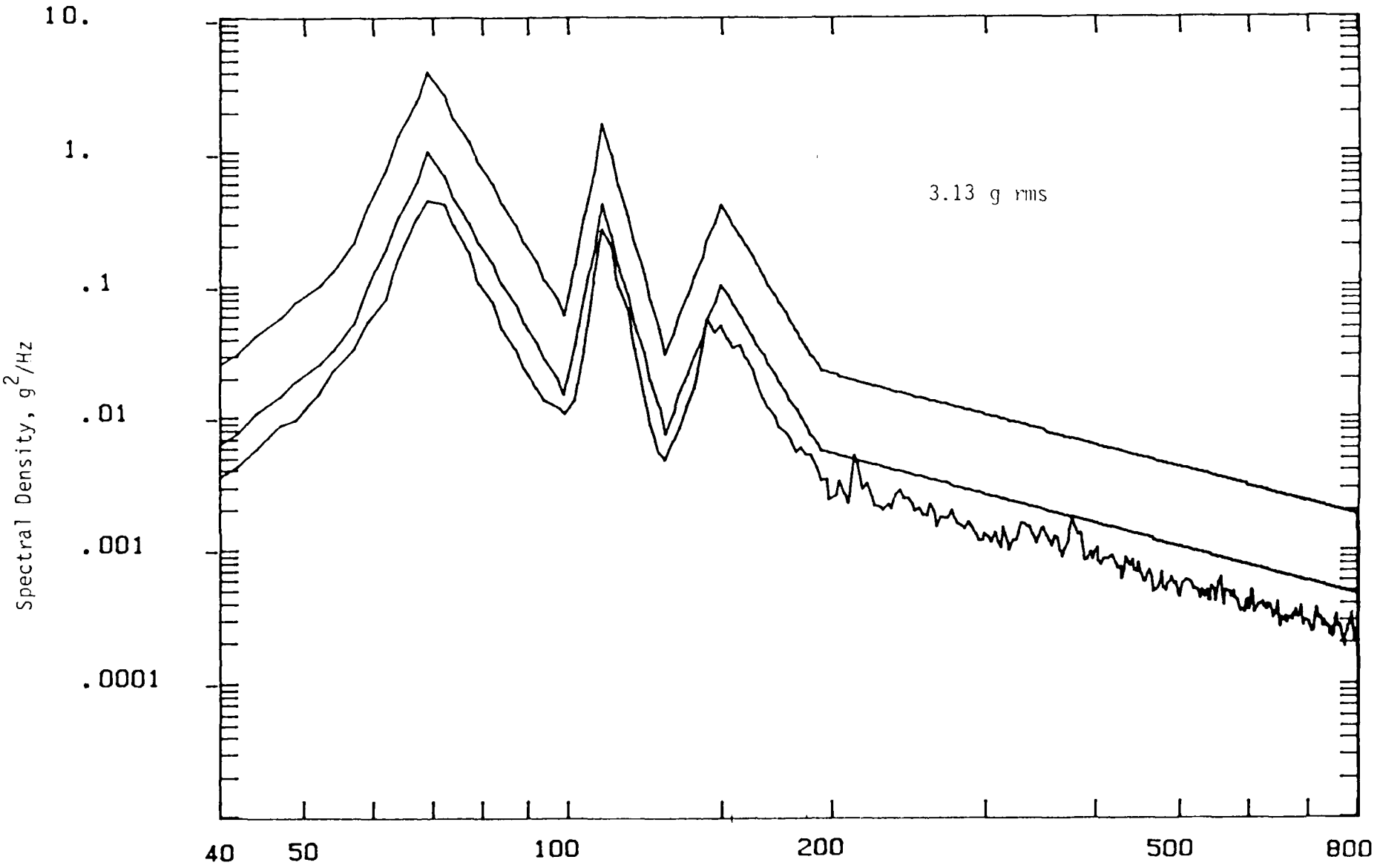

FIGURE 67. NTS SHAKER TABLE SPECTRUM, UNLOADED PANEL SIMULATION.

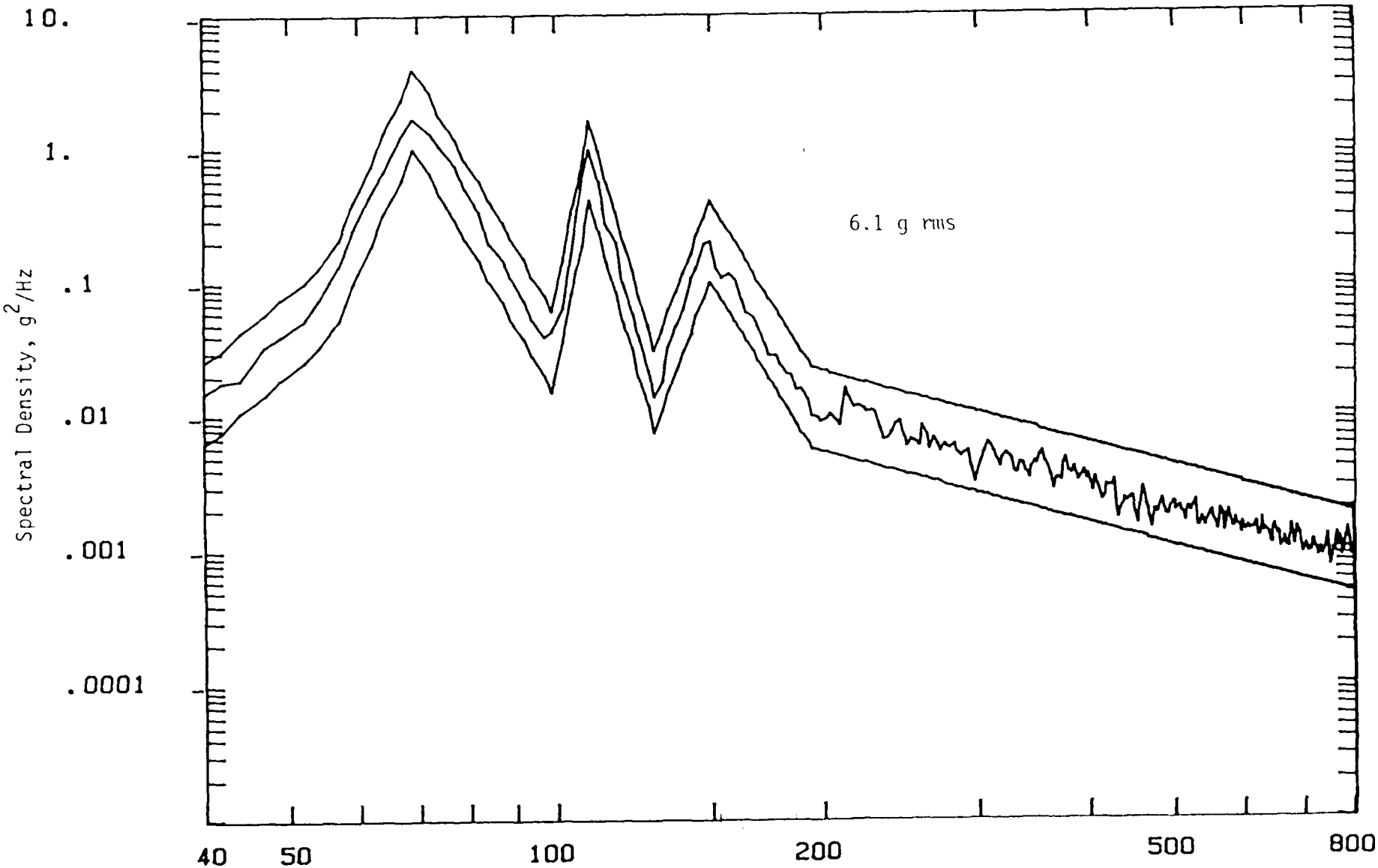

FIGURE 68. NTS SHAKER SPECTRUM, UNLOADED PANEL SIMULATION.

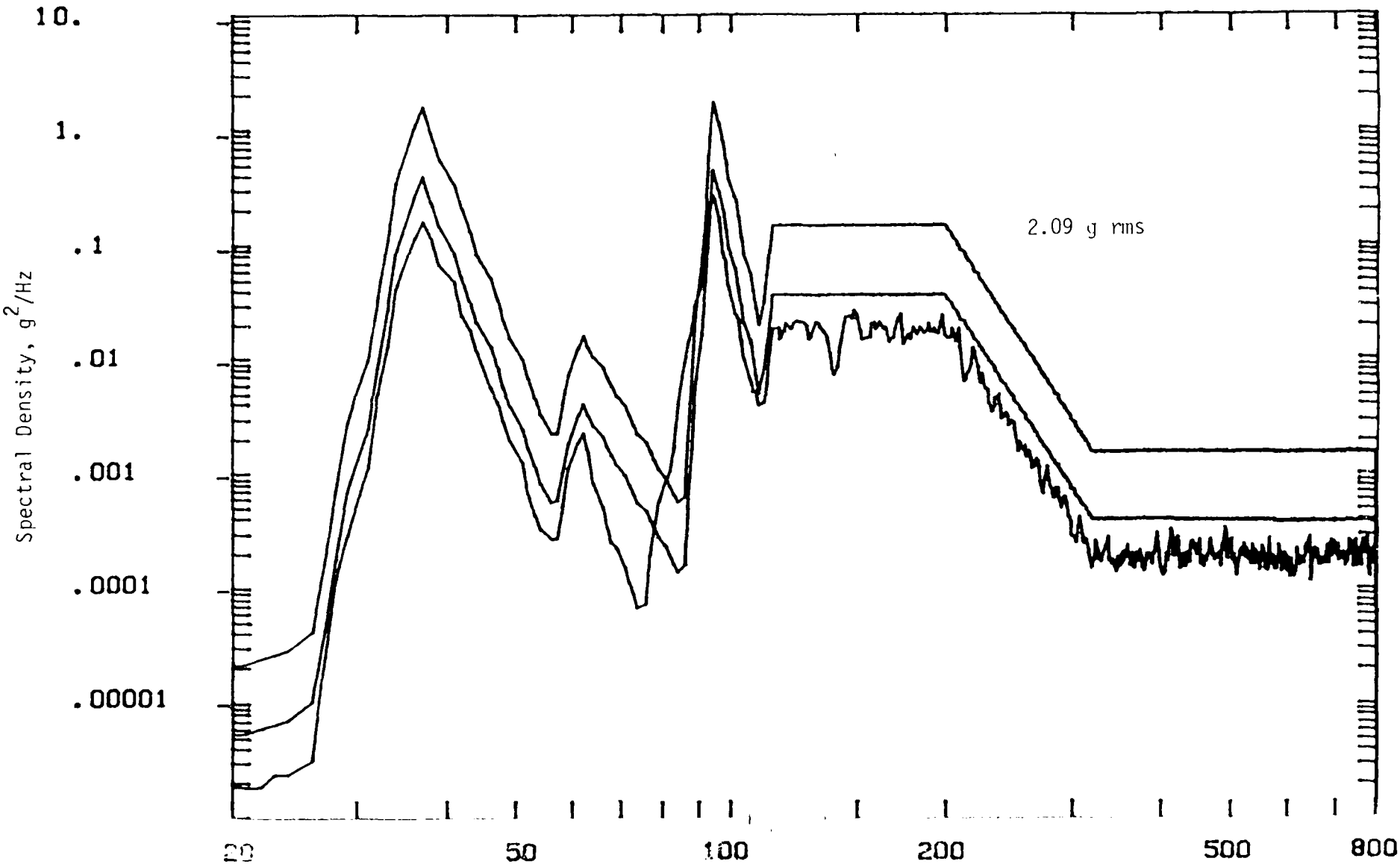

FIGURE 69. NTS SHAKER SPECTRUM, LOADED PANEL SIMULATION.

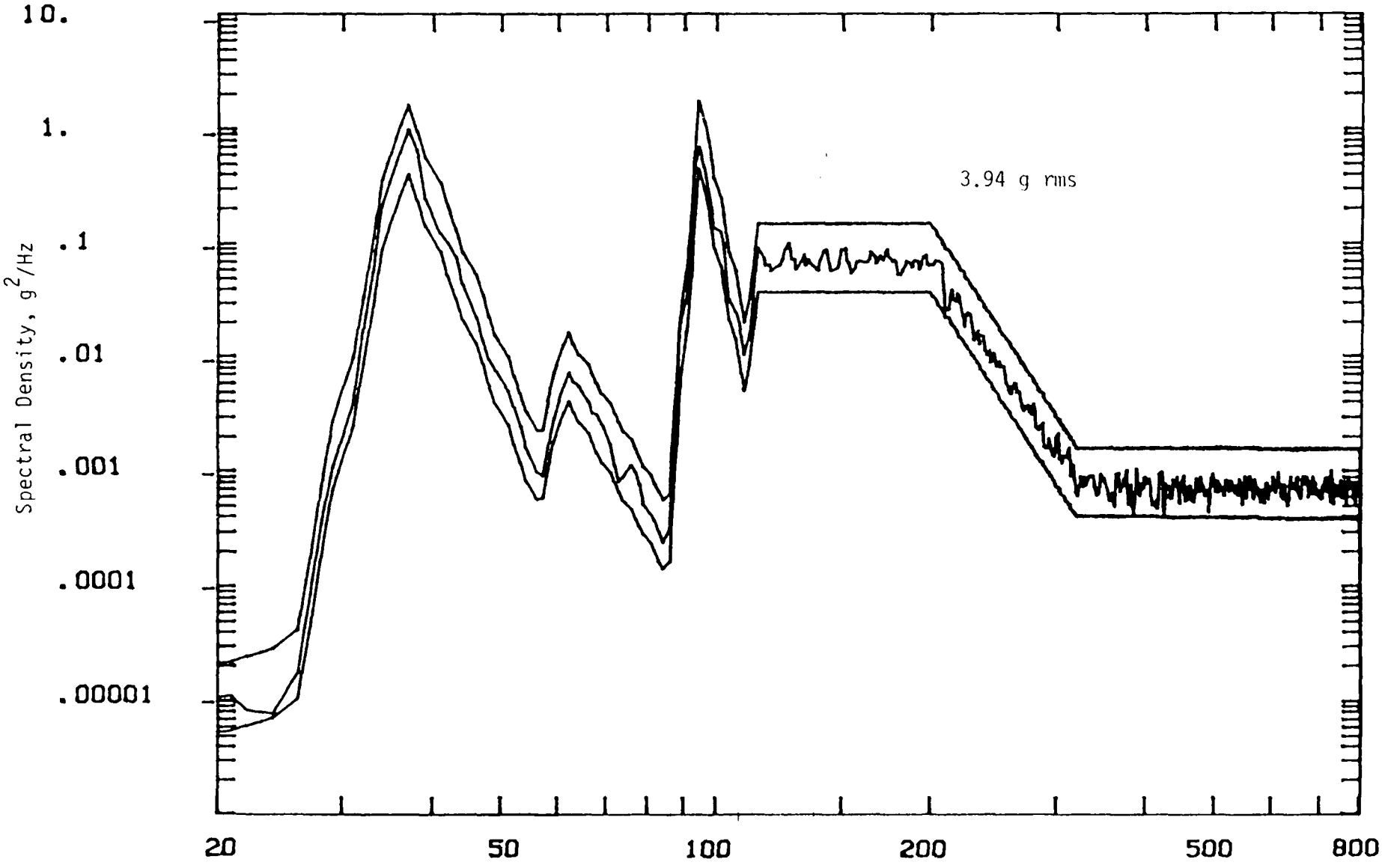

FIGURE 70. NTS SHAKER SPECTRUM, LOADED PANEL SIMULATION.

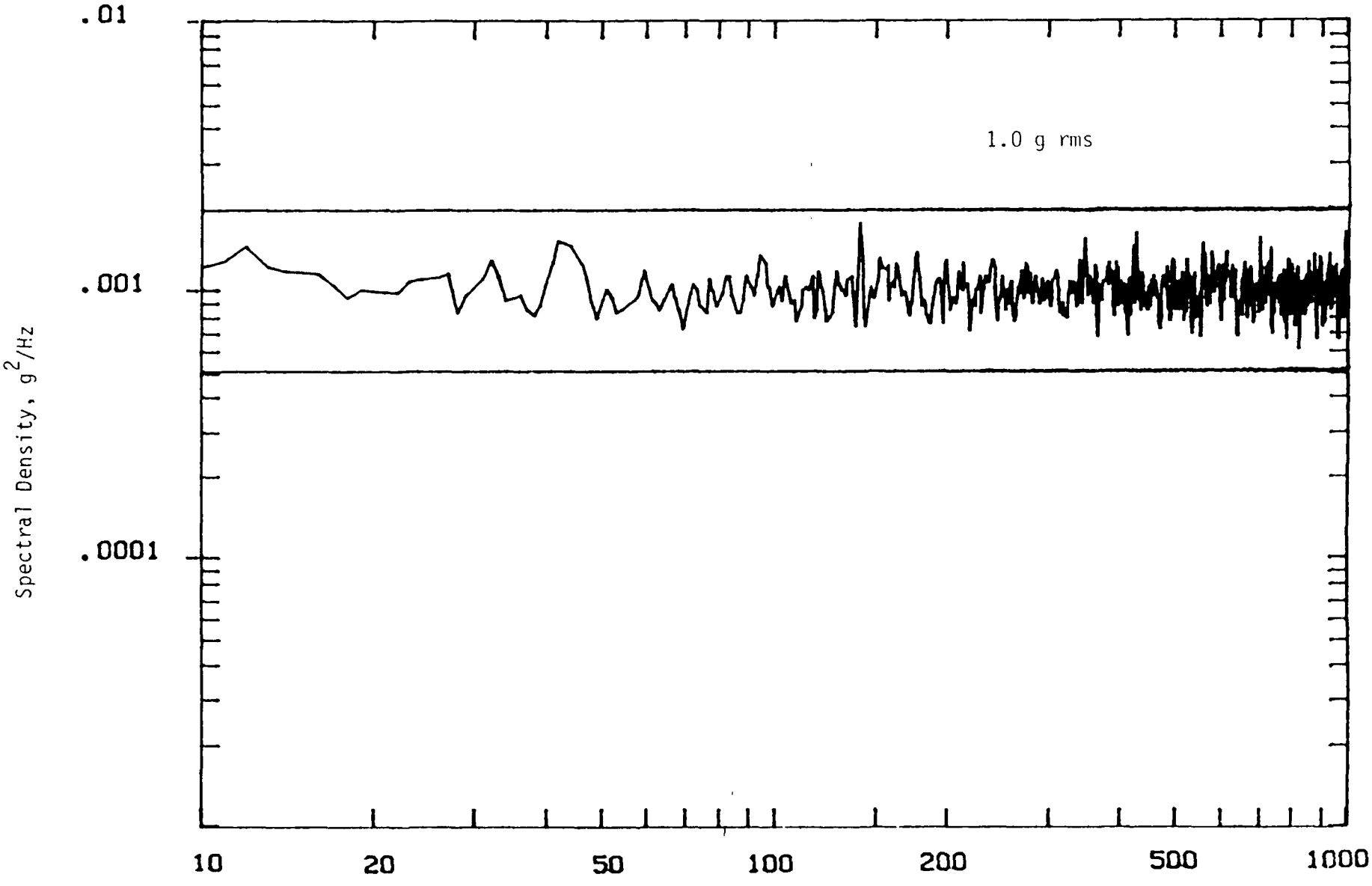

FIGURE 71. NTS SHAKER SPECTRUM, UNIFORM SPECTRUM.

were generated for the three tests. Representative frequency response functions between payload masses and the base are presented in Figures 72 and 73. The relation between excitation current and table acceleration is shown in Figure 74. Note that the current and table acceleration are approximately -180 degrees out of phase over most of the frequency range. In the immediate vicinity of payload resonances the phase changes rapidly, passing through -90 degrees to reach a maximum value and then returning to the -180 degree region. It is at the point where the phase is closest to zero that the acceleration-per-unit of current is minimum, implying that a large force is required to move the payload.

7.3.3 Payload Inertance

Payload inertance, as defined in the context of a shaker test, is the ratio of payload mounting point table acceleration to the total force applied by the shaker. It is presumed that the shaker armature and fixture are rigid, and that all payload mounting points move in unison with the same amplitude. It is equivalent to redefining the payload to have only a single mounting point, and restricting its motion to a single axis.

As noted earlier, the total force applied to a test item by an electromechanical shaker is related to the driving current by the relation

$$F(f) = K(f)C(f) - W_T A(f) \qquad (54)$$

The scale factor K(f) and shaker weights W_T have been determined from earlier tests described in Section 7.3.1. Therefore, the force applied to the payload under test can be determined from the shaker current and acceleration signals. The payload inertance is defined by

$$\text{INERTANCE} = I(f) = H_{FA}(f) = G_{FA}(f)/G_{FF}(f). \qquad (55)$$

From Eqs. 54 and 55, the inertance can be expressed in terms of current and acceleration signals as

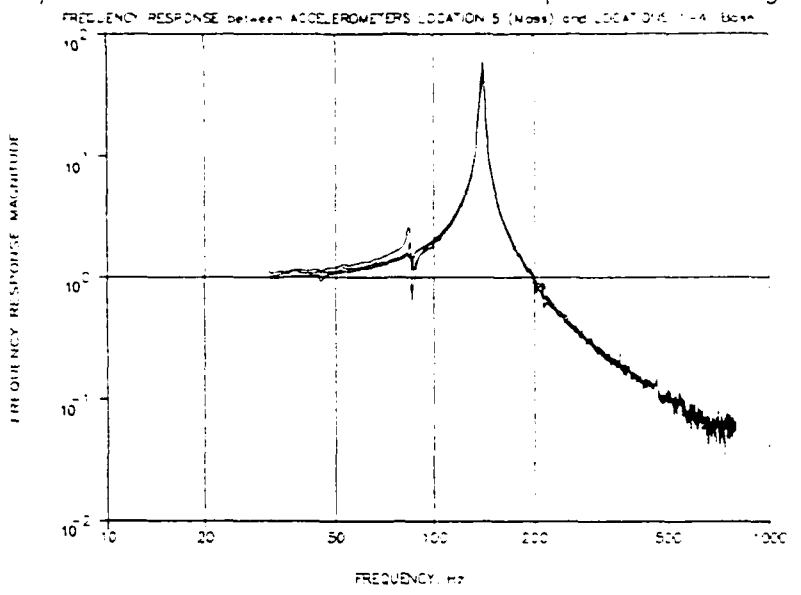

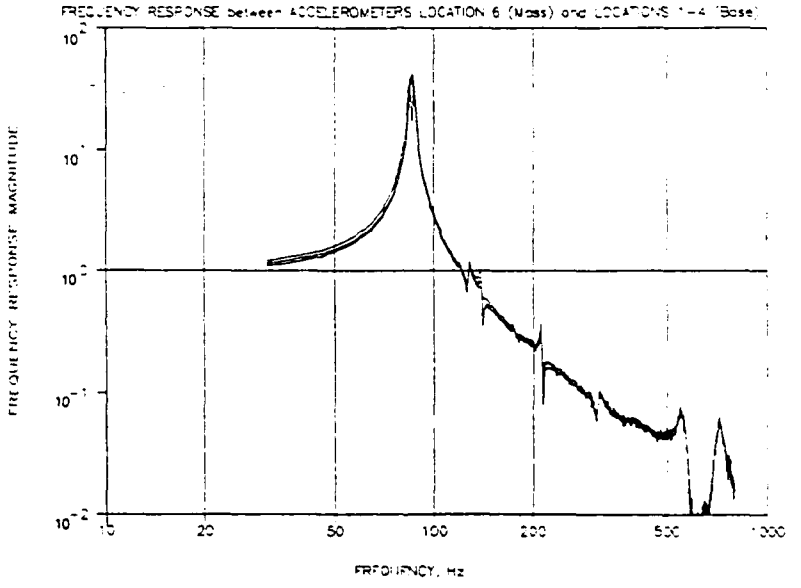

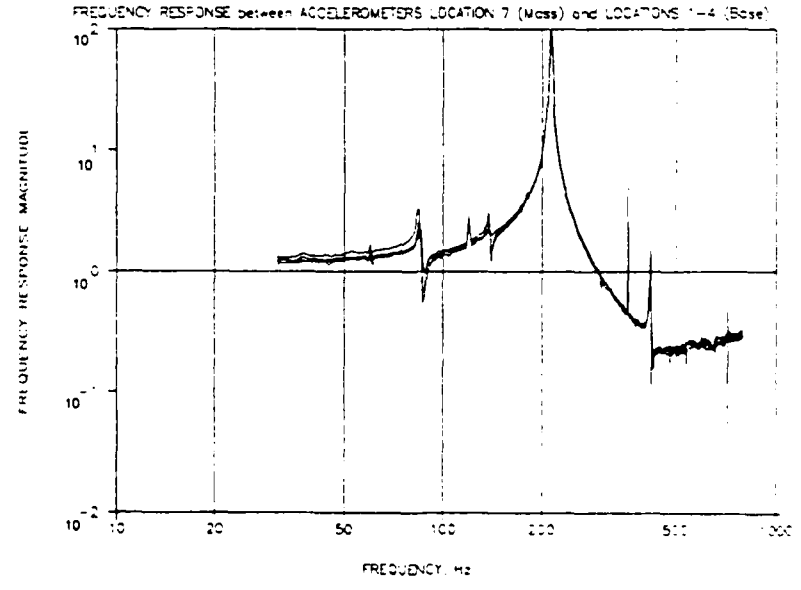

FIGURE 72. FREQUENCY RESPONSE OF PAYLOAD MASS

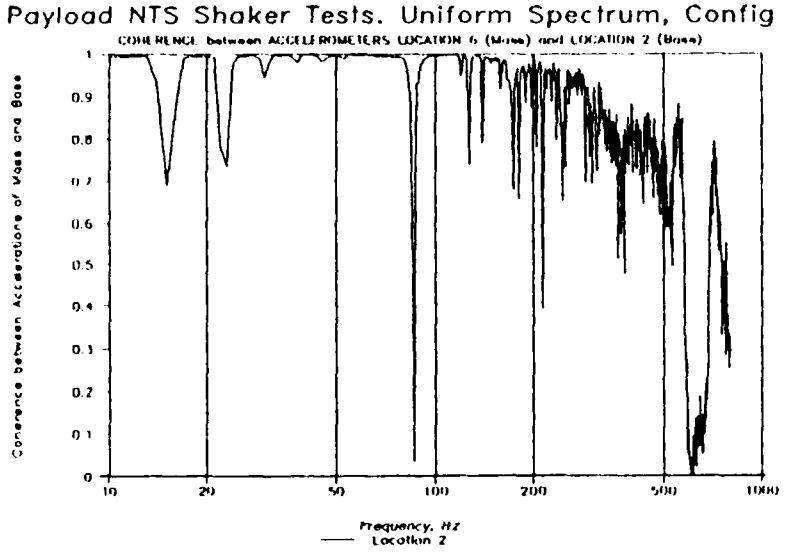

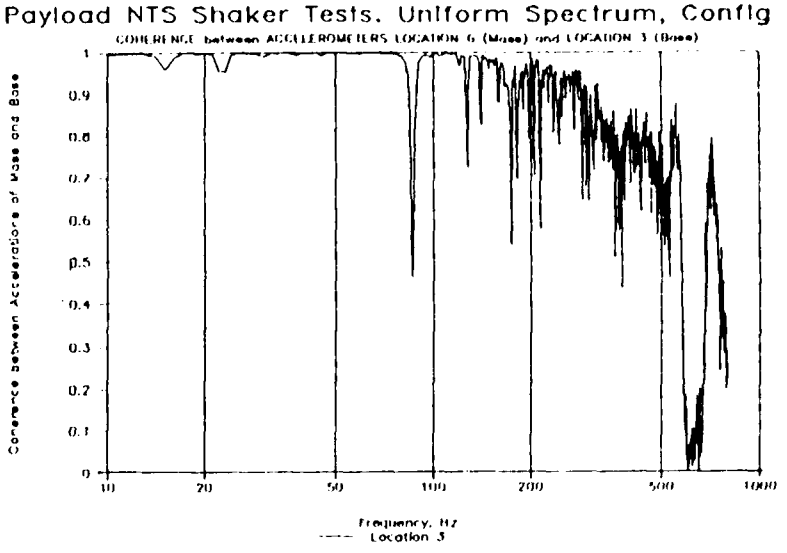

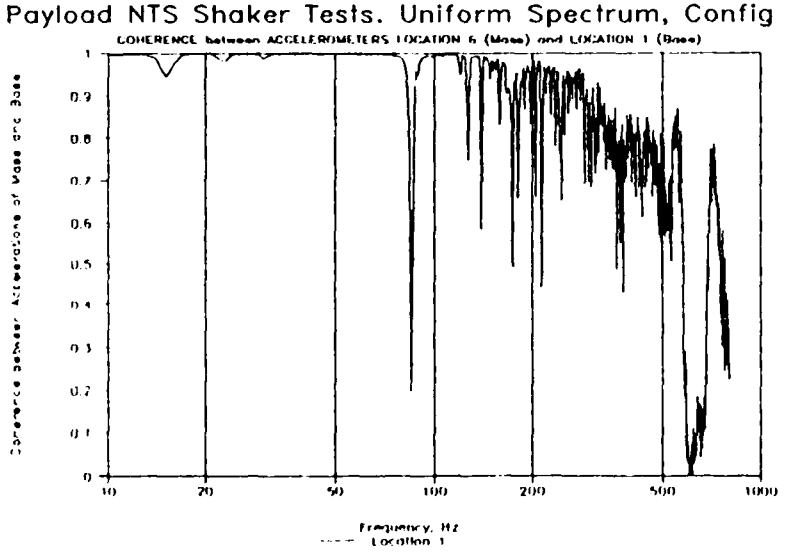

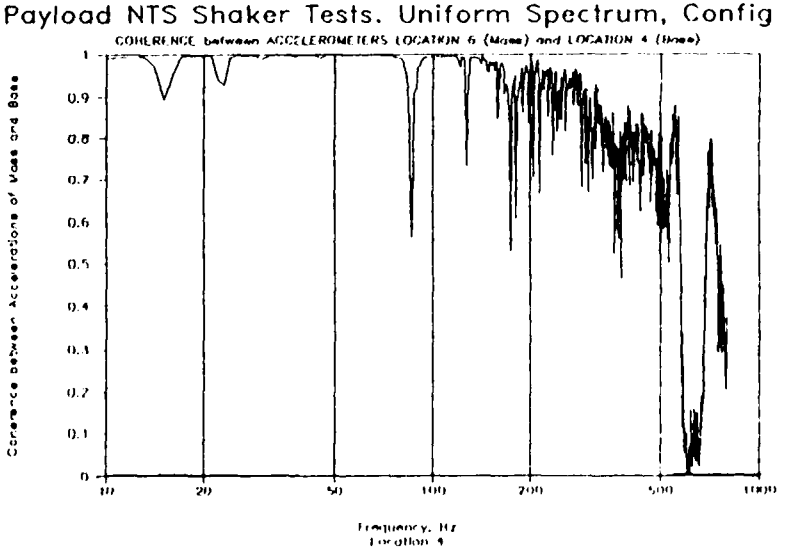

FIGURE 73. COHERENCE OF PAYLOAD MASS 6 AND BASE ACCELEROMETERS.

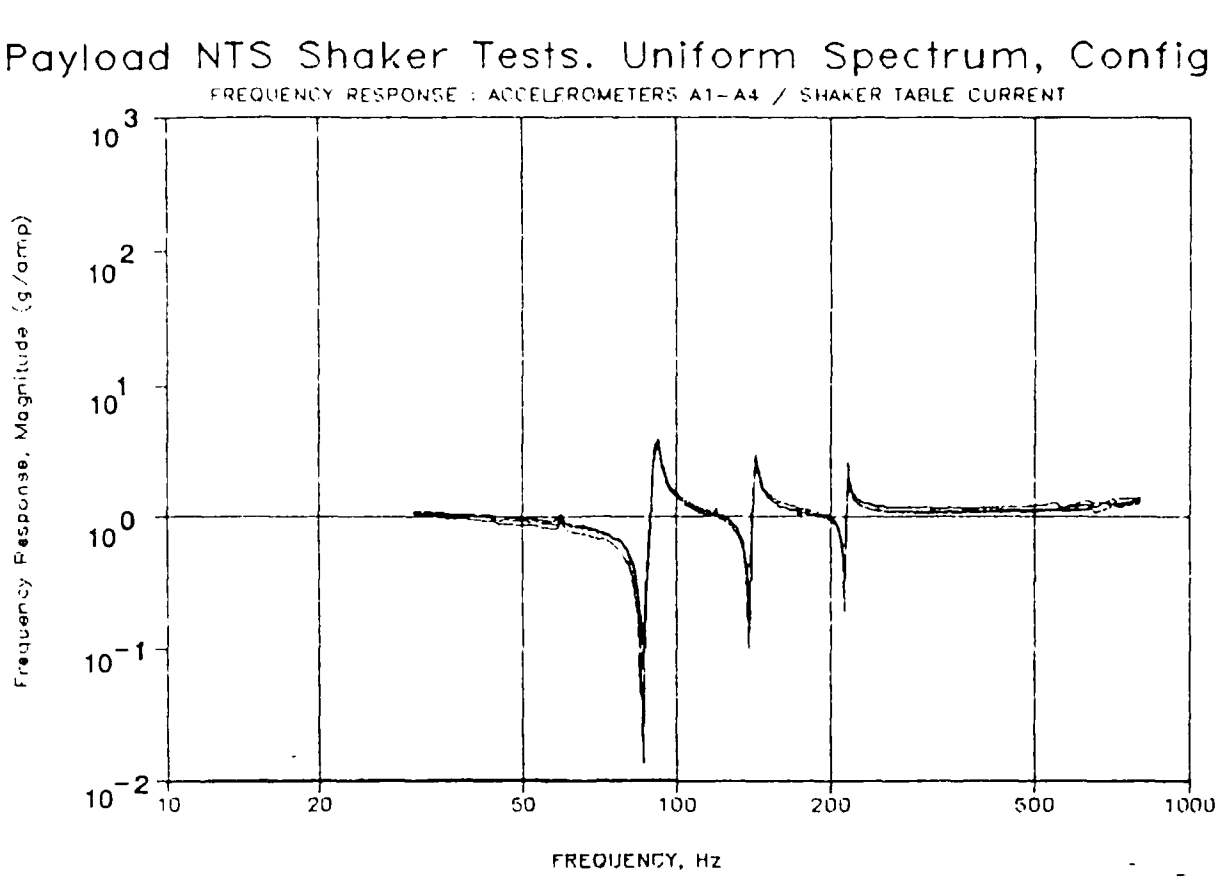

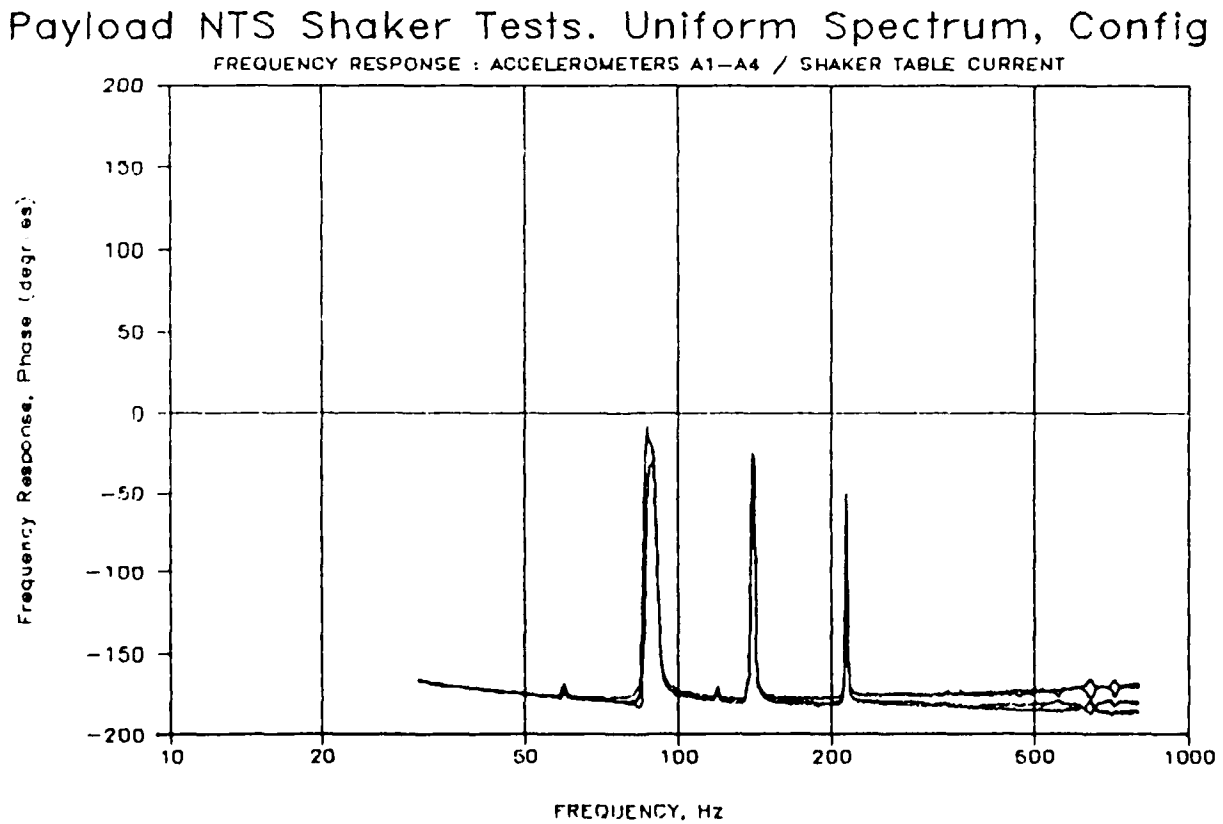

FIGURE 74. FREQUENCY RESPONSE OF SHAKER ACCELERATION AND CURRENT

$$I(f) = \frac{K(f)G_{CA}(f) - W_T G_{AA}(f)}{|K(f)|^2 G_{CC}(f) + W_T^2 G_{AA}(f) - 2W_T \mathrm{Re}[K(f)G_{CA}(f)]} \qquad (56)$$

The inertance function was calculated for the tests, and the results are presented in Figures 75 and 76. The inertance calculated for the loaded panel spectrum excitation used the higher level (3.94 g rms) given in Figure 70. By comparison of Figures 75 and 76 with Figure 74, it is seen that the inertance has minima at those frequencies where the phase between shaker current and acceleration is closest to zero. The phase of the payload inertance is also closest to zero at these frequencies. The inertance measured for the two different excitation spectra should be identical. However, variations in spectral levels and signal-to-noise ratios are reflected by bias and low coherency at certain frequencies, resulting in some differences in inertances calculated from the measured data. Nevertheless, the principal features remain the same, and a smoothed estimate of the function is used in later applications.

7.4 Discussion of Results

The tests described in this section allowed the measurement of payload inertance by two different procedures. It is necessary that the results be compared in similar terms, and correlated with elementary physical models in order to understand the modelling and to verify the measurement and analysis procedures.

Denoting the acceleration at mounting points by the column matrix {A}, the forces applied to the mounting points by {F}, and the inertance matrix by [I], the equations of motion of the payload may be conveniently written as

$$\{A\} = [I]\{F\} \qquad (57)$$

where the harmonic time dependency at frequency f has been suppressed, and the elements of the matrices are allowed to be complex quantities. The elements I_{ij} in the inertance matrix, [I], represent the acceleration of the i-th point

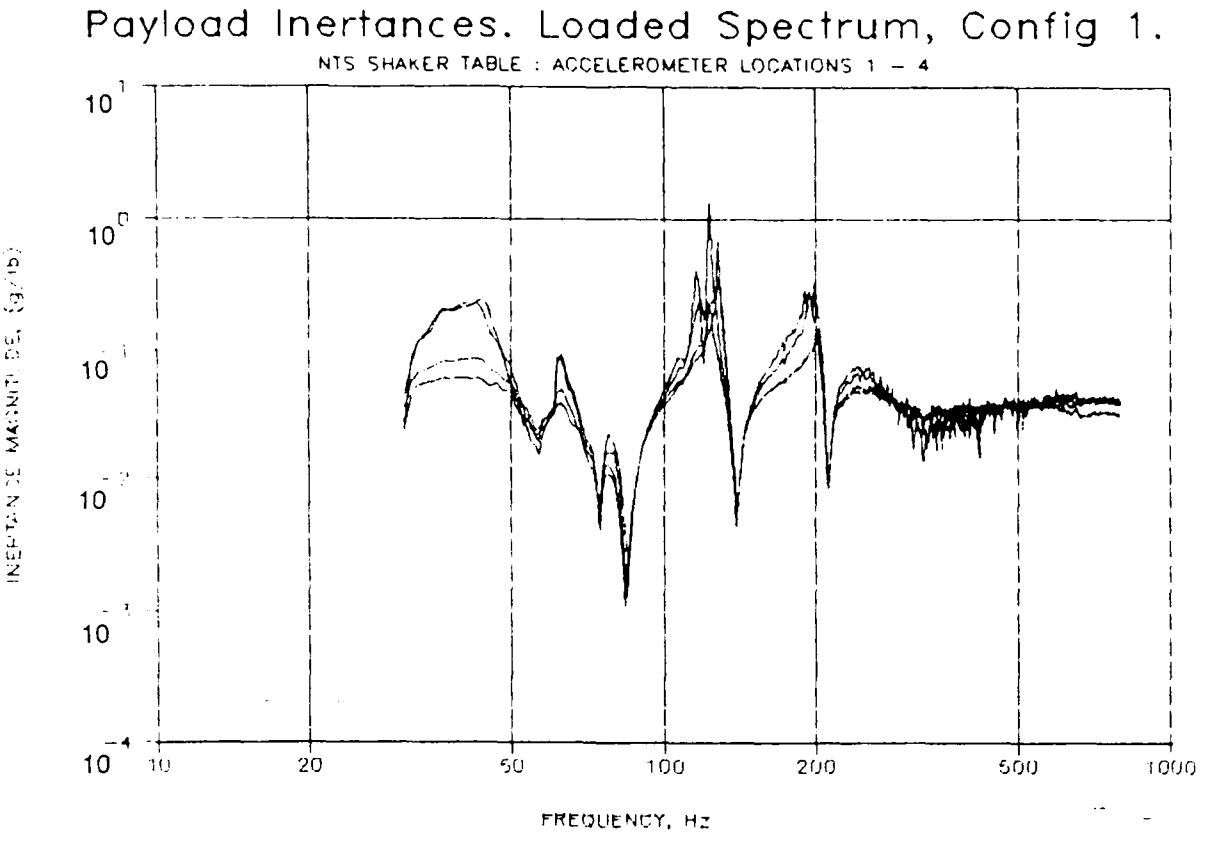

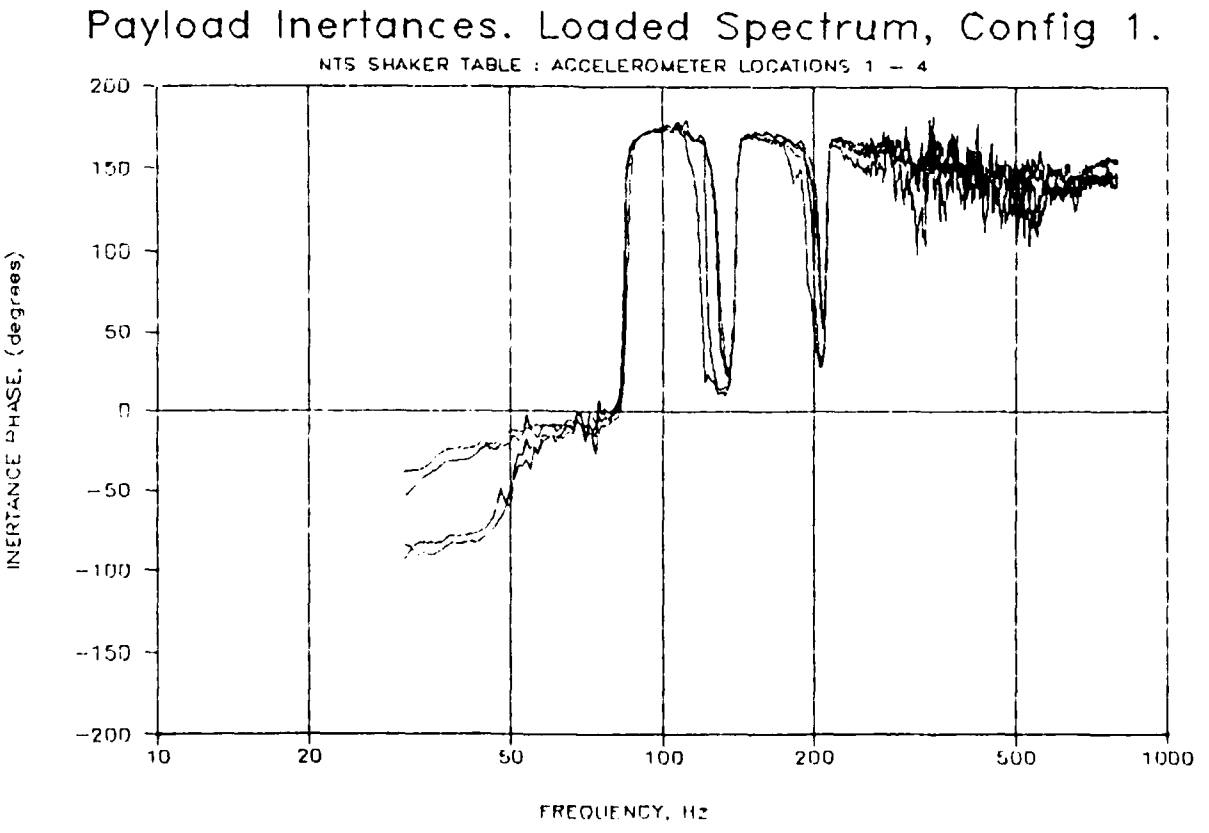

FIGURE 75. PAYLOAD INERTANCE MEASURED ON NTS SHAKER

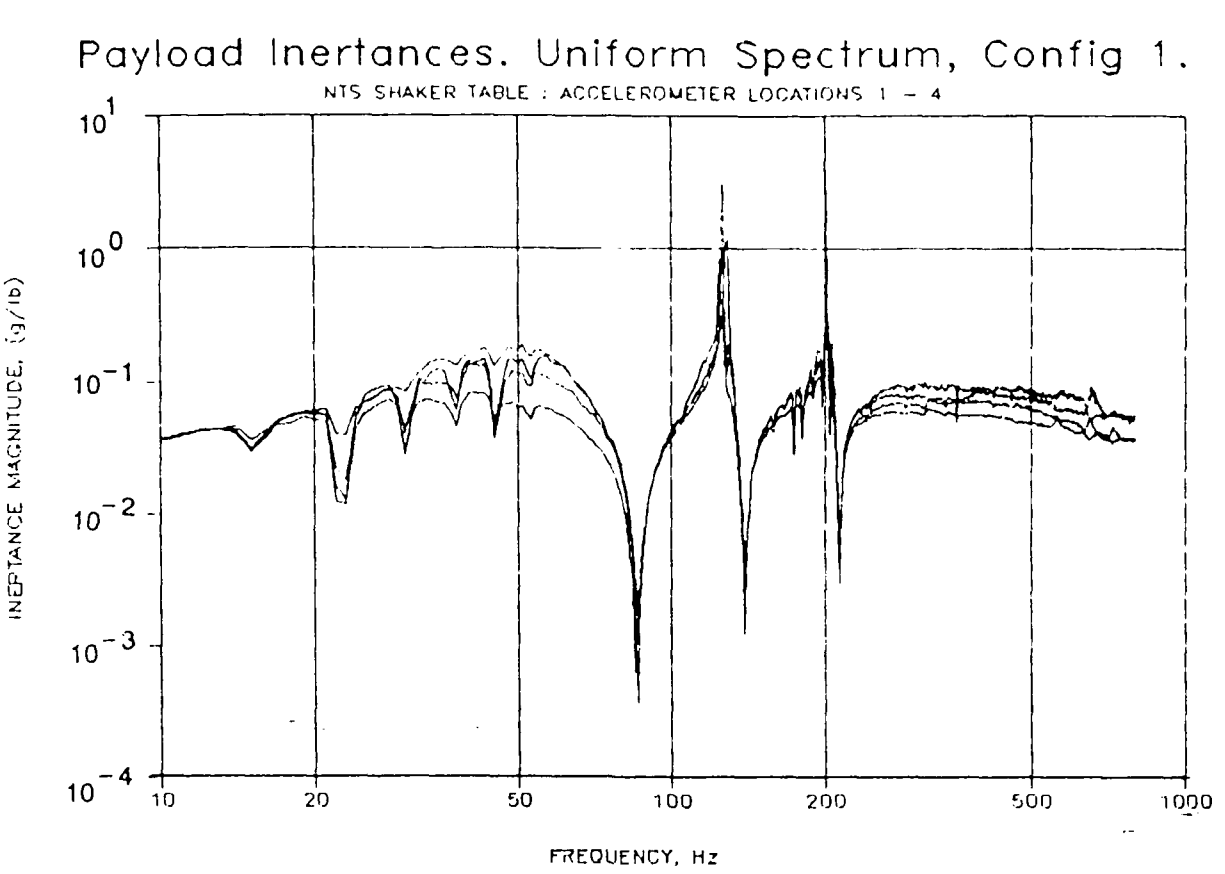

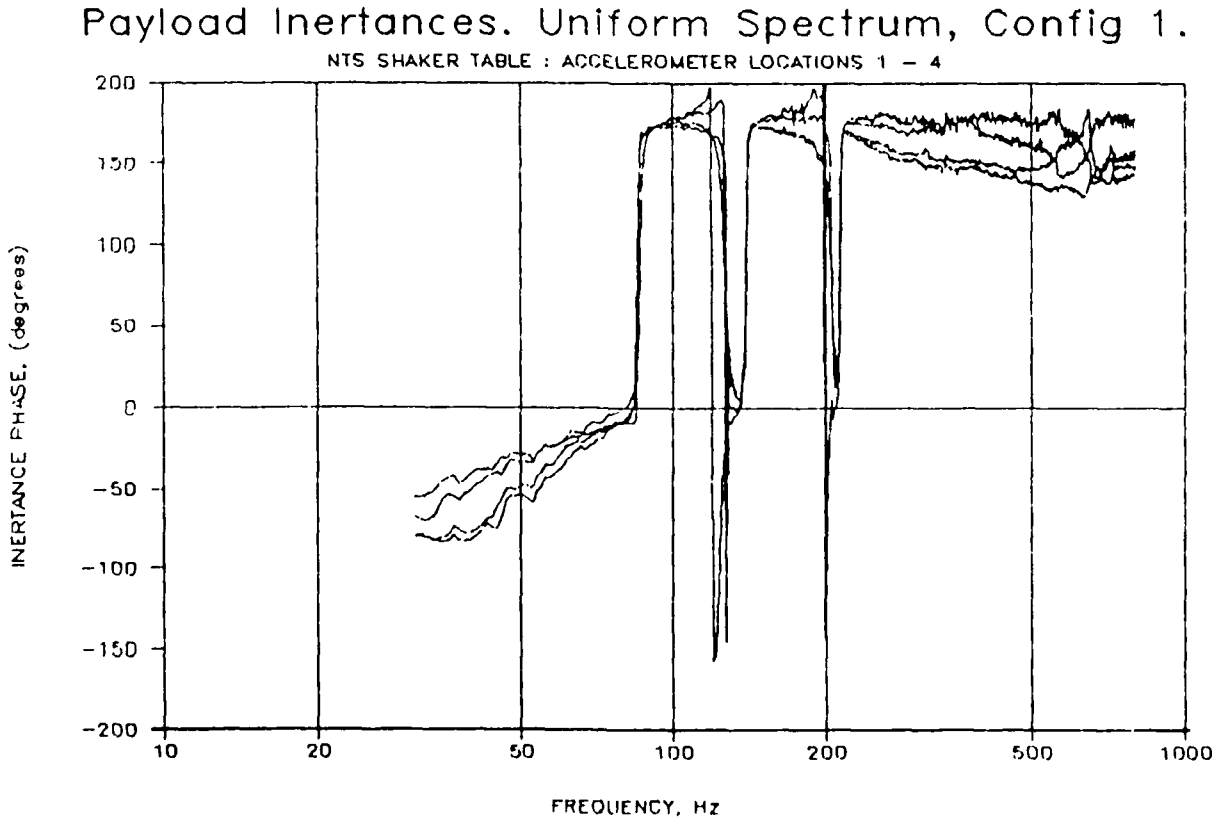

FIGURE 76. PAYLOAD INERTANCE MEASURED ON NTS SHAKER

when a unit force is applied to j-th point and all points are allowed to move freely. This corresponds to a mobility matrix when velocity is the dependent quantity of interest. Following the relationship between mobility and impedance, the apparent weight matrix, [W], is defined as the inverse of the inertance matrix.

Two bounding situations are of interest:

A. All the mounting points are uncoupled and $I_{ij}=0$, $i \neq j$

B. The mounting points are completely coupled and $I_{ij}=1/W$

In the first case, the inertance matrix is

$$[I] = \begin{vmatrix} 1/W_1 & 0 & 0 & 0 \\ 0 & 1/W_2 & 0 & 0 \\ 0 & 0 & 1/W_3 & 0 \\ 0 & 0 & 0 & 1/W_4 \end{vmatrix} \tag{58}$$

and the motion at any point is

$$A_i = I_{ii}F_i = F_i/W_{ii} \tag{59}$$

In this simple case, the apparent weight matrix is also diagonal, and the individual elements are the inverse of the corresponding inertance values. While this result is pleasing from an intuitive standpoint, it must be stressed that the elements of the apparent weight matrix are not, in general, merely the reciprocals of the inertance matrix elements. A more complete discussion of these concepts is presented in the papers of O'Hara [21] and Rubin [22].

The second condition is of considerable interest, for it describes the motion of a rigid body constrained to move only in translation. Application of a force at any mounting point on the item produces uniform motion at all points, and the elements of the inertance matrix are

$$I_{ij} = 1/W, \text{ for all } i,j \tag{60}$$

Because the inverse of the inertance matrix is indeterminate, a slightly different view of apparent weight must be taken. Now, the system is reduced to a single degree of freedom and the inertance is defined as the ratio of acceleration to net force,

$$\text{INERTANCE} = A/[\sum F_i] = (1/n^2) \sum\sum I_{ij} = 1/W \tag{61}$$

and the apparent weight is the total weight.

In the majority of cases with real payloads, the inertance matrix elements are neither identically zero nor unity. When such a payload with multiple mounting points is attached to a testing shaker and the points are constrained to move in unison, then the equation of motion is

$$\{A\} = A\{1\} = [I]\{F\} \tag{62}$$

where the {1} is a column unit vector and A is the amplitude of the acceleration. Multiplying both sides by the inverse of the inertance matrix yields

$$\{F\} = [I]^{-1}\{1\}A \tag{63}$$

The total force on the test item is the in-phase sum of all the forces at the attachment points, or

$$F = \sum F_i = (1)\{F\} \tag{64}$$

where (1) is a row unit vector. Combining the terms yields the inertance of the complete test item as

$$\text{TOTAL INERTANCE} = [\text{APPARENT WEIGHT}]^{-1} = [(1)[I]^{-1}\{1\}]^{-1} \tag{65}$$

Thus, the inertance or apparent weight of a payload may be established by combining individual mounting point inertances measured with a small shaker,

or by mounting the test item on a large shaker and using Eq. 56 to determine the inertance on the basis of current and acceleration measurements. It is this total inertance or apparent weight which must be used in establishing test levels and shaker equalization procedures.

In a launch environment, the payload/structure attachment points are free to vibrate in any motion. During a vibration qualification test however, the payload is mounted on a shaker which moves all attachment points in complete unison (equal magnitude and no phase difference). In establishing an apparent weight for the supporting structure it is this motion which is of interest.

The inertance (or apparent weight) of the supporting panel may be determined from measurements of self- and cross-inertance at the payload mounting points. At low frequencies the panel acts as a spring, with all points moving in phase. Additionally, because the mounting points in the middle bay are very close to the axes of symmetry, they move with almost the same amplitude. The dimensions of the test panel are such that only symmetric modes are excited by the reverberant acoustic field below 140 Hz. Consequently, the payload mounting region behaves much as a rigid plate moving uniformly, and Eq. 61 may be used to estimate the total inertance from the inertance measured at any mounting point. By averaging over measurements made at all the points, minor irregularities are smoothed out, and

$$\text{APPARENT WEIGHT} \approx (1/N^2) \sum_{ij} 1/I_{ij} \tag{66}$$

By the argument employed to derive Eq. 65 for the inertance or apparent weight of the payload, a similar relation may be developed for the support structure when it is forced to move in only uniform translation motion,

$$\text{APPARENT WEIGHT} = (1)\ [I]^{-1}\ \{1\} \tag{67}$$

Because the inertances will, in general, be complex quantities, it is difficult to develop a general approximation or bound for the apparent weight. However, at high frequencies, where the input vibration forces would be uncorrelated, the cross-inertance terms will be similarly vanishingly small.

Under these conditions the inertance matrix will be approximately diagonal, as will its inverse. Consequently,

$$\text{APPARENT WEIGHT} \approx \sum (I_{jj})^{-1} \tag{68}$$

Individual mounting point inertances illustrated in Figure 65 have been combined to estimate an equivalent total inertance using Eq. 66, and are shown in Figure 77. This shows that both payloads satisfy the relation in the region below 40 Hz. As a consequence of the eccentric excitation of the payload, many extraneous modes are excited, resulting in numerous peaks and notches in the inertance function. Nevertheless, the general levels of inertance calculated from Eqs. 66 and 68 are similar to those measured with the payload on the shaker table and presented in Figures 75 and 76. It is expected that a more comprehensive calculation, using all the individual mounting point cross inertances, would result in closer agreement.

On the large shaker table at NTS, all mounting points are moving in unison and the payload acts as a rigid mass at low frequencies. Consequently, the apparent weight should be equal to its true weight, and the inertance the reciprocal of this. Figures 75 and 76 demonstrate that inertance derived from measurements of shaker current and acceleration yield values which are close to theoretical predictions.

Additional supporting data in the form of spectra, cross spectra, coherence and frequency response functions, are contained in Appendix D. All original time histories have been maintained on the tape recordings. All spectral information computed, but not plotted, is stored on 1.2 MB floppy disks and is available for further examination and manipulation.

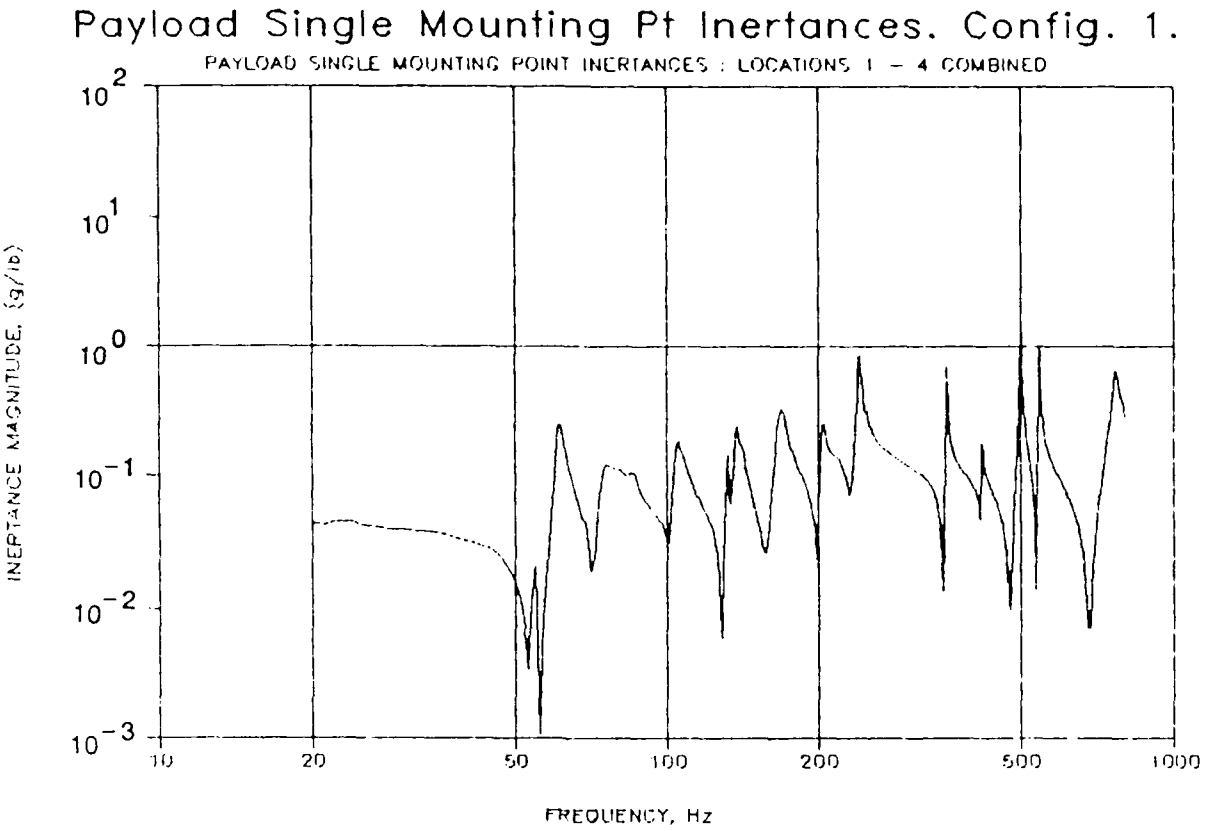

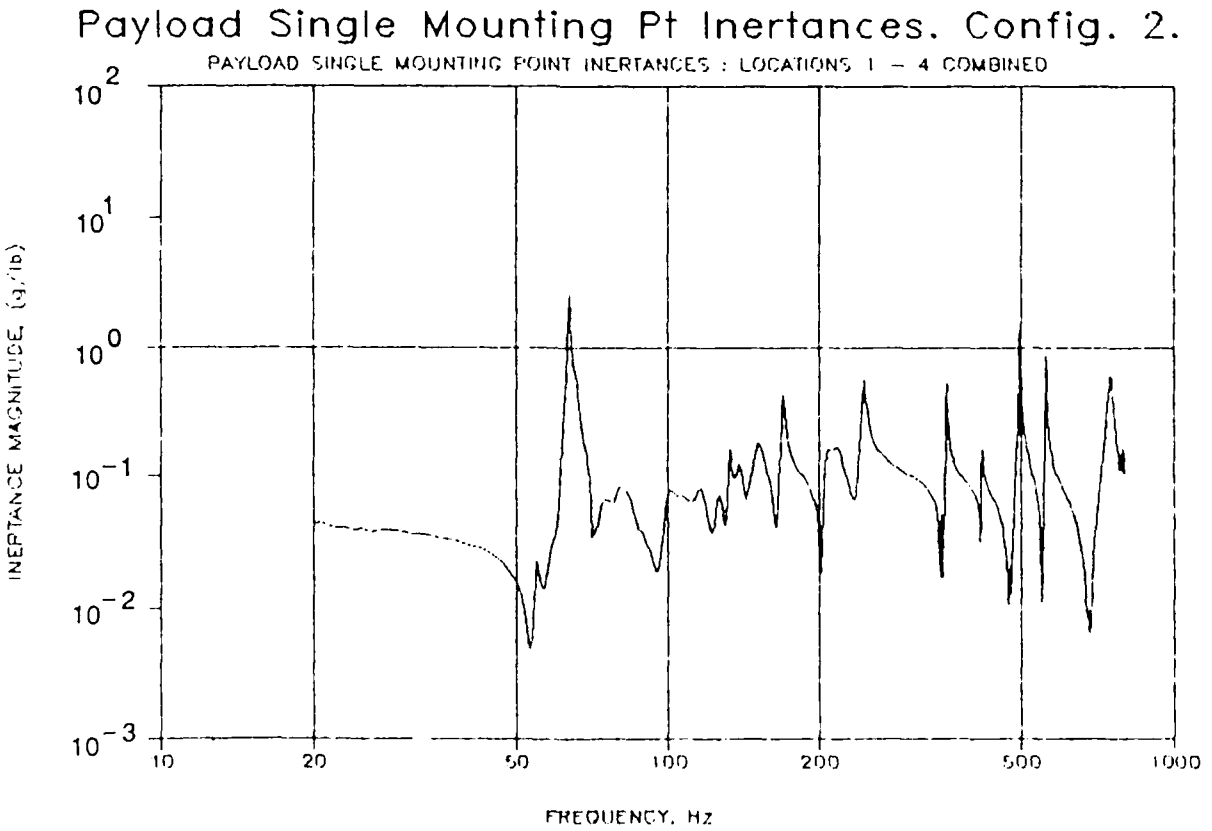

FIGURE 77. EQUIVALENT TOTAL INERTANCE DERIVED FROM MOUNTING POINT TESTS

8. EVALUATION OF TESTING PROCEDURES

Based upon the results of the acoustic and vibration tests summarized in Sections 6 and 7, the three candidate procedures for performing mechanical vibration tests with proper consideration of the mounting point apparent weight of the structure supporting the payload are now evaluated.

8.1 Candidate Procedures and Test Requirements

From Section 2, the three candidate test procedures to be evaluated may be summarized as follows:

1. Input Motion Correction Procedure - Calculate a correction factor for the specified vibration input to account for mounting structure and payload apparent weights.

2. Blocked Force Limit Procedure - Limit the specified vibration input such that shaker-payload interface force never exceeds the "blocked force" for the orbiter sidewall.

3. Apparent Weight Simulation Procedure - Modify the specified vibration input such that the shaker-payload interface force is equal to the payload input force if assuming the unloaded orbiter sidewall vibration were equal to specified level.

All three procedures involve a common basic assumption, namely, the vibration test specification spectrum represents an envelope of the spectra for the unloaded structural vibrations at payload mounting points. This assumption is justified by the fact that the envelope of spectra for loaded structural responses also covers the spectra for unloaded structural responses, as shown in Section 3.8. All three procedures also require the following information and conditions.

1. A conservative estimate of the apparent weight of the orbiter sidewall at payload mounting points (obtained from the OV-101 tests, as detailed in Section 5).

2. A measurement of the shaker-payload interface force using shaker armature current (verified by the vibration tests covered in Section 7).

3. A measurement of the shaker table acceleration (as currently done in conventional vibration tests).

4. A limitation on the frequency range to be below the first resonance frequency of the shaker armature and all fixtures (should not be a problem below 200 Hz).

The vibration testing system required for all three procedures is schematically illustrated in Figure 78. The key new requirement for the vibration testing equipment is the measurement of the armature current and the use of this measurement in the shaker equalization procedures. For the evaluation tests, the required equalization procedure was conducted off-line. Specifically, the shaker input spectrum was adjusted to approximate the spectrum of the input to the payload measured during the acoustic tests (see Figure 67). All payload vibration levels were then scaled as required to satisfy the applicable test criteria. In practice, however, all but the first candidate procedure (input motion correction) will require a change in the shaker equalization software, and perhaps some hardware, to execute the proposed test procedures on-line.

Beyond the need to do all computations off-line, the evaluations of the candidate test procedures were limited by the following problems.

1. The C-60 shaker used for the vibration tests had an armature-fixture weight of about 67 lbs., as compared to the payload weight of only 21.5 lbs., causing the necessary calculations to involve small differences between large numbers.

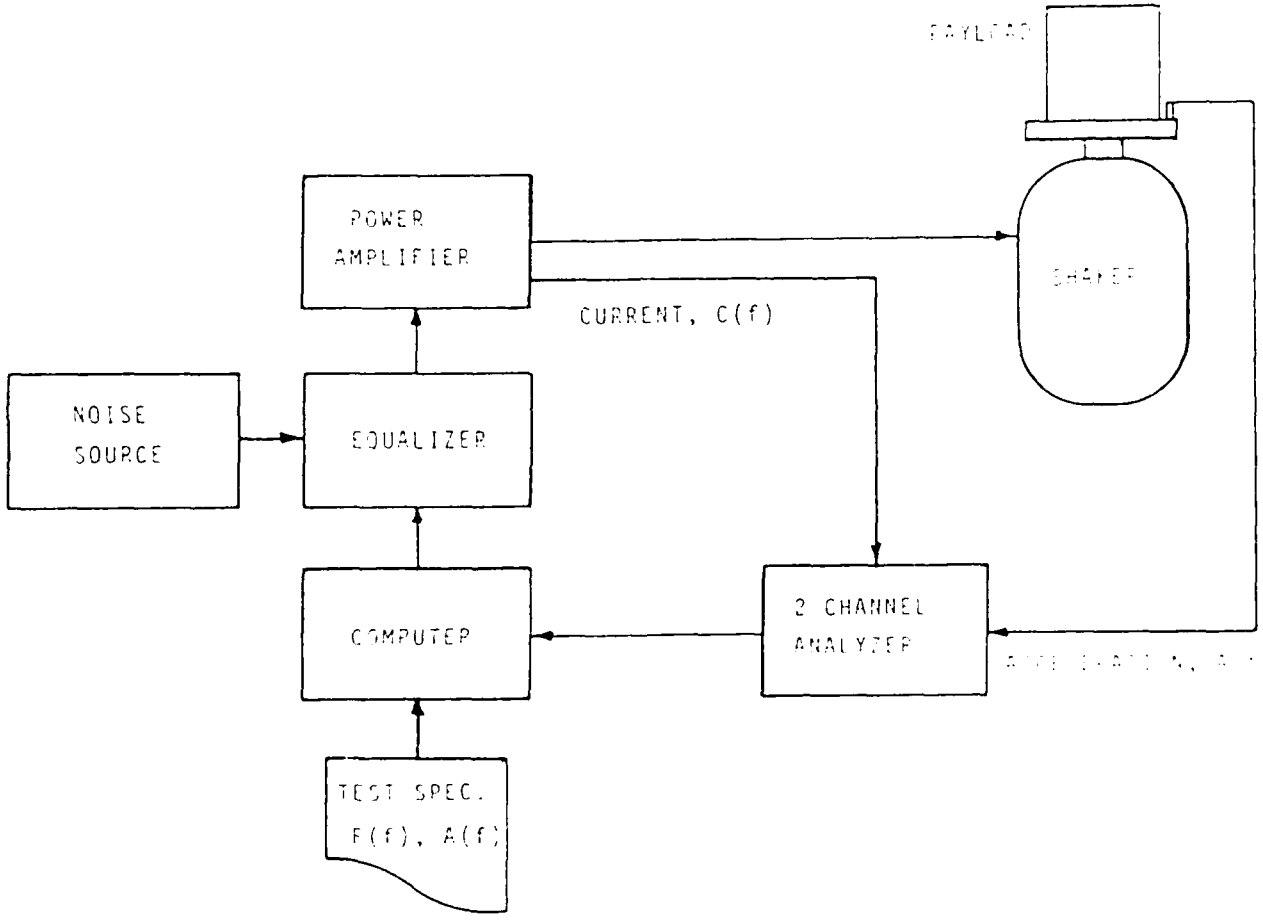

FIGURE 78. REQUIRED VIBRATION TEST EQUIPMENT FOR CANDIDATE TEST PROCEDURES

2. The unloaded panel vibration levels measured during the acoustic tests could not be reproduced in the vibration tests because the payload broke before these levels could be achieved.

3. The apparent weight measurements of the test panel used for the acoustic tests may be too low due to the nonlinear character of the panel (see Section 5).

4. The net apparent weight of the test panel was taken to be the sum of the apparent weights measured at individual points, as given by Eq. 48, which may be too conservative (excluding nonlinear effects) at the lower frequencies.

8.2 Evaluation Techniques

The three candidate procedures were evaluated using the vibration response of the heaviest resonant element of the payload (accelerometer location 6, referred to hereafter as the "payload response") as a basis for comparison. The evaluation was as follows.

1. The payload response was computed for a payload input vibration spectrum equal to the bare panel vibration spectrum measured during the low level acoustic tests (see Figure 60). In other words, the unloaded panel vibration response during the acoustic test was considered to be the basic vibration test specification.

2. The vibration input to the payload was then modified in accordance with each of the three candidate procedures, and the payload response for the corrected input vibration level was computed.

3. The spectrum of the payload response produced by the corrected vibration test was then compared to the actual payload response measured during the acoustic tests.

The spectrum of the payload response produced by the uncorrected vibration test and the spectrum of the actual payload response measured during the

accurate test are shown in Figure 79. Note that the uncorrected vibration test causes an over-test of the payload in excess of four orders of magnitude (40 dB) at the resonance frequency of the payload element being considered (about 86 Hz). This result again clearly demonstrates the severity of the over-test that can occur when the mounting point apparent weight for the payload mounting structure is not considered in performing the test.

It is also seen in Figure 79 that the actual payload response during the acoustic test exceeds the vibration test response levels at frequencies between 30 and 50 Hz. This is due to the coupled panel-payload resonance peak that is not simulated in the vibration test. In practice, however, an under-test at these frequencies will be prevented by the enveloping procedure used to produce the vibration test levels given in the orbiter sidewall test specification (SD-CF-0206), as discussed earlier in Section 3.8.

8.3 Input Motion Correction Procedure

In review, the input motion correction procedure involves the following steps.

1. Compute the net inertance (apparent weight) of the payload on the shaker (the best results will be attained with shaker input levels near the corrected test levels).

2. Compute the corrected input motion to the payload from

$$G_{AA}(f) = G_{SS}(f)/[1 + (W_P/W_S)]^2$$

3. Reduce the specified test level, $G_{TT}(f)$, by the ratio, $G_{AA}(f)/G_{SS}(f)$, at those frequencies where strong payload resonances occur.

The first step was executed on the simulated payload, with the results shown in Figures 75 and 76. It is seen in those figures that the minimum values of the payload inertance at resonances are different for the two different input vibration level. For evaluation purposes, the inertance values in Figure 75 were used, since they were computed with an input vibration level more like the actual input vibration levels measured during the acoustic tests.

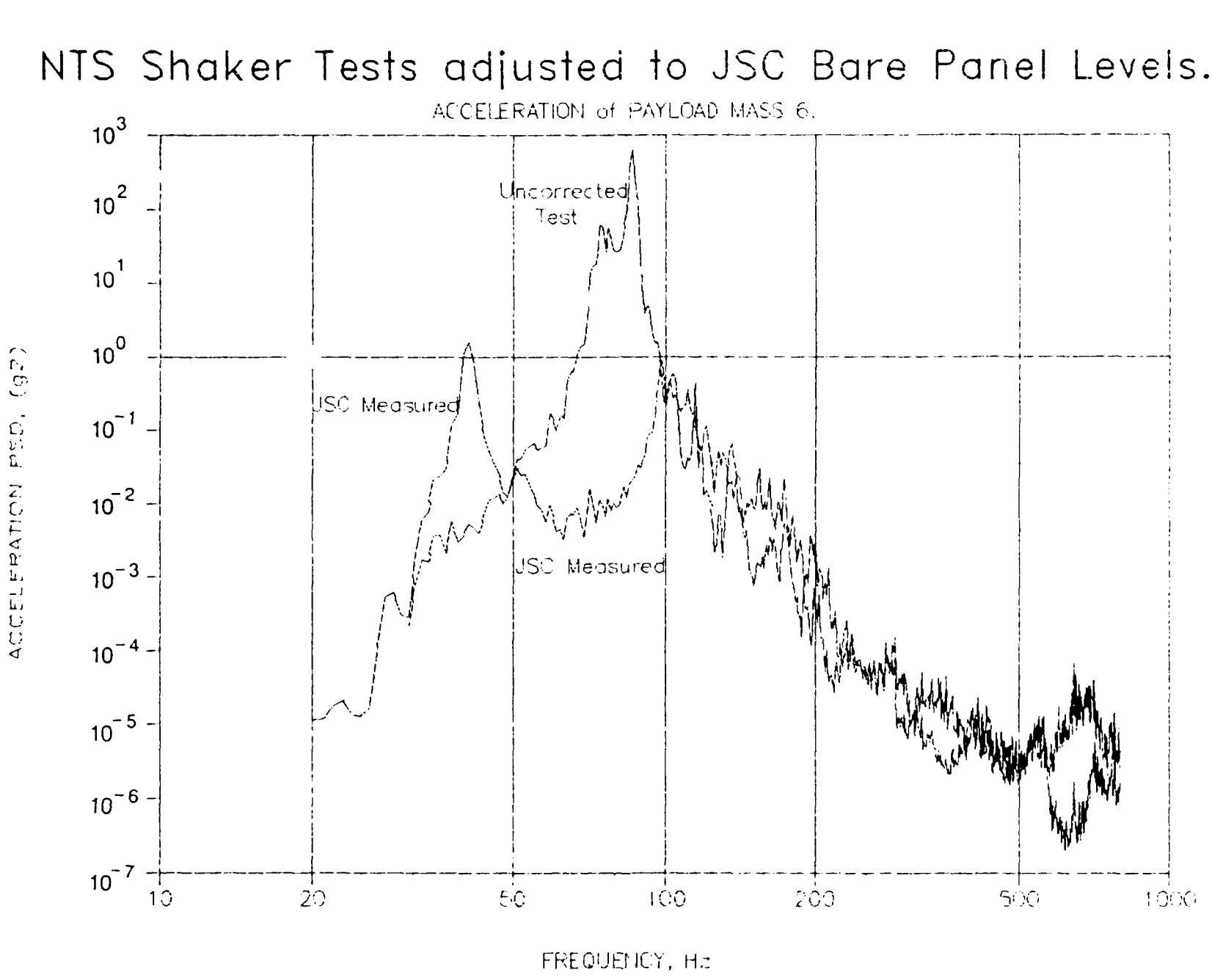

FIGURE 79. PAYLOAD RESPONSE DURING ACOUSTIC TEST AND UNCORRECTED VIBRATION TEST

Using the payload inertance in Figure 75, the input motion correction procedure was applied to the vibration test with the results shown in Figure 80. Comparing the results in Figures 79 and 80, it is seen that the input motion correction procedure reduced the over-test of the payload by over three orders of magnitude (>30 dB) in the frequency range of the resonance frequency of the payload element (about 86 Hz). The payload response levels for the corrected test input in the frequency range of the payload resonance are still higher than the actual levels that were measured during the acoustic test, but by margins generally less than an order of magnitude (<10 dB), which is considered an acceptable degree of overtesting.

As a closing point of caution, had the payload inertance values given in Figure 76 been used to compute the input motion correction, the corrected test results in Figure 80 would have been slightly lower, at some frequencies, than the actual vibration response levels measured during the acoustic tests; i.e., and under-test would have occurred.

In summary, the input motion correction procedure appears to work with the following advantages and disadvantages.

Advantage

The procedure can be accomplished with present shaker equalizer systems.

Disadvantages

1. The procedure requires a preliminary test to measure the net payload apparent weight on the shaker.

2. Personal judgment is required to identify those payload resonances that should reduce (notch) the specified test level.

3. The procedure is vulnerable to errors due to possible nonlinear payload response characteristics, which could cause an unconservative test.

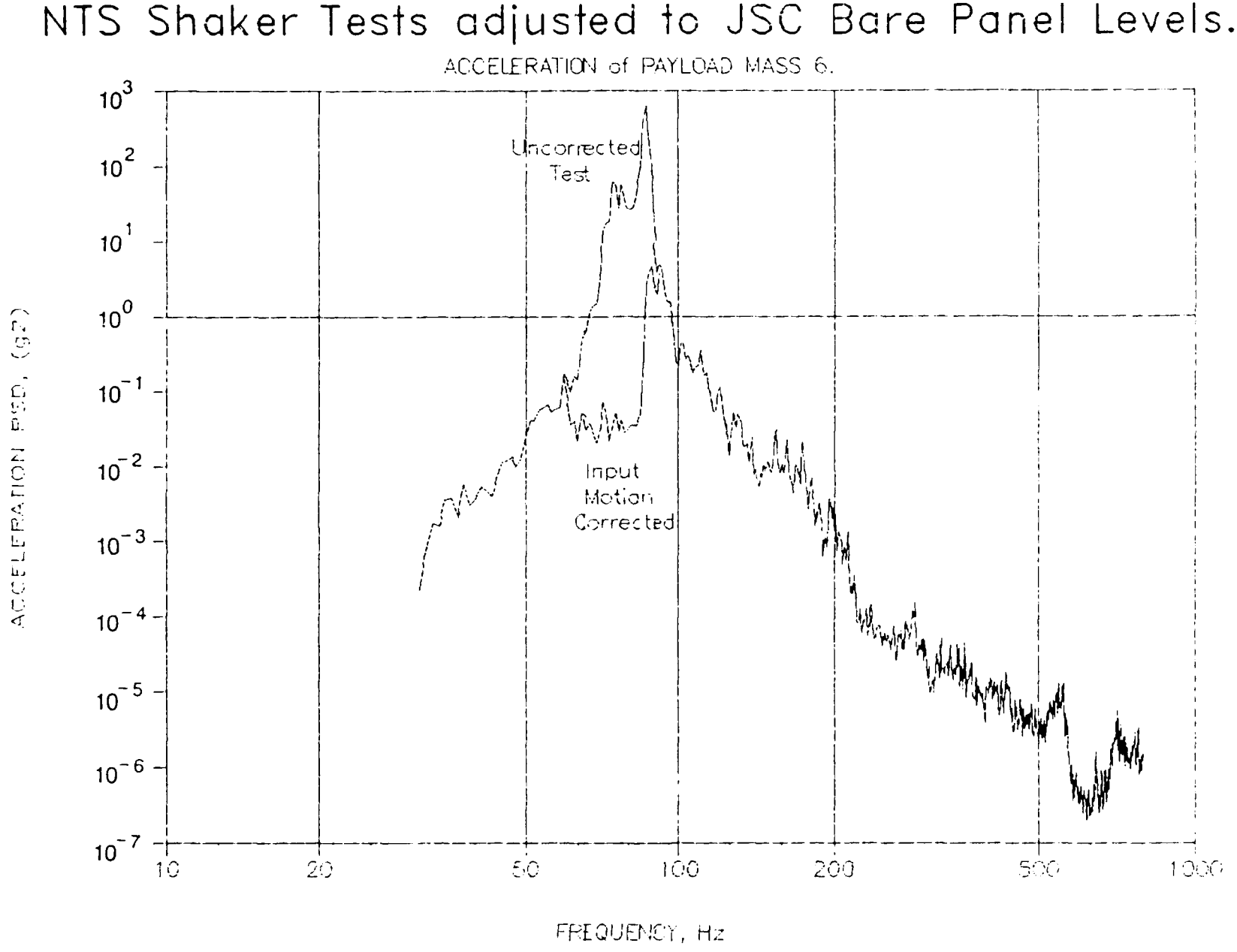

FIGURE 80. PAYLOAD RESPONSE DURING INPUT MOTION CORRECTED AND UNCORRECTED VIBRATION TESTS

8.4 Blocked Force Limit Procedure

In review, the blocked force limit procedure involves the following steps.

1. Compute the shaker table-payload interface force from

$$G_{FF}(f) = |K(f)|^2 G_{CC}(f) + W_T^2 G_{AA}(f) - 2W_T \mathrm{Re}[K(f)G_{CA}(f)]$$

2. Compute the blocked force $G_{BB}(f) = W_S(f)G_{TT}(f)$ for the payload mounting structure.

3. Reduce the specified test level, $G_{TT}(f)$, by rat , $G_{BB}(f)/G_{FF}(f)$, at those frequencies where $G_{FF}(f) > G_{BB}(f)$.

The above procedure was applied to the vibration test of the payload with the results shown in Figure 81.

As for the input motion correction procedure, it is seen in Figure 81 that the blocked force limit procedure reduces the over-test at the resonance frequency of the payload element by about 30 dB, but is still conservative in this frequency region relative to the actual payload response measured during the acoustic test (Figure 79). It is also seen in Figure 81 that the blocked force limit procedure (which is not a simple notching procedure, but applies over the entire frequency range) reduced the payload response somewhat at the frequencies of the other payload element resonances (about 140 and 210 Hz), as well as at all frequencies above 200 Hz. These reductions are somewhat greater than the actual reductions seen in Figure 79, probably because of the suspected under-estimation of the mounting point apparent weight of the acoustic test panel mentioned earlier. In any case, this would not cause an under-test in practice with an enveloped type test specification due to the inherent conservatism of the enveloping procedure discuss in Section 3.8.

In summary, the blocked force limit procedure works well with the following advantages and disadvantages.

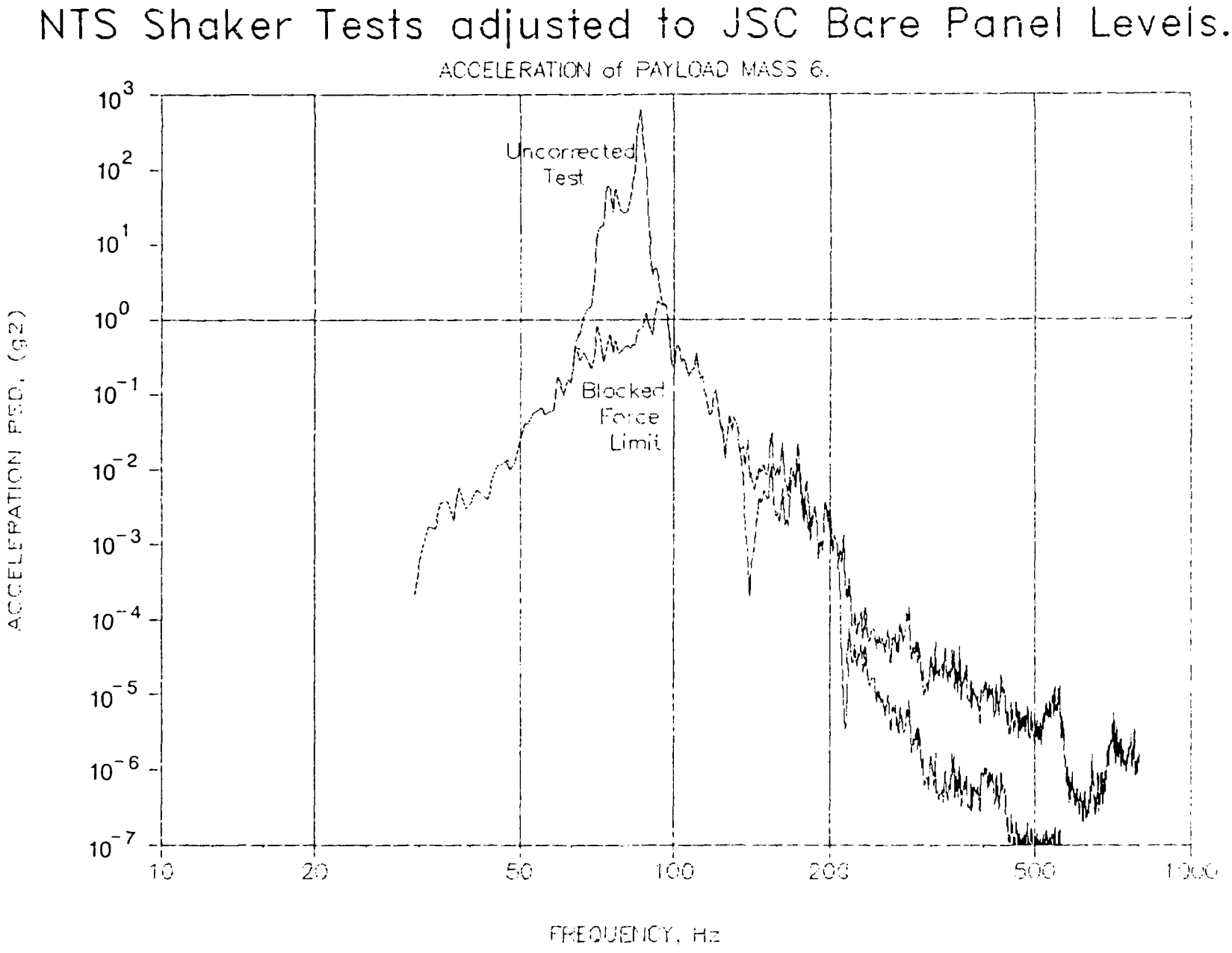

FIGURE 81. PAYLOAD RESPONSE DURING BLOCKED FORCE LIMIT AND UNCORRECTED VIBRATION TESTS

Advantages

1. The procedure requires no knowledge of the payload apparent weight.

2. The procedure is not vulnerable to errors due to possible nonlinear payload characteristics.

3. The procedure automatically corrects the specified test levels for payload weight, as well as resonant responses.

Disadvantages

The procedure requires a modification of the present shaker equalizer systems to be executed online.

8.5 Apparent Weight Simulation Procedure

In review, the apparent weight simulation procedure involves the following steps.

1. Compute the equivalent free vibration level of the mounting structure

$$G'_{SS}(f) = \{|K(f)|^2 G_{CC}(f) + |W_o(f)|^2 G_{AA}(f) + 2Re[K(f)W_o^*(f)G_{CA}(f)]\}/|W_S(f)|^2$$

where $W_o(f) = W_S(f) - W_T$

2. Equalize the shaker to make $G'_{SS}(f) = G_{TT}(f)$, the specified test level, except never let $G_{AA}(f) > G_{TT}(f)$.

The above procedure was applied to the vibration test of the payload with the results shown in Figure 82. Because the shaker equalizer used for the tests was not able to do the online calculation, an iterative procedure was used, as described in Section 8.1, and the final results shown in Figure 82 were scaled from measured data for a close, but not exact, apparent weight simulation input from the shaker.

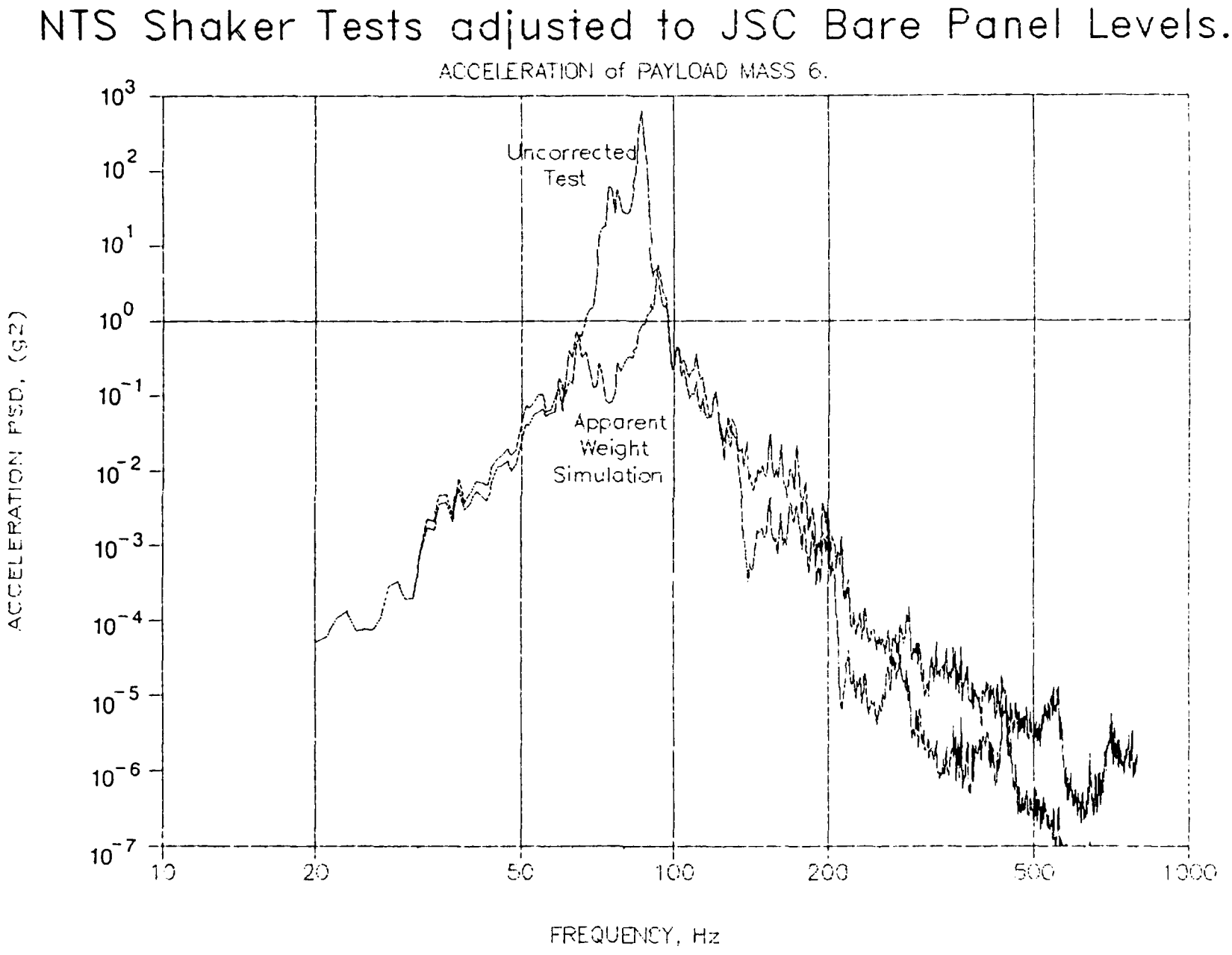

FIGURE 82. PAYLOAD RESPONSE DURING APPARENT WEIGHT SIMULATION AND UNCORRECTED VIBRATION TESTS

Referring to Figure 82, the apparent weight simulation procedure reduces the over-test at the resonance frequency of the payload element by about 30 dB, just as for the input motion correction and blocked force limit procedures. The apparent weight simulation procedure also produces some test level reductions at the resonance frequencies of the other two payload elements, and at most frequencies above 200 Hz, similar to the blocked force limit procedure. However, the reductions at the higher frequencies are not as great as those which occurred for the blocked force limit procedure, and are somewhat closer to the correct result shown in Figure 79.

In summary, the apparent weight simulation procedure works well with the following advantages and disadvantages.

Advantages

1. The procedure provides the most accurate simulation of the input vibration to the payload.

2. The procedure requires no knowledge of the payload apparent weight.

3. The procedure is not vulnerable to errors due to possible nonlinear payload response characteristics.

4. The procedure automatically corrects the specified test levels for payload weight, as well as resonant responses.

Disadvantages

The procedure requires a modification of present shaker equalizer systems to be executed online.

8.6 Summary

All three candidate procedures yielded good results for the test case considered. From a practical viewpoint, the blocked force limit procedure is considered the most attractive of the three approaches because it is generally the simplest to implement. However, the apparent weight simulation procedure

is also attractive if the required algorithms can be implemented in real time on shaker equalizers.

To demonstrate the application of the blocked force limit procedure with a conventional envelope test specification, assume a specification is generated by enveloping the payload input vibration, using a combination of loaded and unloaded mounting structure vibration measurements from the JSC acoustic test, as illustrated in Figure 83. By scaling the vibration test data in Section 7 to this input level, the vibration response of the payload (the response of the heavy resonant element), with and without the blocked force limit applied, would be as shown in Figure 84. Also shown in Figure 84 is the actual payload response measured during the acoustic tests. Again it is seen that the blocked force limit procedures dramatically reduces the overtest of the payload at its resonance frequency by about 30 dB, but still provides a conservative test relative to the actual response measured during the acoustic test.

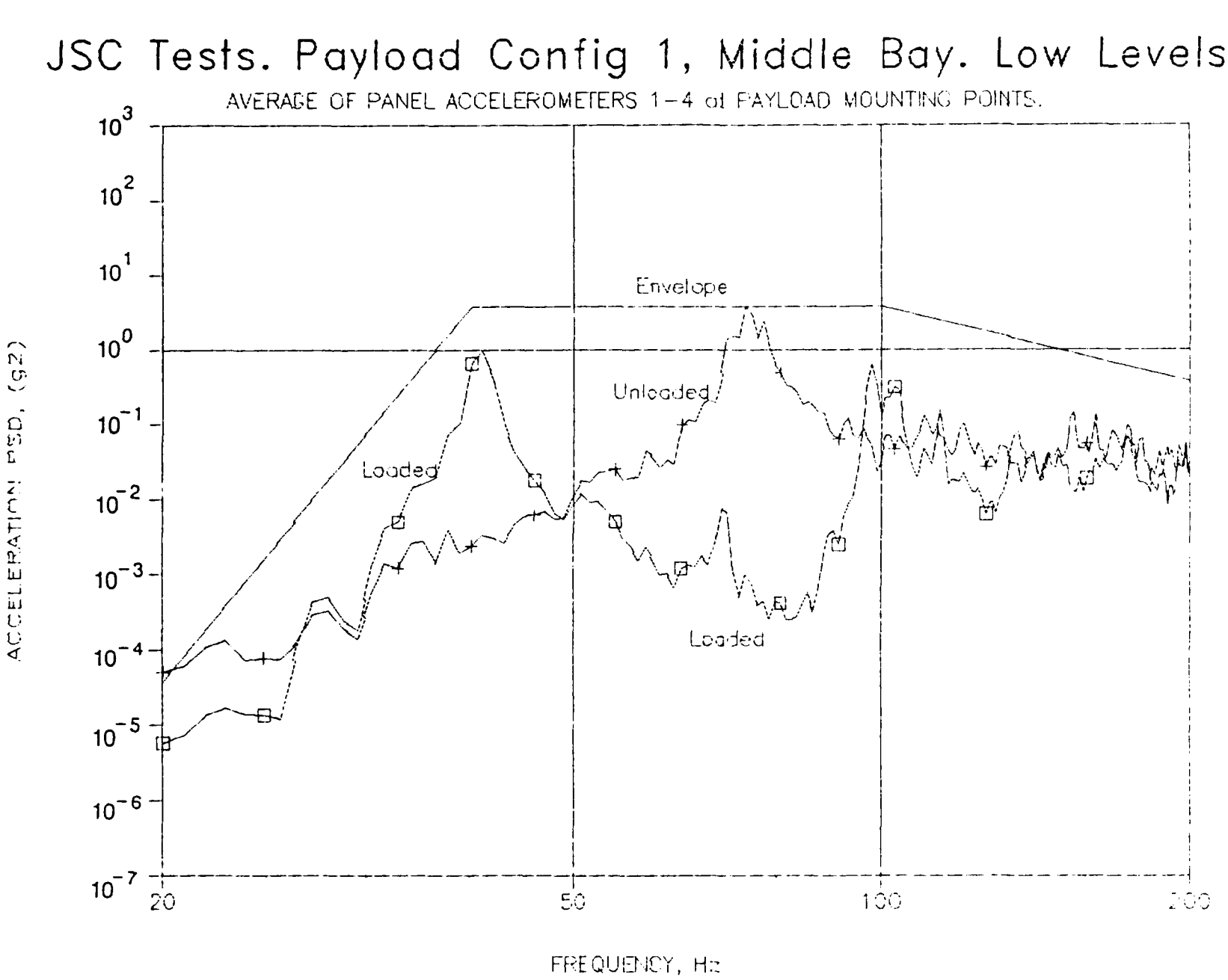

FIGURE 33. DERIVATION OF TEST SPECIFICATION FROM ENVELOPE OF MEASURED MOUNTING STRUCTURE VIBRATION DATA

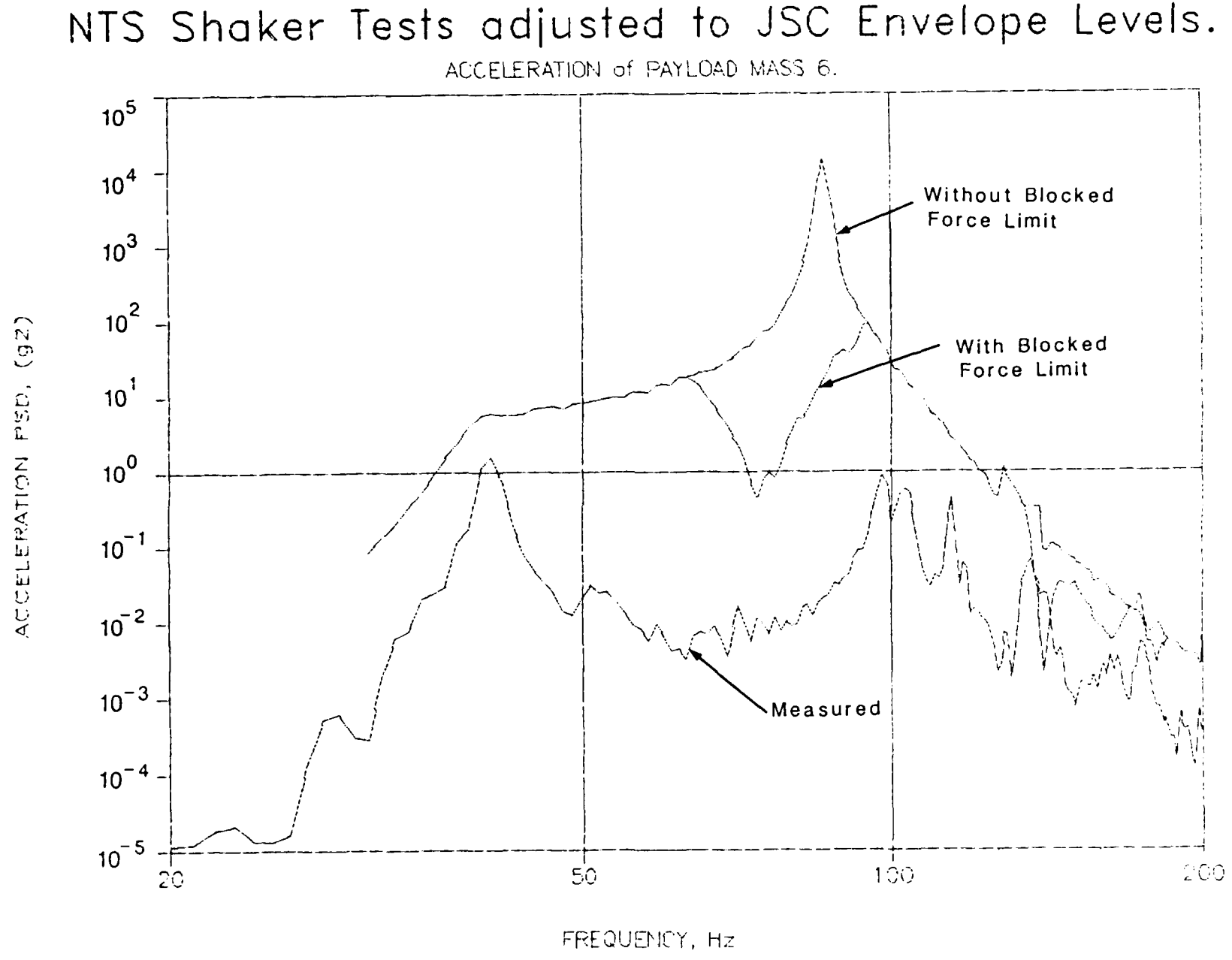

FIGURE 84. PAYLOAD RESPONSE TO CORRECTED AND UNCORRECTED VIBRATION TEST SPECIFICATION

9. CONCLUSIONS AND RECOMMENDATIONS

Three separate procedures have been formulated for performing mechanical vibration tests on orbiter sidewall-mounted payloads in a manner that accounts for the mounting point inertance (or apparent weight) of the orbiter sidewall, and hence, avoids the overtesting problem that commonly occurs in conventional vibration tests at the frequencies of payload resonances. The three procedures are:

(a) A method based upon correcting the vibration test shaker input motion to the payload to account for the mounting point apparent weight (input motion correction procedure),

(b) A method that limits the input force from the vibration test shaker to no more than the blocked force produced by the orbiter sidewall (blocked force limit procedure),

(c) A method that allows the vibration test shaker to simulate, in real time, the apparent weight of the orbiter sidewall (apparent weight simulation procedure).

The three procedures have been experimentally verified using acoustic and vibration test data measured on a special test panel and simulated payload assembly. The test results indicate all three procedures work well, but the blocked force limit procedure is generally the easiest to implement. On the other hand, the apparent weight simulation procedure has the potential for providing the most accurate simulation of the payload vibration environment.

The three procedures require certain common information, as follows:

1. A knowledge of the mounting point apparent weight of the orbiter structure.

2. The ability to measure the interface force delivered by the shaker to the payload.

The blocked force limit and apparent weight simulation procedures also require a shaker equalization system that can simultaneously control the input force and motion from the shaker to the payload. The input motion correction procedure also requires a knowledge of the net driving point apparent weight of the payload.

To determine the mounting point apparent weight of the orbiter structure, a series of experiments were performed on OV-101 (the first orbiter vehicle) to measure the apparent weights of the sidewall along the three orthogonal axes at representative mounting point locations for sidewall-mounted payloads (more specifically, the attachment points for Adaptive Payload Carriers). The results of these tests satisfy Requirement 1 above.

To provide a simple force measurement procedure, extensive tests were performed on an electrodynamic shaker to investigate the relationship between the armature current and the interface force between the shaker table and a load. The results confirmed that there is a highly linear, noise free, relationship between current and force that can be determined for any electrodynamic shaker with a wire-wound armature (a linear current-force relationship will not exist for certain large Unholtz-Dickie shakers).

Concerning the shaker equalization system, present shaker equalizers are designed to control only table motion, not force. However, it appears that the required changes in the present equalizers might be implemented without substituting a completely new equalizer, at least for some models.

For the input motion control procedure, which requires a knowledge of the driving point weight of the payload, a technique has been developed and verified for measuring the driving point apparent weight of any payload on an electrodynamic shaker. The procedure requires the use of the shaker current as a measure of force, but does not require an alteration of the present shaker equalizer systems.

In summary, the following general conclusions are drawn from the studies reported herein.

1. Three different practical and successful techniques have been developed and experimentally verified for performing improved mechanical vibration tests on orbiter sidewall-mounted payloads.

2. All the basic information needed to apply the new vibration test procedures to orbiter sidewall-mounted payloads (assuming they were rigidly attached to the sidewall) has been obtained.

The final remaining problem has to do with the fact that orbiter sidewall-mounted payloads are <u>not rigidly attached to the orbiter sidewall</u>. Instead, sidewall-mounted payloads are attached to Adaptive Payload Carriers (APC) that, in turn, are attached to the orbiter sidewall at three points with loose fits to allow for thermal expansion problems. Along the lateral (y) axis, in particular, the APC attaches to the sidewall with a 25-mil gap at all three attachment points. It is not clear at this time how this gap will influence the improved vibration test procedures that have been developed.

In light of the above noted problem, the following recommendations are made.

1. Investigate the APC mounting gap problem and formulate possible solutions.

2. Perform further acoustic and vibration tests on the test panel and simulated payload assembly used for the present study, but with a gap between the payload and (a) the panel for the acoustic tests, and (b) the shaker for the vibration tests.

3. Re-evaluate the improved test procedures developed in the present study when the payload is loosely mounted, and establish a final appropriate test procedure.

4. Verify the final test procedure through a vibration test of a simulated Oasis 2 payload mounted on an actual APC with a loose attachment to the shaker.

The results of the above recommended activities should permit the final formulation of an improved test procedure for orbiter sidewall mounted payloads that will be effective even with the loosely-mounted APC.

References

1. Piersol, A.G., and Klein, G.J., "The Development of Vibration Test Specifications for Spacecraft Applications", NASA CR-234, Goddard Space Flight Center, Maryland, May 1965.

2. Himelblau, H. et al., "Assessment of Space Vehicle Aeroacoustic-Vibration Prediction, Design, and Testing", NASA CR-1596, Langley Research Center, Virginia, July 1970.

3. Curtis, A.J., et al., Selection and Performance of Vibration Tests, SVM-8, Shock and Vibration Information Center, Washington, D.C., 1971.

4. Scharton, T.D., "Development of Impedance Simulation Fixtures for Spacecraft Vibration Tests", NASA CR-1352, Langley Research Center, Virginia, May 1969.

5. Curtis, A.J., and Hererra, J.G., "Random Vibration Test Level Control Using Input and Test Item Response Spectra", Shock and Vibration Bulletin, No. 37, Part 3, pp. 47-60, January 1968.

6. Piersol, A.G., "Vibration and Acoustic Test Criteria for Captive Flight of Externally Carried Aircraft Stores", AFFDL TR 71-158. Wright-Patterson Air Force Base, Ohio, December 1971.

7. Anon. "Definition of SSV Structure-Borne Random Vibration Environment for DoD Payloads", SD-CF-0206, January 1987.

8. Piersol, A.G., "The Development of Vibration Test Specifications for Flight Vehicle Components", J. Sound Vib., 4, 1, pp. 88-115, January 1968.

9. Hixson, E.L., "Mechanical Impedance", Chapter 10, Shock and Vibration Handbook, (ed: Harris and Crede), 2nd edition, McGraw-Hill, New York, 1976.

10. Wilby, J.F., and Piersol, A.G., "An Evaluation of Shuttle Vibration at Payload Attachments during Lift-Off", Astron Report 7072-01, August 1987.

11. Hipol, P.J., "Finite Element Model of the Space Shuttle Cargo Bay", Astron Report 7128-01, January 1988.

12. Wilson, B., and Tsairides, D., "OEX Autonomous Supporting System (OASIS) Stress Analysis Report", Lockheed Engineering and Management Services Company Report, LEMSCO 24140 Addendum #3, July 1987.

13. Sanders, J.A., "OASIS I, Flights One and Two Data Analysis", Martin Marietta Corp. Report, MCR-86-2019, September 1986.

14. Gockel, M.A., Editor "Handbook for Superelement Analysis, MSC/NASTRAN Version 61", The MacNeal-Schwendler Corporation, 1982.

15. Hipol, P.J., and Piersol, A.G., "Efficient Implementation of Random Pressure Fields with the Finite Element Method", SAE Paper 871740, October 1987.

16. Pope, L.D., and Wilby, J.F., "Space Shuttle Payload Bay Acoustics Prediction Study, Volume II, Analytical Model", NASA Contractor Report CR-159956, March 1980.

17. Piersol, A.G., "Structural Locations for OV-101 Mechanical Impedance Measurements", Astron TM7114-12R to W.F. Bangs (GSFC), 15 May 1987.

18. Bowker, A.H., and Lieberman, G.J., Engineering Statistics, p. 225, Prentice-Hall, Englewood, NJ, 1959.

19. Bendat, J.S., and Piersol, A.G., Random Data: Analysis and Measurement Procedures, 2nd edition, p. 41, Wiley, New York, 1986.

20. op. cit., Bendat and Piersol, p. 54.

21. O'Hara, G.J., "Mechanical Impedance and Mobility Concepts", J. Acous. Soc. Am., Vol. 41, No. 5, pp. 1180-1184, May 1967.

22. Rubin, S., "Mechanical Immittance - and Transmission - Matrix Concepts", J. Acous. Soc. Am., Vol. 41, No. 5, pp. 1171-1179, May 1967.